

ENRICHED ISOGEOMETRIC ANALYSIS FOR
PARAMETRIC DOMAIN DECOMPOSITION AND FRACTURE ANALYSIS

A Dissertation

Submitted to the Faculty

of

Purdue University

by

Chun-Pei Chen

In Partial Fulfillment of the

Requirements for the Degree

of

Doctor of Philosophy

December 2020

Purdue University

West Lafayette, Indiana

THE PURDUE UNIVERSITY GRADUATE SCHOOL
STATEMENT OF DISSERTATION APPROVAL

Dr. Ganesh Subbarayan, Chair

School of Mechanical Engineering

Dr. Marcial Gonzalez

School of Mechanical Engineering

Dr. Thomas Siegmund

School of Mechanical Engineering

Dr. Rodrigo Salgado

School of Civil Engineering

Approved by:

Dr. Nicole Key

Head of the School Graduate Program

*To my family, fiancée and mother
for their unconditional support and love*

ACKNOWLEDGMENTS

When reviewing my life during the past few years at Purdue University, I found myself begin to cherish the journey more than the destination. What is even more precious is the friendship and relationship built during the course of this endless journey of learning. It is the teachers, mentors, colleagues, friends and family that turn a plain period of time into a meaningful life.

I feel extremely privileged to have the chance to work with my advisor, Professor Ganesh Subbarayan. I can still bring back my memory to the first time discussing Green's function in front of the office desk. I still remember the times when I doubting myself after working around the clock for indentation experiments and writing scripts for the simulations. It is his unwaivering patience, insightful thoughts and profound knowledge that inspire me to become a better individual. I owe my deep gratitude to his enlightened guidance in all respects.

I want to sincerely thank my esteemed committee members: Prof. Marcial Gonzalez, Prof. Rodrigo Salgado and Prof. Thomas Siegmund for their constructive suggestions and advice. I also owe my gratitude to Dr. Kamal Sikka from IBM for being my project mentor, and Dr. Siva Gurrum from Texas Instruments for being my internship supervisor. I am also grateful to the financial support from Cooling Technology Research Center, Semiconductor Research Corporation and Purdue University.

I want to extend the acknowledgments to the alumni and members of the HiDAC lab. I would like to thank Hung-Yun for being the first person remotely introducing the lab to me and for being my mentor during the internships. I am thankful to Aniruth for helpful discussion, Tao for our effective collaboration, Yuvraj for our friendship and Yaxiong for our productive cooperation. I also want to thank Chetan, Chung-Shuo, Colin, David, Huanyu, Pavan, Sanjit, Sukshitha, Sudarshan and Travis

for their assistance and company in ME 3139, in the Railway building and in the underground.

Many thanks must go to my friends for their encouragement during my doctoral study. Their constant company, either locally or remotely, have made my life more delightful at West Lafayette. I would like to thank my fiancée for sharing my thoughts, emotions and dreams at every moment. Lastly, my deepest gratitude goes toward my siblings, and most importantly, my mother. As a single parent having five children, her unconditional supports and love throughout my life are beyond words that can be fitted in any form of document.

TABLE OF CONTENTS

	Page
LIST OF TABLES	x
LIST OF FIGURES	xi
ABSTRACT	xix
1. INTRODUCTION	1
1.1 Literature Review	4
1.1.1 Multi-Patch Coupling Isogeometric Analysis	4
1.1.2 Modeling of Crack Tip Singularities and Crack Face Discontinuity	7
1.2 Gaps in Existing Literature	9
1.3 Research Objectives	10
1.4 Outline	10
2. BACKGROUND	12
2.1 Non-Uniform Rational B-Spline Approximation Space	12
2.2 Enriched Isogeometric Analysis	14
2.3 Choice of Weight Function in EIGA	19
2.4 The Need for Distance and Projection	22
3. CONFIGURATIONAL DERIVATIVES, CONFIGURATIONAL FORCES AND CONFIGURATIONAL OPTIMIZATION	26
3.1 Configurational Optimization Problem and Configurational Tensor for Insertion of Arbitrary Heterogeneity	27
3.1.1 The Configurational Optimization Problem and Configurational Derivative	28
3.1.2 Configurational Derivative Corresponding to Translation, Ro- tation, and Scaling of Heterogeneity: Deriving Configurational Forces	35
3.2 Numerical Examples	37
3.2.1 Optimal Location of an Elliptical Hole in a Plate	37
3.2.2 Optimal Orientation of an Elliptical Hole	39
4. IMPLEMENTATION	41
4.1 HiDAC: Hierarchical Design and Analysis Code	41
4.2 HiDAC Key Modules and Their Features	43
4.3 NURBS Geometry Modeler	45
4.4 Analysis Flow	50
4.4.1 Overview	50

	Page
4.4.2 Scripting Interface	51
5. PARAMETRIC STITCHING FOR SMOOTH COUPLING OF SUBDOMAINS WITH NON-MATCHING DISCRETIZATIONS	54
5.1 Construction of Enriched Field Approximations	54
5.2 P-Stitching Formulation for Elasto-Static Problems	57
5.2.1 Discretization for Blending of Two Patches	59
5.3 Patch Test	61
5.3.1 Matching and Hierarchical Discretizations	62
5.3.2 Non-matching Discretizations	65
5.4 Numerical Examples	67
5.4.1 Timoshenko Beam	68
5.4.2 Thick-Walled Cylinder Subjected to Internal Pressure	70
5.4.3 Heat Conduction in Coupled Non-planar Surfaces	72
5.4.4 Three-dimensional Hook	74
6. ISOGEOMETRIC ENRICHMENT FOR STRESS SINGULARITIES IN MULTIMATERIAL WEDGES	78
6.1 Asymptotic Analysis of Stress Singularities	78
6.2 Isogeometric Enrichment for Multi-material Wedges and Cracks	83
6.3 Discretized Equations	88
6.4 Numerical Examples	90
6.4.1 Bi-material Wedge with Bonded Interface	90
6.4.2 Inclined Crack in a Homogeneous Plate	93
6.4.3 Quasi-Static Crack Propagation	95
7. CONFIGURATIONAL FORCE IN ENRICHED ISOGEOMETRIC ANALYSIS 98	
7.1 Configurational Force: A Brief Introduction	98
7.2 Configurational Force as Crack Propagation Criterion	100
7.3 Numerical Evaluation of Configurational Force	100
7.4 Numerical Examples	102
7.4.1 Homogeneous Plate	103
7.4.2 Plate with Hole/Inclusion	105
7.4.3 Bi-material Wedge with Bonded Interfaces	107
7.4.4 Crack in a Homogeneous Plate	108
8. APPLICATION: RATCHETING-INDUCED FRACTURE OF BEOL STRUCTURES OF MICROELECTRONICS	110
8.1 Overview	110
8.2 Modeling Methodology	111
8.3 Global Model and Ratcheting-induced Stress Evolution	112
8.3.1 Global Deformation	115
8.3.2 Evolution of Stress in BEOL films	118
8.4 Load Decomposition and Critical Loading Mode Identification	121

	Page
8.5 EIGA of Stress Singularities in BEOL Structures	124
8.6 Configurational Force Based Crack Propagation in BEOL Structure	129
8.7 Concluding Remarks	129
9. CLOSURE	132
9.1 Summary and Novel Contributions	132
9.2 Recommendation for Future Research	134
9.2.1 Mixed-Type Isogeometric Enriched Field Approximation	134
9.2.2 Three-dimensional P-Stitching with Extraordinary Points	135
REFERENCES	136
A. TENSOR TRANSFORMATION	149
A.1 Transformation of Symmetric Tensor in Voigt Form	150
B. MATERIAL PROPERTIES	153
C. ESTIMATING THE MODULUS AND YIELD STRENGTH OF THE TOP-LAYER FILM ON MULTILAYER BEOL STACKS	154
C.1 Introduction	154
C.2 Theory	158
C.2.1 Classical Indentation Models for Homogeneous Materials	158
C.2.2 Effective Modulus of Multilayer Stacks	160
C.2.3 Dominant Regime Theory	163
C.3 Experimental Data and its Analysis	165
C.3.1 Two-Layer Stack	166
C.3.2 Multilayer Stack	168
C.4 Inverse Finite Element Analysis Procedure	170
C.4.1 Finite Element Model	171
C.4.2 Posing of Property Estimation as an Optimization Problem	174
C.5 Inverse Finite Element Analysis Results	176
C.5.1 Two-layer Stack	176
C.5.2 Multilayer Stack	179
C.6 Conclusion	182
C.7 Proof of the Monotonicity of the Weight Function	183
C.8 Linearization of the Weight Function	184
C.9 Properties of the Modulus Participation Functions	185
D. TOPOLOGY OPTIMIZATION FOR EFFICIENT HEAT REMOVAL IN THREE DIMENSIONAL PACKAGES	186
D.1 Introduction	186
D.2 Thermal Conduction Analysis	187
D.2.1 Finite Element Method	188
D.2.2 Discretization	188
D.3 Topology Optimization	190

	Page
D.3.1 Updating Thermal Conductivities	192
D.3.2 Sensitivity Analysis	192
D.4 Results and Discussion	193
D.4.1 Two Dimensional Heat Spreader Design	193
D.4.2 Heat Spreader Design Validation	195
D.4.3 Thermal Design of TSVs	199
D.5 Conclusion	201
VITA	202

LIST OF TABLES

Table	Page
1.1 Comparison of weak coupling techniques for multi-patch analysis.	6
4.1 NURBS definition of the circular arc shown in Figure 4.2c.	46
6.1 Coefficients of angular function corresponding to symmetric and anti-symmetric loading modes at a crack tip when the strengths of singularity are $\lambda=0.5$	85
6.2 Coefficients of angular function associated with the first two modes of the bi-material wedge with bonded interface obtained by asymptotic analysis.	91
8.1 Dimensions of the aluminum line structure for the global model.	113
8.2 Microelectronics package material properties at room temperature.	114
8.3 Parametric values of line width, line spacing and passivation thickness (SiN). The value with asterisk sign indicates the nominal parameters.	125
8.4 The strength of singularities calculated from asymptotic analysis at six corners of BEOL structure.	127
B.1 Temperature-dependent elastic properties of die attach.	153
B.2 Temperature-dependent elastic properties of mold compound.	153
C.1 TEOS modulus extracted from the TEOS-Si two-layer specimen.	168
C.2 TEOS modulus extracted from the TEOS-Al-Si ₃ N ₄ -Si multilayer specimen.	169
C.3 Nominal mechanical properties used in the model and their literature sources.	172
C.4 Initial parameter values for the optimization problem.	175
C.5 Estimated Young's modulus and yield strength of TEOS film on two-layer stack by IFEA	177
C.6 Estimated Young's modulus and yield strength of TEOS film on multi-layer stack obtained through IFEA	180
D.1 Model thermal conductivities and thicknesses.	199

LIST OF FIGURES

Figure	Page
1.1 (a) cracked polyimide film surrounding a metal line in a back end of line structure [1], and (b) cracked copper/low- κ dual damascene integrated structures [2,3].	1
1.2 Volumetrically partitioned torus solids represented by (a) piecewise polynomial finite elements, and (b) NURBS.	3
2.1 (a) (d) Knot vectors in parametric space. (b) (e) Basis functions in parametric space. (c) (f) NURBS curve and surface approximation in physical space.	14
2.2 Composition of primitive design states to form the complex design state [85].	16
2.3 Enriched Isogeometric approximation is constructed by blending an approximation built on the enriching entity as a function of normal distances with the approximation on the underlying domain.	18
2.4 Illustration of strategies to track internal boundary as well as construct enriched approximations by (a) classical FEM (b) GFEM, and (c) EIGA .	19
2.5 Cubic, quartic and exponential weight function values.	21
2.6 Cubic, quartic and exponential weight function derivatives with respect to normalized, signed distance.	21
2.7 Illustration of steps in constructing the algebraic level sets on Bezier curves [91].	24
2.8 Illustration of steps in constructing the algebraic level sets on NURBS curves [91].	24
2.9 Comparison of the projected foot points obtained using Parametric Iterations, Newton-Raphson Iterations and Algebraic Level Sets. For points close to the curve, all three methods yield an identical solution.	25
3.1 Definition of the configurational optimization problem: (a) Arbitrary subdomain within the solid (b) Elasticity problem associated with the homogeneous subdomain (c) Elasticity problem associated with heterogeneous subdomain created by introducing an arbitrary heterogeneity.	30
3.2 Specific design velocities imposed on the heterogeneity: (a) Translation (b) Rotation about an axis passing through \mathbf{x}_p (c) Scaling with respect to \mathbf{x}_p .	35

Figure	Page
3.3 (a) Configurational optimization problem to determine the optimal location of a elliptical hole. (b) Numerical estimation of structural compliance as a function of location of the elliptical hole.	37
3.4 Von Mises stress contour during configurational optimization at (a) the initial step, (b) intermediate step 1, (c) intermediate step 2, and (d) the end of optimization determining the optimal location of the elliptical hole.	38
3.5 (a) Configurational optimization problem to determine the optimal orientation of an elliptical hole. (b) Calculated structural compliance as a function of orientation of the elliptical hole.	39
3.6 Von Mises stress contour during configurational optimization at (a) the initial step, (b) intermediate step 1, (c) intermediate step 2, and (d) the end of optimization determining the optimal orientation of an elliptical hole.	40
4.1 Code architecture of matlab HiDAC.	43
4.2 NURBS curve representation of (a) a straight spline, (b) rectangular lines, (c) a circular arc, and (d) an arbitrary curve.	47
4.3 NURBS surface representation of (a) a rectangular patch, (b) a cylindrical surface, (c) a ruled surface, and (d) a coons patch.	48
4.4 Extrusion operation of NURBS representation (a) from a curve to a surface, and (b) from a surface to a volume.	49
4.5 Revolution operation of NURBS representation (a) from a curve to a surface, and (b) from a surface to a volume.	49
4.6 Typical flow of control using matlab HiDAC for an enriched isogeometric analysis.	50
4.7 Program (a) initialization script, (b) typical user inputs, and (c) the generated NURBS representation of a volume.	51
4.8 HiDAC environment for (a) analysis, and (b) post-processing.	52
4.9 (a) Temperature solution contour over the outer boundary, and (b) heat flux vectors within the domain.	53
5.1 Illustration of non-matching parametric domains. The interfaces are shown separated for clarity, but $\Gamma_e \equiv \Gamma_i$	55
5.2 Problem domain consisting two subdomains that need to be smoothly coupled.	57
5.3 Support region of the weight field $w(d_i)$ in parametric space and in Euclidean space. The support region is chosen to coincide with the first non-zero knot span in the parametric space of the underlying domain. . . .	59

Figure	Page
5.4 (a) Patch test setup and (b) expanded view of the individual subdomains and the coupling interface.	62
5.5 Example of discretization schemes for two- and three-dimensional patch tests (NURBS degree=1). (a) and (d) matching scheme. (b) and (e) hierarchical scheme. (c) and (c) non-matching scheme. The red dots are control points while blue squares and black lines indicate edges of the spline elements (non-zero knot spans).	63
5.6 Relative L_2 norm of error in displacement with (a) homogeneous and (b) bi-material interface coupled using cubic weight function. (c) Matching and hierarchical discretization were used for refinement.	64
5.7 (a) Relative L_2 norm of error in displacement and (b) in strain energy for homogeneous interface coupled using exponential weight function. (c) The least refined mesh of the two-dimensional matching discretization that was analyzed.	65
5.8 (a) Displacement u_z and (b) normal strain ε_{zz} contours for homogeneous patch test. (c) Displacement u_z and (d) normal strain ε_{zz} contours for bi-material patch test.	66
5.9 Displacement and strain along the paths for (a) homogeneous and (b) bi-material patch test with non-matching discretization. (c) Path along the two- and three-dimensional patches with non-matching discretization along which the solutions are plotted.	67
5.10 (a) The relative L_2 norm of error in displacement for homogeneous coupling and (b) bi-material coupling. (c) The coarsest mesh of the assumed two-dimensional non-matching discretization.	67
5.11 (a) Dimensions, boundary conditions, and (a) NURBS discretization of Timoshenko beam.	68
5.12 (a) Vertical displacements u_y and (b) its relative error $u_y/ u_{max} $ in the Timoshenko beam.	69
5.13 Displacement and stress components along the indicated path in the Timoshenko beam. The dotted line shows the location of coupling interface Γ_e along the length of the beam.	70
5.14 (a) Boundary condition on the cylinder wall subjected to internal pressure, and (b) (c) (d) hierarchical discretizations with the number of subdomains $n_\Omega = 2, 3, 4$, respectively.	71
5.15 Plots of contours of (a) u_r and (b) $\sigma_{\theta\theta}$. Contours of relative error in (c) u_r and (d) von Mises stress σ_{eq}	73

Figure	Page
5.16 (a) Problem definition and discretization of the two coupled non-planar NURBS surfaces, (b) solution temperature contours and (c) temperature value along the path $z \in [-a, a]$ with $r = R, \theta = \pi/4$.	74
5.17 The hook model's (a) coupling structure, (b) dimensions and boundary conditions.	75
5.18 Magnitude of displacement $\ \mathbf{u}\ $ obtained by (a) the present method and (b) the finite element method.	76
5.19 Von Mises stress obtained by (a) the present method and (b) the finite element method.	77
6.1 (a) Bi-material wedge with two bonded interfaces and (b) Bi-material wedge with one bonded interface and a second debonded interface.	81
6.2 Configuration of boundary value problem with (a) singular stress enrichment and (b) hierarchically constructed crack enrichment.	84
6.3 Composition of domain, material interfaces and multi-material junction represented by NURBS.	85
6.4 (a) x -component and (b) y -component of enriching function Ψ_s subjected to Mode I loading. (c) x -component and (d) y -component of enriching function Ψ_s subjected to Mode II loading.	86
6.5 Weight field (a) w_t , (b) $w_e - w_t$, and (c) w_e associated with a single edge notch cracked plate.	87
6.6 (a) Boundary conditions on a bi-material wedge with bonded interfaces. The \bullet in the figure indicates the location of singular enrichment. (b) Contour of weight function w_t used in the enriched filed approximation.	91
6.7 Convergence of generalized stress intensity factors for bi-material wedge with bonded interface.	92
6.8 The von Mises stress obtained using the finite element method with (a) 50, (b) 722, and (c) 2,450 number of DOF. (d) The von Mises stress contour obtained through enriched isogeometric analysis.	93
6.9 (a) Schematic of boundary conditions of a plate containing center inclined crack under tensile traction. (b) The weight field w_e associated with the inclined crack assuming pseudo sharp deflections at both tips.	94
6.10 Comparison of reference and numerically calculated stress intensity factors (K_I and K_{II}) as a function of inclination angle.	95
6.11 The von Mises stress contours in the domain for a crack at an inclination angle of $\beta = 45^\circ$.	96

Figure	Page
6.12 The vertical displacement u_y contours at (a) Step 1, (b) Step 4, (c) Step 7, and (d) Step 10.	97
7.1 Geometry and boundary conditions of the homogeneous square plate with (a) tractions, and (b) with displacement boundary conditions.	103
7.2 Configurational force in a homogeneous plate with (a) traction boundary conditions, and (b) with displacement boundary conditions.	105
7.3 Geometry and boundary conditions of a plate with a heterogeneity.	106
7.4 Configurational force on (a) a plate with circular hole and (b) a plate with stiff inclusion.	106
7.5 Configurational force calculated on the bi-material wedge with singular stress enrichment. The contours of the first principal stress are shown in the figure along with the configurational force.	107
7.6 Schematic of boundary conditions of a plate containing center inclined crack under tensile traction as illustrated in Figure 6.9a.	108
7.7 (a) Calculated configurational force over the domain and (b) detailed view of the configurational force near the crack in a plate with the horizontal crack.	109
7.8 Comparison of crack deflection angle based on the maximum tensile stress criterion of LEFM and configurational force.	109
8.1 (a) Domains, boundaries, and reference coordinate systems in the multi-level models. (b) Modeling procedures to simulate ratcheting induced fracture in metal lines.	111
8.2 (a) The geometry of the test die and package. (b) Metal line patterns on the test die.	112
8.3 Cross section of the three-dimensional model (structure B). Inset figure shows the region enclosing the BEOL structure Ω_l that was analyzed in the local model.	114
8.4 Discretization of microelectronic package cross-section at (a) the package level, and (b) at the BEOL level. The inset red box indicates where the BEOL-level submodel is located.	115
8.5 Demonstration of polynomial fit to the package outline.	116
8.6 Curvature of the microelectronic package during a thermal cycle between 150°C and -65°C.	117

Figure	Page
8.7 Die edge evolution of the first principal stress (unaveraged) (a) in the TEOS films, and (b) in the silicon nitride films of structure B.	118
8.8 Evolution of the first principal stress' local maxima (unaveraged) (a) in the TEOS films, and (b) in the silicon nitride films throughout the BEOL structure B.	119
8.9 Local maxima of the first principal stress (unaveraged) at the end of the thermal cycle (a) in TEOS film, and (b) in silicon nitride film within the line structure listed in Table 8.1.	120
8.10 Load decomposition of boundary condition for local model into (a) tension, (b) shear, and (c) flexure.	122
8.11 The first principal stress contour (averaged) in silicon nitride and TEOS films at the corner of BEOL structure subjected to (a) shear, (b) tension, and (c) flexure loading at 150°C of the 500-th cycle.	123
8.12 The maximum first principal stress (averaged) in silicon nitride film at -65°C, 100°C and 150°C under tensile, shear and flexural loadings.	124
8.13 A schematic illustration of the BEOL structure showing multi-material wedges.	125
8.14 The materials and their included angles forming six distinctive corners identified in the BEOL structure.	126
8.15 Contour of the first principal stress obtained through enrich field analysis in the BEOL structure (unit: Pa).	127
8.16 Comparison of opening-mode generalized stress intensity factors at Corner H and Corner I in the six parametric designs.	128
8.17 Displacement in x-direction and crack path within the BEOL structure predicted by configurational force.	130
8.18 Comparison of crack path predicted by LEFM max tensile stress criterion (Green) and by configurational force (Magenta).	130
C.1 (a) Schematic of indentation using spherical indenter. The thick dashed line indicates the specimen surface under maximum load whereas the thick solid line is the residual impression after unloading. (b) Typical load-displacement response with three regimes.	159
C.2 Schematic of a rigid Berkovich indenter penetrating a multilayer stack consisting of a n -layer film and a substrate. L_k , $k = 1, 2, \dots, n$ represents the k^{th} layer of the stack.	160
C.3 The weight function Φ_0 with different Poisson's ratios.	162

Figure	Page
C.4 Modulus participation functions of a TEOS-Al-Si ₃ N ₄ -Si multilayer stack.	164
C.5 Two test structures with the same top-layer dielectric film: (a) a TEOS-Si two-layer stack and (b) a TEOS-Al-Si ₃ N ₄ -Si multilayer stack.	165
C.6 Load-displacement response of the TEOS-Si two-layer stack at 300 nm and 600 nm penetration depths. Nine tests were carried-out at each depth. . .	166
C.7 Modulus participation functions of the TEOS-Si two-layer stack.	167
C.8 Multi-depth indentation data for the TEOS-Si two-layer stack.	167
C.9 Three repetitions of load-displacement response of the TEOS-Al-Si ₃ N ₄ -Si multilayer stack at 700 nm penetration depth. The stiffness drop and the low elastic recovery are likely a result of the dielectric cracking and material yielding.	168
C.10 Multi-depth indentation data for the TEOS-Al-Si ₃ N ₄ -Si multilayer stack. Linear regression over data from all depths leads to a poor fit.	169
C.11 Multi-depth indentation data for the TEOS-Al-Si ₃ N ₄ -Si multilayer stack. Linear regression over the TEOS dominant regime yields a good fit. . . .	170
C.12 (a) Mesh and boundary conditions of the TEOS-Si two-layer finite element model. (b) Enlarged 30° sweep section of the axi-symmetric model near the indented region (indicated by the red box in (a)).	173
C.13 Load-displacement response curves from experiment and from FEA. The impact of the value of the yield strength of TEOS film on the simulated response is illustrated.	176
C.14 Objective function response surface contours as well as optimized parameter values on the two-layer stack corresponding to indentation depths of: (a) 200 nm (a) 400 nm (c) 600 nm using Eq. (C.14) and (d) from 200 nm to 700 nm using Eq. (C.15).	178
C.15 Load-displacement response on the two-layer stack using the optimized properties compared against the experimental response for 700 nm indentation.	179
C.16 Objective function response surface contours as well as optimized parameter values on the multilayer stack corresponding to indentation depths of: (a) 300 nm (b) 500 nm (c) 700 nm using Eq. (C.14) and (d) from 200 nm to 700 nm using Eq. (C.15).	181
C.17 Load-displacement response on the multilayer stack using the optimized properties compared against the experimental response for 700 nm indentation.	182

Figure	Page
D.1 Representative 3D package.	186
D.2 Isoparametric 8-noded serendipity element.	189
D.3 Representative structure in a 3D package to perform topology optimization for efficient heat removal.	190
D.4 Topology optimization flow of control.	191
D.5 Boundary conditions and power map on a plate 10 by 10 m in size.	194
D.6 Heat spreader design using (a)-(d) minimizing peak temperature and (e)-(h) minimizing stored energy objectives with metallization ratio of 10, 20, 25 and 45%, respectively.	195
D.7 Peak temperature with different metallization ratio using both objective functions and homogeneous distribution of heat spreading material.	195
D.8 Thermal gradient with different metallization ratio using both objective functions and homogeneous distribution of heat spreading material.	196
D.9 Mean temperature with different metallization ratio using both objective functions and homogeneous distribution of heat spreading material.	196
D.10 Boundary conditions and power map on a plate 11 by 11 m in size.	197
D.11 Topology optimization flow of control in Isight.	197
D.12 Temperature profile (a) before and (b) after the topology optimization by Simulia Isight.	198
D.13 Temperature profile (a) before and (b) after the topology optimization by the developed tool.	198
D.14 Schematic of the 3D package which is integrated with a silicon interposer.	199
D.15 Power map for active layer 1 and active layer 2.	200
D.16 Thermal TSV optimal distribution determined by topology optimization.	200
D.17 Temperature profile of the 3D package (a) before and (b) after thermal TSV placement by topology optimization.	201

ABSTRACT

Chen, Chun-Pei Ph.D., Purdue University, December 2020. Enriched Isogeometric Analysis for Parametric Domain Decomposition and Fracture Analysis. Major Professor: Ganesh Subbarayan, School of Mechanical Engineering.

As physical testing does not always yield insight into the mechanistic cause of failures, computational modeling is often used to develop an understanding of the goodness of a design and to shorten the product development time. One common, and widely used analysis technique is the Finite Element Method. A significant difficulty with the finite element method is the effort required to generate an analysis-suitable mesh due to the difference in the mathematical representation of geometry CAD and CAE systems. CAD systems commonly use Non-Uniform Rational B-Splines (NURBS) while the CAE tools rely on the finite element mesh. Efforts to unify CAD and CAE by carrying out analysis directly using NURBS models termed Isogeometric Analysis reduces the gap between CAD and CAE phases of product development. However, several challenges still remain in the field of isogeometric analysis. A critical challenge relates to the output of commercial CAD systems. B-rep CAD models generated by commercial CAD systems contain uncoupled NURBS patches and are therefore not suitable for analysis directly. Existing literature is largely missing methods to smoothly couple NURBS patches. This is the first topic of research in this thesis. Fracture-caused failures are a critical concern for the reliability of engineered structures in general and semiconductor chips in particular. The back-end of the line structures in modern semiconductor chips contain multi-material junctions that are sites of singular stress, and locations where cracks originate during fabrication or testing. Techniques to accurately model the singular stress fields at interfacial corners are relatively limited. This is the second topic addressed in this thesis. Thus, the overall objective of this dissertation is to develop an isogeometric framework for parametric

domain decomposition and analysis of singular stresses using enriched isogeometric analysis.

Geometrically speaking, multi-material junctions, sub-domain interfaces and crack surfaces are lower-dimensional features relative to the two- or three-dimensional domain. The enriched isogeometric analysis described in this research builds enriching approximations directly on the lower-dimensional geometric features that then couple sub-domains or describe cracks. Since the interface or crack geometry is explicitly represented, it is easy to apply boundary conditions in a strong sense and to directly calculate geometric quantities such as normals or curvatures at any point on the geometry. These advantages contrast against those of implicit geometry methods including level set or phase-field methods. In the enriched isogeometric analysis, the base approximations in the domain/subdomains are enriched by the interfacial fields constructed as a function of distance from the interfaces. To circumvent the challenges of measuring distance and point of influence from the interface using iterative operations, algebraic level sets and algebraic point projection are utilized. The developed techniques are implemented as a program in the MATLAB environment named as *Hierarchical Design and Analysis Code*. The code is carefully designed to ensure simplicity and maintainability, to facilitate geometry creation, pre-processing, analysis and post-processing with optimal efficiency.

To couple NURBS patches, a parametric stitching strategy that assures arbitrary smoothness across subdomains with non-matching discretization is developed. The key concept used to accomplish the coupling is the insertion of a parametric stitching or p-stitching interface between the incompatible patches. In the present work, NURBS is chosen for discretizing the parametric subdomains. The developed procedure though is valid for other representations of subdomains whose basis functions obey partition of unity. The proposed method is validated through patch tests from which near-optimal rate of convergence is demonstrated. Several two- and three-dimensional elastostatic as well as heat conduction numerical examples are presented.

An enriched field approximation is then developed for characterizing stress singularities at junctions of general multi-material corners including crack tips. Using enriched isogeometric analysis, the developed method explicitly tracks the singular points and interfaces embedded in a non-conforming mesh. Solution convergence to those of linear elastic fracture mechanics is verified through several examples. More importantly, the proposed method enables direct extraction of generalized stress intensity factors upon solution of the problems without the need to use *a posteriori* path-independent integral such as the J-integral. Next, the analysis of crack initiation and propagation is carried out using the alternative concept of configurational force. The configurational force is first shown to result from a configurational optimization problem, which yields a configurational derivative as a necessary condition. For specific velocities imposed on the heterogeneities corresponding to translation, rotation or scaling, the configurational derivative is shown to yield the configurational force. The use of configurational force to analyze crack propagation is demonstrated through examples.

The developed methods are lastly applied to investigate the risk of ratcheting-induced fracture in the back end of line structure during thermal cycle test of a epoxy molded microelectronic package. The first principal stress and the opening mode stress intensity factor are proposed as the failure descriptors. A finite element analysis sub-modeling and load decomposition procedure is proposed to study the accumulation of plastic deformation in the metal line and to identify the critical loading mode. Enriched isogeometric analysis with singular stress enrichment is carried out to identify the interfacial corners most vulnerable to stress concentration and crack initiation. Correlation is made between the failure descriptors and the design parameters of the structure. Crack path from the identified critical corner is predicted using both linear elastic fracture mechanics criterion and configurational force criterion.

1. INTRODUCTION

Cracks are a critical concern for the reliability of engineered structures. As structures subject to excessive or repeated loadings, microscopic cracks may initiate, coalesce and propagate from where the stress concentrates. Features such as notches, multi-material junctions as well as other heterogeneities such as inclusions or voids, cause most vulnerability to cracking. Eventually, cracks degrade the mechanical integrity of the structure and may lead to catastrophic failure.

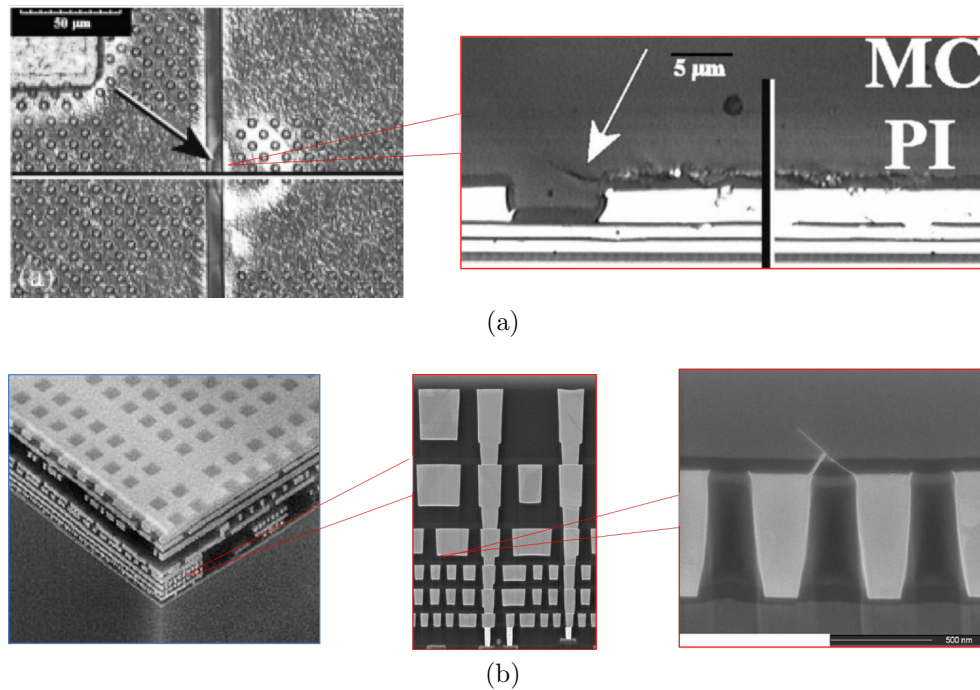


Figure 1.1. (a) cracked polyimide film surrounding a metal line in a back end of line structure [1], and (b) cracked copper/low- κ dual damascene integrated structures [2, 3].

The back end of line (BEOL) of microelectronic devices, as shown in Figure 1.1, is one of those structures susceptible to cracking. The architecture of BEOL consists

of a three-dimensional geometry formed by layering materials including dielectrics, metals and passivation overcoat. It is the electrical network used to route the power and signals between functional circuits and the enclosing package. Therefore, its structural integrity is of crucial importance to the reliability of microelectronic devices. Under physical loading, stress migration and fracture of thin films are both the common causes of mechanical failures in the BEOL structures [4]. Stress concentration resulting from external loads could easily develop in the presence of geometric discontinuities or material heterogeneity. In linear elastic solids, stress fields at the interfacial corner is known to be proportional to $r^{-\lambda}$ where r is the distance to the corner and λ represents the strength of singularity [5–7]. Due to the induced stress singularities, BEOL structures containing brittle dielectrics and passivation films are susceptible to higher risk of failures including delamination as well as cracking.

To better understand the mechanism of failures with the aim of developing a more reliable design, it is important to accurately determine the state of stress. While the finite element method (FEM) is the most common tool used to determine the global state of stress in microelectronic packages, it is often insufficient and inefficient to be used for analyzing the local state of stress for the following reasons. First, the solid element approximates the behavioral field as piecewise polynomial, which poorly describes the singular stress. Therefore, numerical accuracy in the state of stress is achieved only in the limit of mesh refinement. Second, traditional FEM can only track the discontinuity explicitly through the separation of elemental faces. Combining both of the above critical drawbacks, traditional FEM is often not used for complex structures such as those on microelectronic device BEOL to accurately predict the local state of stress.

Ideally, a fixed underlying mesh with embedded interfaces capturing stress singularities as well as moving boundaries will be effective in addressing the gap between specific engineering needs and the commonly used computational tools. In the context of FEM, formulations such as Partition of Unity FEM (PUFEM) [8,9] and eXtended FEM (XFEM) [10,11] are well capable of resolving the challenges. However, genera-

tion of the fixed underlying finite element mesh itself is a non-trivial task in general. It has been observed in industrial practice and documented by Ted Blacker at the Sandia National Laboratories that almost 80% of the the overall analysis time is attributed to generating an analysis-suitable mesh while only 20% of the overall time is actually attributed to the computational solution time. The main bottleneck is the need for converting the models between that used in computer-aided engineering (CAE) and that in computer-aided design (CAD). While CAD systems predominantly adopt Non-Uniform Rational B-Spline (NURBS) as the basis for representing the geometries, FEM approximates the CAD geometry through a finite number of piece-wise polynomial elements. A comparison of volumetric representations of a partitioned torus between FEM and NURBS is illustrated in Figure 1.2. Since the use of piecewise-polynomial element is inevitable and is fundamental to finite element method, alternative analysis methods that use identical basis functions as CAD will efficiently bridge the CAD&E integration challenges.

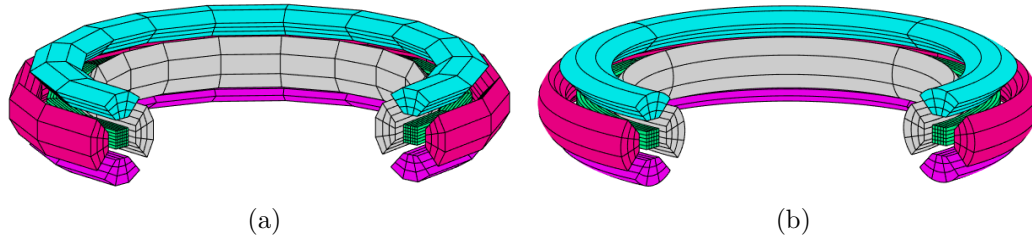


Figure 1.2. Volumetrically partitioned torus solids represented by (a) piecewise polynomial finite elements, and (b) NURBS.

Renken and Subbarayan [12] are among the earliest researchers who carried out analysis directly using NURBS basis functions. Natekar, Zhang and Subbrayan [13] later demonstrated a procedure to achieve integrated design and analysis using NURBS geometry termed as Constructive Solid Analysis (CSA) analogous to the Constructive Solid Geometry (CSG) procedure of CAD. The idea of utilizing the identical basis was later termed as isogeometric analysis (IGA) [14, 15] to contrast with

the traditional finite element analysis (FEA). Despite the fact that the method of isogeometric analysis has been successfully developed in many other areas [16], state of the art IGA framework capable of modeling complex structures, such as the one shown in Figure 1.1, does not exist yet. Given the extensive geometric complexity and material heterogeneity in a cracked engineering body, the following two capabilities are believed to be critical in the context of IGA.

1. Multi-patch coupling for the purpose of domain decomposition or local refinement, and
2. Modeling methodology for multi-material junction stress singularities and crack interface discontinuity

Relevant literature on both topics are surveyed, reviewed and summarized in the next section.

1.1 Literature Review

1.1.1 Multi-Patch Coupling Isogeometric Analysis

Decomposed and incompatible parametric subdomains are common to both CAD and CAE. For instance, boundary representation (B-rep) using trimmed NURBS surfaces to model the geometry of solid objects is the most commonly adopted strategy in commercial CAD systems. Commonly, B-rep models contain multiple NURBS patches due to the rectangular tensor product topology of the representation coupled with the need for local refinement to capture complex free-form shapes. At the present time, in multi-patch models resulting from intersections of parametric surfaces, gaps and overlaps at the intersections is seemingly unavoidable [17]. As a result, trimmed surfaces resulting from commercial CAD systems are rarely compatible and watertight.

A common CAD solution approach to overcome incompatible parametric patches is based on new spline technologies that enable local refinement. These approaches

are similar in philosophy to the subdivision surfaces that enable the modeling of complex free-form surfaces [18–21]. HB-splines [22], T-splines [23, 24], PHT-splines [25], THB-splines [26], LR B-splines [27] and the recently developed U-splines [28] are examples of spline representations that allow local refinement. The ability to perform local refinement allows one to use a single, hierarchically refined, patch to represent a geometry that would otherwise be described by multiple incompatible NURBS patches. Due to the elimination of the need to use multiple patches, geometries represented by these new spline methods naturally achieve watertightness without gaps and overlaps.

The CAD approaches that use alternative spline methods provide an upstream solution that allow seamless integration with downstream CAE operations (see for instance, [29–31]). Their utility lies in enabling a single bi-variate or tri-variate spline patch to describe the geometry, which in turn may be used directly for isogeometric analysis. However, such geometries need to be analysis aware [32, 33] or analysis-suitable [34–36]. Arguably, new spline technologies would have greater impact if they are compatible with NURBS based B-rep paradigm that is widely prevalent in commercial CAD software at the present time. While direct generation of tri-variate spline subdomains from B-rep CAD models has been recently demonstrated [37] and may hold a potential solution for the future, the coupling of volumetric spline subdomains remains a critical unsolved need at the present time.

Interfacial conditions are critical to physical problems involving interactions between separated subdomains, such as those occurring during contact between solid bodies or during fluid structure interaction (FSI). Since discretizations of subdomains are either created independently or partitioned upon creation as a whole (as in domain decomposition methods or DDM), treatment of interfacial interaction between incompatible domains is an important topic in these fields. A number of strategies to couple subdomain discretizations also exist in the analysis realm. Penalty formulations, Lagrange multiplier methods [38–40] as well as Nitsche’s method [41] are among the most common approaches. These methods enforce weak coupling of be-

havioral field values such that compatibility and consistency conditions are satisfied in an average sense along the interface as summarized in Table 1.1. In the context of isogeometric analysis, the first treatment of interfacial compatibility constraints on subdomains discretized using NURBS was demonstrated by Natekar et al. [13]. In the IGA literature, treatment of interfacial interaction have been demonstrated including but not limited to shell problems [42–44], contact problems [45–49], FSI problems [50, 51], and domain decomposition of solids [52–55].

Table 1.1.
Comparison of weak coupling techniques for multi-patch analysis.

Penalty Method	Lagrange Multiplier Method	Nitsche’s Method
✓ Easy to implement	✓ No choice of penalty	✓ No additional DOFs
✓ No additional DOFs	✓ Improved Dirichlet compatibility	✓ P.D. system
✓ P.D. system		
✗ Choice of penalty	✗ Add additional DOFs	✗ Need to determine
• Incompatibility (Small penalty value)	✗ Ill-conditioned	stabilization parameter
• Ill-conditioned (Large penalty value)	✗ Need inf-sup cond.	✗ Choice of Nitsche’s parameter

In general, in domains assembled using multiple patches, C^0 smoothness across the interface between adjacent patches is easily achieved. However, C^1 or higher smoothness across a shared edge of patches is desirable during design as well as analysis, but is challenging to achieve. Towards this end, recently, constructing C^1 continuous smooth approximation spaces over geometrically complex multi-patch domains has been an important focus in the isogeometric analysis community. An early comparison of such approaches was provided by Nguyen et al. [56]. The approaches are broadly aimed at assuring C^1 continuity over the complex domain by utilizing G^1 continuity across the patches [57–60]. These methods are argued as providing “full approximation power” even at extraordinary vertices, where subdivision meth-

ods' convergence rate is reduced. Their relative merits are often discussed in terms of their ability to generate approximations that possess desirable properties such as non-negativity, smoothness, partition of unity as well as local support that NURBS basis functions are known to provide, and therefore are argued as being useful for isogeometric analysis [13, 59].

1.1.2 Modeling of Crack Tip Singularities and Crack Face Discontinuity

In the finite element method, the representation of singularities with singular isoparametric element is well established [61, 62]. The technique allows modeling of stress singularity ahead of the crack tip and represent the crack face explicitly. However, significant effort is needed to generate proper mesh, and it is a non-trivial task to model crack propagation as the mesh deletion and generation needs to be automated [63, 64]. The Partition of Unity Finite Element Method (PUFEM) proposed by Malenk and Babuška guarantees convergence of specialized (enriched) behavioral fields under partition of unity condition [8, 9]. Since then, modeling of features with *a priori* known behaviors became possible due to the introduction of corresponding enriching function and therefore resulting in an expanded approximation space. Convergence of solution hence can be achieved rapidly without the need for extensive mesh refinement. Based on the theory of PUFEM, Dolbow and Moës *et al.* proposed the well known eXtended FEM (XFEM) [10, 11] to model the discontinuity across the crack face and crack tip singularities with minimal re-meshing. The solution space is enriched through the introduction of Heaviside step function H and the tip function $F(r, \theta)$ deriving from the leading terms of linear fracture mechanics (LEFM) solution. Stress singularity due to geometric features such as reentrant corner or holes was also possible to model through generalized FEM (GFEM) [65–67].

In the context of isogeometric analysis, Benson *et al.* and De Luycker *et al.* [68, 69] proposed a similar formulation with respect to GFEM and XFEM, respectively. Ghorashi *et al.* focused on modeling of fracture and termed the technique as eXtended

IGA (XIGA) [70]. While XIGA has successfully demonstrated modeling of fracture with a fixed underlying mesh, the crack face is modeled as the zero level-set in an implicit sense to track the evolution of crack faces. One of the drawback of using level set is that the actual location as well as geometric descriptors such as the geometric normal of the crack face cannot be parametrically traced. Additionally, level sets are described by a first-order hyperbolic equation (Hamilton-Jacobi), which is hard to solve, and the solution to which requires stabilization as well as minimization of oscillation [71].

Strategies using phase field method to model fracture have also been proposed [72–74]. While the phase field method has been used to model difficult problems such as branching of cracks, there are some challenges associated with this method. First, similar to the level set descriptions of the crack mentioned earlier, the phase field method also uses an implicit representation of cracks with the description of phase-field variable β . To converge to the physical solution, a very thin region of discretization generated by adaptive refinement is required to capture the crack face as a numerically diffuse approximation to the sharp interface. Furthermore, phase field methods involve developing diffuse forms of the governing equations which are often non-linear and non-convex. The resulting partial differential equations may be fourth-order [75] and therefore more complicated to solve. They may also not provide the intuitive simplicity provided by the sharp interface representation.

As an alternative to implicit approximations of crack geometry, Tambat proposed a non-conforming mesh, explicit interface method to model fracture [76, 77]. In this method, the crack face is represented by a NURBS curve in a *true* isogeometric sense. The enriching functions and their corresponding degrees of freedom are naturally associated with the control points of the interfaces themselves rather than the control points of underlying domain (as in the sense of XIGA or phase field method). Therefore, it is possible to strongly impose boundary conditions on the enriching interface. Since the chosen tip enriching functions are the same as in the XFEM method, $F(r, \theta) = \{\sqrt{r} \sin(\frac{\theta}{2}), \sqrt{r} \cos(\frac{\theta}{2}), \sqrt{r} \sin(\frac{\theta}{2}) \sin(\theta), \sqrt{r} \cos(\frac{\theta}{2}) \sin(\theta)\}$,

estimation of the stress intensity factor requires an additional post-processing step. Song [78] extends the formulation of Liu *et al.* [79] such that the stress intensity factors at the crack tip could be directly evaluated. Direct evaluation of stress intensity factors at multi-material wedges in the context of IGA does not appear to exist in the existing literature.

1.2 Gaps in Existing Literature

As indicated in the above survey, existing techniques for coupling multiple patches either rely on creating new spline forms needing alternative CAD systems or an analysis-oriented solution to coupling interfaces through penalty or Nitsche methods. The CAD approaches provide a top down solution that allow seamless CAD&E integration. As NURBS is the ubiquitous spline form used internally in commercial CAD systems, coupling of NURBS patch is a critical need. The alternative spline choices will require a fundamental paradigm shift for adoption in the CAD industry. Also, analysis-oriented multi-patch coupling solutions have mostly enabled weakly enforcing the interface conditions. C^1 or higher smoothness across a shared edge of patches is desirable during design as well as analysis, but is challenging to achieve. Clearly, there is a need for a novel technique to couple multiple patches that has the following characteristics. First, the technique should allow the geometry to be represented in NURBS or any other splines that possess the properties of backward compatibility with existing CAD systems as well as analysis suitability. Second, the technique should attain C^1 or higher smoothness across a shared edge of patches.

Another challenge is the modeling of stress singularity near features with geometric discontinuity or material heterogeneity. To evaluate the risk of fracture of a structure, it is desirable to characterize not only the stress ahead of crack tip but also the singular stress in the absence of any pre-existing crack as in multi-material corners. To date, methodologies to model crack tips and the discontinuity across the crack face have been extensively developed. However, an isogeometric strategy to characterize corners

as well as crack tips that both possess $r^{-\lambda}$ singularities does not seem to exist. A unified formulation capable of correlating with commonly seen failures is very much in need.

1.3 Research Objectives

Motivated by the above-identified gaps in the existing literature, the goals of this work are to:

1. Develop a novel methodology for coupling parametrically defined domains (including but not limited to NURBS) with C^1 or higher smoothness across a shared edge of patches.
2. Formulate a general purpose isogeometric enrichment applicable for both multi-material wedges and crack tips that possess $r^{-\lambda}$ stress singularities.
3. Demonstrate the developed procedures on heterogeneous structures such as the device BEOL structures.

Overall, the methodologies presented in this thesis aim to better analyze and understand the fracture failure in practical engineering applications.

1.4 Outline

The rest of the thesis is organized as follows. Chapter 2 provides a review of the methods that form the foundation of the present work. The mathematical form of Enriched Isogeometric Analysis (EIGA) is first reviewed, being the common basis for the majority of this thesis. New weight fields of polynomial form are proposed to have local support and improve numerical solution accuracy. Chapter 3 briefly introduces the configurational optimization problem as well as the derivation of the configuration derivative, which is later shown to be related to the configurational force theory. The implementation, features and architecture of the code is described in Chapter 4. In

Chapter 5 a novel methodology to smoothly couple parametric spline patches is developed. The technique provides an isogeometric formulation to couple incompatible patches for both homogeneous as well as bi-material interfaces. Isogeometric enrichment for corner singular stress is formulated in Chapter 6. The formulation is later extended to crack enrichment by introducing crack face discontinuity. To address the challenge of predicting crack initiation and propagation in a non-linear material, configurational force-based calculation using isogeometric analysis is proposed in Chapter 7. In Chapter 8, the focus is turned to applications of developed techniques to specific problem related to reliability of microelectronic package. Finally, the research is summarized in Chapter 9 with a summary of novel contributions and recommendations for future research.

2. BACKGROUND

This chapter provides a brief background on the methods that form the foundation of the present thesis.

2.1 Non-Uniform Rational B-Spline Approximation Space

In the present work, NURBS is chosen as the representation for the parametric domains as well as for the interface. NURBS are defined on knot vectors in parametric space. A typical non-uniform knot vector is written as [80]:

$$\Xi = \{\xi_1, \xi_2, \dots, \xi_{n_i+p+1}\}. \quad (2.1)$$

where, $\xi_i \in \mathbb{R}$ is the i th knot with $\xi_i \leq \xi_{i+1}$ for $i = 1, \dots, n + p$; n is the number of basis functions, and p is the polynomial degree of the basis functions. In general, the knots are not uniformly spaced in the parametric space. An open knot vector has $p + 1$ repeated knots at each end of the knot vector.

The isoparametric NURBS approximations of geometry and behavioral field are written as

$$\mathbf{x}(\xi, \eta, \zeta) = \sum_{i=1}^{n_i} \sum_{j=1}^{n_j} \sum_{k=1}^{n_k} R_{ijk}(\xi, \eta, \zeta) \bar{\mathbf{x}}_{ijk} \quad (2.2a)$$

$$f(\xi, \eta, \zeta) = \sum_{i=1}^{n_i} \sum_{j=1}^{n_j} \sum_{k=1}^{n_k} R_{ijk}(\xi, \eta, \zeta) \bar{f}_{ijk} \quad (2.2b)$$

where, $\bar{\mathbf{x}}_{ijk}$ is the ijk^{th} control point and \bar{f}_{ijk} is the control point value of the field associated with $\bar{\mathbf{x}}_{ijk}$. n_i , n_j and n_k are the number of control points in the i^{th} , j^{th}

and k^{th} parametric dimension, respectively. R_{ijk} is the rational basis function defined as the tensor product:

$$R_{ijk}(\xi, \eta, \zeta) = \frac{N_{i,p}(\xi)N_{j,q}(\eta)N_{k,r}(\zeta)w_{ijk}}{\sum_{i=1}^{n_i} \sum_{j=1}^{n_j} \sum_{k=1}^{n_k} N_{i,p}(\xi)N_{j,q}(\eta)N_{k,r}(\zeta)w_{ijk}} \quad (2.3)$$

where, $N_{i,p}$ refers to the i^{th} B-spline basis function of degree p . The basis functions are usually evaluated through the recurrence formula [81–83]:

$$N_{i,0}(\xi) = \begin{cases} 1 & \text{if } \xi_i \leq \xi < \xi_{i+1} \\ 0 & \text{otherwise} \end{cases} \quad (2.4a)$$

$$N_{i,p}(\xi) = \frac{\xi - \xi_i}{\xi_{i+p} - \xi_i} N_{i,p-1}(\xi) + \frac{\xi_{i+p+1} - \xi}{\xi_{i+p+1} - \xi_{i+1}} N_{i+1,p-1}(\xi). \quad (2.4b)$$

The NURBS basis functions possess several important properties including partition of unity, compact support, non-negativity and C^{p-m} continuity with m being the knot multiplicity.

1. Partition of unity:

$$\sum_{i=1}^n N_{i,p}(\xi) = 1. \quad (2.5)$$

2. Compact support:

$N_{i,p}(\xi)$ is non-zero only in the half-open interval $[\xi_i, \xi_{i+p+1})$.

3. Non-negativity:

$$N_{i,p}(\xi) \geq 0 \quad \forall \xi \quad (2.6)$$

4. Smoothness: $N_{i,p}(\xi)$ is C^{p-m} continuous, where m is the multiplicity of knot.

Property 1, 2 and 4 are the most critical ones for NURBS to be analysis suitable. Partition of unity property ensures the convergence of the NURBS approximation to a known solution. Compact support ensures that any change to the approximation

locally remains local in its influence. Smoothness is necessary for many physics problems requiring higher degree of continuity. Note that non-negativity is not required for the purpose of analysis, but is important for intuitive geometric modeling and shape control. A demonstration of NURBS approximation is shown in Figure 2.1.

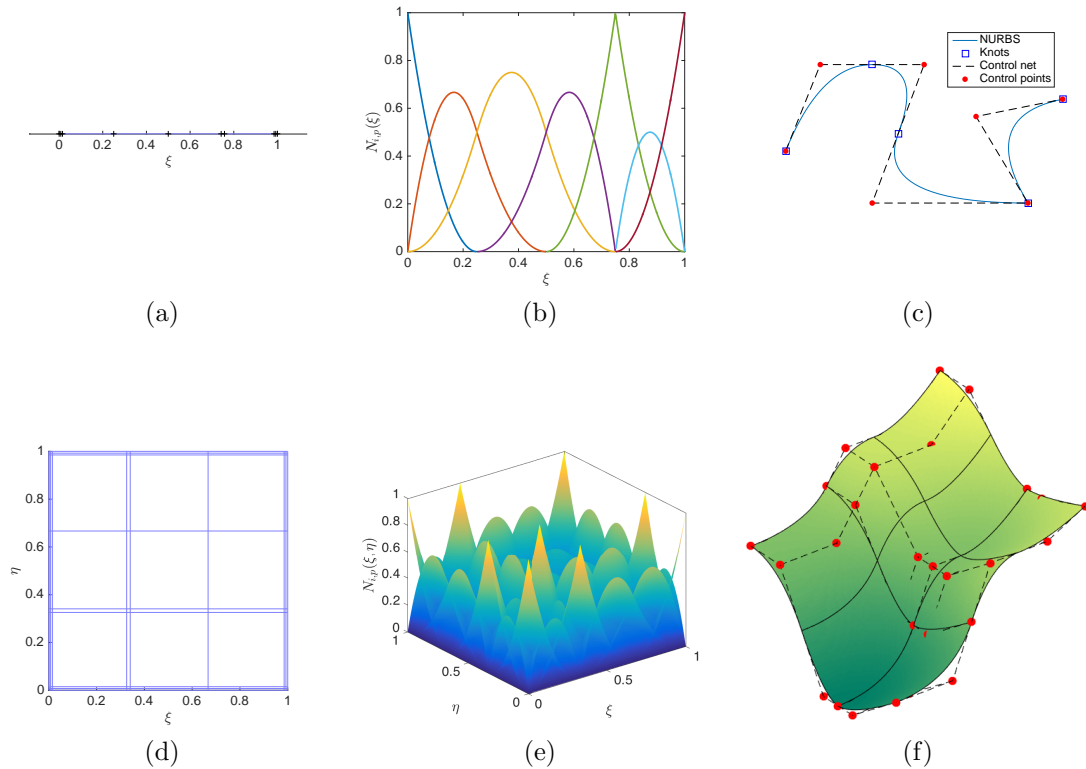


Figure 2.1. (a) (d) Knot vectors in parametric space. (b) (e) Basis functions in parametric space. (c) (f) NURBS curve and surface approximation in physical space.

2.2 Enriched Isogeometric Analysis

Based on the Partition of Unity Finite Element Method (PUFEM) [8], Subbarayan and co-workers developed a procedure to construct field approximations over the domain in which the fields corresponding to a higher level are composed hierarchically using approximations on lower levels. The hierarchical composition is described through

a binary tree in which the leaves form the local approximations and the nodes form the Boolean composition operation on the leaves ($\cap, \cup, -$). This procedural description of analysis was analogous to the Constructive Solid Geometry (CSG) procedure of CAD and was therefore named constructive solid analysis (CSA, [13,84]); the hierarchical composition of subdomain fields to construct approximations on the overall domain was termed Hierarchical Partition of Unity Field Compositions (HPFC, [85]).

In the hierarchical partition of unity field construction, a domain is composed as $\Omega = \Omega_1 * \Omega_2 * \dots * \Omega_{n_\Omega}$, where $*$ represents one of the three regularized Boolean operations ($* \in \{\cap, \cup, -\}$). The intersection operation for any two fields f_{Ω_i} and f_{Ω_j} is defined as,

$$f_{\Omega_i \cap \Omega_j} = w_{ij}(\mathbf{x})f_{\Omega_i} + w_{ji}(\mathbf{x})f_{\Omega_j} \quad \text{in } \Omega_i \cap \Omega_j \quad (2.7)$$

where w_{ij} and w_{ji} are two additional fields with the first subscript i or j denoting the underlying domains on which they are defined and the second subscript denoting the primitive with which the intersection region is shared. The fields w_{ij} and w_{ji} are unrestricted as long as they formed a non-negative partition of unity. That is,

$$w_{ij}(\mathbf{x}) + w_{ji}(\mathbf{x}) = 1 \quad \text{in } \Omega_i \cap \Omega_j \quad (2.8a)$$

$$0 \leq w_{ij}, w_{ji} \leq 1 \quad (2.8b)$$

The intersection operation was then used to define union and subtraction operations. Thus, a hierarchical composition of fields is possible in terms of the fields defined over the subdomains (as illustrated in Figure 2.2), and at any given point \mathbf{x} in the domain, the composed field $f(\mathbf{x})$ is described follows:

$$f(\mathbf{x}) = \sum_i^{n_\Omega} w_{\Omega_i}(\mathbf{x})f_{\Omega_i}(\mathbf{x}) \quad (2.9)$$

where, w_{Ω_i} was the weight field associated with subdomain Ω_i . Specifically, the weight fields were constructed to be non-negative partitions of unity.

$$\sum_i^{n_{\Omega}} w_{\Omega_i}(\mathbf{x}) = 1 \quad (2.10a)$$

$$0 \leq w_{\Omega_i}(\mathbf{x}) \leq 1 \quad (2.10b)$$

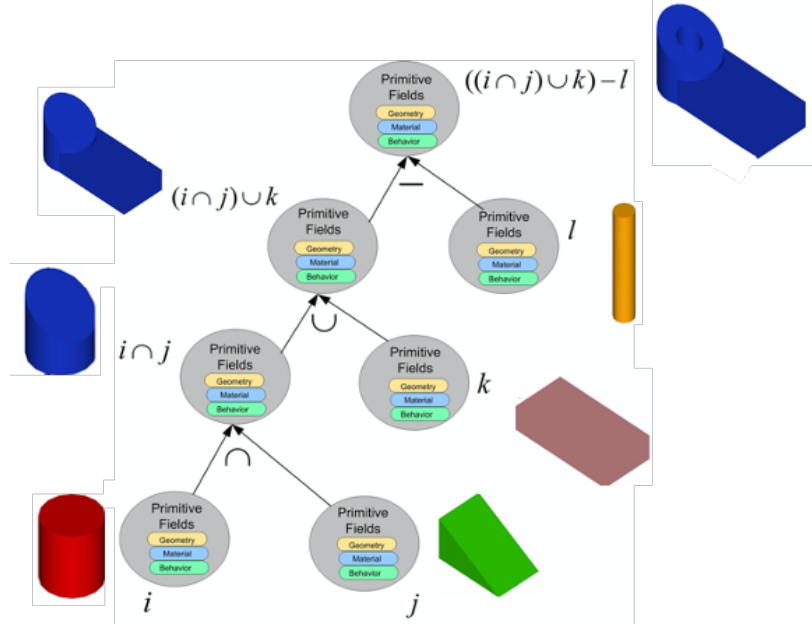


Figure 2.2. Composition of primitive design states to form the complex design state [85].

While, the above-described compositional procedure is for fields defined on the primitive subdomains, Tambat and Subbarayan [76] developed an alternative hierarchical compositional strategy beginning with lower dimensional geometrical entities that formed the boundaries of the subdomains as described below.

Consider a region Ω containing several enriching boundaries Γ_i , the behavioral field can now be constructed to form a partition of unity through a convex combination as follows:

$$f(\mathbf{x}) = (1 - w(d(\mathbf{x}))) f_{\Omega}(\mathbf{x}) + w(d(\mathbf{x})) f_{\Gamma_e}(\mathcal{P}(\mathbf{x})). \quad (2.11)$$

where, f_{Ω} is the continuous approximation associated with the underlying domain Ω , f_{Γ_e} is the enriching approximation defined iso-parametrically on the external or internal boundary Γ_e , and $\mathcal{P}(\mathbf{x})$ is the projection mapping from a spatial point \mathbf{x} in domain Ω to the parameter (ξ, η) of boundary Γ_e , i.e. $\mathcal{P} : \mathbf{x} \mapsto (\xi, \eta)$. Thus, $\mathbf{x}_f(\xi, \eta)$ denotes the foot point of the projection in the physical space that lies on the boundary, and $f_{\Gamma_e}(\xi, \eta)$ its field value corresponding to the spatial location \mathbf{x} . The methodology where the base approximation f_{Ω} is enriched with lower-dimensional approximations f_{Γ_e} , as illustrated in Figure 2.3, was termed as *Enriched Isogeometric Analysis* (EIGA).

A comparison of treatment of internal boundary between traditional finite element method (FEM), generalized finite element method (GFEM), and EIGA is illustrated in Figure 2.4. Crack modeling using piece-wise polynomial approximation of FEM requires the edges or faces of the finite element to align with the crack face. In GFEM, the degrees of freedom corresponding to enriching function are associated with nodes of the underlying mesh. Due to the fact that the interface itself is not associated with any degree of freedom, imposition of boundary condition onto the internal boundary can only be done in a weak sense. EIGA also expands the approximation space by adding enriching function implicitly. However, the boundary is explicitly represented while the DOFs corresponding to enriching basis is associated with the interface itself. Therefore, it is possible to apply the boundary conditions in a strong sense. In addition to the minimal re-meshing needed for moving boundary problems, a critical advantage of EIGA is the ability to exactly evaluate geometric quantities such as

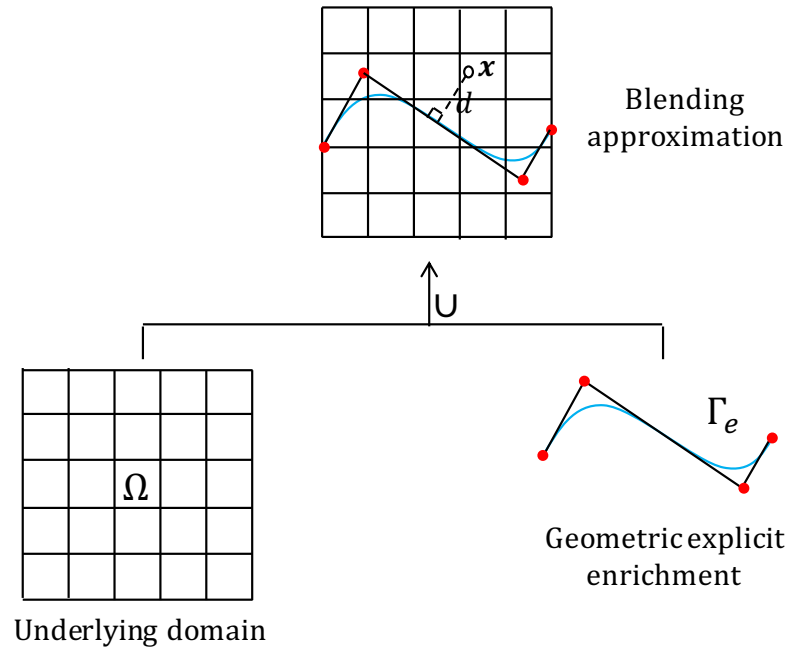


Figure 2.3. Enriched Isogeometric approximation is constructed by blending an approximation built on the enriching entity as a function of normal distances with the approximation on the underlying domain.

normals and curvature. The method often requires fewer number of degrees of freedom in comparison to an implicit geometry scheme such as phase field or level set method.

EIGA has been demonstrated on many applications including fracture problems [76] as well as on Stefan problem modeling evolution of solidification fronts [86]. Furthermore, it has also been used to strongly impose Dirichlet and Neumann boundary conditions through function value enrichment and derivative enrichment [76, 87], respectively. In general, EIGA allows explicitly represented external/internal boundary geometries while implicitly capturing the decaying influence of the local behavior with distance. The above described enriched field approximation serves as the foundation for the present work.

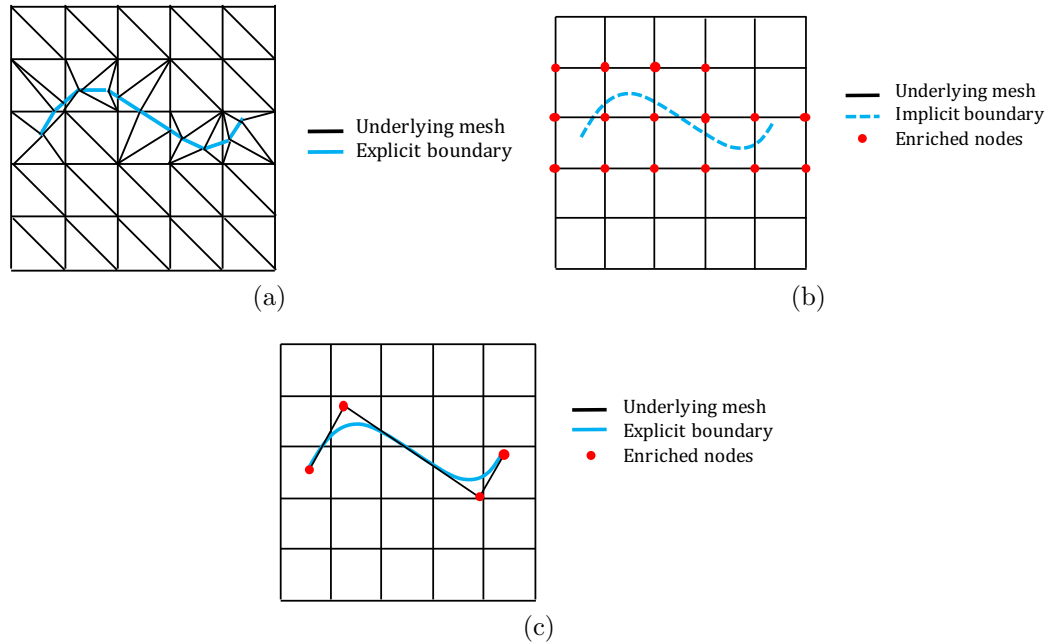


Figure 2.4. Illustration of strategies to track internal boundary as well as construct enriched approximations by (a) classical FEM (b) GFEM, and (c) EIGA

2.3 Choice of Weight Function in EIGA

The weight function plays an important role in the formulation of EIGA by blending fields while ensuring the partition of unity property. In general, the weight field is a function of distance from any spatial point \boldsymbol{x} to the enrichment boundary Γ_e , with a monotonic decrease in the weight value away from the boundary. While there is no restriction on the form of the weight function $w(d(\boldsymbol{x}))$, the following are the minimal requirements on the weight field:

1. $w(0) = 1$ and $w'(0) = 0$
2. $w(d_{max}) = 0$ and $w'(d_{max}) = 0$
3. *Monotonicity*: $1 \geq w(d) > w(d+h) \geq 0$ for $0 \leq |d| < |d+h| \leq d_{max}$
4. *Local support*: $w(d) = 0$ for $|d| \geq d_{max}$

5. $w(d)$ is of the required smoothness as dictated by the governing equations.

Here, d_{max} is the size of the domain influenced by the enrichment. Properties 1 through 3 ensure that the enriched field approximation is a convex blending with the underlying field. Property 4 confines the influence domain to the local region within the neighborhood of enrichment to improve the computational efficiency. Property 5 ensures that the approximation is valid. The above properties also imply non-negativity of the weight field.

Let $\bar{d} = d/d_{max}$ be the normalized distance from the enriching boundary within the influence domain. A few possible choices of the functional form of $w(\bar{d})$ are listed below:

1. Cubic:

$$w(\bar{d}) = \begin{cases} 1 - 3\bar{d}^2 + 2\bar{d}^3 & \text{for } \bar{d} \leq 1 \\ 0 & \text{for } \bar{d} > 1 \end{cases} \quad (2.12a)$$

2. Quartic:

$$w(\bar{d}) = \begin{cases} 1 - 6\bar{d}^2 + 8\bar{d}^3 - 3\bar{d}^4 & \text{for } \bar{d} \leq 1 \\ 0 & \text{for } \bar{d} > 1 \end{cases} \quad (2.12b)$$

3. Exponential:

$$w(\bar{d}) = \begin{cases} 1 - \frac{1 - e^{-(\bar{d}/\alpha)^p}}{1 - e^{-|\bar{d}/\alpha|^p}} & \text{for } \bar{d} \leq 1 \\ 0 & \text{for } \bar{d} > 1 \end{cases} \quad (2.12c)$$

where, α is an arbitrary positive constant, and p is any number greater than 1. All of the above weight functions except for the exponential form satisfy the required properties. The exponential form, proposed by Belytschko et al. [88], only weakly satisfies Property 2 since $w(1) = 0$, but $w'(1) \neq 0$. However, when a proper α and p

are chosen, the derivative of exponential weight function asymptotically vanishes near the boundary of influence domain. That is, $w'(\bar{d}) \rightarrow 0$ when $\bar{d} \rightarrow 1$. For instance, for $\alpha = 0.2$ and $p = 2$, $w'(1) \approx -6.9 \times 10^{-10}$. The functional forms of weight functions listed in Eq. (2.12) are compared in Figures 2.5 and 2.6. It must be noted that the distance used in this work is the signed distance, which may be calculated efficiently using algebraic level sets described in the following subsection.

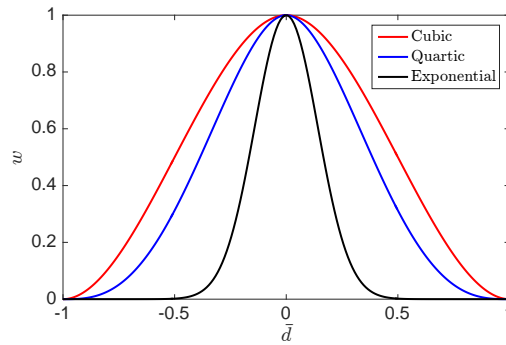


Figure 2.5. Cubic, quartic and exponential weight function values.

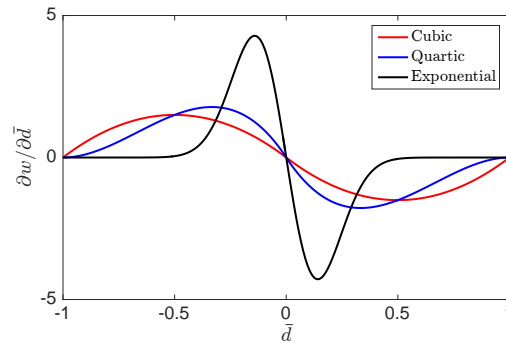


Figure 2.6. Cubic, quartic and exponential weight function derivatives with respect to normalized, signed distance.

2.4 The Need for Distance and Projection

The need for distance measure and point projection requires more elaboration. Consider again the boundary Γ_e , represented by a parametric curve $\mathbf{C}(u)$, embedded in the domain Ω as shown in Figure 2.3. For an arbitrary spatial point \mathbf{x} , a measure of distance is needed to determine the extent of influence of the enriching approximation on the domain field as measured by the weight field in Eq. (2.11). Furthermore, since the enriching field is described isoparametrically on the enriching surface, the foot point $\mathbf{x}_f(\xi, \eta)$ on the parametric surface that is nearest to the spatial location \mathbf{x} needs to be determined. That is, the projection of the current spatial point \mathbf{x} onto the enriching parametric surface Γ_e , $\mathcal{P} : \mathbf{x} \mapsto (\xi, \eta)$, is needed. Such distance estimations as well as projections need to be robust, accurate and efficient.

A relatively simple and inefficient approach to finding distance to a parametric curve is to carryout one-dimensional search on the parameter ξ of the curve that yields a point $\mathbf{x}_f(\xi)$ that is nearest to the domain point \mathbf{x} . Parameter updates may be determined by bisecting the interval, for instance. However, the most common technique for estimating the distance to a parametric curve or surface is using Newton-Raphson iterations [80]. In both one-dimensional search as well as the Newton-Raphson method, the numerical iterations may become expensive since they need to be carried out at every quadrature point on the domain when constructing the stiffness matrix. Additionally, the numerical iterations may lead to non-unique solutions since more than one point on the boundary may be equidistant from current spatial point. The numerical iterations may also not converge to a solution. These concerns make Newton-Raphson iterations less robust, while the numerical iterations makes the method less efficient. An alternative idea is to construct a polytope approximation to the boundary to estimate distance [89,90]. However, a polytope approximation does not retain the parametric description of the boundary that enables one to directly compute normals and curvatures that are critical to the evolution of the boundary under physical forces.

An alternative approach to the Newton-Raphson iterations was recently developed by Subbarayan and co-workers [91,92]. The method is termed signed algebraic level sets and provides both a distance measure as well as point (sign) classification. The algebraic level sets preserve the exact geometry of low-degree (2 or 3) NURBS curves/surfaces while avoiding numerical iterations. Specifically, the algebraic level sets provide an approximate measure of distance to a domain point. This approximate measure is sufficient to construct the weight fields in Eqs. (2.11) and (2.12).

The main idea behind constructing the algebraic level sets is to implicitize the parametric entity and to use the level sets of the implicitized function as a measure of distance. The implicitization of parametric entities is based on the resultant theory, which is described in the seminal research of Sederberg [17]. The resultant of a parametric entity is the determinant of a matrix of the form $\det(\mathbf{M}(\mathbf{x})) = 0$, which gives the implicit representation of the parametric entity. Furthermore, for any point \mathbf{x} that is not on the curve, $\Gamma = \det(\mathbf{M}(\mathbf{x}))$ is a measure of distance from the curve. Generally, algebraic level sets need to be complemented by algebraic point projection [86,93] that enables one to find the projected parametric point on the curves/surfaces from a domain point.

To provide a high-level overview, the procedure to construct the unsigned algebraic level sets is pictorially illustrated in Figures 2.7 and 2.8. The readers are referred to [92] for a detailed description of the procedure on using the resultant to construct signed algebraic level sets.

Close to the parametric curve, parametric iteration, Newton-Raphson iterations as well as algebraic point projection all yield the same foot point on the curve as illustrated in Figure 2.9. Since constructing the algebraic level sets is a non-iterative process, the algebraic distance measure is cheaper to obtain compared to Newton-Raphson or one-dimensional iterations on the parameter value. While the algebraic point projection is non-iterative for points close to the boundary, it does require iterations when points are farther away from the enriching curve or surface. Still,

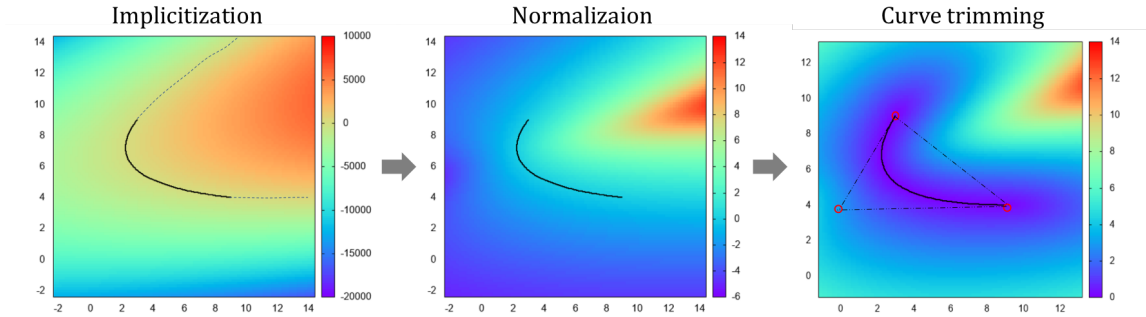


Figure 2.7. Illustration of steps in constructing the algebraic level sets on Bezier curves [91].

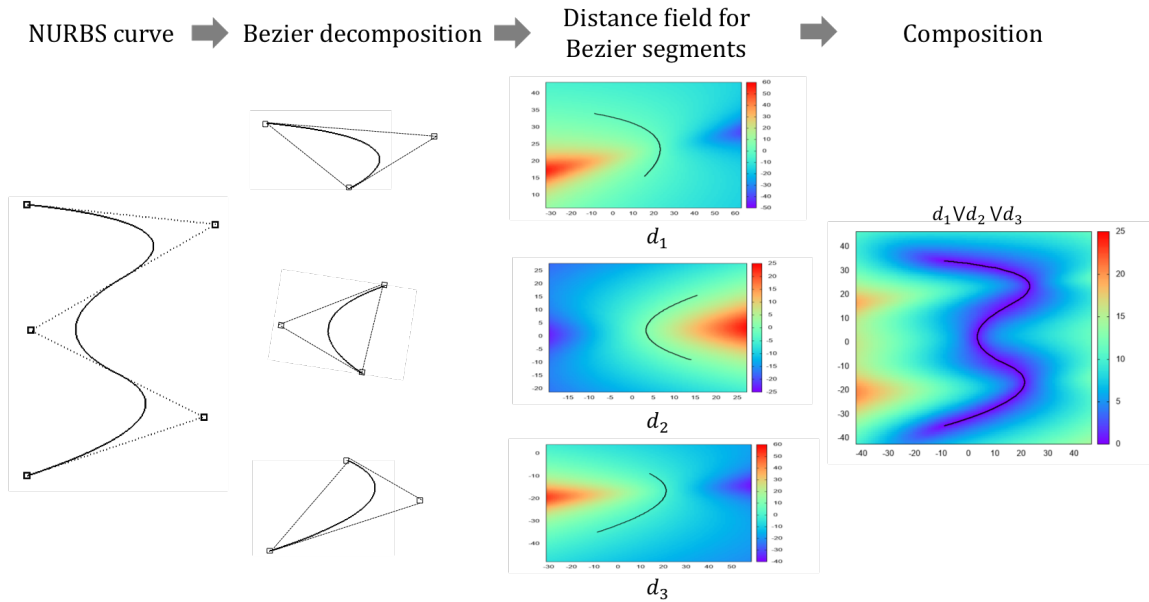


Figure 2.8. Illustration of steps in constructing the algebraic level sets on NURBS curves [91].

the procedure is significantly more robust and efficient compared to Newton-Raphson iterations as demonstrated in [93].

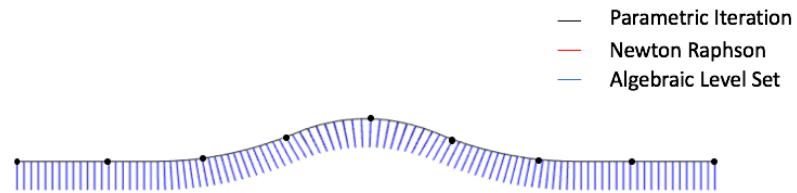


Figure 2.9. Comparison of the projected foot points obtained using Parametric Iterations, Newton-Raphson Iterations and Algebraic Level Sets. For points close to the curve, all three methods yield an identical solution.

3. CONFIGURATIONAL DERIVATIVES, CONFIGURATIONAL FORCES AND CONFIGURATIONAL OPTIMIZATION

The compositional idea of HPFC theory [13, 84, 85] is particularly advantageous for structural optimization problems. While the isogeometric framework avoids the need for constructing behavioral approximations distinct from the geometrical model, its compositional nature brings additional benefit for solving structural optimization problems. As the analysis procedure mirrors the geometry construction procedure, local modifications of the geometry correspond to changes in the contribution of the participating fields in HPFC.

Structural optimization can be classified in terms of representation of boundary shape. Structural optimal design using implicit boundary representation includes solid isotropic material with penalization (SIMP) method [94], level set method [95] and phase field method [96]. As demonstrated in Appendix D, SIMP method iteratively updates the (finite) element material density in accordance with the objective to achieve an optimal material distribution. In the level set method, the optimal structure is achieved by dynamically evolving the level set function, which is used to define the topology and shape of the structure. In the phase field method, topology optimization problem is re-cast into a phase transition problem dependent on the total free energy associated with the system.

Structural optimization using explicit boundary representation such as the bubble method [97] is one of relatively few studies in the literature. In the bubble method, topology change started by identifying the location for introducing holes followed by parametrically describing the holes using a NURBS representation. The domain with holes are then re-meshed and the associated behavior is analyzed by finite element method. Shapes of hole are subsequently and iteratively modified as dictated by the behavior. The notion of topological derivative generalizes the condition used in the

bubble method for determining the locations for introducing infinitesimal holes in the structure. In spirit, this method resembles shape optimal design.

As opposed to redistributing material in the domain or dynamically evolving the boundary into the desired shape, optimal topological design by inserting and optimizing finite-sized inclusions or holes into homogeneous domains is computationally advantageous since relatively few design variables are needed to describe the configuration of such heterogeneities. To this end, Lin proposed configurational optimization problem for determining the optimal location, orientation and shape of a finite-sized heterogeneity inserted into a homogeneous solid domain [98]. The material derivative of an arbitrary objective with respect to arbitrary design modifications of the internal/external boundaries of the domain, termed as the configurational derivative, was derived.

This chapter gives a brief background of the configurational optimization problem and the derivation of configurational derivative. The configurational derivative will later shown to be related to configurational force theory for fracture in Chapter 7.

3.1 Configurational Optimization Problem and Configurational Tensor for Insertion of Arbitrary Heterogeneity

First, the concept of configurational optimization problem [99] for arbitrary objectives defined in a solid subdomain and its boundary surface is generalized. The material time derivative of the objective with respect to arbitrary design modifications of the internal/external boundaries is derived and termed as the configurational derivative. The configurational derivative is further simplified by introducing the notion of configurational tensor. Then, the configurational derivative are specialized for design transformations corresponding to translation, rotation, and scaling of the heterogeneity. These transformations in turn yield the configurational forces complementing the motions.

3.1.1 The Configurational Optimization Problem and Configurational Derivative

Given a homogeneous solid Ω as shown in Figure 3.1a, the linear elastic response of the domain is governed by the principle of virtual work statement:

$$\int_{\Omega} \varepsilon^0 : \mathbf{C}^0 : \varepsilon^{a0} d\Omega - \int_{\Gamma} \mathbf{t}^0 \cdot \mathbf{u}^{a0} d\Gamma = 0 \quad (3.1)$$

where, ε^0 represents the infinitesimal strain tensor; ε^{a0} and \mathbf{u}^{a0} are compatible virtual strains and displacement, respectively; \mathbf{t}^0 denotes the surface tractions prescribed on the domain boundary; \mathbf{C}^0 is the fourth-order isotropic tensor defining the linear elastic constitutive relation $\sigma^0 = \mathbf{C}^0 : \varepsilon^0$ between the stress σ^0 and strain ε^0 in the homogeneous domain. Implicit in the above statement is the requirement that $\mathbf{u}^{a0} = 0$ on the portion of the boundary Γ_u where displacement boundary conditions are applied. Also, Γ_t is the portion of boundary where tractions are prescribed, and the boundary of the domain is decomposed such that $\Gamma = \Gamma_u \cup \Gamma_t$ and $\Gamma_u \cap \Gamma_t = \emptyset$. For convenience, the body forces are ignored in the current study.

Now, an arbitrary subdomain Ω_s bounded by Γ_s can be defined for design purpose (see Figure 3.1b). Here, the traction (defined using the outward normal indicated in Figure 3.1b) as well as displacement boundary conditions (which arise on account of Eq. (3.1)) are appropriately prescribed on Γ_{st} and Γ_{su} , respectively, to ensure that the subdomain remains in static equilibrium. Thus,

$$\int_{\Omega_s} \varepsilon^0 : \mathbf{C}^0 : \varepsilon^{a0} d\Omega - \int_{\Gamma_s} \mathbf{t}^{s0} \cdot \mathbf{u}^{a0} d\Gamma = 0. \quad (3.2)$$

The choice of $\Gamma_s = \Gamma_{su} \cup \Gamma_{st}$ and the choice of the specific subregion Γ_{su} (where displacement boundary conditions are prescribed) are completely arbitrary and dependent on design intent. The only exception is the special case where $\Omega_s = \Omega$ and

$\Gamma_s = \Gamma$. Under such a choice, $\Gamma_{su} = \Gamma_u$ and $\Gamma_{st} = \Gamma_t$ in order to recover the original displacement and traction boundary conditions applied on Γ .

Now, within the homogeneous subdomain that is of interest, a “design transformation” that is continuous with a pseudo “design time” t within the domain can be defined as:

$$\mathbf{x}^0 = \mathbf{x}^0(\mathbf{X}^0, t) \quad (3.3)$$

where, \mathbf{X}^0 is initial position in the domain independent of time. Then, Ω_s and Γ_s will represent the configuration of the subdomain and its boundary at any time instant t . Also, $\Omega_s^{t_0}$ is defined as the initial configuration. As with \mathbf{X}^0 , $\Omega_s^{t_0}$ is assumed to be independent of time. Associated with this design transformation, a “design velocity” may now be defined as:

$$\mathbf{v}^0(\mathbf{x}^0, t) = \frac{\partial \mathbf{x}^0}{\partial t}. \quad (3.4)$$

Therefore, the total derivative of any spatial function (scalar or tensorial) $z^0(\mathbf{x}^0, t)$ defined in the homogeneous domain can be obtained using the material (time) derivative:

$$\frac{Dz^0(\mathbf{x}^0, t)}{Dt} = \dot{z}^0 = \frac{\partial z^0}{\partial t} + \mathbf{v}^0 \cdot \nabla z^0. \quad (3.5)$$

Next, the above homogeneous subdomain is modified by introducing a heterogeneity that is defined over Ω_p bounded by Γ_p (see Figure 3.1c) and located at position \mathbf{x}_p inside Ω_s . In general, the traction and displacement boundary conditions on Γ_{st} and Γ_{su} will differ between those on the homogeneous domain and on the heterogeneous domain. Thus, the virtual work statement on the heterogeneous subdomain is given by:

$$\int_{\Omega_s} \boldsymbol{\varepsilon} : \mathbf{C} : \boldsymbol{\varepsilon}^a d\Omega - \int_{\Gamma_s} \mathbf{t}^s \cdot \mathbf{u}^a d\Gamma = 0 \quad (3.6)$$

where, the notations $\boldsymbol{\varepsilon}$ (strain), $\boldsymbol{\varepsilon}^a$ (virtual strain), \mathbf{u}^a (virtual displacement), and \mathbf{t}^s without the superscript 0 are used to contrast with those defined in Eq. (3.2) for

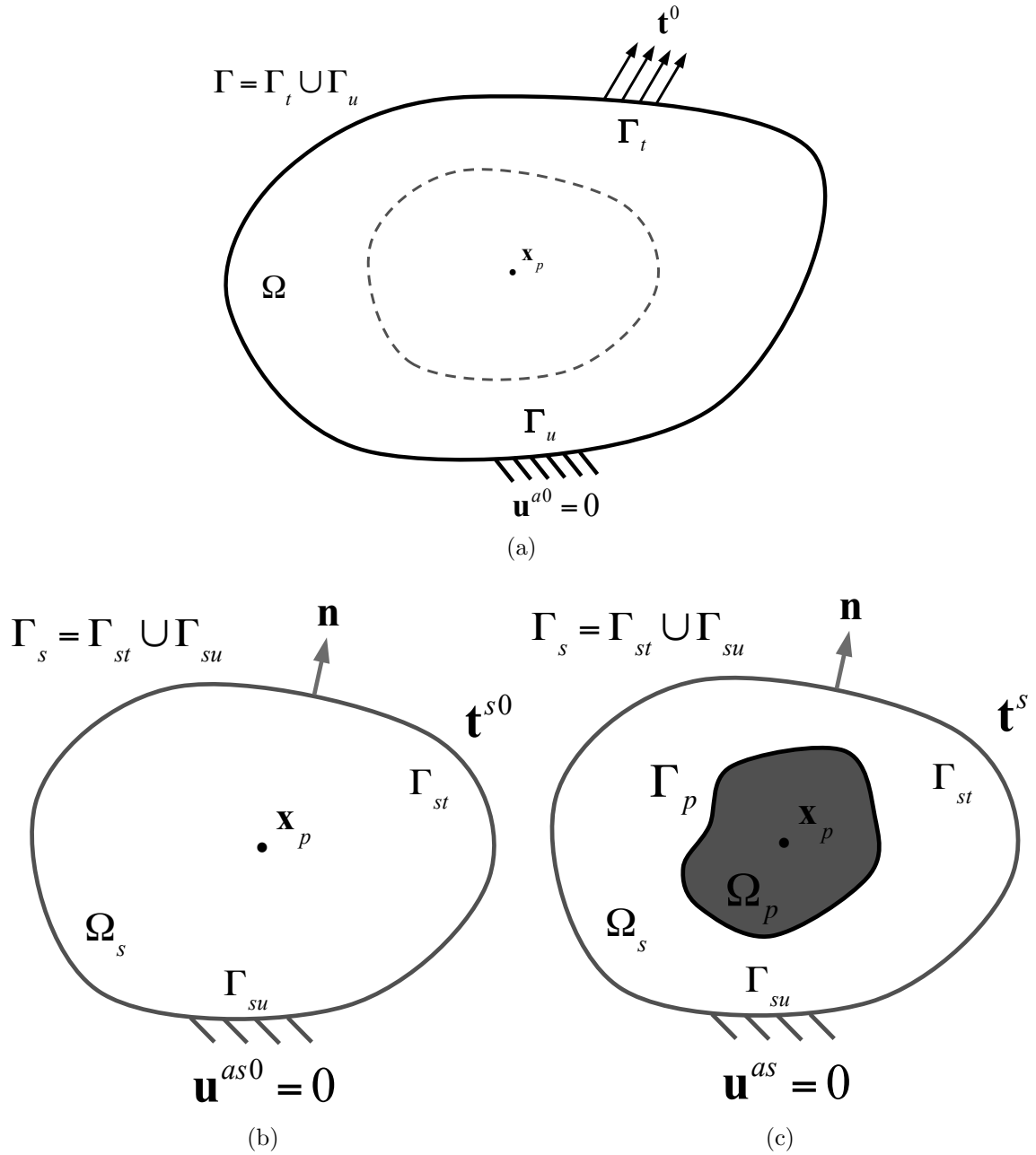


Figure 3.1. Definition of the configurational optimization problem: (a) Arbitrary subdomain within the solid (b) Elasticity problem associated with the homogeneous subdomain (c) Elasticity problem associated with heterogeneous subdomain created by introducing an arbitrary heterogeneity.

the homogeneous subdomain. Further, $\mathbf{C} = \mathbf{C}(\mathbf{x})$ denotes the fourth-order isotropic elasticity tensor explicitly expressed by:

$$\mathbf{C}(\mathbf{x})_{ijkl} = \begin{cases} \lambda^0 \delta_{ij} \delta_{kl} + \mu^0 (\delta_{ik} \delta_{jl} + \delta_{il} \delta_{jk}) & \text{in } \Omega_s - \Omega_p \\ \lambda \delta_{ij} \delta_{kl} + \mu (\delta_{ik} \delta_{jl} + \delta_{il} \delta_{jk}) & \text{in } \Omega_p \end{cases} \quad (3.7)$$

where, λ^0/λ , μ^0/μ are the Lamé constants corresponding to the matrix/heterogeneity.

The design transformation \mathbf{x} , design velocity \mathbf{v} , and material derivative \dot{z} of an arbitrary function z for the heterogeneous solid are defined in a manner analogous to their homogeneous counterparts in Eqs. (3.3) to (3.5), but without the superscript 0.

The following general deformation and load related (performance) objectives are proposed on the heterogeneous and homogeneous subdomains, respectively:

$$f(t) = \int_{\Omega_s} \psi(t, \varepsilon) d\Omega + \int_{\Gamma_s} \phi(t, \mathbf{n}, \mathbf{x}, \mathbf{u}, \mathbf{t}) d\Gamma \quad (3.8)$$

where, ψ and ϕ are arbitrary design criteria evaluated at instant t in the heterogeneous subdomains and their boundaries, respectively. Also, \mathbf{n} is the unit outward normal vector on Γ_s and thus identical in the two subdomains. For ease of reading, the arguments of ψ , and ϕ will be suppressed in the derivations that follow.

In addition to the above deformation related objectives, the amount of total mass of the heterogeneous subdomain is given by:

$$m(t) = \int_{\Omega_s} \rho(t, \mathbf{x}) d\Omega \quad (3.9)$$

where, $\rho(t, \mathbf{x})$ is the density field in the heterogeneous domains. Although the space and time variations of density is allowed here for generality, in the usual design scenarios, it is expected that these quantities do not vary within their domains or

with design time. Similar to the elasticity tensor $\mathbf{C}(\mathbf{x})$, the density field $\rho(\mathbf{x})$ in the heterogeneous subdomain is defined as:

$$\rho(\mathbf{x}) = \begin{cases} \rho^0 & \text{in } \Omega_s - \Omega_p \\ \rho & \text{in } \Omega_p \end{cases}. \quad (3.10)$$

In general, the heterogeneity can be either “stiff” or “soft”. The goal of the configurational optimization problem is to optimally determine the reference location \mathbf{x}_p of the heterogeneity, the orientation \mathbf{n}_p of a reference axis passing through \mathbf{x}_p , and a rotation θ about the reference axis as well as the heterogeneity shape to achieve the greatest/least “effect” in the performance objective for the least/greatest change in the mass of a stiff/soft heterogeneity. Thus, this **configurational optimization problem** is mathematically posed as the following Pareto-Optimal (multi-objective) formulation:

Find $\mathbf{x}_p, \mathbf{n}_p, \theta$ and the optimized shape of heterogeneity to:

$$\begin{aligned} & \text{minimize } g(t) = (1 - w)f(t) + wm(t), \quad 0 \leq w \leq 1 \\ & \text{subject to } c(t) = \int_{\Omega_s} \varepsilon : \mathbf{C} : \varepsilon^a d\Omega - \int_{\Gamma_s} \mathbf{t}^s \cdot \mathbf{u}^a d\Gamma = 0. \end{aligned} \quad (3.11)$$

By imposing the virtual work statements $c(t) = 0$ as the constraints, the adjoint boundary value problems naturally emerge. Also, w is the weight chosen by the designer to reflect the relative emphasis on the performance and mass terms. In general, the weight value has a one-to-one correspondence with the maximum allowable mass change [85]. In other words, this multi-objective optimization yields a family of solutions (the Pareto-Optimal family) corresponding to the various values of w .

In general, the design transformations \mathbf{x} and \mathbf{x}^0 and the corresponding velocities \mathbf{v} and \mathbf{v}^0 in the heterogeneous and homogeneous subdomains, respectively, are arbitrary and dictated by the design intent to move the boundaries of the body. Therefore, the conditions $\mathbf{x} = \mathbf{x}^0$ and $\mathbf{v} = \mathbf{v}^0$ will be imposed in the statement of Problem (3.11).

Also, without loss of generality (since the choice of Γ_{st} and Γ_{su} are arbitrary), it will be assumed that $\mathbf{t}^s = \mathbf{t}^{s0}$ on Γ_{st} . This choice is natural when the boundary Γ_{st} is the same as Γ_t .

The Lagrangian corresponding to Problem (3.11) is formed as:

$$\begin{aligned} G(t) &= g(t) - (1 - w)c(t) \\ &= (1 - w)[f(t) - c(t)] + wm(t). \end{aligned} \quad (3.12)$$

The material time derivative of $G(t)$, termed as the **Configurational Derivative**, is derived following the standard adjoint method for shape design sensitivity analysis [100,101]. Readers are referred to [98] for detailed derivation procedure. The resulting expression is written in terms of surface integrals as:

$$\begin{aligned} \dot{G}(t) &= (1 - w) \left[\int_{\Gamma_p} [[\mathbf{n} \cdot \Sigma]] \cdot \mathbf{v} \, d\Gamma + \int_{\Gamma_s} \mathbf{n} \cdot \Sigma \cdot \mathbf{v} \, d\Gamma \right. \\ &\quad + \int_{\Gamma_s} [(\phi + \mathbf{t} \cdot \mathbf{u}^a) (\nabla \cdot \mathbf{v} - \mathbf{n} \cdot \nabla \mathbf{v} \cdot \mathbf{n}) + \nabla \phi \cdot \mathbf{v} + \phi_{,\mathbf{n}} \cdot \dot{\mathbf{n}}] \, d\Gamma \\ &\quad \left. + \int_{\Gamma_{st}} \dot{\mathbf{t}}^s \cdot (\phi_{,\mathbf{t}} + \mathbf{u}^a) \, d\Gamma + \int_{\Gamma_{su}} (\phi_{,\mathbf{u}} \cdot \dot{\mathbf{u}}^s + \mathbf{t} \cdot \dot{\mathbf{u}}^{as}) \, d\Gamma \right] \\ &\quad + w \int_{\Gamma_p} [[\rho(\mathbf{v} \cdot \mathbf{n})]] \, d\Gamma \end{aligned} \quad (3.13)$$

where, Σ is the **configurational tensor** of the heterogeneous domain and has the following form:

$$\Sigma = (\psi - \sigma : \varepsilon^a) \mathbf{I} + \sigma^a \cdot \nabla \mathbf{u}^T + \sigma \cdot \nabla \mathbf{u}^{aT} \quad (3.14)$$

In Eqs. (3.13) and (3.14), σ^a , ε^a , and \mathbf{u}^a denote the adjoint stress, strain, and displacement to be solved from the following *adjoint boundary value problem* defined in the heterogeneous subdomain:

$$\int_{\Omega_s} \sigma^a : \xi \, d\Omega - \int_{\Gamma_{st}} \mathbf{t}^{as} \cdot \dot{\mathbf{u}} \, d\Gamma = 0 \quad (3.15)$$

where, $\xi = \frac{1}{2}(\nabla \dot{\mathbf{u}} + \nabla \dot{\mathbf{u}}^T)$. The constitutive law:

$$\sigma^a = \mathbf{C} : \varepsilon^a - \psi_{,\varepsilon} \quad \text{in } \Omega_s \quad (3.16)$$

defines the adjoint stress σ^a satisfying the equilibrium condition:

$$\nabla \cdot \sigma^a = 0 \quad \text{in } \Omega_s. \quad (3.17)$$

Also, the following displacement and traction boundary conditions are prescribed on Γ_{su} and Γ_{st} , respectively:

$$\mathbf{u}^{as} = -\phi_{,t} \quad \text{on } \Gamma_{su} \quad (3.18)$$

$$\mathbf{t}^{as} = \mathbf{n} \cdot \sigma^a = \phi_{,u} \quad \text{on } \Gamma_{st}. \quad (3.19)$$

The **configurational derivative** is identical to the material derivative of the objective $g(t)$ if the virtual work constraint $c(t) = 0$ is satisfied at every instant. It is noted that \mathbf{v} is required to be continuous but otherwise arbitrary in $\Omega_s - \Omega_p$ when deriving Eq. (3.13). Also, given the design criteria and the density commonly do not possess explicit dependence on design time t , it is assumed that $\psi_{,t} = \phi_{,t} = \rho_{,t} = 0$.

3.1.2 Configurational Derivative Corresponding to Translation, Rotation, and Scaling of Heterogeneity: Deriving Configurational Forces

Next, as illustrated in Figure 3.2, consider three specific design velocities corresponding to translation, rotation and uniform scaling of the heterogeneity boundary Γ_p described by:

$$\mathbf{v} = \hat{\mathbf{v}} \quad \text{on } \Gamma_p \quad (3.20)$$

$$\mathbf{v} = \hat{\boldsymbol{\omega}} \times \mathbf{r}_p \quad \text{on } \Gamma_p \quad (3.21)$$

$$\mathbf{v} = \alpha(t)\mathbf{r}_p \quad \text{on } \Gamma_p \quad (3.22)$$

with respect to a fixed subdomain boundary (no change in geometry and traction or displacement boundary conditions), i.e.,

$$\mathbf{v} = 0 \quad \text{on } \Gamma_s \quad (3.23)$$

$$\dot{\mathbf{t}}^s = \dot{\mathbf{t}}^{s0} \quad \text{on } \Gamma_{st} \quad (3.24)$$

$$\dot{\mathbf{u}}^s = \dot{\mathbf{u}}^{as} \quad \text{on } \Gamma_{su} \quad (3.25)$$

Here, $\hat{\mathbf{v}}$ is a constant velocity, $\hat{\boldsymbol{\omega}}$ is a constant angular velocity about an arbitrary axis

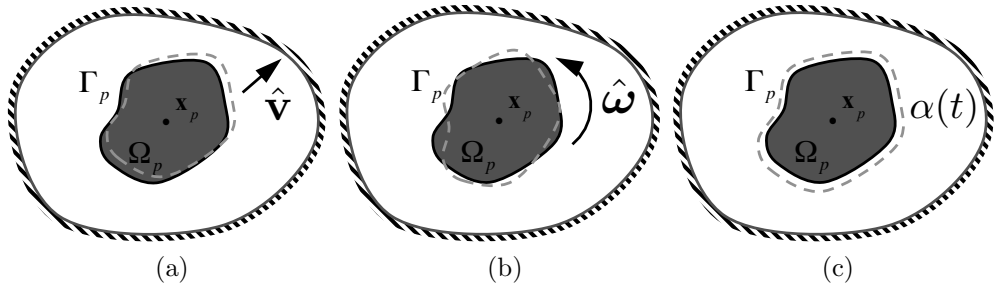


Figure 3.2. Specific design velocities imposed on the heterogeneity: (a) Translation (b) Rotation about an axis passing through \mathbf{x}_p (c) Scaling with respect to \mathbf{x}_p .

oriented along \mathbf{n}_p passing through an arbitrary point \mathbf{x}_p with $\mathbf{r}_p = \mathbf{x} - \mathbf{x}_p$, and $\alpha(t)$ is a parameter, independent of spatial location, defining the scaling of the heterogeneity relative to an arbitrary point \mathbf{x}_p .

Then, under the above three conditions, the configurational derivative $\dot{G}(t)$ by Eq. (3.13) takes the following respective forms:

$$\begin{aligned}\dot{G}^T(t) &= (1 - w) \left(\int_{\Gamma_p} \llbracket \mathbf{n} \cdot \Sigma \rrbracket d\Gamma \right) \cdot \hat{\mathbf{v}} \\ &= (1 - w) I_p^T(t) \cdot \hat{\mathbf{v}}\end{aligned}\tag{3.26}$$

$$\begin{aligned}\dot{G}^R(t) &= (1 - w) \left(\int_{\Gamma_p} \llbracket \mathbf{n} \cdot (-\Sigma \times \mathbf{r}_p) \rrbracket d\Gamma \right) \cdot \hat{\boldsymbol{\omega}} \\ &= (1 - w) I_p^R(t) \cdot \hat{\boldsymbol{\omega}}\end{aligned}\tag{3.27}$$

$$\begin{aligned}\dot{G}^S(t) &= \left[(1 - w) \left(\int_{\Gamma_p} \llbracket \mathbf{n} \cdot \Sigma \cdot \mathbf{r}_p \rrbracket d\Gamma \right) + w \left(\int_{\Gamma_p} \llbracket \rho (\mathbf{n} \cdot \mathbf{r}_p) \rrbracket d\Gamma \right) \right] \alpha \\ &= \left[(1 - w) I_p^S(t) + w \int_{\Gamma_p} \llbracket \rho (\mathbf{n} \cdot \mathbf{r}_p) \rrbracket d\Gamma \right] \alpha\end{aligned}\tag{3.28}$$

which are written in terms of integrals $I_p^T(t)$, $I_p^R(t)$, and $I_p^S(t)$ that are functions of the configurational tensor. The coefficients of the velocities $\hat{\mathbf{v}}$, $\hat{\boldsymbol{\omega}}$, and $\alpha(t)$ in the above expressions yield the **configurational forces** associated with the motion of the boundary Γ_p .

We note that under the translation, rotation, and scaling transformations of the heterogeneity, the corresponding sensitivities are independent of the solutions to the original and adjoint boundary value problems defined in the homogeneous subdomain.

3.2 Numerical Examples

Numerical examples of design through configurational optimization are demonstrated in this section. Optimal location and orientation of holes are determined through the previously described configurational derivative.

3.2.1 Optimal Location of an Elliptical Hole in a Plate

Consider a square plate with an elliptical hole subjected to a quadratic load as illustrated in Figure 3.3a. The elliptical hole was inserted at a random initial location and its optimal location was determined through a steepest descent search using Eq. (3.26) as the gradient. The optimal solution was then confirmed by calculating the structural compliance of the square plate as a function of the position of elliptical hole as shown in Figure 3.3b.

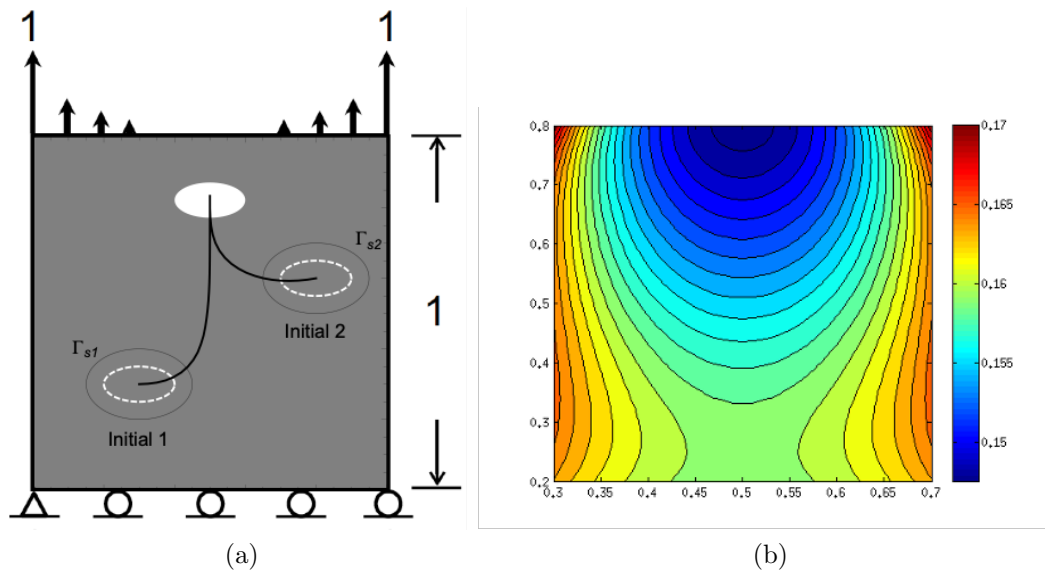


Figure 3.3. (a) Configurational optimization problem to determine the optimal location of an elliptical hole. (b) Numerical estimation of structural compliance as a function of the location of the elliptical hole.

The square plate as well as the inserted hole are approximated by quadratic NURBS entities. Results of von Mises stress over the plate during the process of configurational optimization are demonstrated in Figure 3.4. Stress concentration along the boundary of the elliptical hole gradually decreases as the hole moves toward the top center portion of the plate. The calculated optimal location of the elliptical hole agrees well with the optimal location identified earlier in Figure 3.3b through exhaustive search.

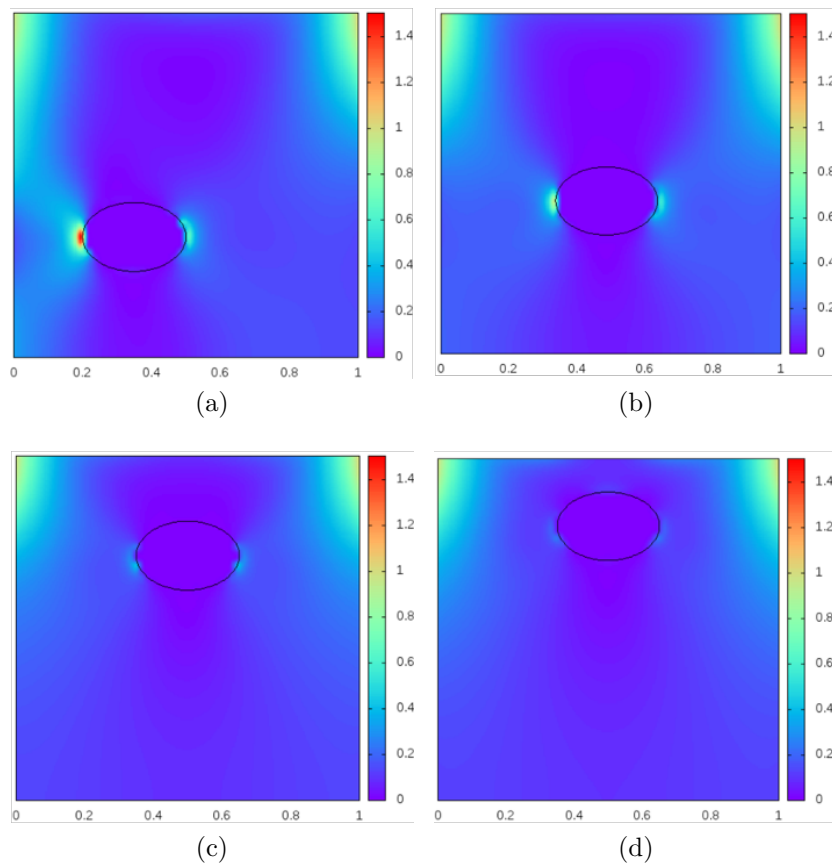


Figure 3.4. Von Mises stress contour during configurational optimization at (a) the initial step, (b) intermediate step 1, (c) intermediate step 2, and (d) the end of optimization determining the optimal location of the elliptical hole.

3.2.2 Optimal Orientation of an Elliptical Hole

Next, consider a similar square plate with an elliptical hole, but subjected to a uniform load as illustrated in Figure 3.3a. The elliptical hole was inserted at the center of the plate and its optimal orientation is obtained by the steepest descent method using Eq. (3.27) as the gradient. The structural compliance of the square plate as a function of the orientation of elliptical hole is numerically evaluated and shown in Figure 3.3b.

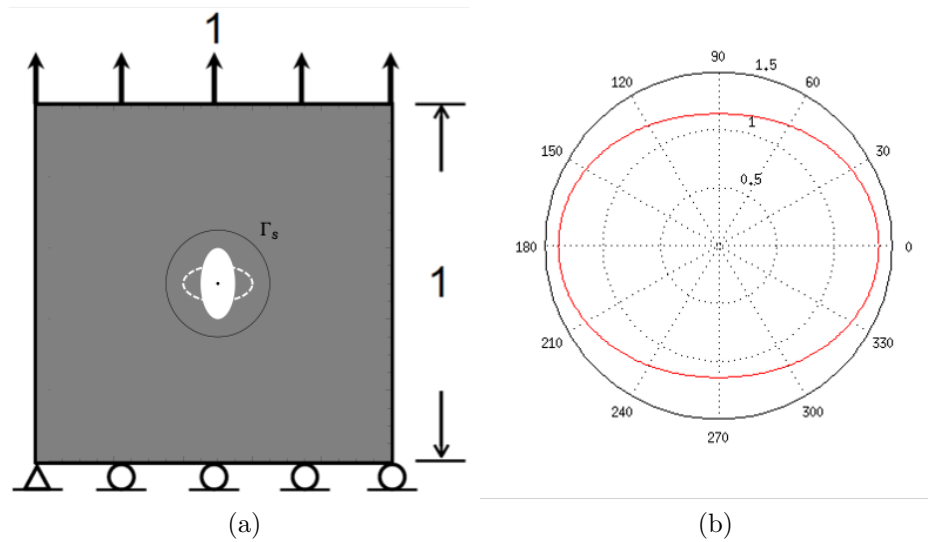


Figure 3.5. (a) Configurational optimization problem to determine the optimal orientation of an elliptical hole. (b) Calculated structural compliance as a function of orientation of the elliptical hole.

The calculated von Mises stress in the plate during the process of configurational optimization is shown in Figure 3.6. Initially, a strong stress concentration can be observed at both ends of the elliptical hole. As the optimization progresses, the orientation of the elliptical hole is gradually turned in the direction of tensile loading. The optimal orientation was eventually determined to be aligned with the vertical axis as the stress concentration is least in this orientation as shown in Figure 3.6d. The calculated optimal orientation matches well with the calculation shown in Figure 3.5b.

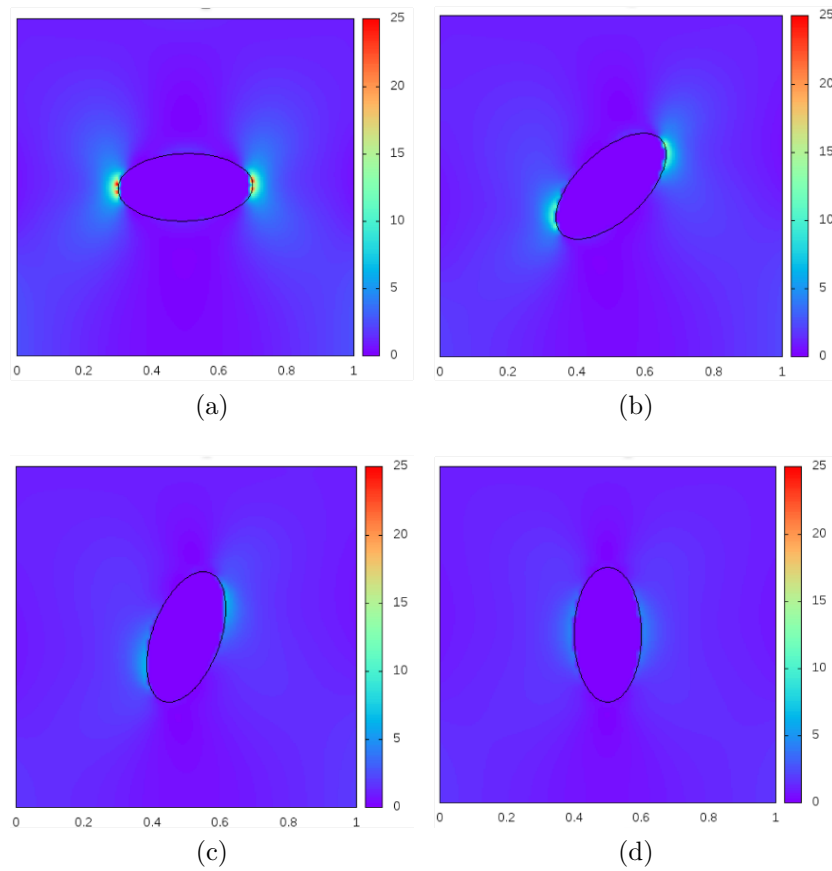


Figure 3.6. Von Mises stress contour during configurational optimization at (a) the initial step, (b) intermediate step 1, (c) intermediate step 2, and (d) the end of optimization determining the optimal orientation of an elliptical hole.

4. IMPLEMENTATION

The techniques and algorithms described in the present thesis are implemented in an object-oriented Hierarchical Design and Analysis Code (HiDAC). The code is developed to emphasize ease of use and sharing over the previously developed Object Oriented Fortran (OOF) version of HiDAC [78]. In addition, the code is also intended to enable quick concept validation during early research exploration. The features of the code as well as the typical flow of control during use of the code are described in detail in the following sections.

4.1 HiDAC: Hierarchical Design and Analysis Code

The code is based on the Matlab programming language (2019) [102]. Matlab is a very popular high-level interpreted language for numerical computation, visualization and object-oriented programming application development. Although the efficiency of Matlab language is generally poorer than compiled languages such as C/C++ and Fortran, it has a number of outstanding advantages that override its weakness. Specifically, in the context of academic research, the ease with which Matlab allows development and validation of new algorithms is of great convenience. First, Matlab provides a vast library of mathematical functions ranging from linear algebra to optimization and many more. The users can hence focus on their specific algorithm without the need to maintain compatible libraries regardless of the operating system in use. Second, the Matlab application environment provides a responsive and interactive interface. These features allow quick tests of algorithmic ideas and thereby accelerate the algorithm development process. Moreover, access to libraries in C++ and Python as well as subroutines written in Fortran are permitted, which gives further flexibility during algorithm development. The adoption of Matlab lan-

guage over the other compiled programming languages is a trade-off for its exceptional maintainability and portability, which may represent acceptable compromises over its inefficiency or problem size limitation.

The HiDAC Matlab code is composed of 34,000 lines and can be used to solve elastostatic or thermal conduction boundary value problems with or without enriched field approximation. Specifically, the enriched approximation enables the coupling of multiple patches through parametric stitching techniques and modeling of singular stress in multi-material wedges or cracks described in the later chapters of this thesis. Implementation was carefully done to ensure optimized performance while maintaining reusability and extensibility of the developed scripts. Highlighted features of the code are briefly summarized as follows.

1. *Problem dimension independence.* The code is developed with problem dimension independence in mind. Functions generally work for one-dimensional, two-dimensional and three-dimensional problems unless exhaustive recursive callings are needed for the particular functions that impact the performance of code.
2. *Prototype-based Object-oriented Programming.* The object-oriented programming (OOP) is implemented in a prototype-based approach instead of class-based syntax commonly seen in C++ or modern Fortran. With the prototype-based OOP, new objects are allowed to be created from scratch or cloned from existing prototypical objects without needing a predefined, explicit definition of a class for instantiation. Although the absence of class declaration degrades the efficiency overall, prototypical objects feature offers the flexibility of arbitrarily changing the created object by adding new fields or type-bound methods during the course of development.
3. *Vectorization.* The implementation throughout the code is highly vectorized that minimizes typical loop-based operations. Vectorization allows the Matlab Just-In-Time compilation to optimize object-oriented function calls, bit-wise calculation and element-wise arithmetic operations. The code is thus capable

of handling moderate sized three-dimensional problems despite the limitations of an interpreted language.

4.2 HiDAC Key Modules and Their Features

HiDAC consists of several key modules in conjunction with external packages as illustrated in Figure 4.1. The attributes of the respective modules are briefly discussed below.

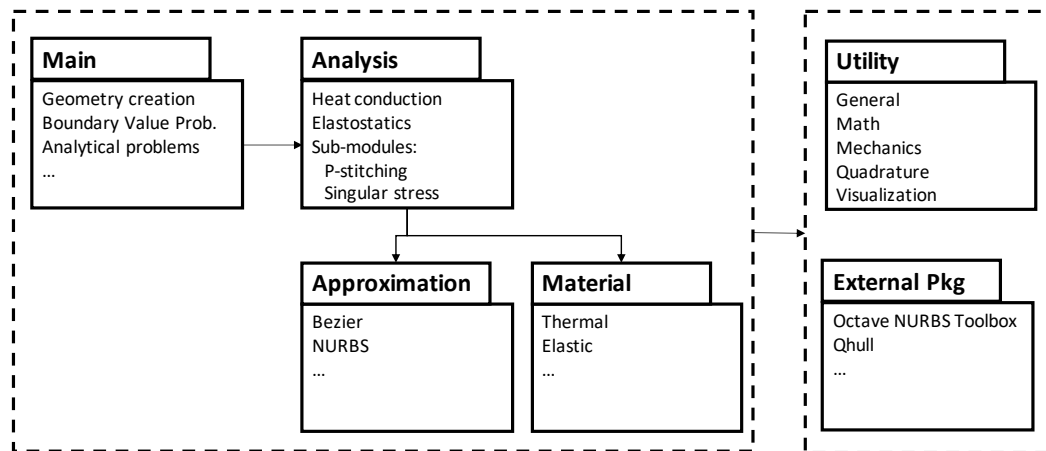


Figure 4.1. Code architecture of matlab HiDAC.

1. **Approximation:** The Approximation module contains two basic parametric splines including Bezier spline and NURBS. In HiDAC, parametric splines are used to provide approximation space for geometry representation, material distribution as well as behavioral fields. Subroutines for querying basis functions, approximated values, and their derivatives as well as Jacobian are defined.

- `getBasis()`, `getBasisDeriv()`
- `getVal()`, `getDeriv()`

- `getJac()`

To facilitate application of boundary conditions, the following functions allow users to extract global indices of relevant vertices, edges or faces with string-based descriptions.

- `getNameSelectCtrlPt()`
- `getNameSelectElem()`

Furthermore, two methods are implemented to visualize arbitrary scalar and vector fields over the geometric representation of domains or boundaries.

- `plotScalarField()`
- `plotVectorField()`

2. **Material:** Material types, properties and the associated methods are handled by the `Material` module. New or extended material models may be simply implemented by adding the collection of attributes and methods as submodules. All material types are implemented with the `getDm()` method to obtain the associated discretized material matrix.
3. **Analysis:** Methods relevant to particular analysis systems are all implemented in the `Analysis` module. The currently available analysis systems include heat conduction and elastostatics as the base modules. Additional submodules add enriched field approximation upon the base modules that in turn enable multi-patch analysis through parametric stitching enrichment, displacement jump across crack face through Heaviside enrichment, and singular stress description through multi-material wedge enrichment.

Functions at different stages of analysis including pre-processing, assembly and post-processing are implemented while operations and algorithms during the solution phase leverage the optimized linear algebra library of Matlab. Each individual base modules and submodules possess a `getDofIdx()` method to

query the associated local or global indices of degrees of freedom for a given point in the space. Similarly, each module is implemented with `getField()` and `getGradField()` type of functions to obtain quantities appropriate for an analysis type. For instance, elastostatics analysis modules with or without multi-patch parametric stitching define the following functions to evaluate the approximated fields at any given point.

- `getDisplacement()`
- `getStrain()`
- `getStress()`

4. **Utility:** The `Utility` module contains independent subroutines that could be used for any type of approximation, material or analysis. These functions are organized into sub-modules including *General*, *Math*, *Mechanics*, *Quadrature* and *Visualization*. Examples of functions include getting rotation matrix between coordinate systems for tensors, querying Gaussian quadrature points of arbitrary order, or obtaining invariants associated with specific physics such as principal stresses or energy density, etc.
5. **ExternalPkg:** All external packages not readily available in the Matlab built-in libraries are treated as sub-modules of the `ExternalPkg` module. Many of the lower-level Bezier and NURBS approximation methods for basic geometry creation, basis function evaluation and visualization are based on Octave NURBS Package [103,104].

4.3 NURBS Geometry Modeler

A key and powerful element of the matlab HiDAC is the NURBS geometry modeler that facilitates generation of analysis-suitable geometric representation. It is developed to enable simple and intuitive geometry generation process over the previously developed OOF-HiDAC.

In OOF-HiDAC, creation of NURBS curves, surfaces and volumes generally requires a good understanding of spline as well as the custom data structures. It relies on Visualization Toolkit (VTK) to visualize geometry or the associated field distribution. However, open source VTK application programming interface (API) for Fortran does not fully support the entire VTK standard. Additional effort must be invested in order to visualize sophisticated drawings that can be easily made by either Matlab or Python. Although the VTK allows scalable distributed-memory parallel processing under Message Passing Interface (MPI), there is very little need for it in the present research, where the main purpose of the numerical implementation is to validate the approximation forms proposed in this study.

The NURBS geometry modeler is part of the Matlab HiDAC's approximation module and it is built upon the Octave NURBS toolbox package [103,104]. It supports direct input of knots and control points, but also provides a number of handy auxiliary functions for ease of use. Figure 4.2 demonstrates some representative NURBS curves that can be effortlessly generated. With the help of auxiliary functions, users can intuitively define the geometry by parameters such as the coordinates of end points or the dimensions of the rectangle without difficulty. For instance, while the circular arc shown in Figure 4.2c is explicitly defined in terms of polynomial degree, knots and control points as listed in Table 4.1, the control points are much more intuitively defined using coordinate system location $(0, 0)$, radius $r = 10$, starting angle $\theta_1 = 48^\circ$ and ending angle $\theta_2 = 312^\circ$.

Table 4.1.

NURBS definition of the circular arc shown in Figure 4.2c.

Polynomial degree (p)	2
Knots (ξ)	0, 0, 0, 1/3, 1/3, 2/3, 2/3, 1, 1, 1
Control points x	6.6913, -0.3490, -7.1934, , -10, -7.1934, -0.3490, 6.6913
Control points y	7.4314, 9.9939, 6.9466, 0, -6.9466, -9.9939, -7.4314
Control points w	1, $1/\sqrt{(2)}$, 1, $1/\sqrt{2}$, 1, $1/\sqrt{2}$, 1

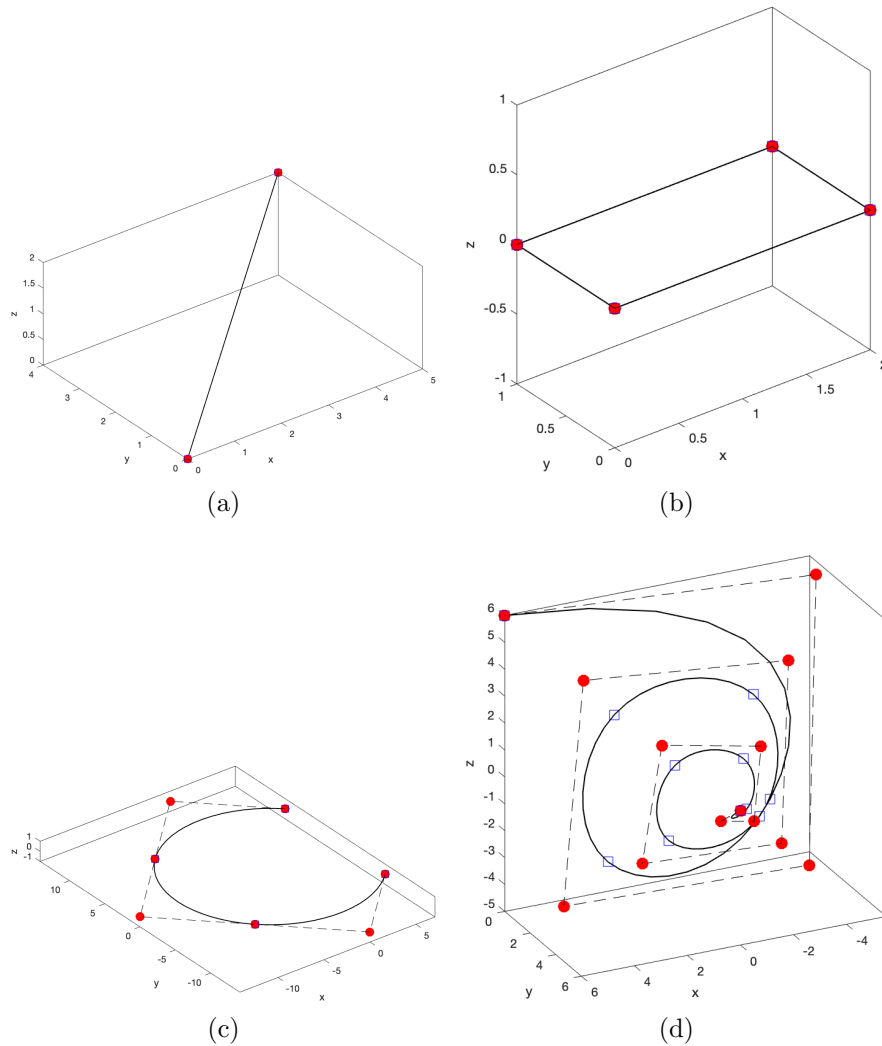


Figure 4.2. NURBS curve representation of (a) a straight spline, (b) rectangular lines, (c) a circular arc, and (d) an arbitrary curve.

The advantage of the Matlab HiDAC geometry modeler is even more obvious especially for geometries of higher dimension. Figure 4.3 shows a number of NURBS representations including a square patch, a cylindrical surface, a ruled surface and a coons patch without the need to define knots and control points in a point-wise manner. Users simply define the geometric parameters to model the square patch as well as the cylindrical surface. The NURBS representation of the ruled surface or

the coons patch are constructed from two curves or four curves, respectively. The highlighted red curves in Figures 4.3c and 4.3d indicate the curves used for the construction of the surfaces.

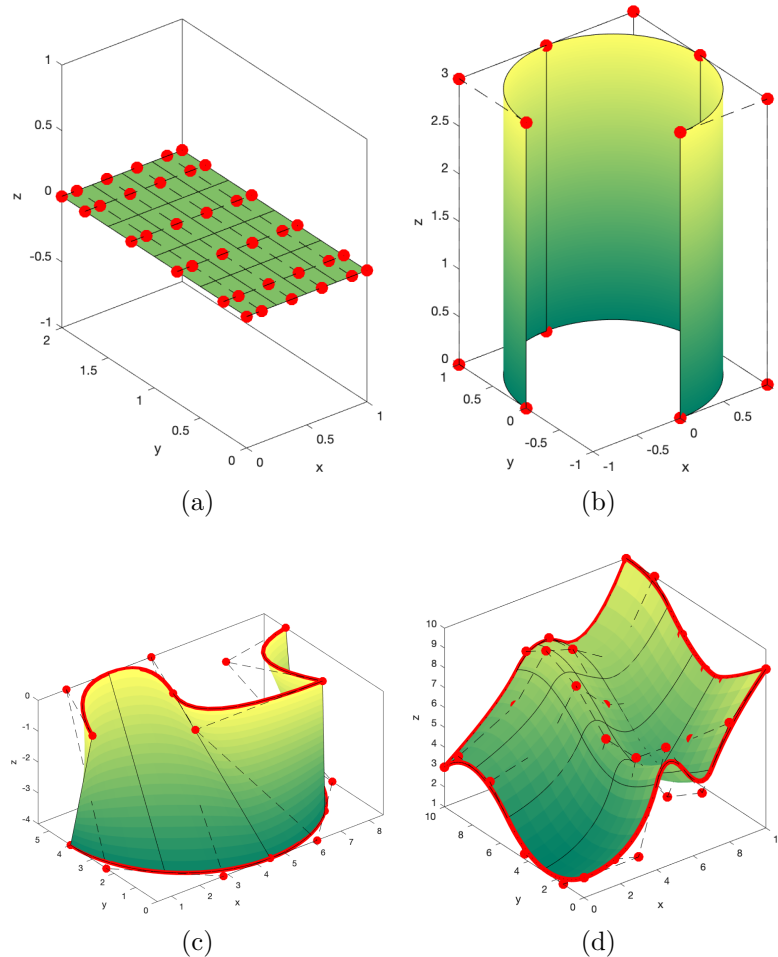


Figure 4.3. NURBS surface representation of (a) a rectangular patch, (b) a cylindrical surface, (c) a ruled surface, and (d) a coons patch.

In addition to methods used for construction of curves and surfaces, basic CAD operations including extrusion and revolution are also available to aid generation of NURBS representations. Curve or surface can easily be extruded or revolved into a surface or a volume from a lower dimensional geometry. As shown in Figure 4.4 and Figure 4.5, these two operations further alleviate the difficulties in defining the

NURBS representations of two or three dimensional geometries. In the figures, the red curves and discretized surfaces indicate the source entities used for the construction of the higher dimensional geometry.

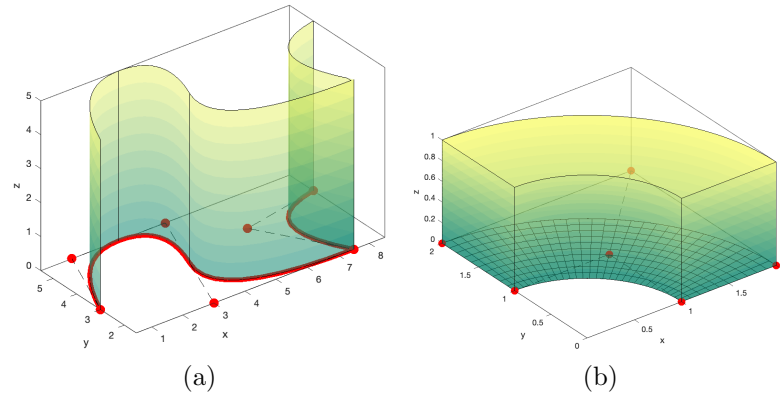


Figure 4.4. Extrusion operation of NURBS representation (a) from a curve to a surface, and (b) from a surface to a volume.

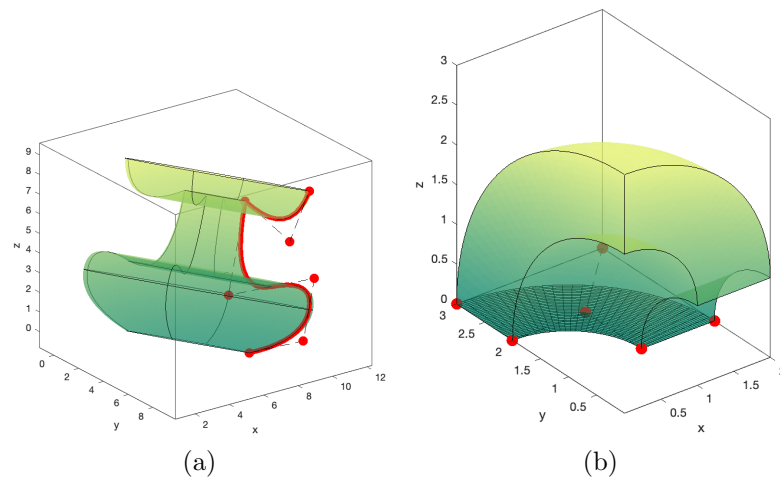


Figure 4.5. Revolution operation of NURBS representation (a) from a curve to a surface, and (b) from a surface to a volume.

4.4 Analysis Flow

4.4.1 Overview

Figure 4.6 illustrates a typical analysis flow for elastostatic problems with the enriched field approximation technique. The geometric representation of the problem domain is first defined by parametric domains. Then, material properties are defined and associated with each part of the problem domain. Next, enriching interfaces are defined and introduced into the problem. In general, the enriching interfaces could be embedded into the domain, inserted along the edges of the patches being coupled, or placed on the external boundaries of the overall problem domain. The specified boundary conditions are then assigned onto the external boundaries of the problem domain. Before the assembly process, the augmented composed domain is formed by joining each individual patch with the enriching interfaces. Once the problem definition is complete with the above pre-processing procedure, the linear system of the problem is then assembled and solved in parallel. The solution is post-processed, output and visualized in the desired format.

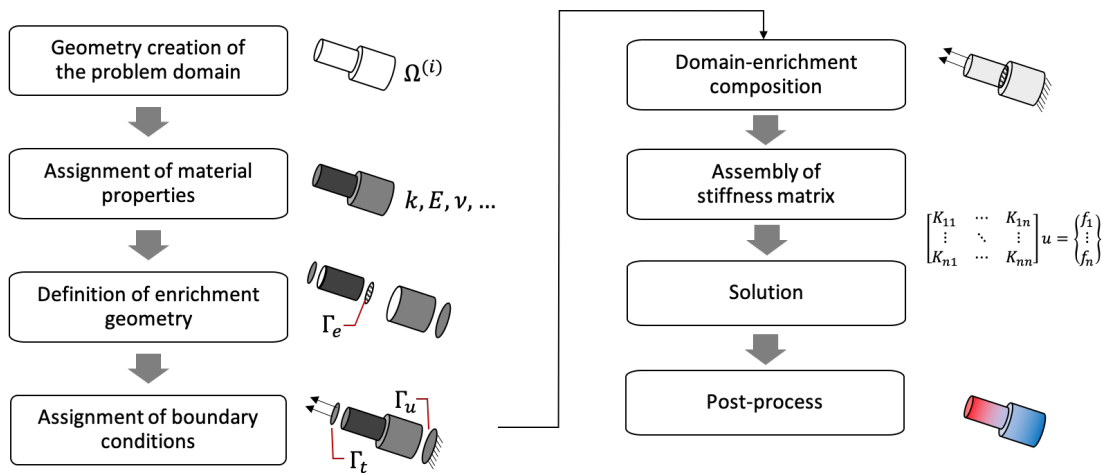


Figure 4.6. Typical flow of control using matlab HiDAC for an enriched isogeometric analysis.

4.4.2 Scripting Interface

The implemented scripting interface is demonstrated through a three-dimensional heat conduction example. An initialization block is usually called upfront as shown in Figure 4.7a. The function `initializeHiDAC` frees up the memory and loads the basic parameters for the analysis. Next, relevant modules are loaded into the program by calling `addModule` function. Subsequently, the geometry, materials, boundary conditions and analysis parameters are further defined by the user as illustrated in Figure 4.7b. The generated NURBS representation of the volume using the geometry modeler is shown in Figure 4.7c.

```

%% initialize
initializeHiDAC;
addModule(envVar, dirs.HIDAC_ROOTDIR, 'Analysis/HeatConduction');
addModule(envVar, dirs.HIDAC_ROOTDIR, 'Material/Thermal');
addModule(envVar, dirs.HIDAC_ROOTDIR, 'Approximation/Nurbs');
addModule(envVar, dirs.HIDAC_ROOTDIR, 'Utility');
addModule(envVar, dirs.HIDAC_ROOTDIR, 'ExternalPkg/NurbsToolBox_1.3.13');
addModule(envVar, dirs.HIDAC_ROOTDIR, 'Main/Geometry/HeatConduction');

```

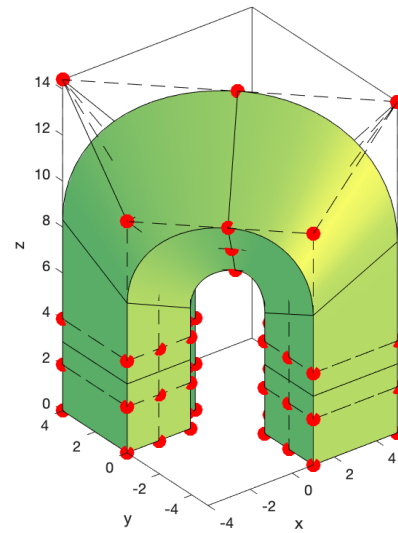
(a)

```

%% User input
% Geometry
nrb = getNurbsGeometry();
% Material
material = struct();
material.type = 'isotropic';
material.k = 1;
% Boundary conditions - essential
bc = struct();
bc.essential(1) = struct();
bc.essential(1).nameSelectEntity = '(u,v,w1)';
bc.essential(1).dof = 1;
bc.essential(1).val = 0;
% Boundary conditions - natural
bc.natural(1) = struct();
bc.natural(1).nameSelectEntity = '(u,v,wn)';
bc.natural(1).dof = 1;
bc.natural(1).val = 2;
% Analysis parameters
analysisPar = struct();
analysisPar.qdType = 'gauss';
analysisPar.qdOrder = 2;

```

(b)



(c)

Figure 4.7. Program (a) initialization script, (b) typical user inputs, and (c) the generated NURBS representation of a volume.

Once the problem is fully defined, the analysis and post processing are subsequently performed as illustrated in Figure 4.8. The functions for assembly and boundary condition imposition are implemented in other analysis systems also. Figure 4.9 illustrates the temperature field as well as the flux field on the example heat conduction problem. The function `getNrbKntOnBound` and `getNrbKntInDomain` are used to generate uniformly distributed query points on the boundaries and within the domain, respectively. Then, `getTempAtKnot` and `getFluxAtKnot` are called to evaluate the fields at the query points. Similar functions are also available for elastic analysis and other types of enriched isogeometric analysis. To plot the evaluated field on the boundaries or in the domain, `plotScalarField` and `plotVectorField` are called with the desired plotting attributes.

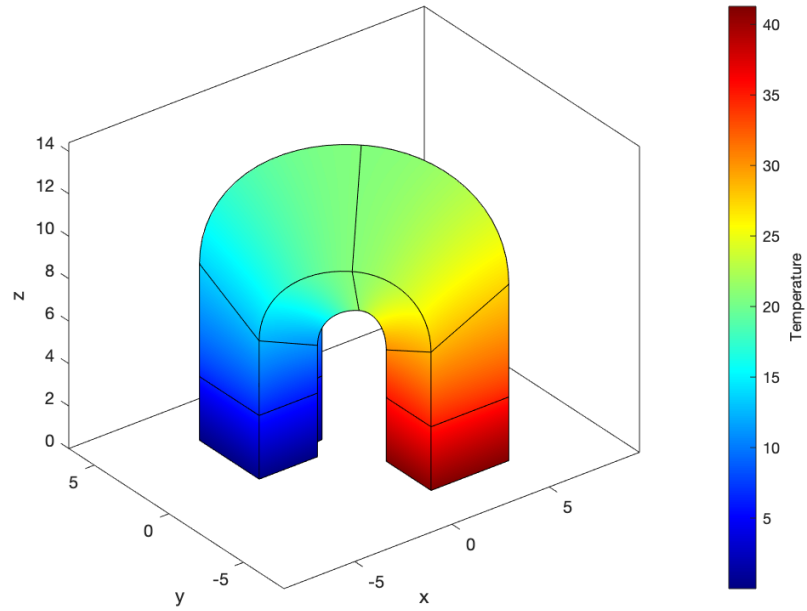
```
%% Analysis
K = Assemble(nrb, material, bc, analysisPar);
f = applyNaturalBc(nrb, bc, analysisPar);
[K, f] = applyEssentialBc(nrb, bc, analysisPar, K, f);
u=K\f;
```

(a)

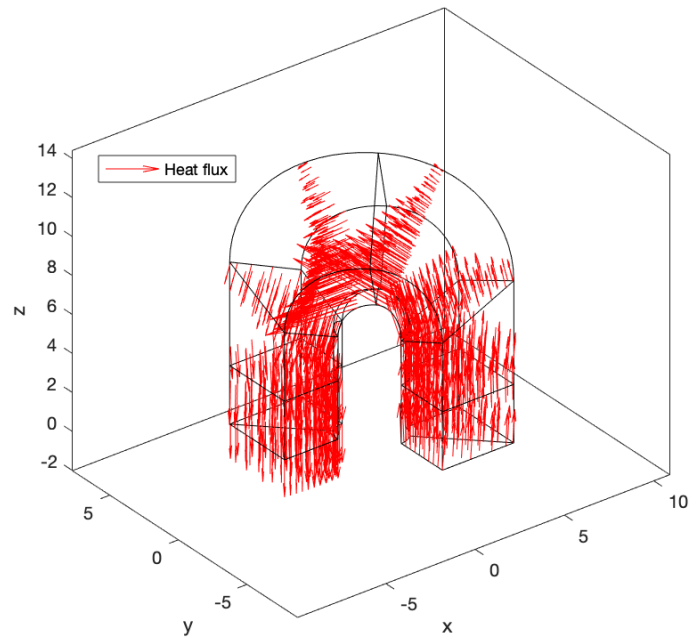
```
%% Post-process
subd = [1,1,1]*20;
% temperature
figure();
hold on; box on; axis equal; view(3); xlabel('x'); ylabel('y'); zlabel('z'); colorbar;
for bd=1:6
knt = getNrbKntOnBoundSubdPlot(nrb, subd, bd);
[u_appr] = getTempAtKnot_HeatConduction(nrb, u, knt);
plotScalarField(nrb, u_appr, knt);
end
% flux
figure();
hold on; box on; axis equal; view(3); xlabel('x'); ylabel('y'); zlabel('z');
knt = getNrbKntInDomainSubdPlot(nrb, subd);
[q_appr] = getFluxAtKnot_HeatConduction(nrb, material, u, knt);
plotVectorField(nrb, q_appr, knt, 'FaceColor', 'k', 'FaceAlpha', 0.0);
```

(b)

Figure 4.8. HiDAC environment for (a) analysis, and (b) post-processing.



(a)



(b)

Figure 4.9. (a) Temperature solution contour over the outer boundary, and (b) heat flux vectors within the domain.

5. PARAMETRIC STITCHING FOR SMOOTH COUPLING OF SUBDOMAINS WITH NON-MATCHING DISCRETIZATIONS

In this chapter, a unified formulation to smoothly couple non-matching parametric domains for both geometric modeling and analysis of behavior is presented. The key concept used to accomplish the coupling is a “parametric stitching” or p -stitching interface between the incompatible patches. Specifically, p -stitching permits independently varying fields with assured, arbitrary smoothness at the interface between the coupled subdomains. The developed procedure enables modular construction of coupling problems with compatible interfaces as well as the ability to characterize sharp changes in gradient, as at dissimilar material interfaces. Fundamental to the developed methodology is enriched field approximations. The base approximations in the subdomains are enriched by the interfacial fields constructed as a function of distance from the coupling interfaces. The proposed method is argued to be the smooth extension of the dual-primal method such as the localized version of the Lagrange multiplier method. Non-uniform rational B-splines (NURBS) are chosen for discretizing the parametric subdomains. The developed procedure though is valid for other representations of subdomains whose basis functions obey partition of unity. The proposed method was validated through patch tests and demonstrate the approach on several two- and three-dimensional elastostatic as well as heat conduction numerical examples.

5.1 Construction of Enriched Field Approximations

Considering Figure 5.1, we begin with the coupling interface Γ_i of each patch that are part of the boundary of the associated patch $\partial\Omega_i$. We will assume that the two patches share a compatible interface geometry denoted by Γ_e , i.e., $\Gamma_e \equiv \Gamma_i$.

We construct an enriching approximation from the coupling interface Γ_e over the subdomain Ω_i . We observe that we can construct an enriched field approximation (Eq. (2.11)) as a function of the normal distance from the boundary Γ_e . Thus, at a parametric location (ξ, η) on the enriching boundary, in the direction normal to the boundary, we can express the enriching approximation through a generalized Taylor's series expansion of the form:

$$f_{\Gamma_e}(\xi, \eta, d) = f^0(\xi, \eta) + \sum_{m=1}^{\infty} \frac{1}{m!} f'^m(\xi, \eta) d^m \quad (5.1)$$

where, f^0 is the constant term and $f'^m = \frac{\partial^m f}{\partial n^m}$ is the m^{th} directional derivative of the field in the normal direction at the parametric location (ξ, η) of the boundary, and d is the distance in the normal direction at the point on the boundary. When constructing the approximation, the term f^0 and the derivatives f'^m are in turn isoparametrically approximated as described in Eq. (2.2). Thus,

$$f^0(\xi, \eta) = \sum_{k=1}^{n_k} \sum_{l=1}^{n_l} R_{kl}(\xi, \eta) \bar{f}_{kl}^0 \quad (5.2)$$

$$f'^m(\xi, \eta) = \sum_{k=1}^{n_k} \sum_{l=1}^{n_l} R_{kl}(\xi, \eta) \bar{f}'_{kl}{}^m \quad (5.3)$$

with $\bar{f}_{kl}^0, \bar{f}'_{kl}{}^m$ being the unknowns that are obtained during the solution process.

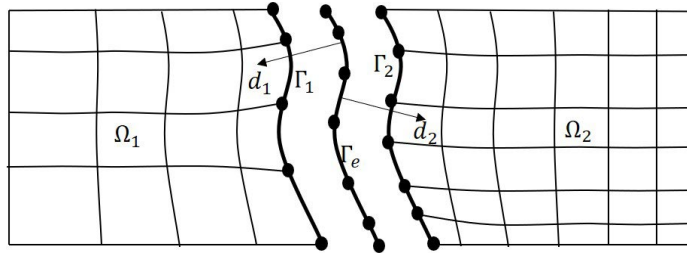


Figure 5.1. Illustration of non-matching parametric domains. The interfaces are shown separated for clarity, but $\Gamma_e \equiv \Gamma_i$.

Now, the coupling of the two subdomains at the interface is achieved by defining the function f_{Γ_e} in Eq. (2.11) as corresponding to the interface geometry Γ_e . Thus, the approximate blended field within *each* subdomain Ω_i is

$$f_i(\mathbf{x}) = [1 - w(d_i(\mathbf{x}))] f_{\Omega_i}(\mathbf{x}) + w(d_i(\mathbf{x})) f_{\Gamma_e}(\xi, \eta, d_i(\mathbf{x})) \quad (5.4)$$

where, $d_i(\mathbf{x})$ and $w(d_i(\mathbf{x}))$ denote the distance from the boundary Γ_e to a point in the domain Ω_i , and the weight value that provides the influence of the field approximation on the boundary Γ_e as a function distance, respectively. $f_{\Omega_i}(\mathbf{x})$ is the underlying field approximation in the domain Ω_i , f_{Γ_e} is the enrichment intended for subdomain Ω_i , and $f_i(\mathbf{x})$ is the resulting blended approximation in Ω_i . In general, using identical values of \bar{f}_{kl}^0 and $\bar{f}'_{kl}{}^m$ in Eqs. (5.2) and (5.3) in both domains ensures the continuity of the field across the interface. However, one may choose to keep the value of \bar{f}_{kl}^0 the same between the two subdomains but keep two distinct values of \bar{f}'_{kl} to allow derivative discontinuity as at a material interface. The advantage of this formulation is that it may be expanded to arbitrary order to achieve the desired smoothness across the boundary. The constructed approximation allows arbitrary smoothness, but additional unknowns are introduced at the control points of the enriching interface Γ_e as defined in Eqs. (5.2) and (5.3).

While the NURBS approximation for $f_{\Gamma_e}(\mathbf{x})$ in Eq. (5.1) is arbitrary, it may be convenient to use the approximation corresponding to the underlying approximation on Γ_i , that is, f_{Γ_e} is the value of f_{Ω_i} along the patch boundary Γ_i . In this study, we chose f_{Γ_e} as corresponding to the boundary with the coarser discretization (for example, Γ_1 in the illustration of Figure 5.1).

This choice along with enforcement of derivative continuity leads to the value of the field at the interface being captured by a set of unknowns representing the interface, namely, \bar{f}_{kl}^0 and $\bar{f}'_{kl}{}^m$.

Since the normal derivatives are defined independent of the underlying subdomain approximations, the interacting physical forces are fully described by the unknowns

\bar{f}_{kl}^0 and \bar{f}_{kl}^m in each subdomain. Therefore, no interaction between the subdomains needs to be considered when constructing the system stiffness matrix – the interfacial unknowns fully describe the coupling. Thus, the proposed methodology enables parallel assembly as well as a modular procedure to construct the coupling problem.

5.2 P-Stitching Formulation for Elasto-Static Problems

The proposed general formulation for coupling fields is specialized for elasto-static problems in this section. Consider an elastic object with subdomains as illustrated in Figure 5.2. The body is subjected to Dirichlet boundary conditions $\bar{\mathbf{u}}$ on Γ_u and traction $\bar{\mathbf{t}}$ is enforced on Γ_t with $\Gamma_u \cap \Gamma_t = \emptyset$. While the developed procedure is generally valid for stitching overlapping domains, for simplicity, the domain illustrated here is composed of two non-overlapping subdomains Ω_1 and Ω_2 such that $\bigcup_{\alpha=1}^2 \Omega_\alpha = \Omega$, and $\bigcap_{\alpha=1}^2 \Omega_\alpha = \Gamma_e$ where Γ_e is the coupling interface.

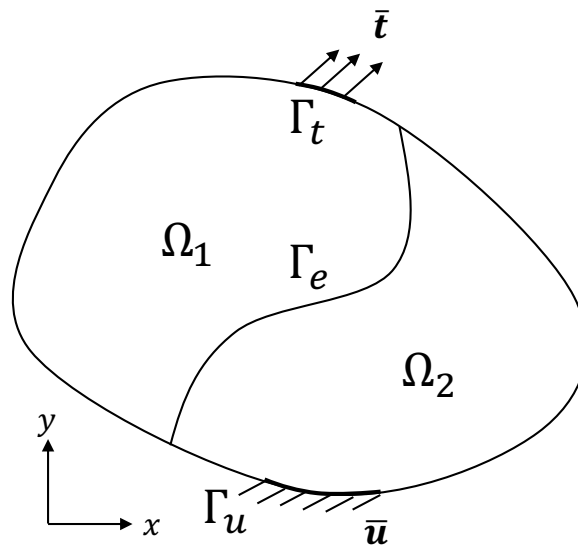


Figure 5.2. Problem domain consisting two subdomains that need to be smoothly coupled.

With displacement compatibility and traction reciprocity conditions enforced along the coupling interface, the elasticity problem is written as follows:

$$\nabla \cdot \boldsymbol{\sigma} + \mathbf{b} = \mathbf{0} \quad \text{in } \Omega \quad (5.5a)$$

$$\mathbf{u} = \bar{\mathbf{u}} \quad \text{on } \Gamma_u \quad (5.5b)$$

$$\mathbf{t} = \bar{\mathbf{t}} \quad \text{on } \Gamma_t \quad (5.5c)$$

$$\mathbf{u}^{(1)} - \mathbf{u}^{(2)} = \mathbf{0} \quad \text{on } \Gamma_e \quad (5.5d)$$

$$\mathbf{t}^{(1)} + \mathbf{t}^{(2)} = \mathbf{0} \quad \text{on } \Gamma_e \quad (5.5e)$$

In this work, we consider the expansion of the coupling field to the first order in Eq. (5.1). The displacement field $\mathbf{u}(\mathbf{x})$ is the unknown that is required to be compatible along the coupling interface. The gradients of the displacements may or may not be compatible depending on the nature of the materials in the two subdomains. Thus, a first-order reduction of Eq. (5.4), specialized for the current elasticity problem is:

$$\mathbf{u}_i(\mathbf{x}) = (1 - w(d_i))\mathbf{u}_{\Omega_i}(\mathbf{x}) + w(d_i)(\mathbf{u}_{\Gamma_e}^0(\mathcal{P}(\mathbf{x})) + \mathbf{u}'_{\Gamma_e}(\mathcal{P}(\mathbf{x})) d) \quad (5.6)$$

where, the subscript i denotes the subdomain, \mathbf{u}_{Ω_i} is the displacement approximation on Ω_i , $\mathbf{u}_{\Gamma_e}^0$ is the displacement approximation on the coupling boundary Γ_e , and \mathbf{u}'_{Γ_e} is the approximation of the displacement gradient normal to the coupling interface, that is, $\mathbf{u}'_{\Gamma_e} = \partial \mathbf{u} / \partial n$.

Over the support region of the associated weight field $w(d_i)$, the composed displacement is a blending of the displacement associated with neighboring domains and the first-order approximated displacement associated with the coupling boundary. For points outside of the support region, the displacement field is fully resolved by the approximation on the associated parametric domains.

Since the size of the blending region (that is, the support region of $w(d_i)$) is arbitrary, one choice is to make the support edge coincide with the Euclidean locations corresponding to the knots of the underlying domain. However, this leads to a non-

uniform d_{max} in Eq. (2.12) over the blending region. Therefore, in the present study, d_{max} is held fixed while the integration is carried out over the first non-zero knot span of the domain, as illustrated in Figure 5.3.

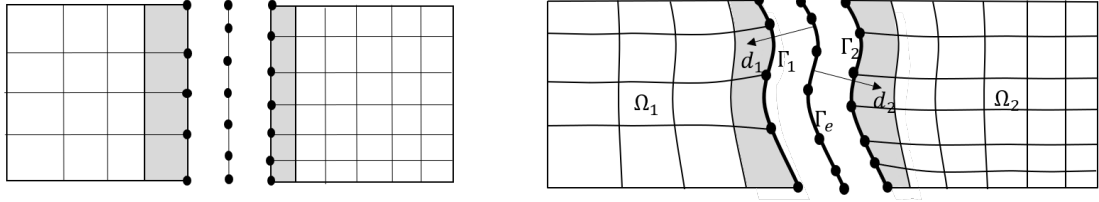


Figure 5.3. Support region of the weight field $w(d_i)$ in parametric space and in Euclidean space. The support region is chosen to coincide with the first non-zero knot span in the parametric space of the underlying domain.

5.2.1 Discretization for Blending of Two Patches

The discretized form of the coupling approximation Eq. (5.6) is:

$$\mathbf{u}(\mathbf{x}) = \left[(1 - w(d_i))\mathbf{R}_{\Omega_i}(\mathbf{x}) \quad w(d_i)\mathbf{R}_{\Gamma_e}(\mathcal{P}(\mathbf{x})) \quad w(d_i)d_i\mathbf{R}_{\Gamma_e}(\mathcal{P}(\mathbf{x})) \right] \begin{Bmatrix} \bar{\mathbf{u}}_{\Omega_i} \\ \bar{\mathbf{u}}_{\Gamma_i}^0 \\ \bar{\mathbf{u}}'_{\Gamma_i} \end{Bmatrix} \quad (5.7a)$$

$$= [\mathbf{R}_{\Omega_i} \quad \mathbf{R}_{\Gamma_e}^0 \quad \mathbf{R}'_{\Gamma_e}] \{\bar{\mathbf{u}}\} \quad (5.7b)$$

$$= [\mathbf{R}] \{\bar{\mathbf{u}}\} \quad (5.7c)$$

where, \mathbf{R}_{Ω_i} and \mathbf{R}_{Γ_e} are the basis function matrices associated with the subdomains and the coupling interface, respectively. $\bar{\mathbf{u}}_{\Omega_i}$, $\bar{\mathbf{u}}_{\Gamma_i}^0$, $\bar{\mathbf{u}}'_{\Gamma_i}$ are the degrees of freedom corresponding to the nodal unknowns of the fields \mathbf{u}_{Ω} , $\mathbf{u}_{\Gamma_i}^0$ and \mathbf{u}'_{Γ_i} , respectively.

The strain field approximation is now obtained in the standard manner as:

$$\boldsymbol{\varepsilon} = \nabla_s \mathbf{u} = [\mathbf{B}] \{\bar{\mathbf{u}}\} \quad (5.8)$$

where, ∇_s is the symmetric gradient operator and for three-dimensional problem it is defined as

$$\nabla_s = \begin{bmatrix} \partial/\partial x & 0 & 0 \\ 0 & \partial/\partial y & 0 \\ 0 & 0 & \partial/\partial z \\ 0 & \partial/\partial z & \partial/\partial y \\ \partial/\partial z & \partial/\partial x & 0 \\ \partial/\partial y & \partial/\partial x & 0 \end{bmatrix}$$

The strain-displacement matrix $[\mathbf{B}]$ takes the following form:

$$[\mathbf{B}] = [\mathbf{B}_{\Omega_i} \ \mathbf{B}_{\Gamma_e}^0 \ \mathbf{B}'_{\Gamma_e}] \quad (5.9a)$$

$$= \begin{bmatrix} -[\mathbf{R}_{\Omega_i}]^T [\nabla w]^T + (1-w)[\nabla \mathbf{R}_{\Omega_i}]^T \\ [\mathbf{R}_{\Gamma_e}]^T [\nabla w]^T + w[\nabla \mathbf{R}_{\Gamma_e}]^T \\ d_i [\mathbf{R}_{\Gamma_e}]^T [\nabla w]^T + w[\mathbf{R}_{\Gamma_e}]^T [\nabla d_i]^T + w d_i [\nabla \mathbf{R}_{\Gamma_e}]^T \end{bmatrix}^T \quad (5.9b)$$

The discretized weak form of Eq. (5.5) may be expressed as $[\mathbf{K}]\{\bar{\mathbf{u}}\} = \{\mathbf{f}\}$, which could be further expanded into block matrices as follows.

$$\begin{bmatrix} \mathbf{K}_{\Omega_1 \Omega_1} & \mathbf{0} & \mathbf{K}_{\Omega_1 \Gamma_e^0} & \mathbf{K}_{\Omega_1 \Gamma'_{e1}} & \mathbf{0} \\ \mathbf{0} & \mathbf{K}_{\Omega_2 \Omega_2} & \mathbf{K}_{\Omega_2 \Gamma_e^0} & \mathbf{0} & \mathbf{K}_{\Omega_2 \Gamma'_{e2}} \\ \mathbf{K}_{\Omega_1 \Gamma_e^0}^T & \mathbf{K}_{\Omega_2 \Gamma_e^0}^T & \mathbf{K}_{\Gamma_e^0 \Gamma_e^0} & \mathbf{K}_{\Gamma_e^0 \Gamma'_{e1}} & \mathbf{K}_{\Gamma_e^0 \Gamma'_{e2}} \\ \mathbf{K}_{\Omega_1 \Gamma'_{e1}}^T & \mathbf{0} & \mathbf{K}_{\Gamma_e^0 \Gamma'_{e1}}^T & \mathbf{K}_{\Gamma'_{e1} \Gamma'_{e1}} & \mathbf{0} \\ \mathbf{0} & \mathbf{K}_{\Omega_2 \Gamma'_{e2}}^T & \mathbf{K}_{\Gamma_e^0 \Gamma'_{e2}}^T & \mathbf{0} & \mathbf{K}_{\Gamma'_{e2} \Gamma'_{e2}} \end{bmatrix} \begin{bmatrix} \bar{\mathbf{u}}_{\Omega_1} \\ \bar{\mathbf{u}}_{\Omega_2} \\ \bar{\mathbf{u}}_{\Gamma_e^0} \\ \bar{\mathbf{u}}'_{\Gamma'_{e1}} \\ \bar{\mathbf{u}}'_{\Gamma'_{e2}} \end{bmatrix} = \begin{bmatrix} \mathbf{f}_{\Omega_1} \\ \mathbf{f}_{\Omega_2} \\ 0 \\ 0 \\ 0 \end{bmatrix} \quad (5.10)$$

where, $\mathbf{K}_{IJ} = \int_{\Omega} [\mathbf{B}_I]^T [\mathbf{D}] [\mathbf{B}_J] d\Omega$ with $I, J = \Omega_i, \Gamma_e^0, \Gamma'_{ei}$ for $i = 1, 2$ and $[\mathbf{D}]$ is the constitutive matrix. The discrete force vector \mathbf{f}_{Ω_i} associated with the subdomains is

$$\{\mathbf{f}_{\Omega_i}\} = \int_{\Omega} [\mathbf{R}]^T \{\bar{\mathbf{b}}\} d\Omega + \int_{\Gamma_t} [\mathbf{R}]^T \{\bar{\mathbf{t}}\} d\Gamma \quad (5.11a)$$

where $\bar{\mathbf{b}}$ is the prescribed body force per unit volume, and $\bar{\mathbf{t}}$ is the prescribed traction over the Neumann boundary Γ_t .

5.3 Patch Test

The developed methodology was first validated through two-dimensional and three-dimensional patch tests in which unit traction was applied as illustrated in Figure 5.4. The non-overlapping subdomains, Ω_1 and Ω_2 , were coupled through a stitching interface Γ_e along the shared boundary using the above-described methodology. Subdomains with identical as well as dissimilar materials were considered to test the ability to reproduce discontinuities in the displacement derivatives across the stitching interface. Elastic modulus of $E = 1$ and Poisson's ratio of $\nu = 0.3$ were assumed when modeling homogeneous domains. For bi-material domains, we chose subdomain Ω_1 to have $E = 1$ and $\nu = 0.1$, while subdomain Ω_2 had $E = 2$ and $\nu = 0.2$ to ensure compatible lateral contraction. The degrees of the NURBS basis functions used to approximate the subdomains, either linear or quadratic, were kept identical for both subdomains as well as the coupling interface in all the tests. Standard Legendre-Gauss numerical integration was used and the order of quadrature depended on the chosen weight function form. Quadrature that ensured exact numerical integration was chosen when the weight functions were of polynomial form. Six and eight point quadrature were used when the weight function was of exponential form.

Three types of discretization schemes including matching, hierarchical and non-matching were considered. The matching scheme assumes a conforming discretization for both subdomains with the size of $h_1 = h_2 = 1/3i$ with i taking on sequential values that produced refined meshes. The hierarchical scheme had a periodically matching discretization for Ω_1 and Ω_2 with $h_1 = 1/3i$ and $h_2 = 1/6i$, respectively. In the non-matching refinement, the two subdomains had a non-conforming discretization of $h_1 = 1/(4i - 1)$ and $h_2 = 1/(8i - 1)$. The value of i ranged from 1 to 25 and the discretization of stitching interface always conformed to Ω_1 . Illustrations of the three

discretization schemes represented by NURBSs in their coarsest refinement density ($i = 1$) are shown in Figure 5.5.

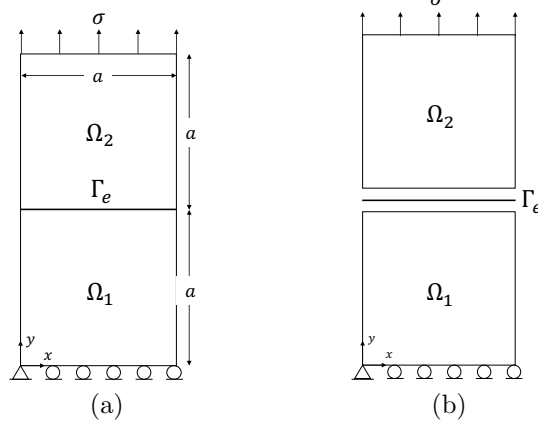


Figure 5.4. (a) Patch test setup and (b) expanded view of the individual subdomains and the coupling interface.

To judge convergence rate, we used the relative L_2 norm of the error in displacement and strain energy as defined below:

$$\bar{e}_{L_2} = \frac{\|\mathbf{u}^{ex} - \mathbf{u}^h\|_{L_2}}{\|\mathbf{u}^{ex}\|_{L_2}} = \frac{\left\{ \int (\mathbf{u}^h - \mathbf{u}^{ex})^T (\mathbf{u}^h - \mathbf{u}^{ex}) d\Omega \right\}^{1/2}}{\left\{ \int (\mathbf{u}^{ex})^T (\mathbf{u}^{ex}) d\Omega \right\}^{1/2}} \quad (5.12a)$$

$$\bar{e}_{en} = \frac{\|\mathbf{u}^{ex} - \mathbf{u}^h\|_{en}}{\|\mathbf{u}^{ex}\|_{en}} = \frac{\left\{ \frac{1}{2} \int (\boldsymbol{\varepsilon}^h - \boldsymbol{\varepsilon}^{ex})^T \mathbf{D} (\boldsymbol{\varepsilon}^h - \boldsymbol{\varepsilon}^{ex}) d\Omega \right\}^{1/2}}{\left\{ \frac{1}{2} \int (\boldsymbol{\varepsilon}^{ex})^T \mathbf{D} (\boldsymbol{\varepsilon}^{ex}) d\Omega \right\}^{1/2}} \quad (5.12b)$$

5.3.1 Matching and Hierarchical Discretizations

We begin with matching and hierarchical discretizations using a polynomial weight function for blending. Figure 5.6 shows the two-dimensional patch test's relative error in L_2 norm of displacement with homogeneous and bi-material interfaces coupled using a cubic weight function. The results demonstrate immediate convergence to the

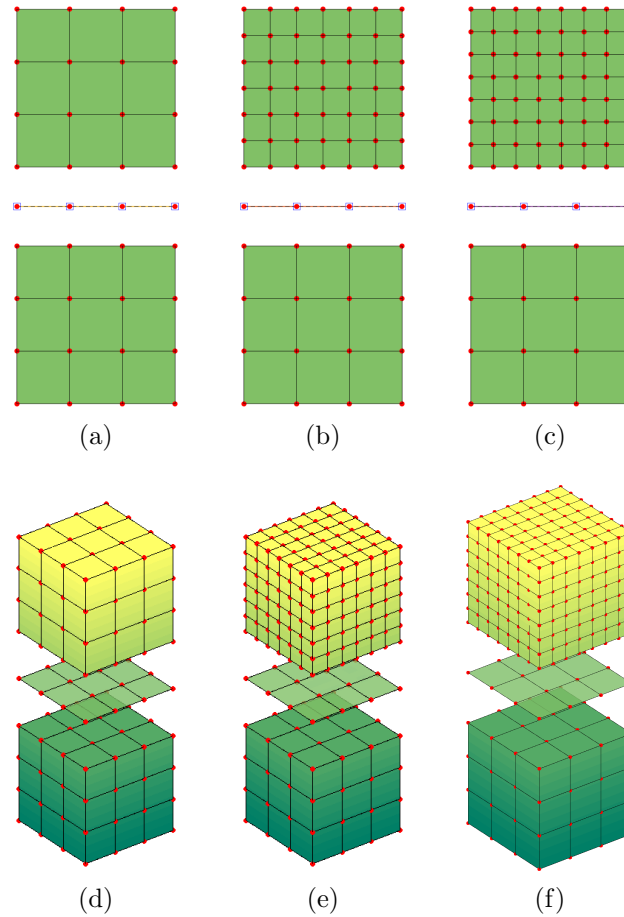


Figure 5.5. Example of discretization schemes for two- and three-dimensional patch tests (NURBS degree=1). (a) and (d) matching scheme. (b) and (e) hierarchical scheme. (c) and (c) non-matching scheme. The red dots are control points while blue squares and black lines indicate edges of the spline elements (non-zero knot spans).

solution with errors that fluctuate in the range of 10^{-13} to 10^{-10} . Both h-refinement and p-refinement do not further improve the accuracy of the solution. Our observation suggests that the solution accuracy is on the same level as the accuracy with which distance as well as the gradients of distance may be numerically evaluated (that is, to function precision). Results of three-dimensional patch tests are not shown here for reasons of brevity, but they too exhibited an accuracy that approached function precision.

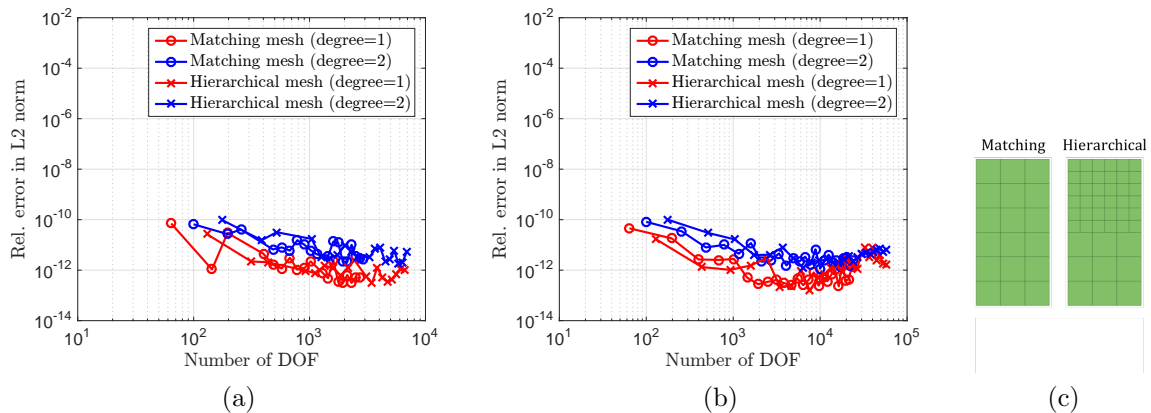


Figure 5.6. Relative L_2 norm of error in displacement with (a) homogeneous and (b) bi-material interface coupled using cubic weight function. (c) Matching and hierarchical discretization were used for refinement.

Next, the patch test was conducted on the refined meshes with the exponential weight function (Eq. (2.12c)). Figure 5.7 demonstrates the convergence of solution for homogeneous interface coupling when using an exponential weight function. It is seen that the solution accuracy is poorer in comparison to the error that was demonstrated with the cubic weight function, which was at the level of function precision. The solution accuracy improved only when the order of Gaussian quadrature was raised, or when the discretization was refined. Since exponential function can be characterized by an infinite power series $\sum_{k=0}^{\infty} x^k/k!$, numerical integration is inexact for standard finite-order Gaussian quadrature. Since the coupling support only extends to the edge of the first non-zero knot span, refining the mesh helps improve the solution accuracy by confining the quadrature error to a smaller region. Given the above observations and the fact that evaluation of exponential function is generally computationally more expensive than for polynomials, we chose to use cubic polynomial weight functions in the rest of the present work.

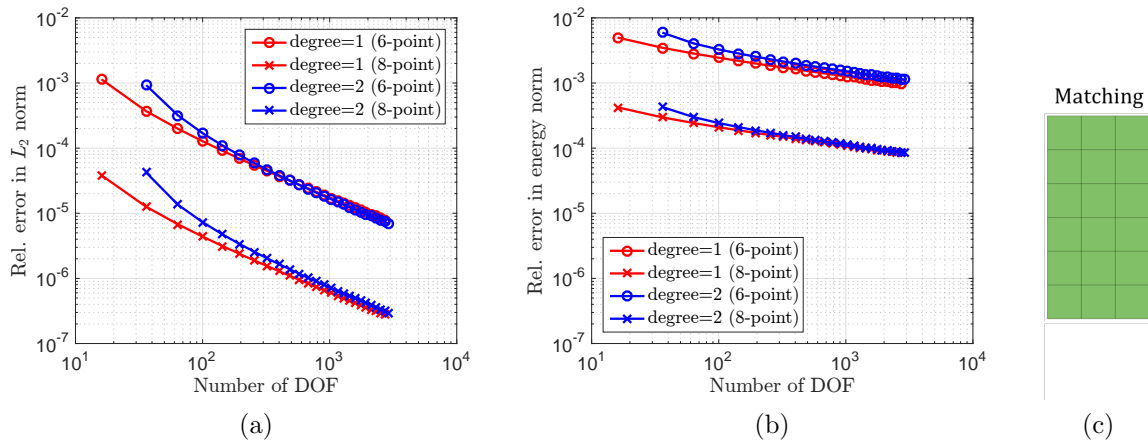


Figure 5.7. (a) Relative L_2 norm of error in displacement and (b) in strain energy for homogeneous interface coupled using exponential weight function. (c) The least refined mesh of the two-dimensional matching discretization that was analyzed.

5.3.2 Non-matching Discretizations

Next, we conducted patch tests with non-matching discretizations for two- and three-dimensional test geometries. Figure 5.8 shows the contours of displacement u_z and normal strain ε_{zz} for three-dimensional patch tests with the coarsest non-matching discretization. While coupling subdomains of identical materials provides the expected smooth solution across the interface, the bi-material coupling interface successfully captured the jump in normal strain. Overall, the solution near the coupling interface was smooth and without any variations from its expected value.

The values of displacement and strain plotted in Figure 5.8 were further examined along a chosen path through the geometry. The solution along $\{y \in [0, 2a] | x = 0.5a\}$ in the planar geometry and along $\{z \in [0, 2a] | x = 0.5a, y = 0\}$ in the three-dimensional geometry are plotted in Figure 5.9. These plots confirm that displacement compatibility is achieved across the coupling interface. In addition, the normal strain across the bi-material interface exhibits the expected jump.

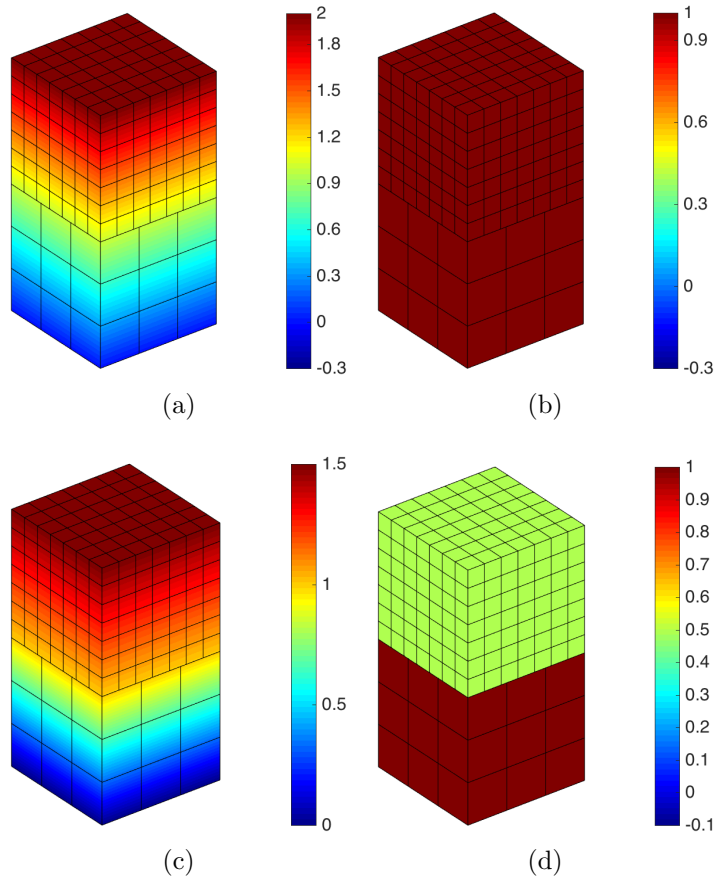


Figure 5.8. (a) Displacement u_z and (b) normal strain ε_{zz} contours for homogeneous patch test. (c) Displacement u_z and (d) normal strain ε_{zz} contours for bi-material patch test.

In Figure 5.10, the solution convergence on a two-dimensional patch with non-matching discretization is plotted. The observed convergence rate was nearly optimal with h-refinement, while an exponential convergence rate was observed with p-refinement. The three-dimensional patch tests on non-matching discretization showed a similar trend.

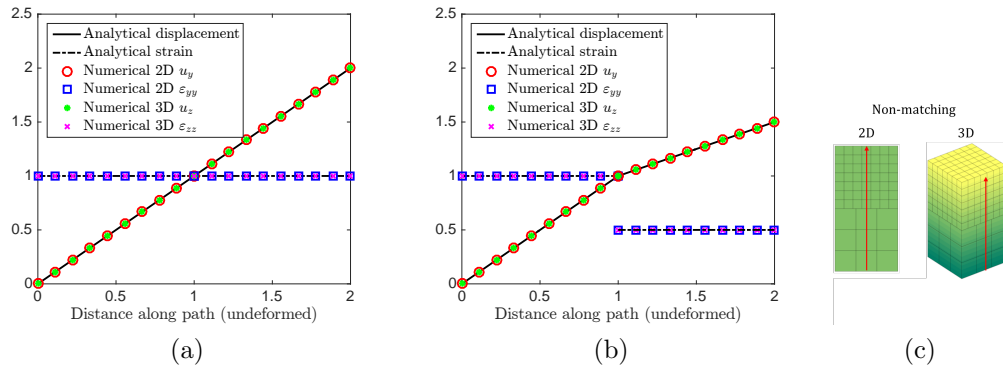


Figure 5.9. Displacement and strain along the paths for (a) homogeneous and (b) bi-material patch test with non-matching discretization. (c) Path along the two- and three-dimensional patches with non-matching discretization along which the solutions are plotted.

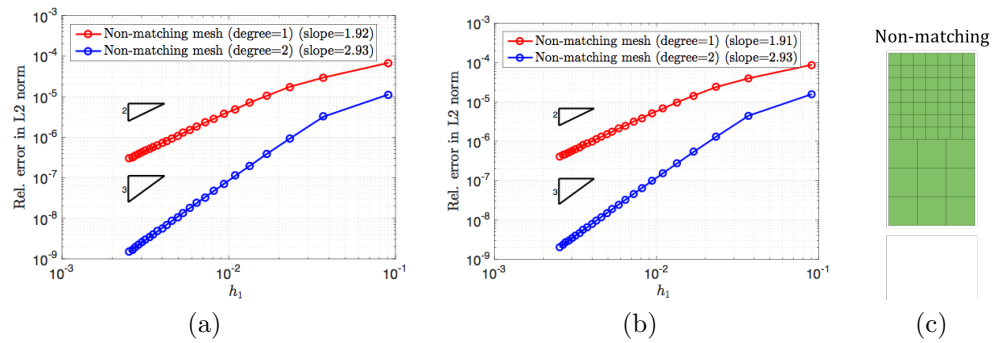


Figure 5.10. (a) The relative L_2 norm of error in displacement for homogeneous coupling and (b) bi-material coupling. (c) The coarsest mesh of the assumed two-dimensional non-matching discretization.

5.4 Numerical Examples

Several two-dimensional and three-dimensional examples are solved using the developed p -stitching procedure in the following.

5.4.1 Timoshenko Beam

Consider a beam with dimensions L by D , and of unit thickness, subjected to parabolically distributed shear traction t_y along the free end given by:

$$t_y = \frac{-P}{2I} \left(\frac{D^2}{4} - y^2 \right) \quad (5.13)$$

where, P is the resultant load and $I = D^3/12$ is the cross-sectional moment of inertia. Along the boundary, $\Gamma_u = \{x = 0, -D/2 \leq y \leq D/2\}$, the x -displacements were set to zero. The y -displacement was also restrained at $x = 0, y = 0$. The beam was decomposed into two equal sized halves represented by two bi-cubic NURBS patches. A coupling interface defined by $\Gamma_e = \{x = L/2, -D/2 \leq y \leq D/2\}$ was introduced between the two patches. The two subdomains were discretized into 10×10 and 21×21 uniform “elements” (non-zero knot spans), respectively. Figure 5.11 shows the geometric dimensions, boundary conditions, decomposed subdomains as well as their discretizations.

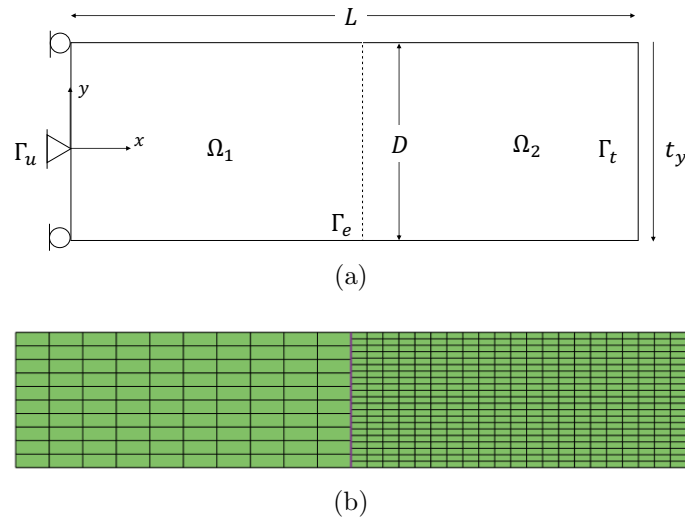


Figure 5.11. (a) Dimensions, boundary conditions, and (a) NURBS discretization of Timoshenko beam.

The analytical solution to this problem is [105]:

$$u_x = \frac{Py}{6EI} \left[(6L - 3x)x + (2 + \nu) \left(y^2 - \frac{D^2}{4} \right) \right] \quad (5.14a)$$

$$u_y = \frac{-P}{6EI} \left[3\nu y^2(L - x) + (4 + 5\nu) \frac{D^2}{4} x + (3L - x)x^2 \right] \quad (5.14b)$$

$$\sigma_{xx} = \frac{P(L - x)y}{I} \quad (5.14c)$$

$$\sigma_{yy} = 0 \quad (5.14d)$$

$$\sigma_{xy} = \frac{-P}{2I} \left(\frac{D^2}{4} - y^2 \right) \quad (5.14e)$$

For the purposes of numerical computation, the elastic properties of the two subdomains were chosen to be identical and equal to $E = 1000$ and $\nu = 0.25$. The specific value of dimensions were $L = 100$ and $D = 20$, and the tip load value was $P = 8$.

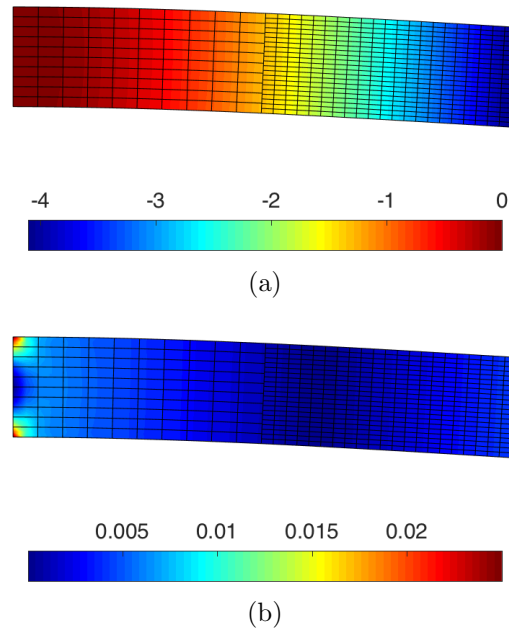


Figure 5.12. (a) Vertical displacements u_y and (b) its relative error $u_y/|u_{max}|$ in the Timoshenko beam.

Figure 5.12 shows the vertical displacement and its relative error with respect to absolute values of the maximum deflection $u_{max} = \max|u_y|$. Overall, the error

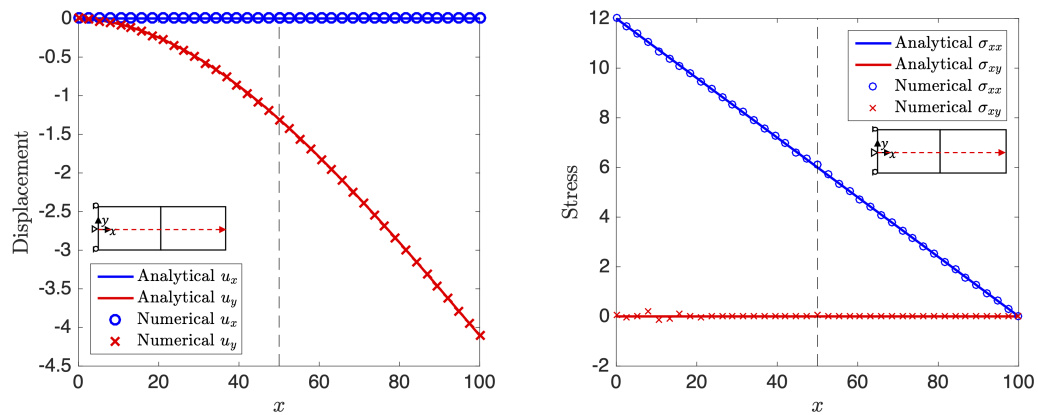


Figure 5.13. Displacement and stress components along the indicated path in the Timoshenko beam. The dotted line shows the location of coupling interface Γ_e along the length of the beam.

introduced by the enforcement of non-homogeneous essential boundary conditions was larger than the error near the coupling field. Only smooth variations about the expected value of the field were observed near the coupling interface.

Displacements and stresses along the path $y = 0$ are plotted in Figure 5.13 and compared against the analytical solution. The displacement results show good agreement without any visible deviation from the analytical solution near the coupling interface. Stresses near the coupling boundary were also smooth.

5.4.2 Thick-Walled Cylinder Subjected to Internal Pressure

A thick-walled cylinder subjected to internal pressure p was modeled using NURBS with the number of subdomains $n_\Omega = 2, 3$, and 4. Figure 5.14a shows the problem definition and boundary conditions. The specific dimensions of the cylinder were $a = 0.3$ m and $b = 0.5$ m. A plane stress condition was assumed with elastic modulus of $E = 30$ GPa and Poisson's ratio of $\nu = 0.3$. Uniform internal pressure of $p = 30$ MPa was applied.

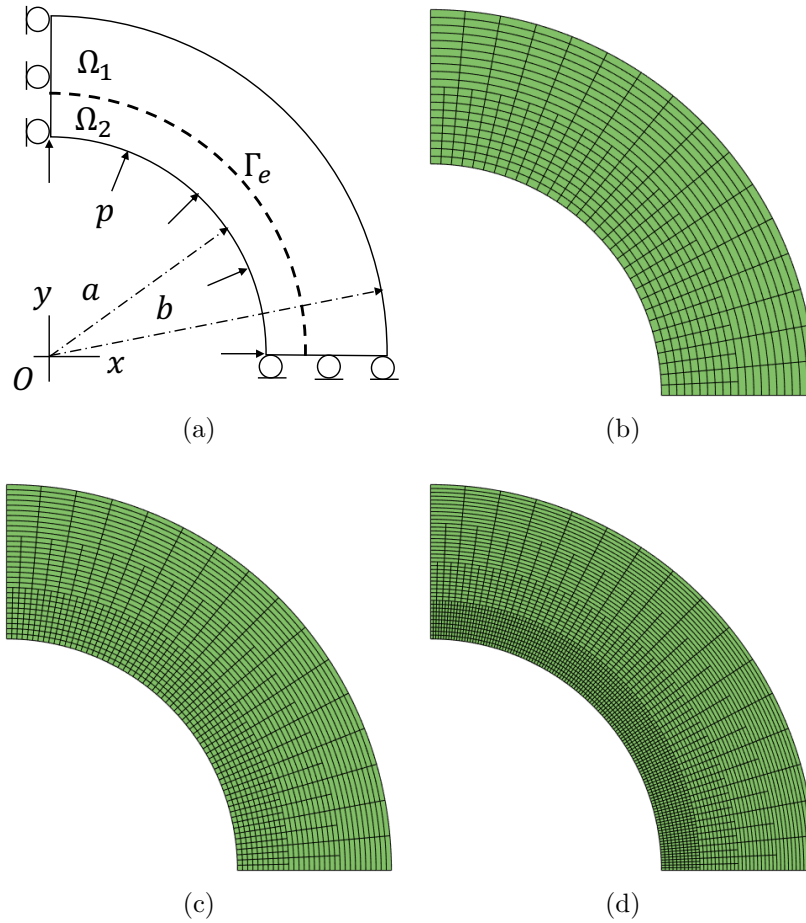


Figure 5.14. (a) Boundary condition on the cylinder wall subjected to internal pressure, and (b) (c) (d) hierarchical discretizations with the number of subdomains $n_\Omega = 2, 3, 4$, respectively.

The cylindrical wall was modeled with 2, 3 and 4 bi-quadratic NURBS patches with hierarchical discretization as illustrated in Figures 5.14b to 5.14d. Each NURBS patch Ω_i was hierarchically discretized into 10 by $4 \times 2^{(i+1)}$ (for i from 1 to n_Ω) uniformly distributed knot spans in the radial and hoop directions, respectively.

The analytical solution to this problem is given below [105]. The displacement components expressed in polar coordinates are:

$$u_r = \frac{pra^2}{E(b^2 - a^2)} \left[(1 - \nu) + \frac{b^2}{r^2} (1 + \nu) \right] \quad (5.15a)$$

$$u_\theta = 0 \quad (5.15b)$$

The solution to stress components are as follows:

$$\sigma_{rr} = \frac{pa^2}{b^2 - a^2} \left(1 - \frac{b^2}{r^2} \right) \quad (5.16a)$$

$$\sigma_{\theta\theta} = \frac{pa^2}{b^2 - a^2} \left(1 + \frac{b^2}{r^2} \right) \quad (5.16b)$$

$$\sigma_{r\theta} = 0 \quad (5.16c)$$

Contours of the displacements and stresses, as well as the relative error on the analytical solution are plotted in Figure 5.15. Generally, the errors were confined to the coupling region on both sides of the interfaces. This is due to the fact that only first order normal derivative continuity was imposed on the solution along the coupling interface. Still, the solution is of good accuracy with the error on the order of 0.0001% in displacement and 0.1% in stress.

5.4.3 Heat Conduction in Coupled Non-planar Surfaces

The proposed formulation is also applicable to non-planar surface-surface coupling in three-dimensional space in addition to typical planar surface-surface or volume-volume coupling. In this example, a simple heat conduction problem on two quarter-circular patches revolving about the z -axis is considered. Both subdomains are modeled with bi-quadratic NURBS surfaces with non-matching discretization as shown in Figure 5.16a. The value of R was 2 and that of a was 2.5, and the thermal conductivity k for both subdomains was set to unity.

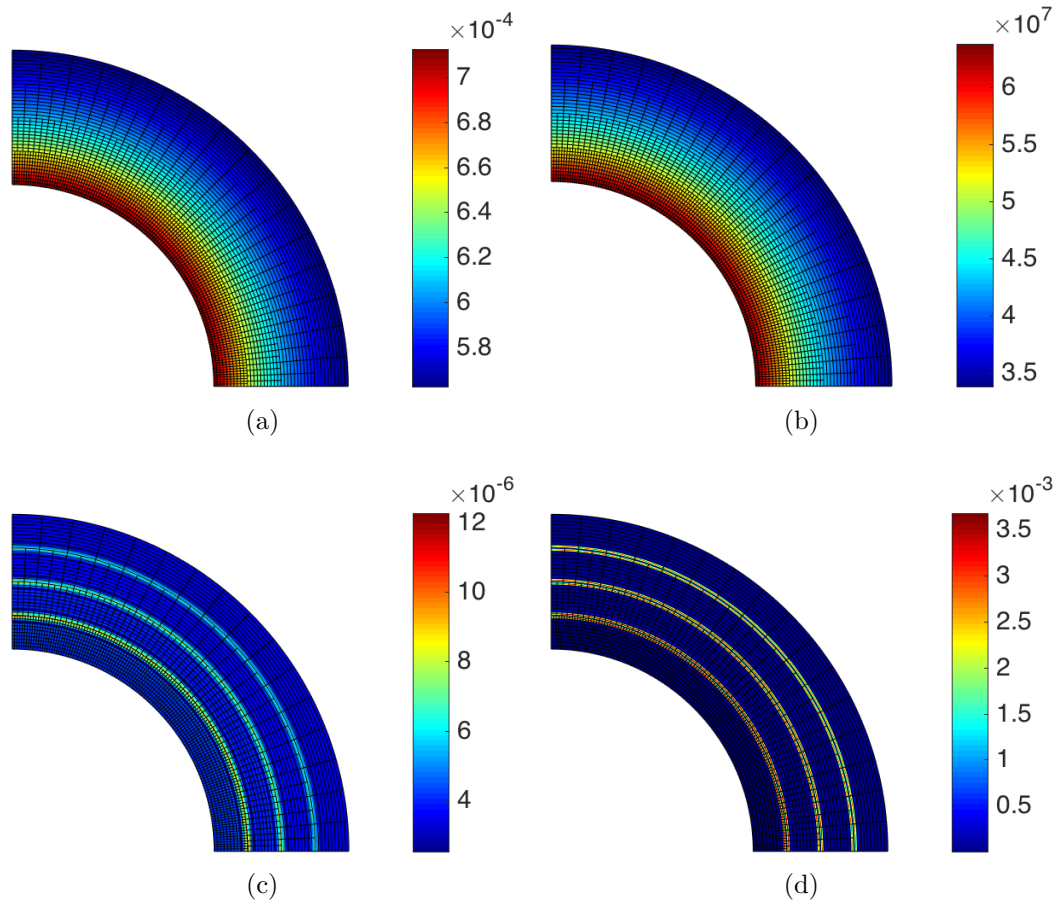


Figure 5.15. Plots of contours of (a) u_r and (b) $\sigma_{\theta\theta}$. Contours of relative error in (c) u_r and (d) von Mises stress σ_{eq} .

The resulting temperature contour and its value along the path $z \in [-a, a]$ are shown in Figures 5.16b and 5.16c. The solution contour shows smooth transition with no non-smooth variations that could be visually observed near the coupling interface. Since the temperature field varies linearly with respect to the z coordinate, the solution is as accurate as those observed in the patch tests earlier.

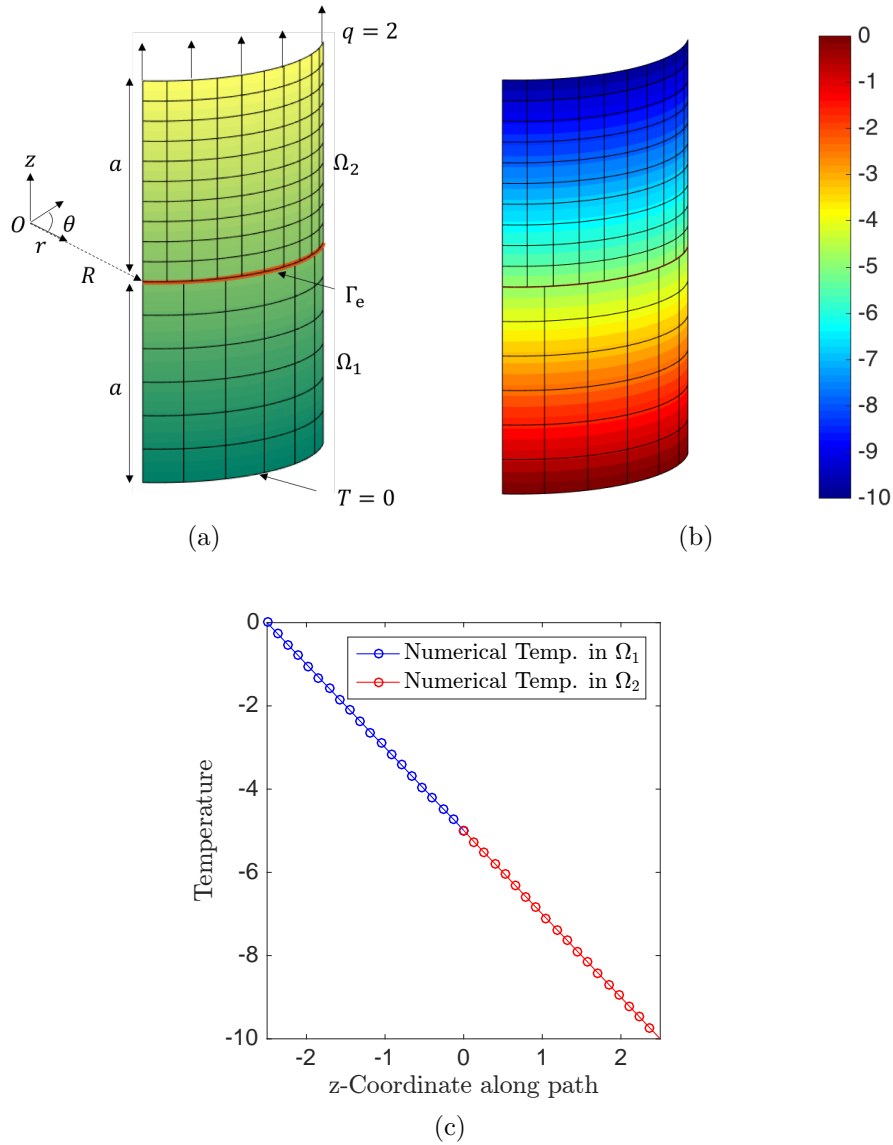


Figure 5.16. (a) Problem definition and discretization of the two coupled non-planar NURBS surfaces, (b) solution temperature contours and (c) temperature value along the path $z \in [-a, a]$ with $r = R, \theta = \pi/4$.

5.4.4 Three-dimensional Hook

In the last example, we consider a three-dimensional hook to demonstrate the ability of the developed methodology to analyze complex volumetric domains decom-

posed into constituent elements as in the volumetric modeling procedure described in [37].

The hook model consists of three tri-quadratic NURBS subdomains with both hierarchical and non-matching coupling interfaces in three-dimensional space. The geometric dimensions, material properties, boundary conditions and coupling structure are described in Figure 5.17. The fixed boundary is fully clamped on the top surface ($z = 0$), while the hook is subjected to a uniform traction p pointing in the $-z$ direction. In total, the model contained 548 NURBS “elements” (non-zero knot spans) that resulted in 8,781 degrees of freedom.

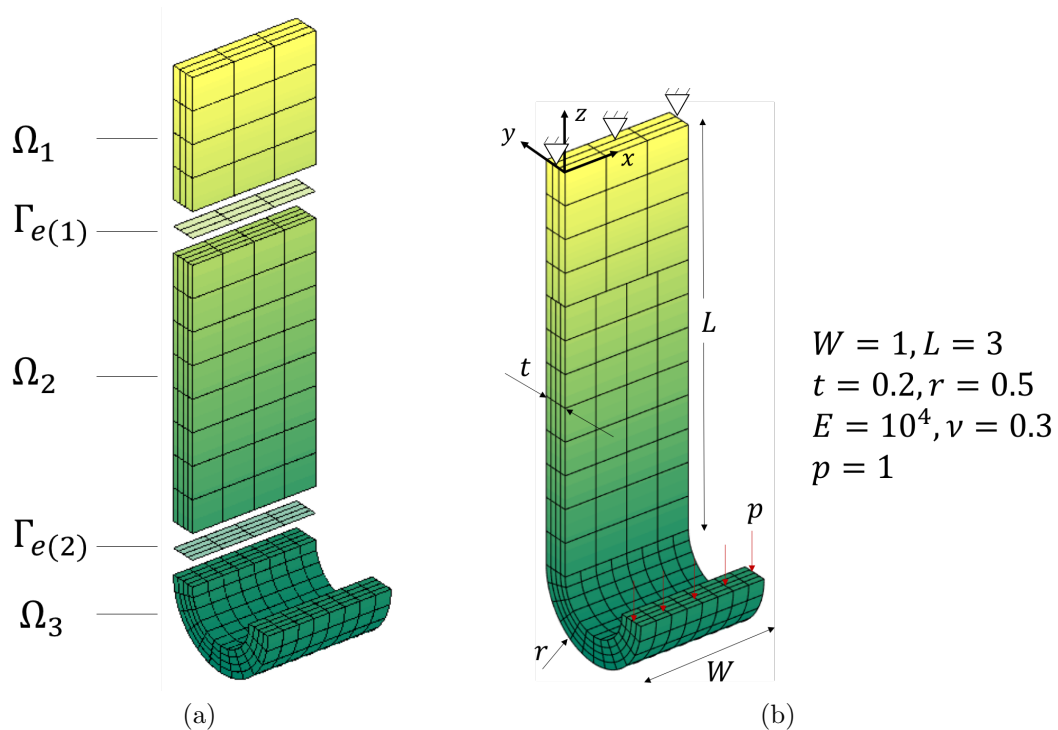


Figure 5.17. The hook model’s (a) coupling structure, (b) dimensions and boundary conditions.

Figures 5.18 and 5.19 show the magnitude of the displacement and the von Mises stress in comparison to the solution contours obtained from the commercial finite element code ABAQUS. The finite element model was meshed with an average element

size of 0.05 and contained 6,720 quadratic elements, resulting in 100,155 degrees of freedom. The finite element model did not have decomposed subdomains or a coupling interface. Since p -stitching naturally assures compatibility at the interface, displacements are continuous across the coupling interfaces as expected. Jumps in displacement across the interface, which are often observed when compatibility is weakly enforced, do not arise with the developed approach. Overall, the displacement contours show consistency with the finite element solution. Some non-smooth variation in von Mises stress can be observed near the coupling interfaces. This is mainly due to the fact that only the constant term and first order normal derivatives were used in building the interfacial approximation. Otherwise, stress contours (including the variation in the through-thickness direction due to bending) also agree well with the finite element solution.

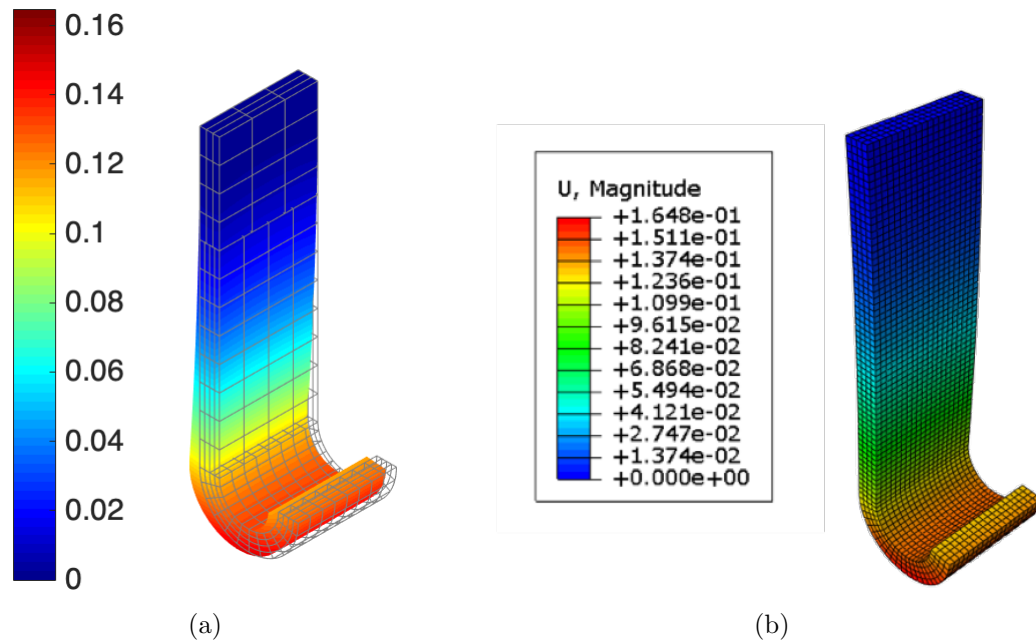


Figure 5.18. Magnitude of displacement $\|\mathbf{u}\|$ obtained by (a) the present method and (b) the finite element method.

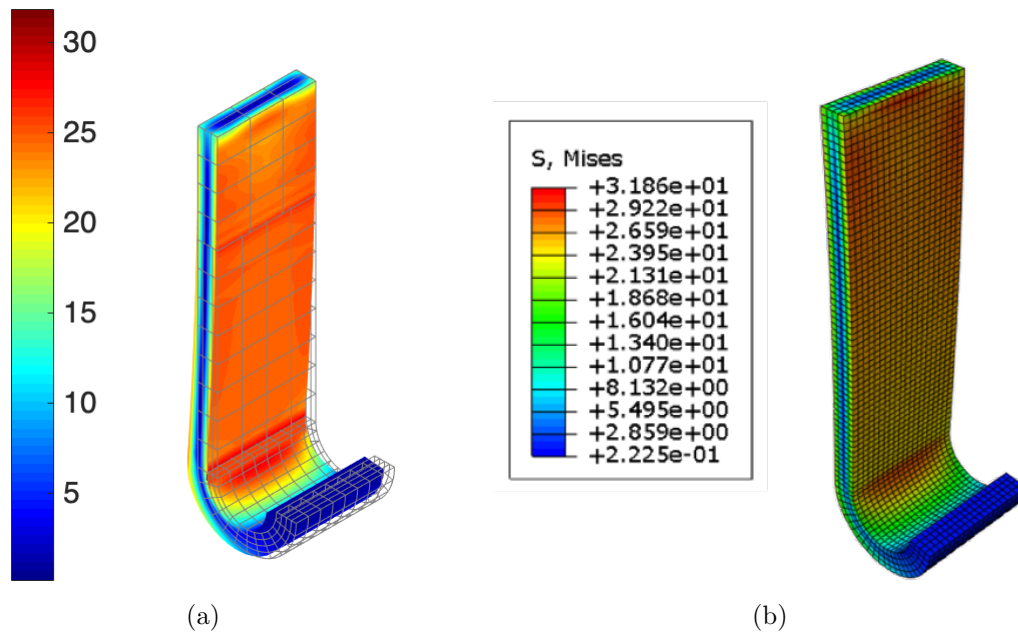


Figure 5.19. Von Mises stress obtained by (a) the present method and (b) the finite element method.

6. ISOGEOMETRIC ENRICHMENT FOR STRESS SINGULARITIES IN MULTI-MATERIAL WEDGES

The isogeometric enrichment of multi-material wedges with bonded or de-bonded interfaces is proposed in this chapter with the ultimate goal of characterizing failures in engineering structures induced by stress singularities. In accordance with formulation of EIGA, material junctions, crack tips and the debonded interfaces are explicitly represented by parametrically defined geometries. The enriched field approximations are isoparametrically and hierarchically constructed in an increasing order of parametric dimensionality.

The formulation developed in this chapter enables explicit representation of interfaces within the body while allowing direct extraction of generalized stress intensity factors upon solution of planar elastic boundary value problems, without additional calculation of *a posteriori* path-independent integral. Numerical implementation is demonstrated through examples of a bi-material wedge and fracture in a homogeneous solid.

6.1 Asymptotic Analysis of Stress Singularities

Asymptotic analysis of stress singularities is first described prior to formulating the enriched field approximation. The assumptions and derivations generally follow those given by Seweryn and Molski [106] for homogeneous solids as well as the extension made by Luo and Subbarayan [107] for multi-material wedges.

Consider a multi-material wedge in a polar coordinate system (r, θ) . The two independent components of displacement are u_r and u_θ . The three strain components in polar coordinates are as follows:

$$\varepsilon_{rr_i} = \frac{\partial u_{r_i}}{\partial r_i}, \quad (6.1a)$$

$$\varepsilon_{\theta\theta_i} = \frac{u_{r_i}}{r_i} + \frac{1}{r_i} \frac{\partial u_{\theta_i}}{\partial \theta_i}, \quad (6.1b)$$

$$\gamma_{r\theta_i} = \frac{1}{r_i} \frac{\partial u_{r_i}}{\partial \theta_i} + \frac{\partial u_{\theta_i}}{\partial r_i} - \frac{u_{\theta_i}}{r_i} \quad (6.1c)$$

where, the subscript i refers to the i^{th} material joined at the wedge. Assuming plane strain conditions, the components of stress are given by

$$\sigma_{rr_i} = \Lambda_i(\varepsilon_{rr_i} + \varepsilon_{\theta\theta_i}) + 2\mu_i\varepsilon_{rr_i}, \quad (6.2a)$$

$$\sigma_{\theta\theta_i} = \Lambda_i(\varepsilon_{rr_i} + \varepsilon_{\theta\theta_i}) + 2\mu_i\varepsilon_{\theta\theta_i}, \quad (6.2b)$$

$$\tau_{r\theta_i} = \mu_i\gamma_{r\theta_i} \quad (6.2c)$$

where, Λ_i and μ_i are the Lamé's constants of material i . The equations of equilibrium in polar system are

$$\frac{\partial \sigma_{rr_i}}{\partial r_i} + \frac{1}{r_i} \frac{\partial \tau_{r\theta_i}}{\partial \theta_i} + \frac{\sigma_{rr_i} - \sigma_{\theta\theta_i}}{r_i} = 0, \quad (6.3a)$$

$$\frac{\partial \tau_{r\theta_i}}{\partial r_i} + \frac{1}{r_i} \frac{\partial \sigma_{\theta\theta_i}}{\partial \theta_i} + 2 \frac{\tau_{r\theta_i}}{r_i} = 0 \quad (6.3b)$$

Following Seweryn and Molski [106], the displacements are assumed to have the form of $u_{r_i}(r, \theta) = r^\lambda f(\theta)$, $u_{\theta_i}(r, \theta) = r^\lambda g(\theta)$. Substituting Eqs. (6.1) and (6.2) into Eq. (6.3) we get

$$(\kappa_i - 1)f''(\theta_i) + (\kappa_i + 1)(\lambda^2 - 1)f(\theta_i) + 2(\lambda - \kappa_i)g'(\theta_i) = 0, \quad (6.4a)$$

$$(\kappa_i - 1)g''(\theta_i) + (\kappa_i - 1)(\lambda^2 - 1)g(\theta_i) + 2(\lambda + \kappa_i)f'(\theta_i) = 0 \quad (6.4b)$$

where, κ_i is the Kolosov constant that has the value of $(3 - \nu_i)/(1 + \nu_i)$ under plane stress condition and $3 - 4\nu_i$ under plane strain condition.

The two unknown angular functions have the following general form [106]:

$$\begin{aligned}
 f_i(\theta) &= A_i \cos(1 + \lambda)\theta_i + B_i \sin(1 + \lambda)\theta_i + C_i \cos(1 - \lambda)\theta_i + D_i \sin(1 - \lambda)\theta_i, \\
 g_i(\theta) &= B_i \cos(1 + \lambda)\theta_i - A_i \sin(1 + \lambda)\theta_i \\
 &\quad + \frac{\kappa_i + \lambda}{\kappa_i - \lambda} D_i \cos(1 - \lambda)\theta_i - \frac{\kappa_i + \lambda}{\kappa_i - \lambda} C_i \sin(1 - \lambda)\theta_i
 \end{aligned} \tag{6.5}$$

With the above explicit form of angular functions, the general solution for the displacements can then be expressed as

$$\begin{aligned}
 u_{r_i} &= r^\lambda [A_i \cos(1 + \lambda)\theta_i + B_i \sin(1 + \lambda)\theta_i + C_i \cos(1 - \lambda)\theta_i + D_i \sin(1 - \lambda)\theta_i], \\
 u_{\theta_i} &= r^\lambda [B_i \cos(1 + \lambda)\theta_i - A_i \sin(1 + \lambda)\theta_i \\
 &\quad + \frac{\kappa_i + \lambda}{\kappa_i - \lambda} D_i \cos(1 - \lambda)\theta_i - \frac{\kappa_i + \lambda}{\kappa_i - \lambda} C_i \sin(1 - \lambda)\theta_i
 \end{aligned} \tag{6.6}$$

The order of singularity λ and its associated constants (A, B, C, D) are solvable by forming a system of transcendental equations based on the specific set of loading conditions. For instance, in the bi-material wedge symmetric about the x-axis with bonded interface as shown in Figure 6.1a, the wedge could either be applied a symmetric (open) mode, or an anti-symmetric (shear) mode conditions:

1. Symmetric (opening) mode

Continuity conditions:

$$\begin{aligned}
 u_{r_1} &= u_{r_2}, u_{\theta_1} = u_{\theta_2}, \\
 \sigma_{\theta\theta_1} &= \sigma_{\theta\theta_2}, \tau_{r\theta_1} = \tau_{r\theta_2} \quad \text{at } \theta = \pm\alpha
 \end{aligned}$$

Loading conditions:

$$\begin{aligned}
 u_{\theta_1} &= 0, \tau_{r\theta_1} = 0 \quad \text{at } \theta = 0, \\
 u_{\theta_2} &= 0, \tau_{r\theta_2} = 0 \quad \text{at } \theta = \pi
 \end{aligned}$$

2. Anti-symmetric (shear) mode

Continuity conditions:

$$u_{r_1} = u_{r_2}, u_{\theta_1} = u_{\theta_2},$$

$$\sigma_{\theta\theta_1} = \sigma_{\theta\theta_2}, \tau_{r\theta_1} = \tau_{r\theta_2} \text{ at } \theta = \pm\alpha$$

Loading conditions:

$$u_{r_1} = 0, \sigma_{\theta_1} = 0 \text{ at } \theta = 0,$$

$$u_{r_2} = 0, \sigma_{\theta_2} = 0 \text{ at } \theta = \pi$$

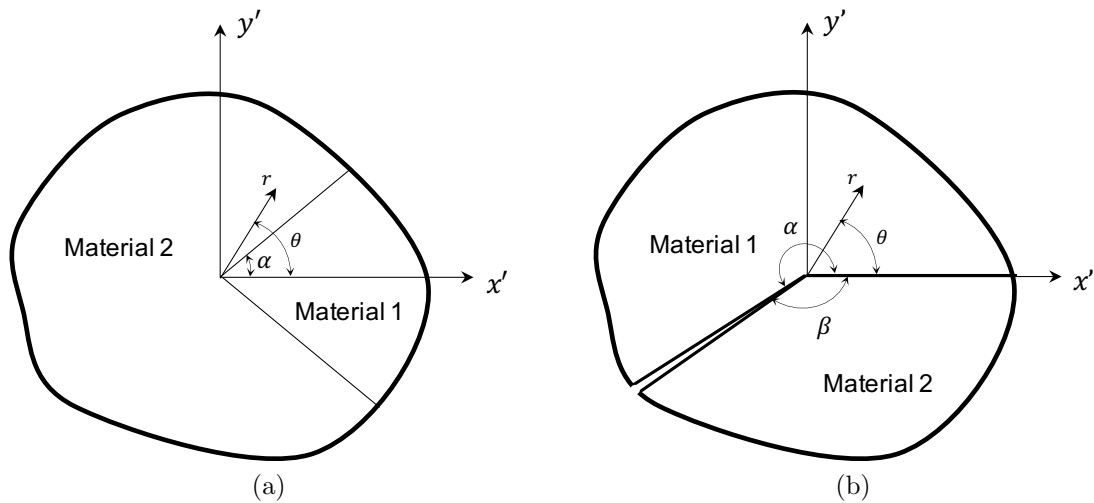


Figure 6.1. (a) Bi-material wedge with two bonded interfaces and (b) Bi-material wedge with one bonded interface and a second debonded interface.

Each of the above modes (symmetric or anti-symmetric) results in a set of eight equations in the constants $(A_i, B_i, C_i, D_i), i = 1, 2$ as well as λ upon application of the continuity and load conditions. To ensure a non-trivial solution to the constants (A_i, B_i, C_i, D_i) , the determinant of the eigenvalue problem must be zero, which leads

to a set of transcendental equations in λ . Values of the strength of singularity λ are the eigenvalues that are then numerically determined by solving the transcendental equations. Correspondingly, the constants (A_i, B_i, C_i, D_i) are the components of the associated eigenvector. For bonded interfacial corner with more than two materials ($N > 2$), the above description is easily extended - the continuity conditions at all the interfaces result in $4N$ equations, and the eigenvalue-eigenvector problem needs to be similarly solved.

In the case of a bi-material wedge with one interface debonded as illustrated in Figure 6.1b, the continuity conditions are:

$$\begin{aligned} u_{r_1} &= u_{r_2}, u_{\theta_1} = u_{\theta_2}, \\ \sigma_{\theta\theta_1} &= \sigma_{\theta\theta_2}, \tau_{r\theta_1} = \tau_{r\theta_2} \quad \text{at } \theta = 0 \end{aligned}$$

The loading conditions ensure that the debonded interface is traction-free, that is

$$\begin{aligned} \sigma_{\theta\theta_1} &= 0, \sigma_{r\theta_1} = 0 \quad \text{at } \theta = \alpha, \\ \sigma_{\theta\theta_2} &= 0, \sigma_{r\theta_2} = 0 \quad \text{at } \theta = -\beta \end{aligned}$$

The above conditions for the wedge with debonded interface also results in an eigenvalue problem in which λ and $(A_i, B_i, C_i, D_i), i = 1, 2$ are the eigenvalues and eigenvectors as before.

Now, the general solution for displacements in multi-material wedges can be expressed in matrix-vector notation as

$$\begin{Bmatrix} u_r \\ u_\theta \end{Bmatrix} = [\Psi'_s][K_I, K_{II}, \dots, K_{n\lambda}]^T \quad (6.7)$$

where,

$$[\Psi'_s(r, \theta)] = [\Psi'_{s_I}, \Psi'_{s_{II}}, \dots, \Psi'_{s_{n_\lambda}}] = \begin{bmatrix} r^{\lambda_I} f(\theta), r^{\lambda_{II}} f(\theta), \dots, r^{\lambda_{n_\lambda}} f(\theta) \\ r^{\lambda_I} g(\theta), r^{\lambda_{II}} g(\theta), \dots, r^{\lambda_{n_\lambda}} g(\theta) \end{bmatrix} \quad (6.8)$$

Here, K_i represents the generalized stress intensity factors (SIF) associated with the i -th mode of stress singularity, and n_λ is the number of non-trivial singularities. In the above equations, the prime symbol is intended to signify the local displacement field Ψ_s expressed in the polar system. The values of the generalized SIFs are obtained by solving the boundary value problem with appropriate far-field loading.

6.2 Isogeometric Enrichment for Multi-material Wedges and Cracks

An enriched field isogeometric approximation for an elastic body containing a multi-material wedge is developed in this section.

Consider a singular stress enrichment embedded in the domain Ω as shown in Figure 6.2a. The domain is composed of N materials with bonded or debonded interfaces Γ_{e_i} . The multi-material junction enrichment and its associated degrees of freedom are iso-parametrically represented by the control point at O' . The enriched domain is represented by NURBS and the associated EIGA composition is illustrated in Figure 6.3. The enriched field approximation of the displacement field within the domain Ω takes the following form

$$\mathbf{u} = (1 - w_t(d))\mathbf{u}_c(\mathbf{x}) + w_t(d)[\mathbf{u}_t + \Psi_s(r, \theta)\mathbf{u}_s] \quad (6.9)$$

where, \mathbf{u}_c is the continuous elastic displacement field associated with the underlying domain, \mathbf{u}_t is the displacement of the multi-material junction, and $\Psi_s(r, \theta)\mathbf{u}_s$ is the enriching displacement associated with the stress singularities. Specifically, the term \mathbf{u}_s is a vector of generalized stress intensity factors, which are computed during the solution process, and which depend on the far field loading on the system. The

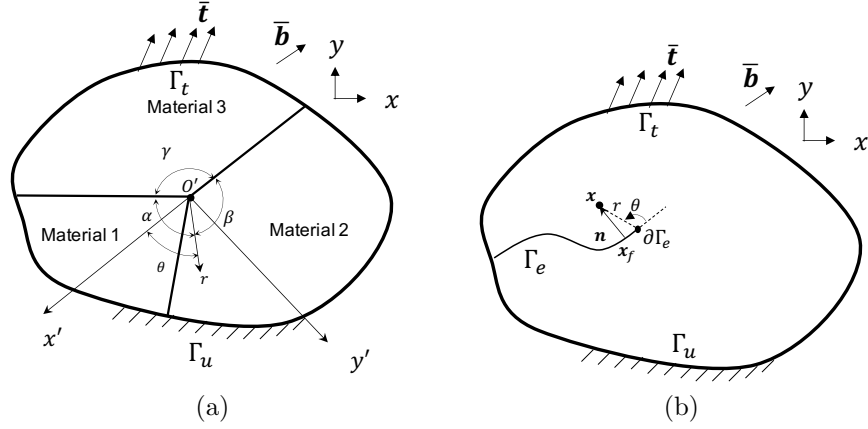


Figure 6.2. Configuration of boundary value problem with (a) singular stress enrichment and (b) hierarchically constructed crack enrichment.

enriching function transform as vectors from the local polar coordinate system to the global coordinate system using transformation matrices similar to those described in Appendix A: $\Psi_{s_i} = \mathbf{T}_u^{-1}(\theta)\Psi'_{s_i}$ for $i = 1, \dots, n_\lambda$. The function w_t is the weight field associated with the multi-material junction vertex. In general, this formulation is valid for re-entrant corners in homogeneous solids, as well as for bi-material or multi-material wedges with bonded interfaces.

The above enriched field approximation may also be extended to model behavioral field of crack tips by making the singular stress enrichment as corresponding to that of the debonded interface. The asymptotic analysis described earlier leads to a value of $\lambda_I = \lambda_{II} = 0.5$ for the strength of the singularity for a plane strain linear elastic solid. The corresponding constants for the angular function of respective modes are listed in Table 6.1. When the constant m attains a value of $1/\sqrt{8\pi\mu^2}$, the absolute values of the generalized SIFs reduce to those of linear elastic fracture mechanics [108]. With the specialized form of singular stress enrichment defined, the enriched field approximation in Eq. (6.9) is next extended to modeling cracks.

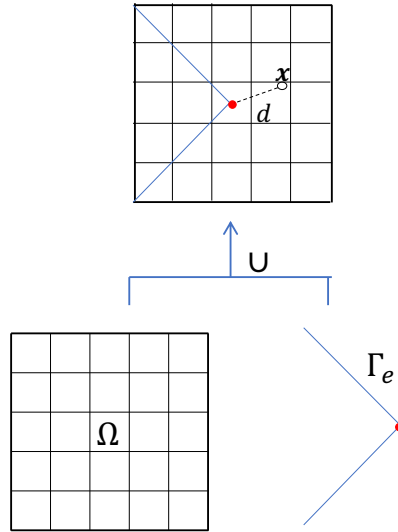


Figure 6.3. Composition of domain, material interfaces and multi-material junction represented by NURBS.

Table 6.1.

Coefficients of angular function corresponding to symmetric and anti-symmetric loading modes at a crack tip when the strengths of singularity are $\lambda=0.5$.

Mode	A	B	C	D
I (Symmetric)	$-m/2$	0	$(\kappa-1/2)m$	0
II (Anti-symmetric)	0	$3m/2$	0	$(-\kappa+1/2)m$

Consider a crack face Γ_e with the crack tip at $\partial\Gamma_e$ that is iso-parametrically defined in the domain Ω as illustrated in Figure 6.2b. The enriched field approximation of the displacement field within such domain Ω takes the following form

$$\mathbf{u} = (1-w_e)\mathbf{u}_c(\mathbf{x}) + (w_e-w_t)[\mathbf{u}_e(\mathcal{P}(\mathbf{x})) + \mathcal{H}(\mathbf{x})\mathbf{u}_H(\mathcal{P}(\mathbf{x}))] + w_t[\mathbf{u}_t + \Psi_s(r, \theta)\mathbf{u}_s] \quad (6.10)$$

where, \mathbf{u}_e is the displacement of the explicitly represented crack face, $\mathcal{H}\mathbf{u}_H$ is the discontinuous displacement of crack openings, and w_e is the weight field associated

with the crack face Γ_e . Specifically, the enriching function \mathcal{H} is a modified Heaviside function given by

$$H(\mathbf{x}) = \begin{cases} +1 & \text{if } \mathbf{n}(\mathcal{P}(\mathbf{x})) \cdot (\mathbf{x} - \mathbf{x}_f) \geq 0 \\ -1 & \text{if } \mathbf{n}(\mathcal{P}(\mathbf{x})) \cdot (\mathbf{x} - \mathbf{x}_f) < 0 \end{cases} \quad (6.11)$$

where, \mathbf{x}_f is the foot point on Γ_e projected from spatial point \mathbf{x} , and \mathbf{n} is the normal vector of the explicitly represented crack face at the foot point \mathbf{x}_f . The components of the crack tip enriching functions Ψ_s are pictorially illustrated in Figure 6.4 for the asymptotic analysis result listed in Table 6.1.

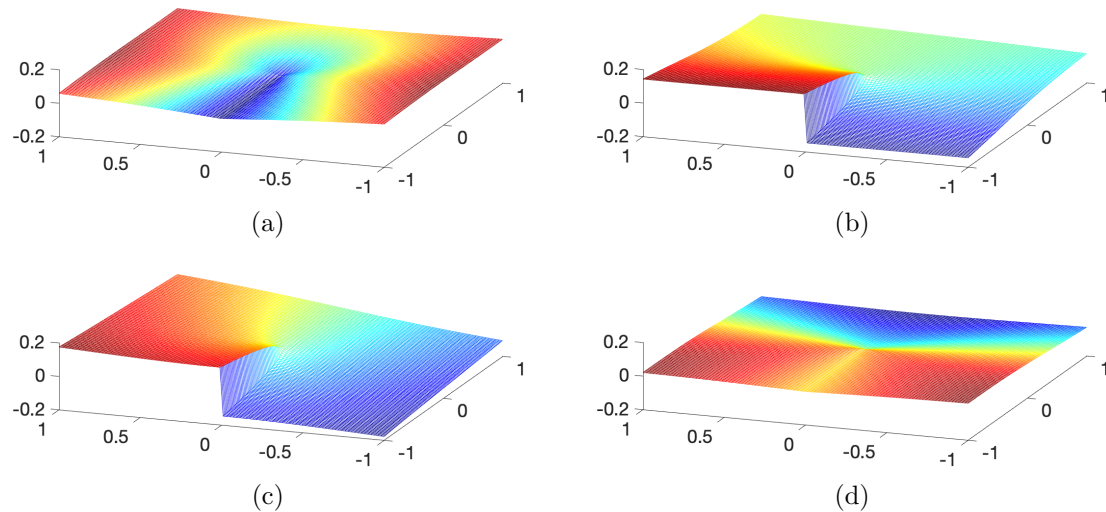


Figure 6.4. (a) x -component and (b) y -component of enriching function Ψ_s subjected to Mode I loading. (c) x -component and (d) y -component of enriching function Ψ_s subjected to Mode II loading.

The weight fields in Eq. (6.10) are pictorially illustrated in Figure 6.5. The field w_e denotes the weight associated with the crack face Γ_e and attains a value of unity on the interface. The influence of the asymptotic crack tip displacement on the domain is described by the weight field w_t while the continuous field associated with the underlying domain is $1 - w_e$. The region behind the crack tip, where singular stress

weakens and crack opening grows, is described by $w_e - w_t$. It can be clearly seen that Eq. (6.10) satisfies partition of unity property everywhere in the domain. In general, it is required that the associated weight fields do not overlap with each other so that the convergence of solution is assured through the partition of unity principle.

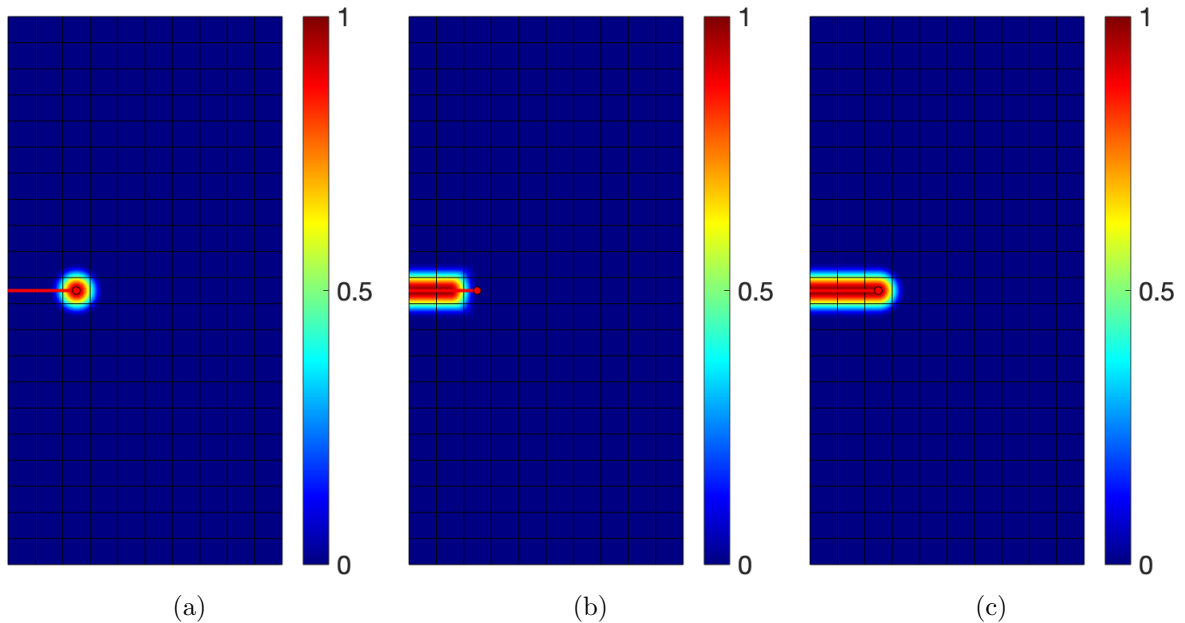


Figure 6.5. Weight field (a) w_t , (b) $w_e - w_t$, and (c) w_e associated with a single edge notch cracked plate.

The proposed enriched field approximation adequately describes the displacement in an arbitrary elastic body containing simple cracks. Specifically, the $\mathcal{H}(\mathbf{x})\mathbf{u}_H$ term of Eq. (6.10) naturally ensures the traction-free condition since it lacks the gradient in the direction normal to the crack in the enriched approximation of Eq. (5.1). Since the gradient with respect to the normal direction of the crack face are not included, the tractions normal to the crack interfaces Γ_e^+ and Γ_e^- automatically vanish.

6.3 Discretized Equations

In this section, the discretized equations of the enriched approximation and the resulting weak form governing equations are developed. Development is focused on the system containing cracks with the enriched field described by Eq. (6.10). The discretized forms for a body with a multi-material wedge is easily obtained by simply ignoring the terms associated with the crack face Γ_e .

The discretization of continuous displacement field approximation $\mathbf{u}_c, \mathbf{u}_e, \mathbf{u}_t$ have the following form:

$$\mathbf{u}_c = \sum_i^{n_c} R_{c_i} \mathbf{q}_{c_i} = [\mathbf{R}_c] \{\mathbf{q}_c\}, \quad (6.12a)$$

$$\mathbf{u}_e = \sum_i^{n_e} R_{e_i} \mathbf{q}_{e_i} = [\mathbf{R}_e] \{\mathbf{q}_e\}, \quad (6.12b)$$

$$\mathbf{u}_t = \sum_i^{n_t} R_{t_i} \mathbf{q}_{t_i} = [\mathbf{R}_t] \{\mathbf{q}_t\} \quad (6.12c)$$

where, R_{c_i}, R_{e_i} and R_{t_i} are the NURBS basis functions of the underlying domain, crack faces and crack tips, respectively. $\mathbf{q}_{c_i}, \mathbf{q}_{e_i}$ and \mathbf{q}_{t_i} are the displacement degrees of freedom associated with the control points $\bar{\mathbf{x}}_i$ of the parametrically defined geometry of the crack face. The enriching parts of the displacement field approximation are discretized as:

$$\mathcal{H}\mathbf{u}_H = \mathcal{H}(\mathbf{x}) \sum_i^{n_e} R_{e_i} \mathbf{q}_{\mathcal{H}_i} = \mathcal{H}(\mathbf{x}) [\mathbf{R}_e] \{\mathbf{q}_{\mathcal{H}}\}, \quad (6.13a)$$

$$\Psi_s \mathbf{u}_s = \sum_i^{n_t} R_{t_i} \Psi_{s_i}(r, \theta) \mathbf{q}_{s_i} = [\mathbf{R}_t] [\Psi_s(r, \theta)] \{\mathbf{q}_s\} \quad (6.13b)$$

where, $\mathbf{q}_{\mathcal{H}}$ and \mathbf{q}_s are generalized coordinates associated with discontinuous displacement and crack tip (or multi-material wedge vertex) displacement, respectively. Com-

binning the above equations, the displacement can be expressed in matrix form as $\mathbf{u} = \mathbf{N}\mathbf{q}$ in which \mathbf{N} and \mathbf{q} are

$$\mathbf{N} = \left[(1 - w_e)\mathbf{R}_c, (w_e - w_t)\mathbf{R}_e, (w_e - w_t)\mathcal{H}\mathbf{R}_e, w_t\mathbf{R}_t, w_t\mathbf{R}_t\Psi_s \right], \quad (6.14a)$$

$$\mathbf{q} = [\mathbf{q}_c, \mathbf{q}_e, \mathbf{q}_H, \mathbf{q}_t, \mathbf{q}_s]^T \quad (6.14b)$$

The corresponding strain field is given by

$$\boldsymbol{\varepsilon} = \mathbf{B}\mathbf{q} \quad (6.15)$$

The strain-displacement matrix \mathbf{B} takes the following form:

$$\mathbf{B} = \begin{bmatrix} (1 - w_e)[\nabla\mathbf{R}_c]^T - [\mathbf{R}_c]^T[\nabla w_e]^T \\ (w_e - w_t)[\nabla\mathbf{R}_e]^T + [\mathbf{R}_e]^T[\nabla(w_e - w_t)]^T \\ (w_e - w_t)\mathcal{H}[\nabla\mathbf{R}_e]^T + \mathcal{H}[\mathbf{R}_e]^T[\nabla(w_e - w_t)]^T \\ w_t[\nabla\mathbf{R}_t]^T + [\mathbf{R}_t]^T[\nabla w_t]^T \\ w_t[\Psi_s]^T[\nabla\mathbf{R}_t]^T + w_t[\nabla\Psi_s]^T[\mathbf{R}_t]^T + [\Psi_s]^T[\mathbf{R}_t]^T[\nabla w_t]^T \end{bmatrix}^T \quad (6.16)$$

Note that the derived strain from the asymptotic displacement is transformed from strain expressed in polar system by $\nabla\Psi_{s_i} = \mathbf{T}_\varepsilon^{-1}\nabla\Psi'_{s_i}$ using the transformation matrix \mathbf{T}_ε derived in Appendix A.

The discretized version of the governing equation is of the form

$$\mathbf{K}\mathbf{q} = \mathbf{f} \quad (6.17)$$

where,

$$\begin{aligned} \mathbf{K} &= \int_{\Omega} [\mathbf{B}]^T [\mathbf{D}] [\mathbf{B}] d\Omega, \\ \mathbf{f} &= \int_{\Omega} [\mathbf{N}]^T \{\bar{\mathbf{b}}\} d\Omega + \int_{\Gamma_t} [\mathbf{N}]^T \{\bar{\mathbf{t}}\} d\Gamma \end{aligned}$$

The resulting system and its implementation has two major advantages. First, classification of control points (or nodes) in the underlying domain as being in the region influenced by crack is not needed to construct the enriched field approximation. This is since the enriching strategy isoparametrically associates generalized displacement degrees of freedom directly on the parametrically defined crack geometry. The need to classify enriching control points is eliminated through the algebraically constructed distance field from the crack geometry. The second (and the most important) advantage is that the generalized stress intensity factors \mathbf{q}_s , included in the generalized displacement vector \mathbf{q} , directly provide the solution to Eq. (6.17) without needing *a-posteriori* calculation of path-independent integrals to determine the SIFs.

6.4 Numerical Examples

To validate the proposed formulation, numerical examples were solved of a bi-material wedge with bonded interfaces as well as of a body with a fracture.

6.4.1 Bi-material Wedge with Bonded Interface

Consider a square patch of size $l = 1$ in which a square heterogeneity is included as illustrated in Figure 6.6a. Thus the configuration is an example of a bi-material wedge with bonded interfaces and a sharp corner at which singular stress is expected. The two materials are elastic with the properties $E_1 = 100$, $\nu_1 = 0.3$ and $E_2 = 1$, $\nu_2 = 0.3$, respectively. Assuming the plane strain condition, a uniform traction $t_y = 1$ is applied along the top edge of the body.

A bi-cubic NURBS patch is used to approximate the underlying patch with an isogeometric singular stress enrichment vertex inserted at the junction. The weight field w_t , associated with the junction enrichment, is confined in the domain by setting $d_{max} = l/4$ as shown in Figure 6.6b. Two non-trivial stress singularities λ with their corresponding eigenvectors were obtained by solving the transcendental equations described earlier in Section 6.1. Mode I (symmetric) condition yields the dominant

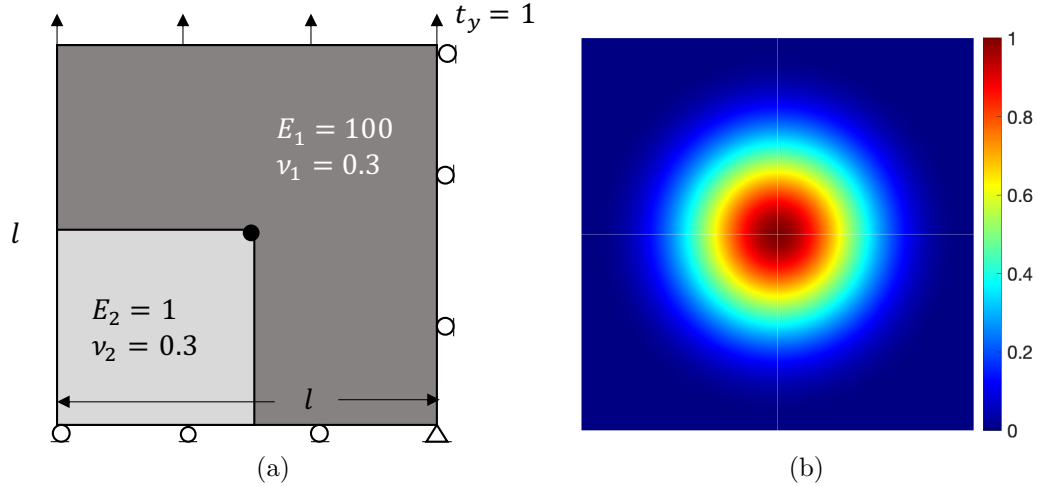


Figure 6.6. (a) Boundary conditions on a bi-material wedge with bonded interfaces. The \bullet in the figure indicates the location of singular enrichment. (b) Contour of weight function w_t used in the enriched filed approximation.

Table 6.2.

Coefficients of angular function associated with the first two modes of the bi-material wedge with bonded interface obtained by asymptotic analysis.

Material	Mode	A	B	C	D
1	I	-0.025995	0.140303	0.037942	0.204783
	II	0.075719	0.265855	0.163379	-0.573638
2	I	-0.806594	0	0.534479	0
	II	0	0.437278	0	-0.613696

singularity with $\lambda_I = 0.4416$ while (anti-symmetric) Mode II yields a weaker singularity with $\lambda_{II} = 0.08832$. The coefficient values in each material that together determine the eigenvectors of each individual mode are summarized in Table 6.2.

The boundary value problem was solved with uniformly refined discretization having 342, 726, 1,926, 6,054 and 21,222 degrees of freedom. The generalized stress intensity factors associated with the singular stress enriching function directly result during the solution process as the degrees of freedom \mathbf{q}_s . As shown in Figure 6.7, the

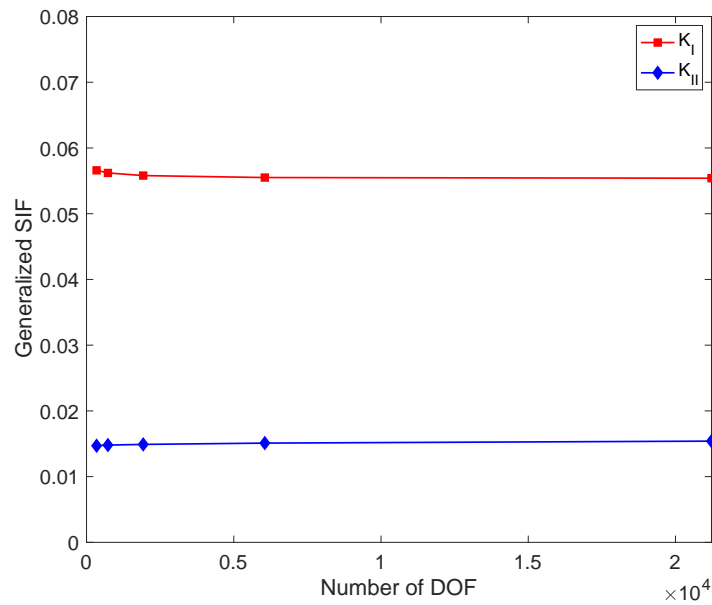


Figure 6.7. Convergence of generalized stress intensity factors for bi-material wedge with bonded interface.

generalized stress intensity factors rapidly converged to $K_I = 0.0566$ and $K_{II} = 0.0147$ from which the dominance of the symmetric mode is clear. As can be seen from the figure, the convergence to the solution is very rapid and achieved even under coarse discretizations.

In Figure 6.8, the von Mises stress solution in the body obtained through finite element analysis is compared against that obtained through enriched isogeometric approximation. It is clear that the approximation to the singular stress requires significant mesh refinement when using the finite element method. The C^0 finite element leads to stress fields that are less smooth than that obtained using enriched isogeometric analysis even when a very coarse discretization is used for the enriched analysis.

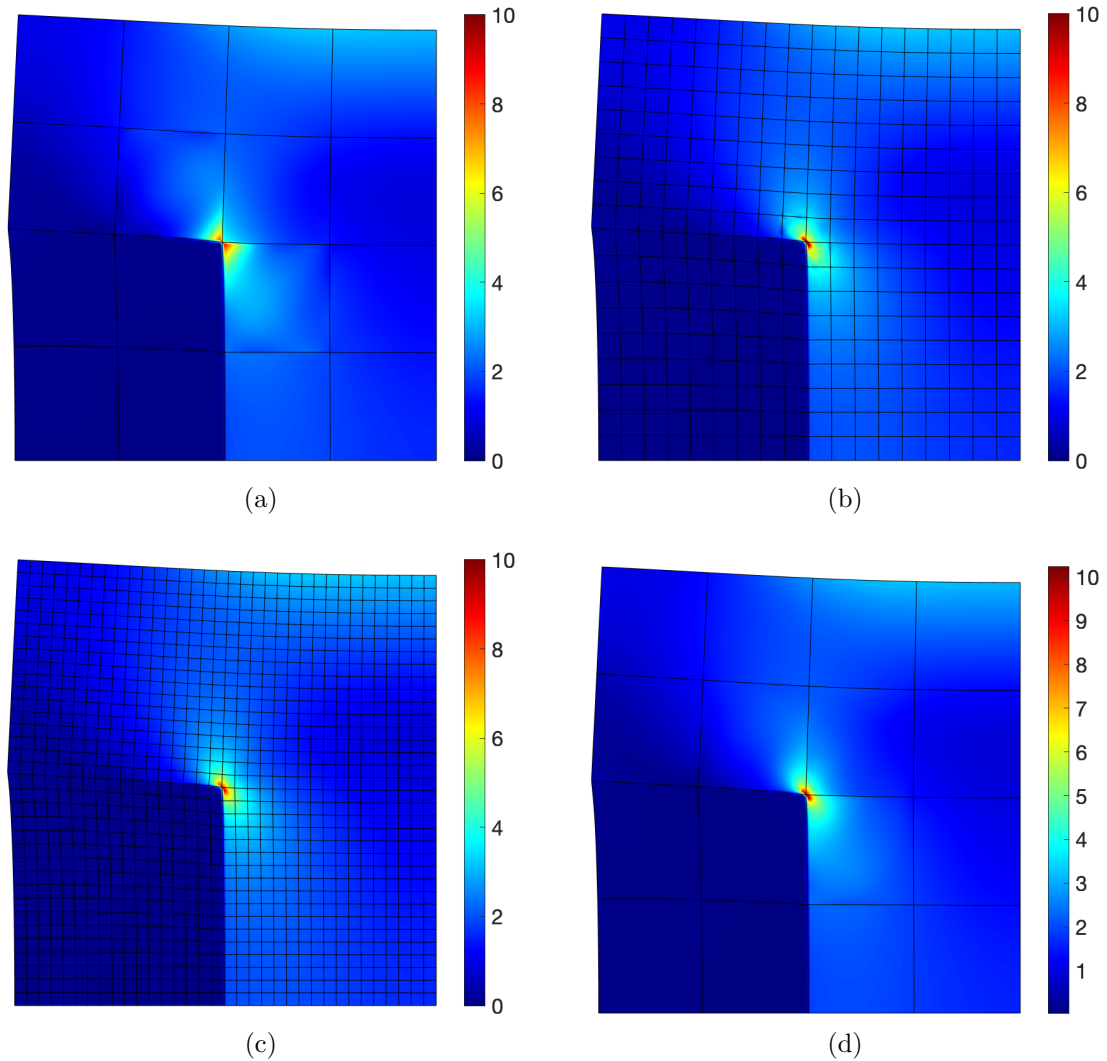


Figure 6.8. The von Mises stress obtained using the finite element method with (a) 50, (b) 722, and (c) 2,450 number of DOF. (d) The von Mises stress contour obtained through enriched isogeometric analysis.

6.4.2 Inclined Crack in a Homogeneous Plate

Next, an inclined crack in a homogeneous plate is modeled using enriched isogeometric analysis. A square plate of $l = 20$ with a center inclined crack of length $2a = 3$ under uniaxial tensile load $t_y = 1$ as illustrated in Figure 6.9a is analyzed. Linear elastic behavior and plane strain condition is assumed with property values for elastic

modulus and Poisson ratio of $E = 10^3$ and $\nu = 0.3$ respectively. If the inclined crack were to be in an infinite sized plate under uniaxial loading, the stress intensity factors have the following analytical form [108]:

$$K_I = \sigma \sqrt{\pi a} \sin^2 \beta, \quad (6.18a)$$

$$K_{II} = \sigma \sqrt{\pi a} \sin \beta \cos \beta \quad (6.18b)$$

where, β is the angle of inclination with respect to the vertical axis.

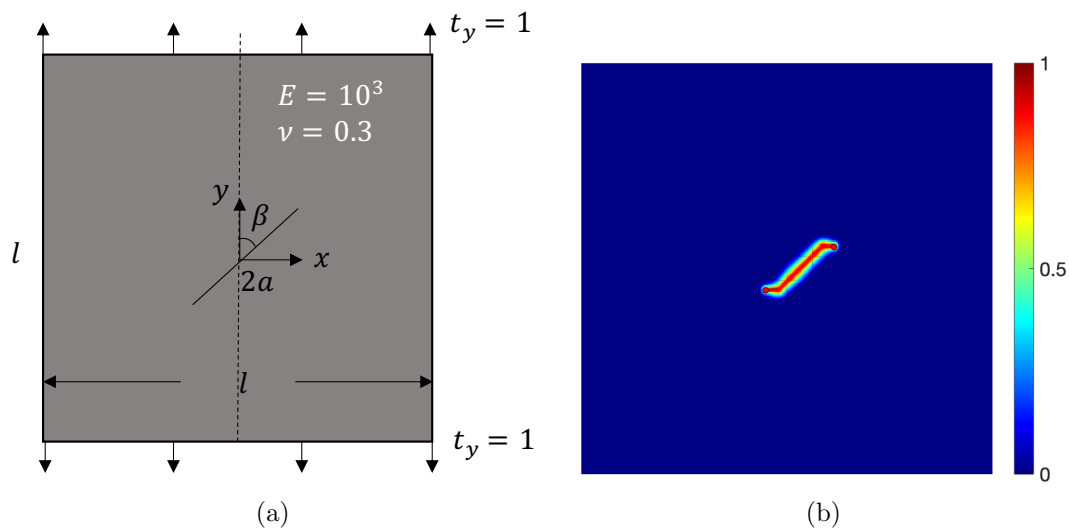


Figure 6.9. (a) Schematic of boundary conditions of a plate containing center inclined crack under tensile traction. (b) The weight field w_e associated with the inclined crack assuming pseudo sharp deflections at both tips.

A bi-cubic NURBS patch was used to represent the underlying domain along with an isogeometric enrichment of crack face and crack tips. The end points of the crack face and crack tips were given the same physical coordinates initially, but were not otherwise numerically constrained to be tied to each other. The displacement solution determined the positions of the crack tip and crack face. Figure 6.9b demonstrates

the weight field w_e associated with the crack face obtained using the smooth algebraic level sets.

First, the variation of the stress intensity factors with the angle of inclination is studied. Figure 6.10 demonstrates the calculated stress intensity factors as the inclination angle β varied from 0 to 90 degrees in increments of ten degrees. Overall, the solution agrees well with the reference values given in Eq. (6.18). Figure 6.11 shows the calculated von Mises stress contour for the crack at an inclination of $\beta = 45^\circ$. The traction-free condition naturally achieved through the enrichment can be clearly observed on the crack face. Furthermore, both crack tips remained attached to the end of the crack face $\partial\Gamma_e$ without a need to apply additional tie constraints.

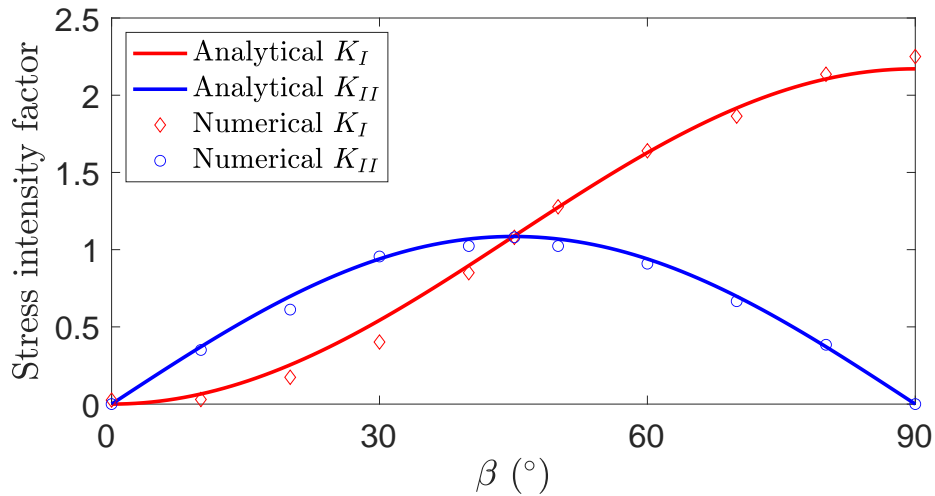


Figure 6.10. Comparison of reference and numerically calculated stress intensity factors (K_I and K_{II}) as a function of inclination angle.

6.4.3 Quasi-Static Crack Propagation

Next, the quasi-static propagation of crack at an angle $\beta = 45^\circ$ is modeled. The configuration of the plate, including dimensions, material properties and loading were as in the earlier example. Ten steps of crack propagation simulation were carried out

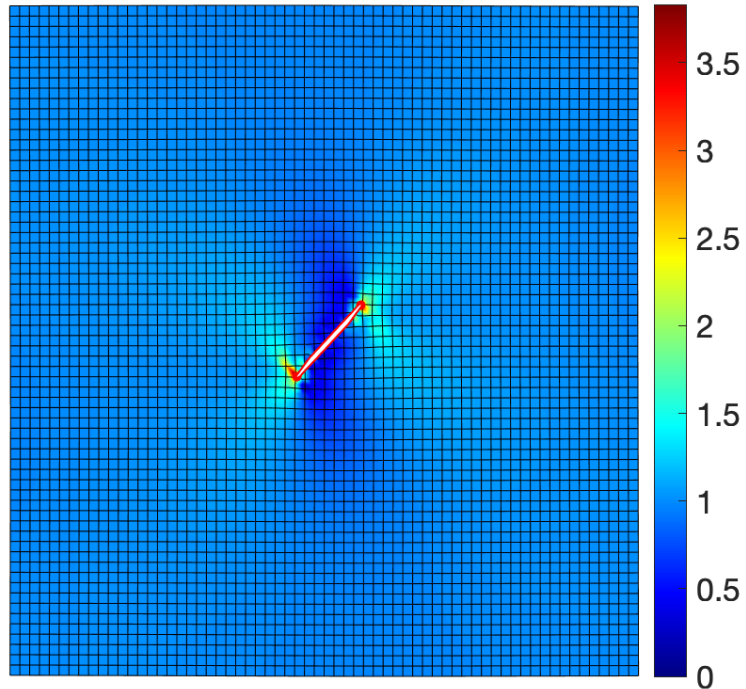


Figure 6.11. The von Mises stress contours in the domain for a crack at an inclination angle of $\beta = 45^\circ$.

with a fixed step size of $\Delta h = 0.6$. The crack deflection angle at each step was determined using the maximum tensile stress criterion [108]:

$$\Delta\theta = 2 \tan^{-1} \frac{1 \pm \sqrt{1 + 8(K_{II}/K_I)}}{4K_{II}/K_I} \quad (6.19)$$

where, the stress intensity factors results directly from the enriched solution as explained earlier.

At each step of quasi-static propagation of crack, new knots are inserted and additional control points were added at both ends of the NURBS curve (representing the crack face) at the angle of deflection calculated through Eq. (6.19). The discretization of the bi-cubic NURBS patch was not changed as the crack was propagated on the underlying domain. Figure 6.12 summarizes the sequential crack propagation path

with the contours of vertical displacement u_y . It can be seen that the predicted crack path immediately deflected in the horizontal direction under the tensile load.

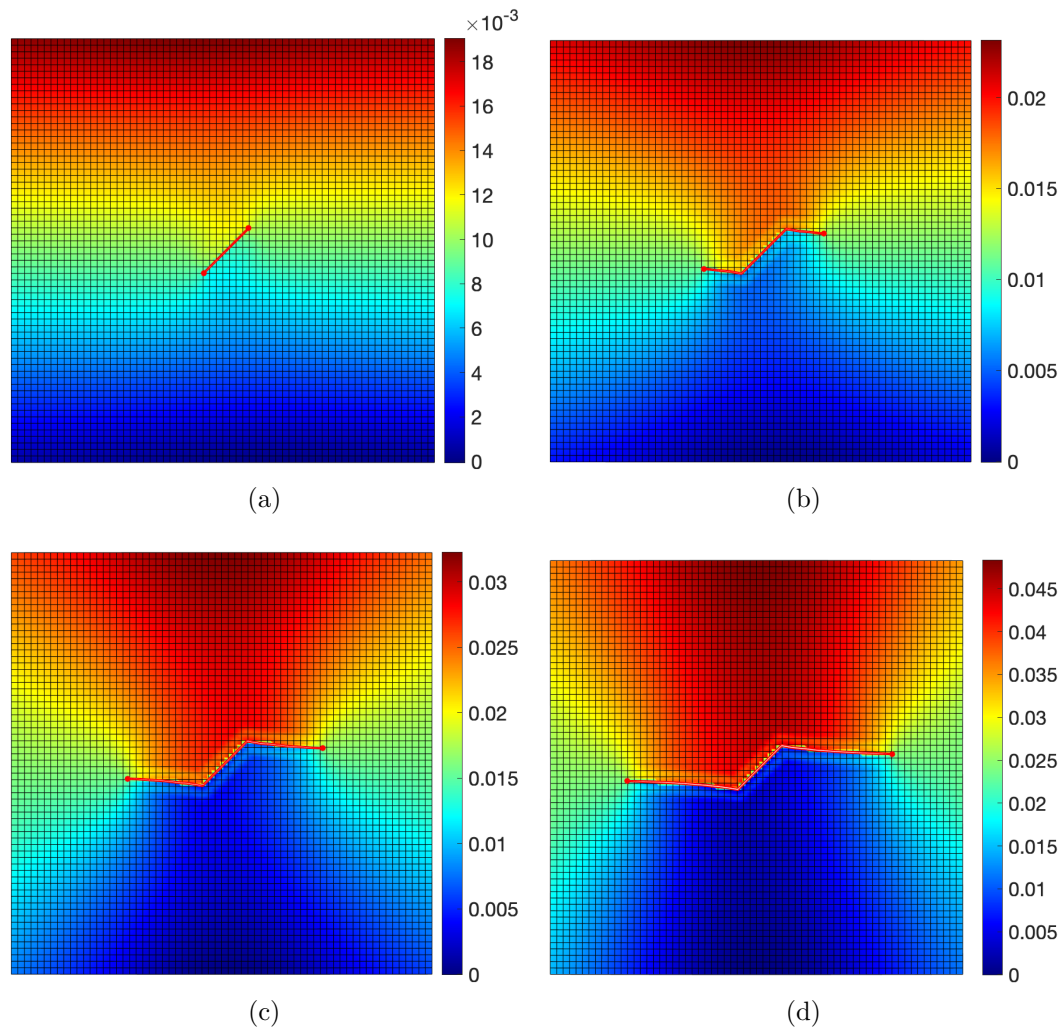


Figure 6.12. The vertical displacement u_y contours at (a) Step 1, (b) Step 4, (c) Step 7, and (d) Step 10.

7. CONFIGURATIONAL FORCE IN ENRICHED ISOGEOMETRIC ANALYSIS

In Chapter 6, stress singularities at multi-material junctions were described by enriching a continuous field with the linear elastic general solution proposed by Seweryn and Molski [106]. In addition to utilizing stress intensity factor as the measure to characterize the propensity for failure as already demonstrated, it is also possible to measure the risk of failure using configurational force or material force. The configurational force associated with a moving interface, as derived in Eqs. (3.26) to (3.28) is closely related to the energy release rate associated with a progressing crack. Although the earlier derivation is based on an assumed elastic behavior, in general, the configurational force is a statement of entropic inequality [109–111] and is therefore independent of material constitutive behavior. Configuration force can be used to characterize systems with inelastic behavior. Applications of configurational force calculation using the finite element method exists in the literature [112–118], however, in the context of isogeometric analysis, computation of configurational force is relatively limited [119]. This chapter provides a brief overview of configurational force and demonstrate its use for singular tip enrichment through EIGA.

7.1 Configurational Force: A Brief Introduction

The theory of configurational force can be traced back to the fundamental theories proposed by Eshelby [120, 121]. It has been used to characterize the rate of energy change due to change in configuration of material inhomogeneities or defects [109, 122] such as interstitial points, dislocations lines, cracks surfaces, voids or inclusions. The theory is briefly reviewed below.

The equilibrium of stress in the reference configuration requires the satisfaction of

$$\nabla \cdot \mathbf{P} + \mathbf{f}_0 = 0 \quad (7.1)$$

where, \mathbf{P} is the first Piola-Kirchhoff stress, and \mathbf{f}_0 is the body force in reference configuration. By rearranging the material gradient of the strain energy of the system, it can be shown that the equation for the configurational force \mathbf{g} is given by [113]

$$\nabla \cdot \Sigma + \mathbf{g} = 0 \quad (7.2)$$

The quantity Σ is the Eshelby energy-momentum tensor, defined as

$$\Sigma = \psi \mathbf{I} - \boldsymbol{\sigma} \cdot (\nabla \mathbf{u})^T \quad (7.3)$$

with ψ being the free energy density, which for an elastic structure is $\psi = \frac{1}{2} \boldsymbol{\varepsilon} : \mathbf{C} : \boldsymbol{\varepsilon}$. The configurational force \mathbf{g} is introduced into the equation such that the forms of Eq. (7.2) and Eq. (7.1) are similar. If the body is homogeneous and no body forces are applied, it can be shown from Eq. (7.2) that the divergence of the Eshelby stress tensor vanishes everywhere except the boundaries, i.e. $\nabla \cdot \Sigma = 0$ is satisfied in the domain. This is one of the important properties that can be applied to measure material inhomogeneity or singularity as shown below.

The weak form of Eq. (7.2) may be constructed as,

$$\int_{\Omega_0} (\nabla \cdot \Sigma + \mathbf{g}) \cdot \mathbf{w} d\Omega = 0 \quad (7.4)$$

where, \mathbf{w} is the test function. Integration by part yields

$$\int_{\partial\Omega_0} (\Sigma \cdot \mathbf{N}) \cdot \mathbf{w} d\Gamma - \int_{\Omega_0} \Sigma : \nabla \mathbf{w} d\Omega + \int_{\Omega_0} \mathbf{g} \cdot \mathbf{w} d\Omega = 0 \quad (7.5)$$

where, the first integral becomes zero by choosing a test function that vanishes on the boundary $\partial\Omega_0$ in the reference configuration. Comparing Eqs. (3.26) and (7.4),

configurational force essentially measures the configurational derivative with respect to the translation of material point. The direction of the configurational force indicates the direction of the material point translation which leads to a decreasing strain energy of the overall structure.

7.2 Configurational Force as Crack Propagation Criterion

Miehe *et al.* [123,124] outlined a consistent thermodynamics framework for crack propagation in elastic solids using the configurational force. From the second axiom of thermodynamics, they related the rate of energy dissipation to the configurational force by the *reduced global dissipation inequality*

$$\dot{\delta} = \int_{\partial\Gamma} -\mathbf{g} \cdot \mathbf{v} d\Gamma \geq 0 \quad (7.6)$$

where, \mathbf{v} was the rate of extension at the crack tip. At the point of the crack tip $\mathbf{x} \in \partial\Gamma$, the crack front was extended based on the *maximum local dissipation principle*, namely

$$|\mathbf{g} \cdot \mathbf{h}| \geq |\mathbf{g}^* \cdot \mathbf{h}| \quad \text{for all } \mathbf{g}^* \quad (7.7)$$

where, $\mathbf{h} = \int \mathbf{v} dt$ was the vector of extension at the crack tip. Considering a Griffith-type crack criterion, the crack extends when $|\mathbf{g}| = g_c$ in the direction of $-\mathbf{g}/|\mathbf{g}|$ where g_c is a material parameter. This method provides an alternative, unified approach to determining both crack extension and the direction of crack propagation. As stated earlier, the configurational force criterion is valid for nonlinear elastic or inelastic materials as well.

7.3 Numerical Evaluation of Configurational Force

Evaluation of configurational force, in general, does not need solution of additional governing equations. Instead, it only requires post processing of the solution that

was obtained for the original boundary value problem. Choosing a test function that vanishes on the boundary, the discretized form of Eq. (7.5) is

$$\sum_{c=1}^{n_{cell}} \mathbf{w}^T \left[- \int_{\Omega_e} \nabla \mathbf{R} \cdot \boldsymbol{\Sigma} d\Omega + \int_{\Omega_e} \mathbf{R} \cdot \mathbf{g} d\Omega \right] = 0 \quad (7.8)$$

where, \mathbf{R} is the basis function associated with the underlying domain represented by a NURBS patch. Since the Eshelby energy-momentum tensor is not symmetric in general, the gradient operator ∇ will have the following form [113]

$$\nabla = \begin{bmatrix} \frac{\partial}{\partial x} & 0 \\ 0 & \frac{\partial}{\partial y} \\ \frac{\partial}{\partial y} & 0 \\ 0 & \frac{\partial}{\partial x} \end{bmatrix} \quad (7.9)$$

We enforce Eq. (7.8) locally by writing the local configurational force in each *element* Ω_e (here, an element signifies the non-zero knot span of the NURBS patch) as

$$\mathbf{g}_c = \int_{\Omega_e} \mathbf{R}_I \cdot \mathbf{g}_I d\Omega = \int_{\Omega_e} \nabla \mathbf{R}_I \cdot \boldsymbol{\Sigma}_I d\Omega \quad (7.10)$$

The discrete configurational forces are then assembled to form the global configurational force vector associated with the control points of the underlying domain

$$\mathbf{g} = \sum_{c=1}^{n_{cell}} \mathbf{g}_{el} \quad (7.11)$$

The evaluation of configurational force requires assembly of the global vector \mathbf{g} , but it does not require solution to a new boundary value problem since the Eshelby stress only depends on quantities such as $\nabla \mathbf{u}, \boldsymbol{\sigma}$ and ψ that are available upon displacement solution. Due to the fact that enriched isogeometric analysis explicitly describes behavior at the crack faces as well as crack tips, the subsequent approximation of configurational force at the crack tips can be accurately determined. Unlike the complex node doubling and mesh update required for the finite element method

described in [123, 124], the enriched isogeometric analysis simplifies the algorithm for crack propagation. Algorithm 1 summarizes the evaluation of the configurational force as well as the determination of crack extension based on the previously discussed Griffith-type criterion.

Algorithm 1 Crack propagation using configurational-forces through Enriched Iso-geometric Analysis

Input Crack propagation step α , field solutions $\mathbf{u}, \nabla \mathbf{u}, \boldsymbol{\sigma}, \psi$, critical value g_c
Output Boolean value *isPropagate*, Crack propagation vector \mathbf{h}

```

1: function CONFIGURATIONAL_FORCE_CRACKPROPAGATION( $\alpha, \mathbf{u}, \nabla \mathbf{u}, \boldsymbol{\sigma}, \psi, g_c$ )
2:    $\mathbf{g} \leftarrow 0$  (Initialize global discrete configurational force vector)
3:   for  $c \leftarrow 1, n_{cell}$  do
4:      $\mathbf{x}, w \leftarrow$  Initialize quadrature points and weights
5:      $\mathbf{g}_{cell} \leftarrow 0$  (Initialize discrete configurational force vector in the cell)
6:     for  $qp \leftarrow 1, n_{qp}$  do
7:        $\mathbf{R} \leftarrow$  Evaluate basis function matrix at  $(\mathbf{x}_{qp})$ 
8:        $\mathbf{B} \leftarrow$  Evaluate strain-displacement matrix at  $(\mathbf{x}_{qp})$ 
9:        $\boldsymbol{\Sigma}_{ij}(\mathbf{x}_{qp}) \leftarrow \psi(\mathbf{x}_{qp}) \boldsymbol{\delta}_{ij} - \boldsymbol{\sigma}_{kj}(\mathbf{x}_{qp}) \mathbf{u}_{k,i}(\mathbf{x}_{qp})$ 
10:       $\mathbf{g}_{cell} \leftarrow \mathbf{g}_{cell} + \sum w_{qp} \mathbf{B}(\mathbf{x}_{qp})^T \boldsymbol{\Sigma}_{ij}(\mathbf{x}_{qp}) |J|$ 
11:    end for
12:     $\mathbf{g} \leftarrow \mathbf{g} + \sum_c \mathbf{g}_{cell}$ 
13:  end for
14:  if  $g(\mathbf{x}_{tip}) < g_c$  then
15:    isPropagate  $\leftarrow$  False
16:     $\mathbf{h} \leftarrow 0$ 
17:  else
18:    isPropagate  $\leftarrow$  True
19:     $\mathbf{h} \leftarrow -\|\alpha\| \frac{g(\mathbf{x}_{tip})}{|g(\mathbf{x}_{tip})|}$ 
20:  end if
21: end function

```

7.4 Numerical Examples

The configurational force calculation and its use for crack propagation, numerical examples of a homogeneous plate, a plate with heterogeneity, a bi-material wedge and a homogeneous plate containing horizontal crack are solved.

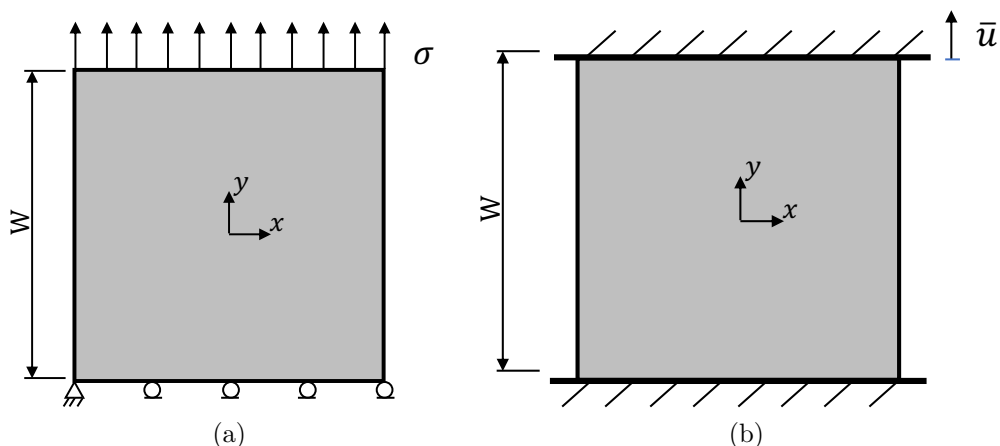


Figure 7.1. Geometry and boundary conditions of the homogeneous square plate with (a) tractions, and (b) with displacement boundary conditions.

7.4.1 Homogeneous Plate

The homogeneous square plate illustrated in Figure 7.1 is considered first. Two types of boundary conditions were considered. In the first case, a uniform traction $\sigma = 1$ is imposed on the top, while the bottom is fixed in the vertical direction. The second boundary condition set constrains the displacement at both top and bottom, and the top surface is displaced by $\bar{u} = 0.2$ relative to the bottom face. The square plate has a width (W) of unity and is approximated by a bi-linear NURBS patch. The plate is assumed to behave elastically with Lamé's constants of $\lambda = 1000$ and $\mu = 400$.

Figure 7.2 shows the configurational force as vectors on the NURBS patch. The first set of boundary condition leads to a configurational force value of zero ($|\mathbf{g}| \in [10^{-20}, 10^{-14}]$) in the interior of the domain. This verifies that the configurational force vanishes in a homogeneous body in the absence of a body force. Since the second set of boundary conditions was also applied on a homogeneous plate without body force as shown in Figure 7.1b, one may expect the configurational force to

vanish as well. However, the configurational force within the domain is non-zero at some interior locations as indicated by the small vectors visible in the plot. This is due to the fact that the discretization is not optimal leading to spurious, numerically calculated configurational forces [125]. In general, components of the configurational force are related to the potential energy of the system through [114]

$$g_i = -\frac{\Pi^h}{\partial x_i} \quad (7.12)$$

where, Π^h is the approximated potential energy. Hence, when the discretization is sub-optimal, the numerically computed potential energy may be further reduced by changing the discretization – a non-zero configuration force will be observed even in a homogeneous structure free of body force.

It is known that FEM or IGA obtain solution based on the *principle of minimum potential energy* of approximation theory. Hence, the discrete configurational results demonstrated in Figure 7.1b indicates that the approximation solution close to the edge of plate is less accurate than the approximation in the middle of plate. Based on Eq. (7.12), it means the potential energy of the system may be further reduced and the approximated solution may be further improved by optimizing the position of control points associated with the underlying domain. Specifically, the interior control point may be updated in the direction of configurational force, e.g. $\bar{\mathbf{x}}_{ijk} \rightarrow \bar{\mathbf{x}}_{ijk} + c\mathbf{g}_{ijk}$ where c is a small number to avoid excess distortion and negative Jacobian.

Studies have proposed methodologies to create problem specific optimal finite element meshes by updating nodal positions using the spurious configurational force that was calculated [113–115, 126]. Control points of the NURBS patch can similarly be updated based on the configurational force, but such an adaptive meshing strategy is outside the scope of this study.

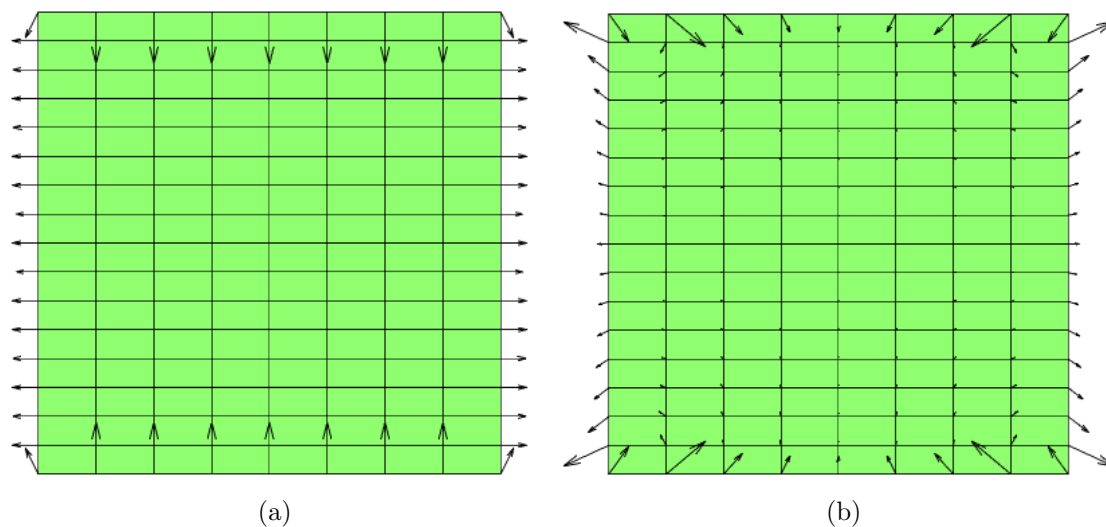


Figure 7.2. Configurational force in a homogeneous plate with (a) traction boundary conditions, and (b) with displacement boundary conditions.

7.4.2 Plate with Hole/Inclusion

Next, a square plate with either a circular hole or an inclusion at the center is considered. The heterogeneity has a radius of R such that $R/W = 0.25$ as illustrated in Figure 7.3. Holding the Poisson's ratio fixed at $\nu = 0.3$, the elastic modulus of the heterogeneity was chosen to be either $E = 10^{-9}$ (hole) or as $E = 10^9$ (stiff inclusion).

The configurational force in the plate with the two types of heterogeneities is plotted in Figure 7.4. In both cases, nearly vanishing, but spurious configurational forces are observed within the domain due to suboptimal discretizations. In general, the configurational force provides sensitivity to the movement of the material point and its vector points in the direction of potential energy decrease. Thus, the configurational forces around the heterogeneity's interface with the surrounding material point in the direction that agrees with Eq. (7.12) [112]. Overall, the configurational force point toward the hole along the horizontal axis and point away from the stiff inclusion along the vertical axis. For the circular hole, the shrinkage of the circle into an ellipse decreases the potential energy when its major axis is aligned with the vertical axis.

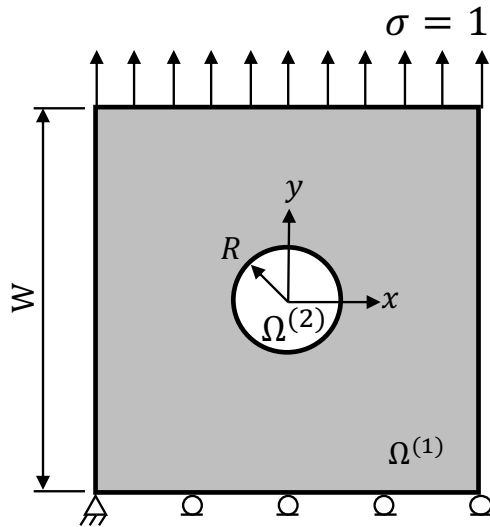


Figure 7.3. Geometry and boundary conditions of a plate with a heterogeneity.

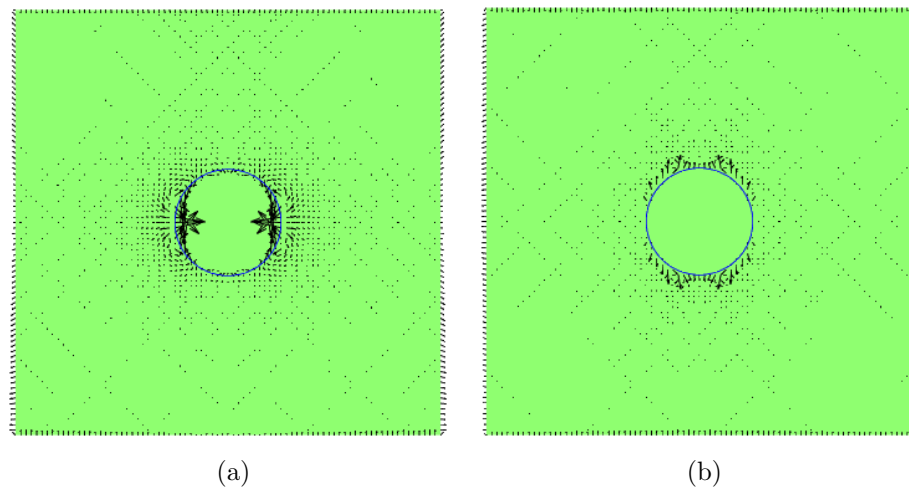


Figure 7.4. Configurational force on (a) a plate with circular hole and (b) a plate with stiff inclusion.

For the stiff inclusion, the growth of inclusion leads to decrease in potential energy of the system.

7.4.3 Bi-material Wedge with Bonded Interfaces

In this example, the configurational force at interfacial corners is evaluated. The bi-material wedge considered is identical to the one shown in Figure 6.6a. All of the geometric dimension, material properties and loading conditions remained unchanged. The singular stress enrichment described earlier was used at the vertex of the bi-material wedge to capture the stress variation in the vicinity of the vertex accurately.

Figure 7.5 shows the configurational force within the structure. The pattern of configurational force bears resemblance to what has been reported in the literature for a plate with a hole [115]. Similar to the plate with a hole, the configurational force points toward the softer material along the interface. Also, it is clear that a significantly large configurational force occurs at the junction vertex where stress singularity exists.

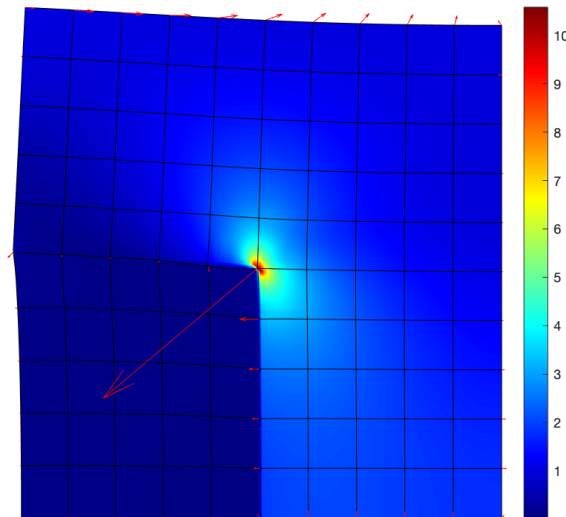


Figure 7.5. Configurational force calculated on the bi-material wedge with singular stress enrichment. The contours of the first principal stress are shown in the figure along with the configurational force.

7.4.4 Crack in a Homogeneous Plate

Configurational force in an elastic plate with crack is next calculated. The plate with the inclined crack that was used earlier as shown in Figure 7.6a is considered again, but with a $\beta = 90^\circ$.

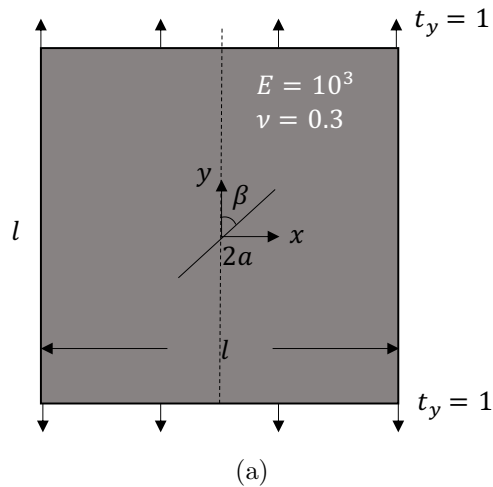


Figure 7.6. Schematic of boundary conditions of a plate containing center inclined crack under tensile traction as illustrated in Figure 6.9a.

In Figure 7.7 the configurational force is plotted on the problem domain. In addition to the non-zero value along the boundaries, configurational forces ahead of the crack tips are large and aligned with the crack due to pure mode I configuration. Since the horizontal line crack is the limiting case of an elliptical hole, the pattern of the configurational force in Figure 7.4a and Figure 7.7 exhibit similarity in the locations where the configurational force reaches its largest value. The crack propagation direction is governed by the maximum dissipation principle or related to the direction in which the configurational force is maximum. Thus, the angle of crack deflection is analyzed for various crack orientation angles from $\beta = 10^\circ$ to $\beta = 90^\circ$. The results are then compared against the theoretical reference value and the previously determined numerical values shown in Figure 6.10 based on the maximum tensile stress criterion of LEFM. From Figure 7.8, it is clear that the maximum dissipation criterion yields

the same crack deflection angle as LEFM. It should be noted that the maximum dissipation criterion unifies crack extension decision as well the angle of crack extension, i.e., it does not require the maximum tensile stress criterion for crack extension angle determination

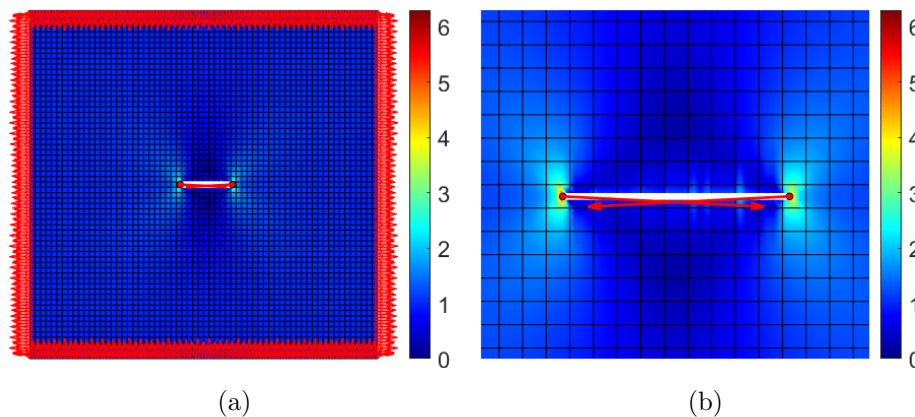


Figure 7.7. (a) Calculated configurational force over the domain and (b) detailed view of the configurational force near the crack in a plate with the horizontal crack.

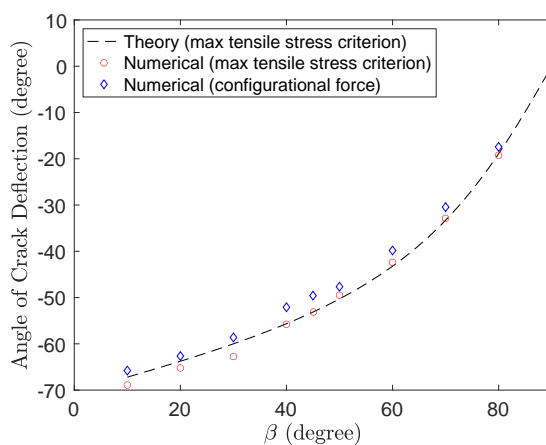


Figure 7.8. Comparison of crack deflection angle based on the maximum tensile stress criterion of LEFM and configurational force.

8. APPLICATION: RATCHETING-INDUCED FRACTURE OF BEOL STRUCTURES OF MICROELECTRONICS

8.1 Overview

Metal line ratcheting and passivation cracking in Back End of Line structures are significant reliability concerns for microelectronic packages. These failures often occur when metal line undergoes plastic deformation under cyclic thermal loading. When metal lines plastically deform due to ratcheting, tensile stress builds up in the passivation overcoat with thermal cycling. Eventually, susceptible interfacial corners in the film fracture due to stress concentration.

Studying ratcheting-induced fracture in BEOL structures is challenged by two facts: (1) the problem is inherently multi-scale in dimension from package level (mm) to BEOL level (μm), and (2) experimental approach yields very few insight into the local state of stress. Therefore, a modeling procedure to study the mechanistic cause of fracture is necessary to analyze the failure.

To address the above challenges, a modeling procedure is developed based on Finite Element Analysis and Enriched Isogeometric Analysis. The global deformation of the microelectronic package was simulated by FEA. Local stress concentration and crack propagation were modeled by EIGA. Several techniques were developed to study the cause of failure and to accurately determine the state of stress in the localized region. Specifically, this chapter demonstrates

1. A decomposition of the applied load to provide insight into the loading mode that is most responsible for passivation cracks.
2. A novel numerical implementation that enables embedding analytical asymptotic solutions to accurately capture the singular stress at BEOL material corners.

3. Numerical simulations of crack propagation in BEOL structures based on configurational forces.

The developed procedure provides a comprehensive and efficient strategy for modeling stress concentration and fracture in BEOL structures.

8.2 Modeling Methodology

The modeling procedure begins with a finite element analysis to simulate the global deformation of the microelectronic package. We denote the domain occupied by the microelectronic package as Ω_g and the domain enclosing the BEOL structure as Ω_l such that $\Omega_l \subset \Omega_g$ as shown in Figure 8.1a. Following the simulation, the displacements on the boundaries of the local region $\partial\Omega_l$ were extracted for two purposes. First, it was used to identify the most critical loading mode with the potential to cause fracture in passivation layer. Specifically, the displacements were decomposed into tensile, shear and flexural loading. Second, the extracted displacements were imposed as the boundary condition for further analysis in local model using EIGA.

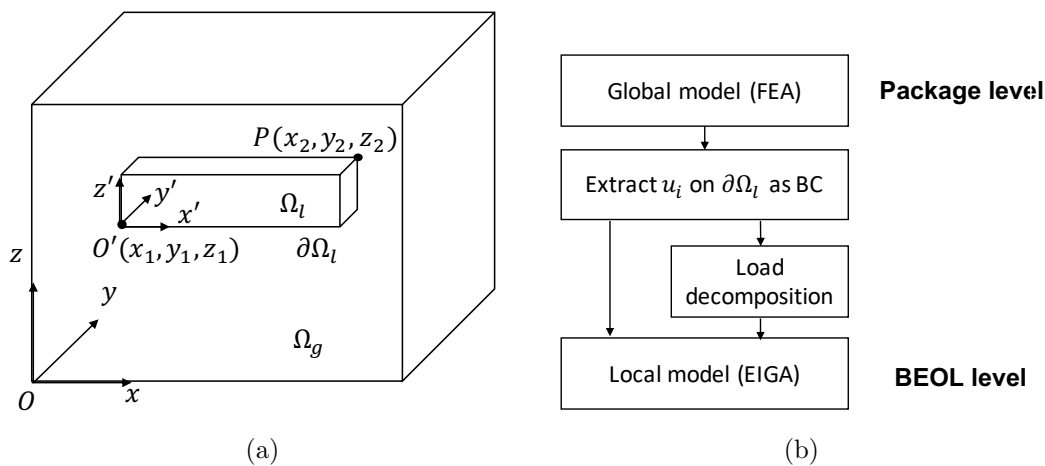


Figure 8.1. (a) Domains, boundaries, and reference coordinate systems in the multi-level models. (b) Modeling procedures to simulate ratcheting induced fracture in metal lines.

At package level, the deformation is driven by the mismatch in coefficient of thermal expansion (CTE) and the differences in rigidities between the leadframe, silicon substrate as well as the epoxy mold compound, as presented below. While the global deformation drives the local state of stress, the modeling procedures assume that changes in local state of stress are unlikely to influence the global deformation significantly. A summary of the procedure is illustrated in Figure 8.1b and details of each step are described in the following sections.

8.3 Global Model and Ratcheting-induced Stress Evolution

A $8\text{ mm} \times 8\text{ mm} \times 0.9\text{ mm}$ test package was modeled in the present work. This package geometry formed the global domain. The overall structure and the aluminum line structures are shown in Figure 8.2. The test die of size $3.9\text{ mm} \times 1.7\text{ mm}$ contained four different sets of metal line structures, each with different combinations of line widths and pitches as listed in Table 8.1. Each line structure consisted of pairs of wide lines and narrow lines with widths denoted as w_1 and w_2 , respectively.

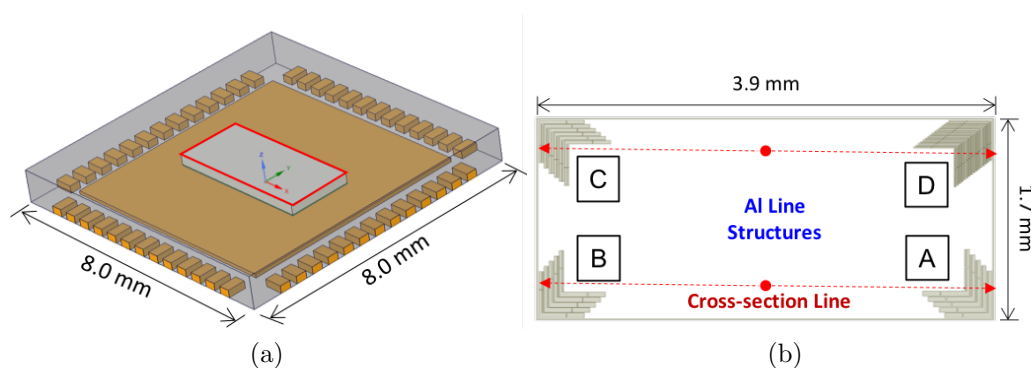


Figure 8.2. (a) The geometry of the test die and package. (b) Metal line patterns on the test die.

The BEOL structure in the package contained TEOS, silicon nitride, aluminum, and epoxy mold compound materials. In the present study, all materials except the aluminum metal lines were treated as elastic, but with temperature dependent ma-

Table 8.1.
Dimensions of the aluminum line structure for the global model.

Structure	$w_1(\mu m)$	$w_2(\mu m)$	Pitch (μm)	Number of Line Pairs
A	25	10	6	5
B	25	10	4	5
C	20	15	4	6
D	8	6	3	16

terial behavior. The Al metal line’s temperature-dependent yield strength, elastic modulus and CTE are based on reported values from literature [4, 127]. The temperature coefficients were assumed -0.069 and 1.65×10^{-8} for elastic modulus and CTE, respectively. For aluminum, kinematic hardening model was assumed upon yielding. The mold compound and die attach were considered temperature-dependent, but rate-independent to capture the change due to glass transition under a quasi-static loading. The temperature dependent behavior of mold compound was felt to be critical to the observed behavior, but the material’s time-dependent response was perceived to be not as important owing to the slower time-dependent response relative to the cycling time. The mechanical properties at the room temperature that were used in the model may be found in Table 8.2. Specifically, mechanical properties of TEOS are estimated by indentation and inversed finite element analysis as described in Appendix C and literature [128]. Additional temperature-dependent mechanical properties are tabulated in Appendix B.

The test structure was assumed stress-free at 175°C , at which temperature the last step of fabrication occurred. Complete thermal cycles of the package from -65°C to 150°C up to five hundred cycles were simulated. Such elaborate simulations were necessary to accurately account for the accumulation of plastic strains in the metal lines due to ratcheting. To reduce the computational cost of three-dimensional modeling, symmetries of the global deformation with respect to xz -plane and yz -plane were assumed so that only one fourth of the entire structure was modeled. The cross-

section of the local model for line structure B, along the red dashed line indicated in Figure 8.2b is shown in Figure 8.3.

Table 8.2.
Microelectronics package material properties at room temperature.

Material	E (GPa)	ν	α (ppm/°C)	σ_Y (MPa)
Aluminum	70	0.33	23	100
Die attach	10	0.35	50	-
Leadframe	120	0.30	17.6	-
Mold compound	30	0.35	10	-
Silicon	131	0.28	2.61	-
Silicon nitride	160	0.25	1.8	-
TEOS	75	0.18	1.6	-

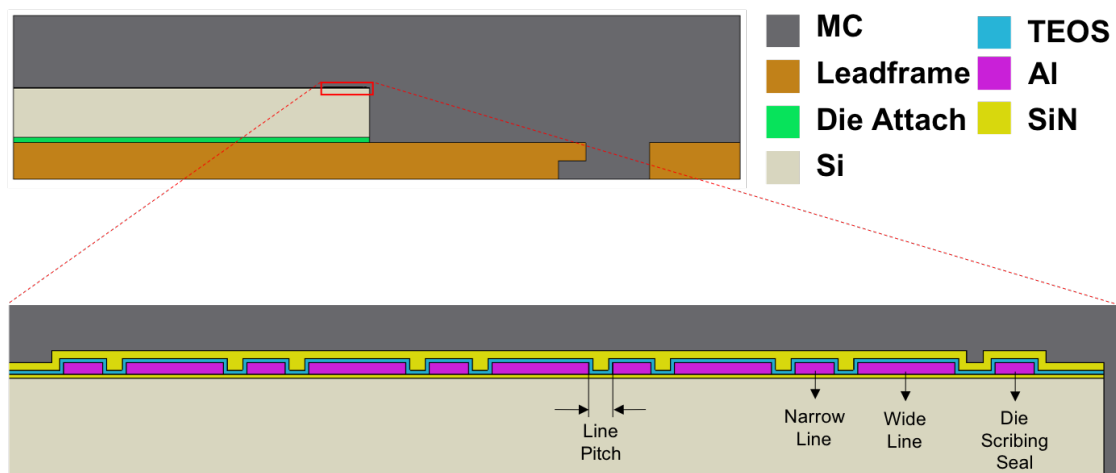


Figure 8.3. Cross section of the three-dimensional model (structure B). Inset figure shows the region enclosing the BEOL structure Ω_l that was analyzed in the local model.

The global finite element model used to identify the most critical loading mode and to extract displacement was based on commercial tool ABAQUS/Standard&CAE [129]. Due to out-of-plane constraint enforced by the geometry, the model was discretized by plane strain elements. Figure 8.4 demonstrate the discretizations of the

overall package model as well as the submodel at the BEOL level to more accurately characterize the local state of stress. The densities of mesh were carefully calculated such that simulation of five hundred thermal cycles is within computational and temporal limits using available resources. Overall, the global model used 11,783 nodes and the submodel used 10,744 nodes. Minimum size of the mesh is assumed $1 \mu m$ and $0.3 \mu m$ for global model and submodel, respectively.

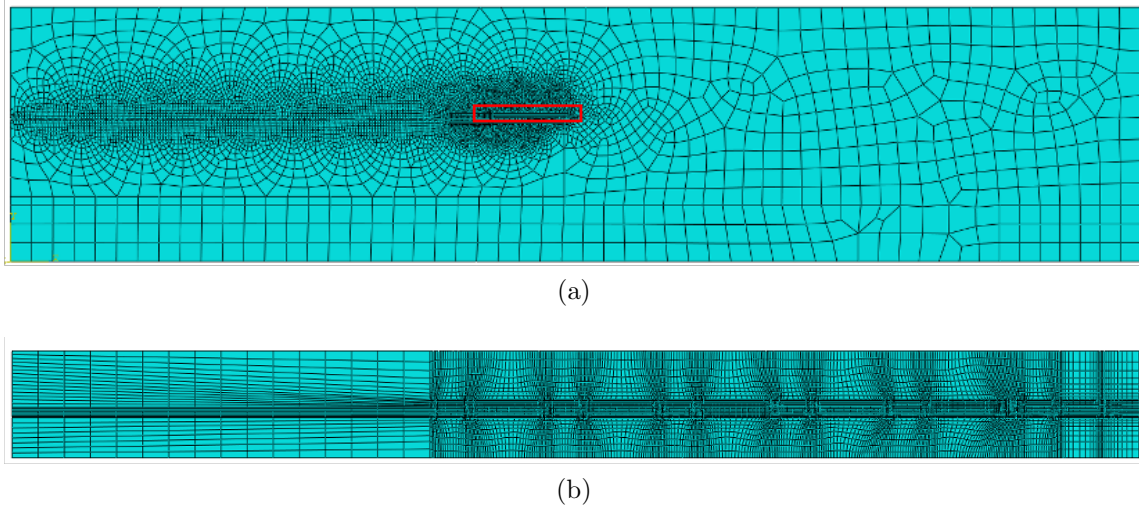


Figure 8.4. Discretization of microelectronic package cross-section at (a) the package level, and (b) at the BEOL level. The inset red box indicates where the BEOL-level submodel is located.

8.3.1 Global Deformation

To understand the overall deformation of the structure driven CTE mismatch, attempts were made to extract the curvature of the package at different temperatures. First, analytical methods to estimate curvature was sought. It is known that the curvature induced by temperature change from T_0 to T of a bi-material strip is given by Timoshenko's equation [105]

$$\frac{1}{\kappa} = \frac{6(\alpha_2 - \alpha_1)(T - T_0)(1 + m)^2}{h(3(1 + m)^2 + (1 + mn)(m^2 + 1/(mn)))} \quad (8.1)$$

where, m is the ratio of thickness t_1/t_2 , n is the ratio of elastic modulus E_1/E_2 , and h is the total thickness of the strip. However, this equation is valid only when interaction involves two materials and when both materials possess constant mechanical properties. Further generalization of curvature solution for multi-layer structures does not seem to appear in the existing literature.

Since microelectronic package contains multiple layers of materials with temperature-dependent properties, estimation of curvature was turned to numerical approach. Figure 8.5 illustrates an intermediate step to extract curvature from the finite element solution. Once the model is solved, quadratic polynomials were fitted to the deformed outline along the top side of the package at various temperature steps. The resulted coefficient of determination R^2 at the minimum of 99.9% is observed for all read points. Next, the curvature is calculated based on the following equation using the quadratic polynomials

$$\frac{1}{\kappa} = \left| \frac{(1 + y'^2)^{2/3}}{y''} \right| \quad (8.2)$$

where, y' and y'' denote the first and second derivative of the polynomial, respectively.

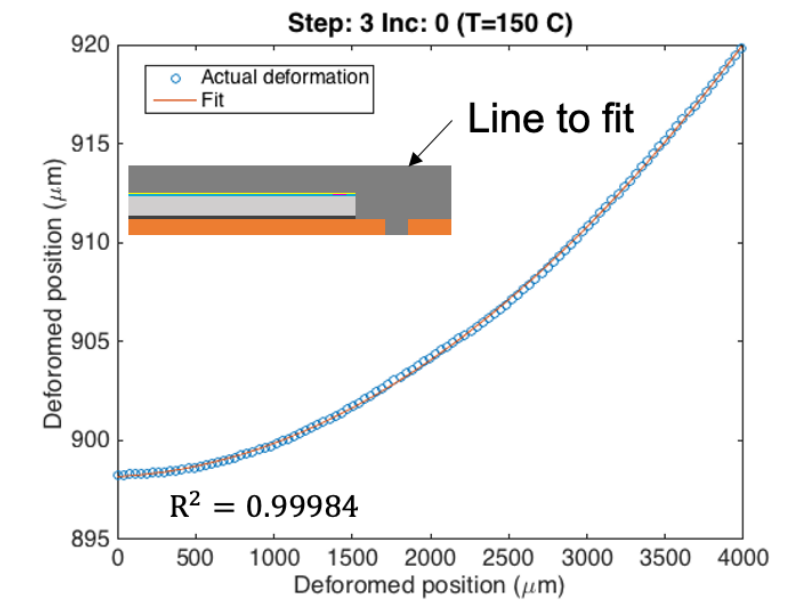


Figure 8.5. Demonstration of polynomial fit to the package outline.

The simulated curvature of the microelectronic package during a thermal cycle is shown in Figure 8.6. It is found that the variation of curvature can be broken down into two parts driven by the interaction between mold compound and leadframe.

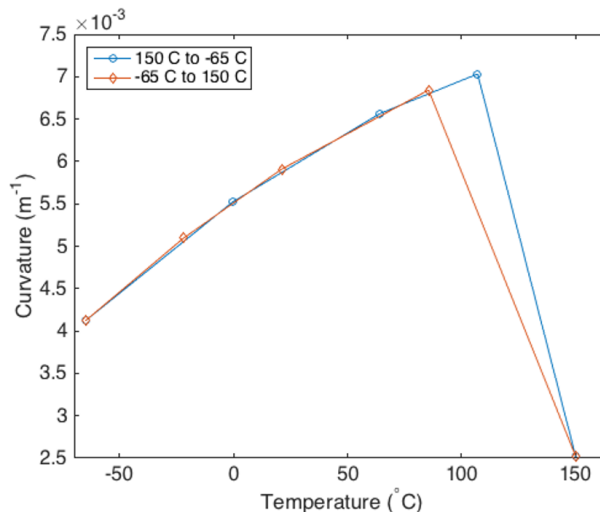


Figure 8.6. Curvature of the microelectronic package during a thermal cycle between 150°C and -65°C.

Overall, similar trend is shared by the cooling ramp as well as the heating ramp. Cooling from 150°C to the glass transition temperature, the mold possesses the highest value of CTE (40 ppm). As the temperature progressively decreases, shrinkage of the mold dominated in the package such that the curvature continuously increased and caused the package to bend concave up. At the glass transition temperature, transitions of the mold compound's CTE occurred and curvature reached the highest value. During the second part of cooling ramp from glass transition temperature to -65°C, the CTE of mold compound dropped to only 10 ppm. As the CTE of lead frame (17.6 ppm) became larger than the counterpart of mold compound in this regime, the shrinkage of the package is no longer dominated by the mold compound alone. The curvature remained to be concave up, but the magnitude decreased with the temperature. The heating ramp reversed the entire process and returned to the

original curvature. Since the global model only accounted the elasticity of materials, the changes in curvature overall did not show the effect of plasticity.

8.3.2 Evolution of Stress in BEOL films

A detailed analysis on the evolution of stress in the passivation films was performed. Since one of the main failure modes observed in the test package is fracture, the first principal stress was chosen as one of the failure sensitivity parameter to be observed in the rest of this chapter.

To begin with, the analysis of the stress was started from structure B. Figure 8.7 demonstrates the evolution of the first principal stress for line structure B throughout the thermal cycles. Specifically, only the lines close to the edge of the die, i.e. the last large-width line (the second from the right side) and the die seal line (the first from the right side), are compared against each other. It is clear that the accumulation of stress started as soon as the repeated thermal loading begins. Furthermore, the rate of ratcheting-induced stress exhibit a linear rate of increase. Although the rates of increase are indistinguishable between the two lines, the large-width line appears to be suffered from a higher tensile stress.

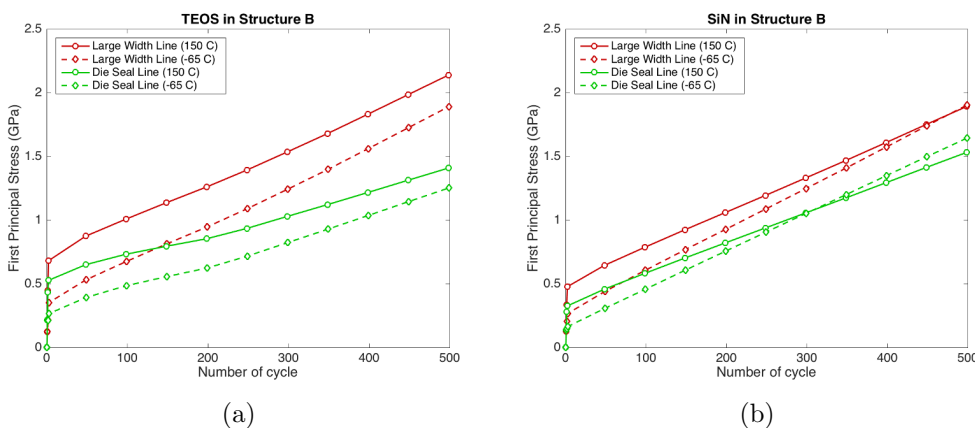


Figure 8.7. Die edge evolution of the first principal stress (unaveraged) (a) in the TEOS films, and (b) in the silicon nitride films of structure B.

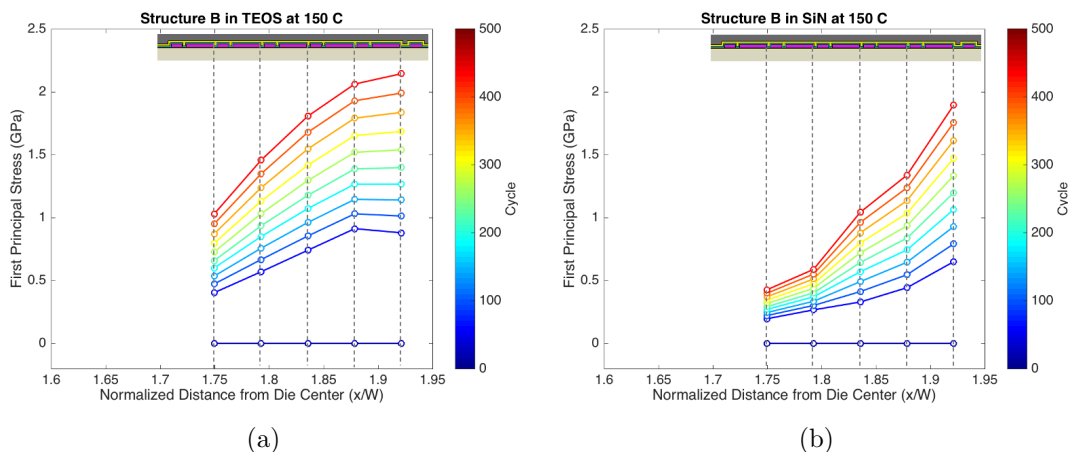


Figure 8.8. Evolution of the first principal stress' local maxima (unaveraged) (a) in the TEOS films, and (b) in the silicon nitride films throughout the BEOL structure B.

To further study the spatial trend of stress, the first principal stress in the passivation films of the entire BEOL structure B was analyzed. Figure 8.8 traced the first principal stress' local maxima in the TEOS film as well as in the silicon nitride film. In addition to the demonstrated results close to the die edge shown in Figure 8.7, a clear trend of steady increase of the stress across the BEOL structure can be observed for every 50 cycles. Furthermore, it appears that stress increases with the distance to the center of the silicon die.

Comparing Figures 8.7 and 8.8, it is observed that the line closest to the die edge is not necessarily the one that possesses the highest stress. As the die seal line locates closest to the edge of the die, based on the trend of Figure 8.8, one would expect the first principal stress in the TEOS film and silicon nitride film is supposed to be the highest in the BEOL structure. However, Figure 8.7 indicates that the die seal line is not the line that suffer the most from the tensile stress. Instead, it is the last large-width line (the second from the right) that exhibit the largest first principal stress.

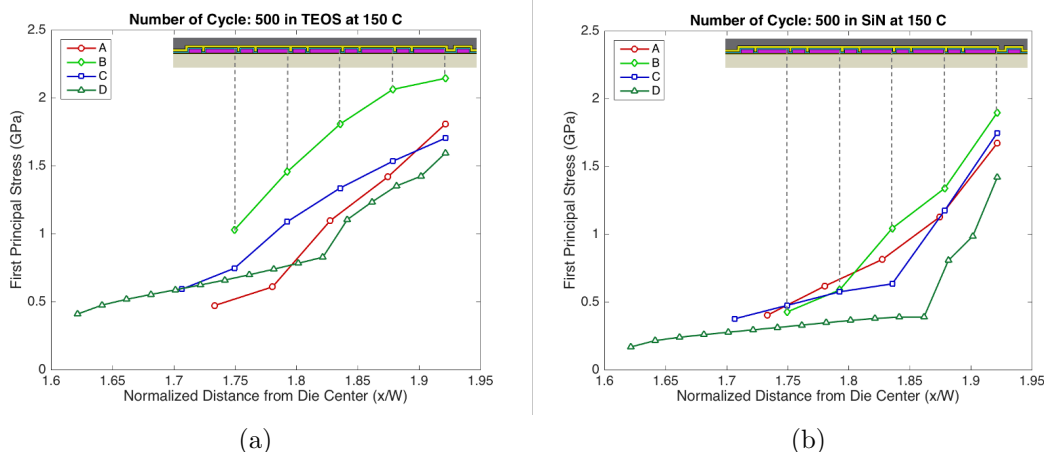


Figure 8.9. Local maxima of the first principal stress (unaveraged) at the end of the thermal cycle (a) in TEOS film, and (b) in silicon nitride film within the line structure listed in Table 8.1.

Similar simulations were performed for structure A, C and D. Their results demonstrate consistent trend. As summarized in Figure 8.9 at the end of the thermal cycles, structure B resulted in the highest stress at the die edge whereas structure D exhibited the lowest stress. Reviewing Table 8.1 reveals that structure B possesses the largest width while structure D has the narrowest width. Both structures share similar pitch of 3 and 4 μm .

Comparing structure B, C and structure D, smaller line width help reduce the first principal stress in the passivation films. The width of the metal lines is hence identified as one of the most critical design parameters which may explain why the die seal line exhibit lower stress. Comparing structure B and structure A, larger pitch seems to mitigate the magnitude of the tensile stress. Overall, the stress accumulation within structure A and structure C is insignificantly different. No further conclusion can be drawn from these two cases alone.

8.4 Load Decomposition and Critical Loading Mode Identification

In the last section, global deformation of the package and the evolution of stress in the BEOL structure were extensively analyzed through multiple finite element analysis. However, the mechanistic causes of the accumulated stress still remains to be unknown. To better understand the critical loading mode that leads to the failures, a load decomposition strategy is proposed below.

In general, the effect of the displacements applied on the local model may be understood better if they were to be decomposed into well understood loading modes such as *tension*, *shear* or *flexure*. Thus, the displacements from the global model are separated into the above mentioned three modes and applied independently on the local model to infer their individual effects. Specifically, for a given Dirichlet boundary condition $u = u_0$, $v = v_0$, and $w = w_0$ on $\partial\Omega_l$, we may decompose it into in-plane tension (Eq. (8.3)), shear (Eq. (8.4)) and flexure (Eq. (8.5)) in the reference coordinate system of the model (see Figure 8.1a).

Tension:

$$\begin{aligned}
 u &= v = w = 0 \text{ at } O' \\
 u|_{x=x_1} &= v|_{y=y_1} = 0 \\
 u|_{x=x_2} &= u_0|_{x=x_2} - u_0|_{x=x_1} \\
 v|_{y=y_2} &= v_0|_{y=y_2} - v_0|_{y=y_1}
 \end{aligned} \tag{8.3}$$

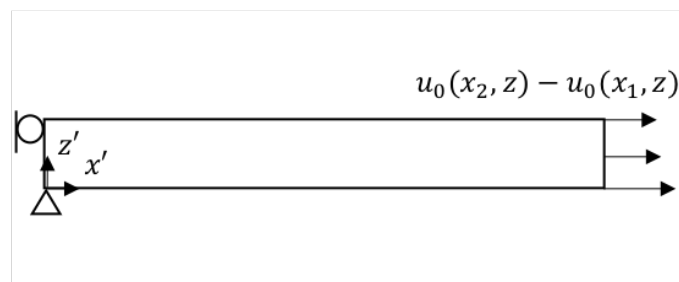
Shear:

$$\begin{aligned}
 w &= 0 \text{ at } O' \\
 u &= u_0 \text{ at } z = z_1 \text{ and } z = z_2 \\
 v &= v_0 \text{ at } z = z_1 \text{ and } z = z_2
 \end{aligned} \tag{8.4}$$

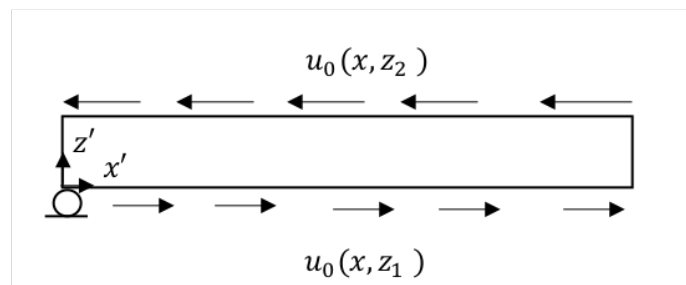
Flexure:

$$\begin{aligned}
 u|_{x=x_1} = v|_{y=y_1} &= 0 \\
 w &= w_0 \text{ at } z = z_1 \text{ and } z = z_2
 \end{aligned}
 \tag{8.5}$$

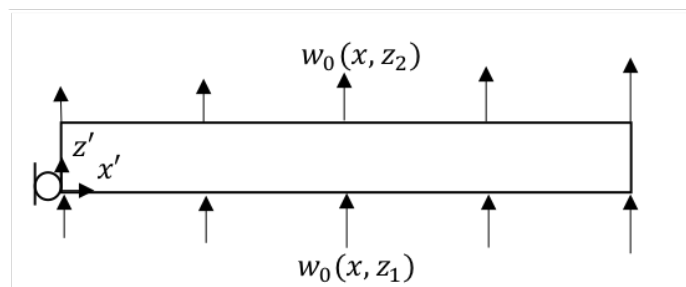
For a two-dimensional model, one may simplify Eqs. (8.3) to (8.5) by taking any plane that is parallel to the xz -plane or the yz -plane. An example of two-dimensional load decomposition analysis and in the xz -plane is shown in Figure 8.10.



(a)



(b)



(c)

Figure 8.10. Load decomposition of boundary condition for local model into (a) tension, (b) shear, and (c) flexure.

Figure 8.11 demonstrates the contour of the first principal stress in the silicon nitride film and in the TEOS film at 150° of the 500-th cycle based on the described load decomposition scheme. The stress contour indicates that shear mode leads to stress concentration at the interfacial corners. While the tensile loading leads to tensile stress state in the horizontal part of the passivation film, it did not cause significant stress concentration to the material corners. Interestingly, the flexural loading resulted in a relative uniform stress which is at least an order of magnitude smaller than the stress induced by shear or tensile loadings.

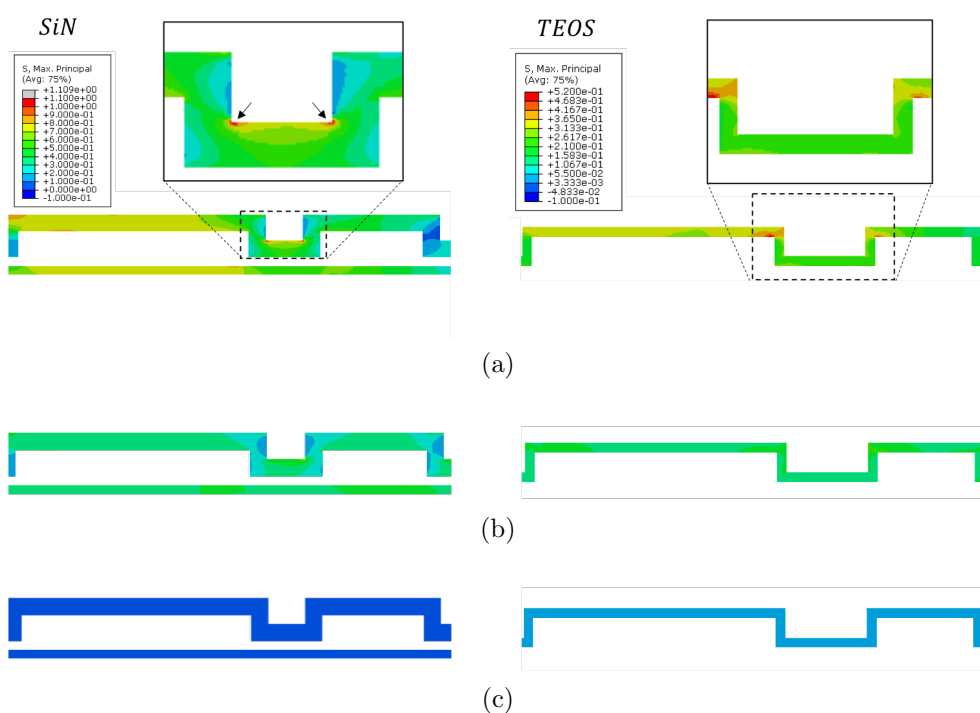


Figure 8.11. The first principal stress contour (averaged) in silicon nitride and TEOS films at the corner of BEOL structure subjected to (a) shear, (b) tension, and (c) flexure loading at 150°C of the 500-th cycle.

Figure 8.12 further summarizes the maximum first principal stress in silicon nitride at -65°C, 100°C and 150°C under tensile, shear and flexural loadings. It is shown that the first principal stress attributed most to the shear loading and second to the tensile loading. The flexural loading indeed contributes the least while the variation

of the flexure-induced stress matches the variation of package curvature observed in Figure 8.6.

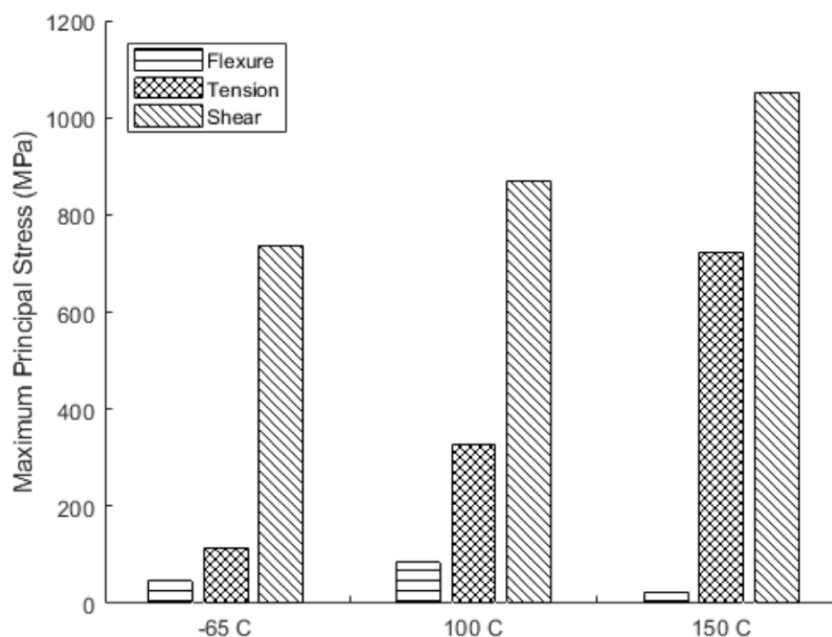


Figure 8.12. The maximum first principal stress (averaged) in silicon nitride film at -65°C , 100°C and 150°C under tensile, shear and flexural loadings.

8.5 EIGA of Stress Singularities in BEOL Structures

Analysis of the BEOL structure presented thus far in this chapter was using the finite element method. In general, extensive care needs to be taken to properly partition the geometry and efficiently refine the mesh during FEA. Such efforts are critical to accurately characterize stress singularities at material corners. Moreover, refinement needs to remain consistent so that the results are comparable across different designs. To address these challenges, BEOL structure is further analyzed here using Enriched Isogeometric Analysis with singular stress enrichments developed in Chapter 6. Without the loss of generality, a simplified BEOL structure similar to

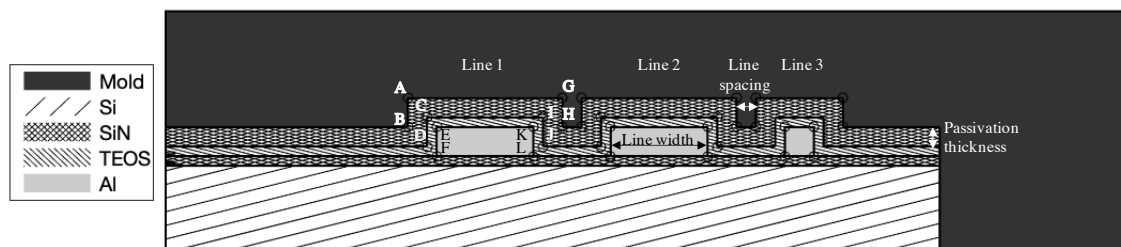


Figure 8.13. A schematic illustration of the BEOL structure showing multi-material wedges.

Table 8.3.

Parameteric values of line width, line spacing and passivation thickness (SiN). The value with asterisk sign indicates the nominal parameters.

Parameter	Dimension (μm)
Line width	10*, 15
Line spacing	0.5, 2*
Passivation thickness (SiN)	2*, 3

the one shown in Figure 8.3 was considered. Figure 8.13 illustrates the equivalent two-dimensional structure analyzed by EIGA. Specifically, the impact of width and spacing of metal lines as well as the thickness of silicon nitride passivation listed in table 8.3 are studied in the models.

The domain shown in Figure 8.13 is representative of the local region containing the key metal line features near the edge of a silicon die on the back side. Overall, the length of the domain is $100 \mu\text{m}$ and the height is $25 \mu\text{m}$. A $1\text{-}\mu\text{m}$ blanket film of silicon nitride caps the underlying structure, which is treated as the homogenized silicon substrate. Metal lines are assumed to be $3 \mu\text{m}$ in thickness covered by a $1\text{-}\mu\text{m}$ TEOS layer. The same set of the elastic properties of materials listed in Table 8.2 was assumed.

Six distinct bi- or multi-material wedges are observed within the representative back end of line structure. As illustrated in Figure 8.14, each type of corner is formed

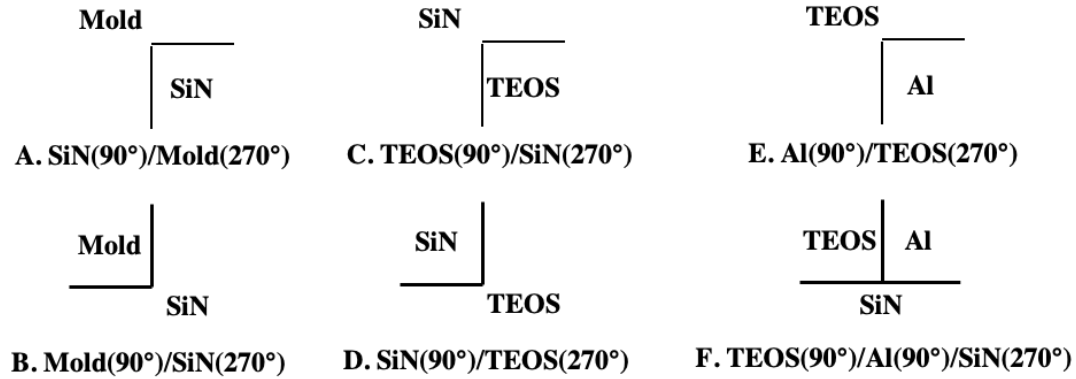


Figure 8.14. The materials and their included angles forming six distinctive corners identified in the BEOL structure.

by material wedges at which the included angle of the various materials varies. Corner G, H, I, J, K and L are in mirror symmetry with Corner A, B, C, D, E and F, respectively. Consequently, they possess the exact same strength of singularity and associated angular function coefficients.

Asymptotic analysis was first carried out to analyze the strength of singularity associated with each corner. The dominant and the secondary strengths of singularities associated with each corner illustrated in Figure 8.14 are summarized in Table 8.4. For Corners A through E, modes 1 and 2 correspond to the symmetric and anti-symmetric loading, respectively. Based on the results of asymptotic analysis, Corners A and B (or G and H) are identified as the most susceptible wedges based on their strengths of singularities. Corner E and F, on the other hand, are of lower risk as the elastic properties of TEOS and metal line (aluminum) are well matched, which nullifies the risk of singular stress.

To study the stress concentration at susceptible corners, the generalized stress intensity factors are calculated using the enriched field analysis developed in this thesis. In total, six designs were explored with the nominal design corresponding to metal line width of $10\ \mu\text{m}$, metal line spacing of $2\ \mu\text{m}$ and silicon nitride passivation thickness of $2\ \mu\text{m}$. The rest of the geometric parameters can be found in Table 8.3.

Table 8.4.

The strength of singularities calculated from asymptotic analysis at six corners of BEOL structure.

Corner	A/G	B/H	C/I	D/J	E/K	F/L
Singularity (I)	1.376E-1	2.181E-1	9.732E-2	8.447E-2	0	0
Singularity (II)	1.037E-1	3.996E-2	7.736E-3	1.056E-2	4.007E-5	0

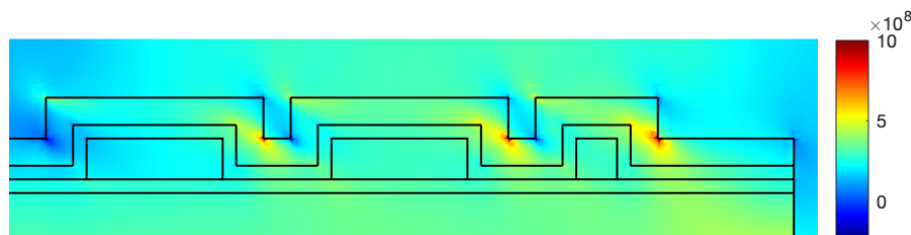


Figure 8.15. Contour of the first principal stress obtained through enrich field analysis in the BEOL structure (unit: Pa).

A separate package-level finite element analysis, which imposed a temperature drop from 150°C to -65°C, was carried out and the boundary conditions from this global model was extracted and applied to the local region during analysis of the local singular stresses.

Figure 8.15 shows the contours of the first principal stress in the nominal design of the BEOL structure. It is clear that Corners H and I are subject to larger tensile stresses than Corner A for both lines. Furthermore, the magnitudes of stress at these corners are higher in Line 2 than in Line 1, with Line 2 being closer to the edge of the silicon die. These trends are consistent across all six designs as well with the observations made earlier using the finite element models.

In addition to using the first principal stress as a failure descriptor, the generalized stress intensity factor associated with the symmetric (opening) loading was also characterized. The impact of varying the design parameters are further studied at Corners H and I. Using the stress intensity factor $K_I^* = 133 \times 10^6$ of Corner I in Line

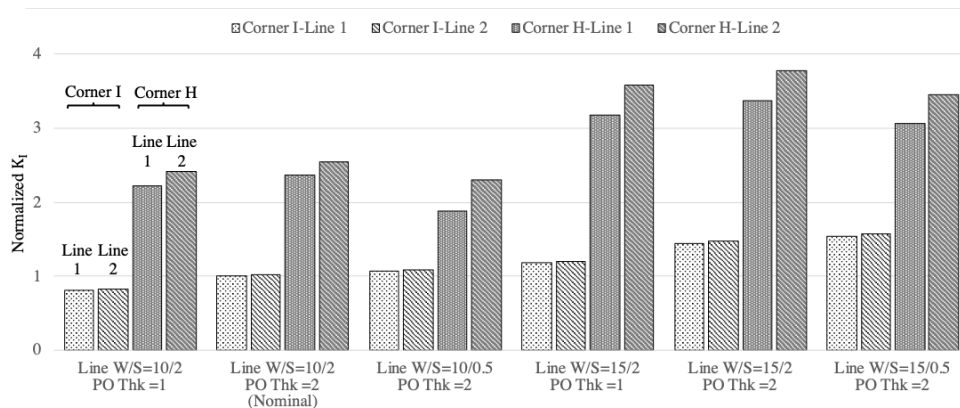


Figure 8.16. Comparison of opening-mode generalized stress intensity factors at Corner H and Corner I in the six parametric designs.

1 as a reference value, in Figure 8.16, the normalized stress intensity factors of opening mode is summarized for all six designs. The generalized stress intensity factors of all corners were directly extracted from the EIGA solution, which improves the efficiency of analyzing complex structures with multiple junctions. The introduction of the singular stress enrichment also eliminates the need to maintain consistent mesh refinement in order to compare the failure descriptors across all designs.

Overall, the width of metal lines and the thickness of silicon nitride passivation film demonstrate a positive correlation with the generalized stress intensity factors. Comparing designs 1 through 3 with designs 4 through 6, a 50 percent increase in the width of metal lines leads to an increase in generalized stress intensity factor of 40 to 50 percent. The comparison between designs 1 and 2 as well as designs 4 and 5 demonstrate the impact of passivation thickness on the stress intensity factor. Reduction in thickness of silicon nitride passivation weakens the SIF by 18 percent and 5 percent for Corners I and H, respectively. Both of the above trends are qualitatively consistent with the relation proposed by Huang et al. [130] for thin film structures. Observing designs 2 and 3 for 10- μm lines or designs 5 and 6 for 15- μm lines, the impact of line spacing has an opposite effect for both corners. A smaller line gap

leads to 6 percent higher mode 1 SIF for Corner I whereas an almost 10 percent drop of SIF is observed for Corner H.

8.6 Configurational Force Based Crack Propagation in BEOL Structure

To understand the ensuing crack path following the ratcheting loads, a fracture analysis is further performed using Enriched Isogeometric Analysis. As previously shown, the introduction of singular stress enrichment into isogeometric formulation naturally yielded non-zero configurational forces near the interfacial corners and crack tips. Configurational force criterion introduced in Chapter 6 and the crack propagation algorithm outlined in Algorithm 1 were further used to determine crack propagation within the passivation film of the BEOL structure. Since modeling of crack within the passivation film requires implementation of adaptive local refinement, the analysis was performed in previously developed object-oriented Fortran HiDAC instead of in the Matlab implementation.

Assuming an unit cell of the metal line subjected to shear loading, Figure 8.17 shows the crack path along with the contours of horizontal displacement. The crack initiated from the material corner between aluminum line and TEOS then propagated into the corner formed by TEOS and silicon nitride films. Figure 8.18 further compares the crack path predicted by LEFM max tensile stress criterion and by configurational force criterion.

8.7 Concluding Remarks

In this chapter, an analysis methodology is developed to characterize the stress singularities in the BEOL structure and correlate to the reported failures. Following the finite element analysis to model the global deformation and the critical loading mode through load decomposition, Enriched Isogeometric Analysis was used to further analyzed the failure sensitive parameters with improved resolution and predict the crack propagation path. The methodology demonstrates a simpler and less labo-

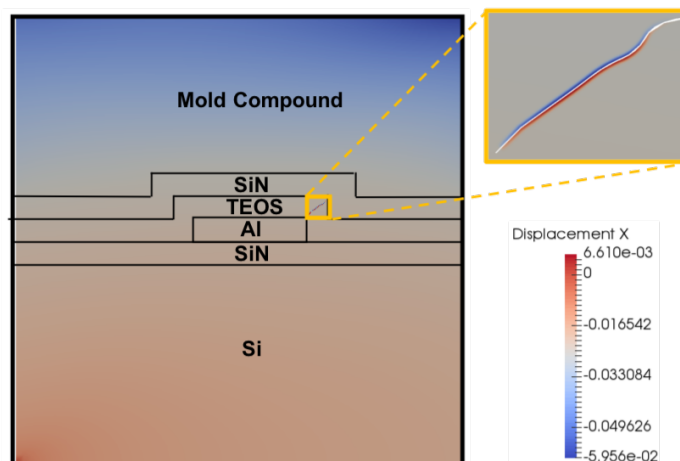


Figure 8.17. Displacement in x-direction and crack path within the BEOL structure predicted by configurational force.

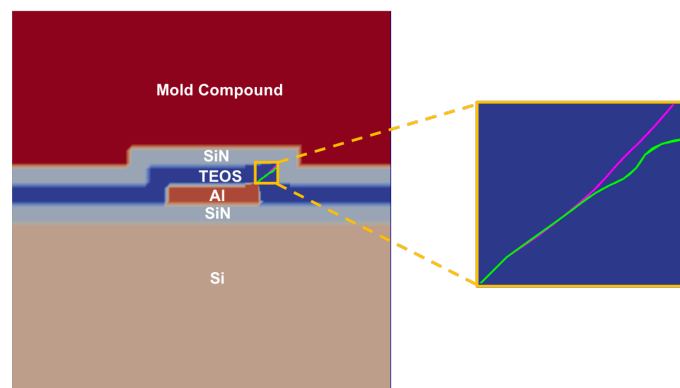


Figure 8.18. Comparison of crack path predicted by LEFM max tensile stress criterion (Green) and by configurational force (Magenta).

rious procedure, but it was able to provide meaningful results that correlating to the reported failures. The analysis indicates the width of the metal line and the thickness of the passivation film are positively correlated to the failure sensitive parameters including the first principal stress and the stress intensity factor associated with opening mode. Furthermore, the line pitch was demonstrated to have an opposite effect on the two most critical material corners. The developed techniques demonstrate a com-

prehensive and efficient workflow that can be used to facilitate the design of BEOL structures.

9. CLOSURE

9.1 Summary and Novel Contributions

The main focus of this thesis was to develop enriched isogeometric formulations with applications to parametric domain decomposition and fracture analysis. First, a literature survey of the existing multi-patch analysis methods was presented. These methods are either inspired by CAD needs to ensure water-tightness of the geometric model or by CAE needs to tie behaviors of two subdomains. The CAD approaches use alternative spline methods to provide an upstream solution that allow seamless integration with downstream CAE operations. The main challenges are their backward compatibility with the existing spline technology in modern CAD systems that are largely based on NURBS and the analysis-suitability of the approximation space. The CAE inspired approaches enforce weak coupling of behavioral field values such that compatibility and consistency conditions are satisfied in an average sense along the interfaces. Methods that weakly couple behavior has been demonstrated on problems with interfaces governed by a variety of physics. However, due to weak coupling, behavioral field across the interface is discontinuous or non-smooth in general. Second, the literature relating to isogeometric fracture analysis was reviewed. While the common approach of using implicit crack representation on a non-conforming mesh (e.g., XFEM) alleviates the need for remeshing, these methods often lead to additional unknowns and auxiliary evolution equations that are difficult to solve. The present thesis described enriched isogeometric formulations that provided solutions to smooth coupling of subdomains with non-matching discretizations and to problems with singular stress.

The techniques developed in the present study are implemented in a 34,000 line of Hierarchical Design and Analysis Code (HiDAC) written in Matlab. Overall, im-

provements were made in terms of simplicity and maintainability over the previously developed Fortran code for isogeometric analysis. Despite being implemented using an interpreted language, the code is highly vectorized and is capable of solving moderate sized two- and three-dimensional problems. Most critical functions support problem dimension independent calling without needing extensive change by users. Modular architecture of the code allows access to the existing modules when developing new algorithms. The implementation sticks to prototype-based object-oriented programming style to provide flexibility during the concept validation phase in research settings.

A smooth coupling method based on enriched isogeometric analysis, termed as parametric stitching, was proposed that satisfies the compatibility condition at every point along the interface while allowing non-matching NURBS discretizations on the subdomains that are coupled. The key concept used to accomplish the coupling is the *parametric stitching* interface between the incompatible patches. Behavioral fields between the sub-domains are blended through a weighted composition of approximation associated with the adjacent patches and the stitching interface. The developed technique enables modular construction of coupling problems with arbitrary smoothness across the interface including sharp changes in gradient, as at dissimilar material interfaces. The solution convergence rate on the coupled domains was demonstrated to be near-optimal through patch tests. Numerical examples of elastostatic and heat conduction problems with multiple two- or three-dimensional subdomains were also demonstrated.

An enriched field approximation was developed for characterizing stress singularities at junctions of general multi-material wedges including crack tips. Using enriched isogeometric analysis, the developed method explicitly tracks the singular points and interfaces embedded in a non-conforming mesh. The recently developed algebraic level sets of parametric surfaces was used as a robust and smooth measure of distance to construct the weight field using which the enriching behavioral field was blended with the underlying approximation. The proposed method enables direct extraction

of generalized stress intensity factors upon solution of the problems without the need to use *a posteriori* path-independent integral such as the J-integral. The present work also described the calculation of configurational force using enriched isogeometric analysis. Configurational force was demonstrated to be an alternative criterion for crack initiation and propagation. Several examples were solved to estimate the configurational force including a bi-material wedge, a plate with heterogeneity, and crack in a homogeneous plate.

The developed techniques were applied to analyze ratcheting failure in semiconductor device back end of line structures. A package-level finite element analysis was performed to study the evolution of the local state of stress and the mechanistic causes of failures. In order to study the risk of ratcheting-induced fracture with different combinations of design parameters, the generalized stress intensity factors at critical material junctions were analyzed and compared between cases. Overall, the systematic study of back end of line structure reveals that the opening-mode stress intensity factors could be used to facilitate the development of design rules.

9.2 Recommendation for Future Research

9.2.1 Mixed-Type Isogeometric Enriched Field Approximation

The method of isogeometric enriched field approximation [76] has demonstrated its capability and advantages in a variety of applications including domain decomposition in this work. Prior to the development of this methodology, the problem domain used to be restricted to a single patch, which posed a significant challenge to model parts with complex geometry. With the proposed parametric stitching technique developed in this study, potential research on mixed-type isogeometric enriched field approximation becomes possible. Specifically, the formulation of parametric stitching can be mixed with subdomains meshed using finite elements. Also, the evolution of solidification front or crack faces across partitioned domains is now possible.

9.2.2 Three-dimensional P-Stitching with Extraordinary Points

A natural extension of the present work is three-dimensional parametric stitching on domains with extraordinary vertices. Two-dimensional parametric stitching on domains with extraordinary vertices was recently demonstrated in a fellow researcher and collaborator's research [131]. The developed hierarchical stitching procedure blends the behavioral field beginning with the vertex all the way to volumetric regions. Given a point surrounding the extraordinary vertex in the domain, the behavioral field is first constructed as a weighted composition of the field associated with the subdomain and the field associated with the stitching interface at the projected point. Similarly, the field at the projected point on the stitching interface is a weighted composition of the field associated with the interface and the field at the extraordinary point.

Recently, a volumetric spline generation starting with B-rep CAD models named v-rep was proposed [37]. The resulting trivariate splines is decomposed but covers the original B-rep domain. However, the decomposed domains remain uncoupled. The three-dimensional parametric stitching technique will allow smooth coupling of the v-rep partitioned domains. A challenge that needs a solution for this effort is an efficient and robust three-dimensional point projection algorithm for the purpose of constructing blended behavioral field.

REFERENCES

REFERENCES

- [1] P. Alpern, P. Nelle, E. Barti, H. Gunther, A. Kessler, R. Tilgner, and M. Stecher. On the Way to Zero Defect of Plastic-Encapsulated Electronic Power Devices Part III: Chip Coating, Passivation, and Design. *IEEE Transactions on Device and Materials Reliability*, 9(2):288–295, June 2009.
- [2] T. Gupta. Dielectric Materials. In T. Gupta, editor, *Copper Interconnect Technology*, pages 67–110. Springer, New York, NY, 2009.
- [3] G. B. Alers, K. Jow, R. Shaviv, G. Kooi, and G. W. Ray. Interlevel dielectric failures in copper/low-k structures. *IEEE Transactions on Device and Materials Reliability*, 4(2):148–152, June 2004.
- [4] P. Alpern, P. Nelle, E. Barti, H. Gunther, A. Kessler, R. Tilgner, and M. Stecher. On the Way to Zero Defect of Plastic-Encapsulated Electronic Power Devices Part I: Metallization. *IEEE Transactions on Device and Materials Reliability*, 9(2):269–278, June 2009.
- [5] M. L. Williams. Stress Singularities Resulting From Various Boundary Conditions in Angular Corners of Plates in Extension. *ASME Journal of Applied Mechanics*, 19(4):526–528, December 1952.
- [6] D. B. Bogy. Edge-Bonded Dissimilar Orthogonal Elastic Wedges Under Normal and Shear Loading. *Journal of Applied Mechanics*, 35(3):460–466, September 1968.
- [7] V. L. Hein and F. Erdogan. Stress singularities in a two-material wedge. *International Journal of Fracture Mechanics*, 7(3):317–330, September 1971.
- [8] J. M. Melenk and I. Babuška. The partition of unity finite element method: Basic theory and applications. *Computer Methods in Applied Mechanics and Engineering*, 139(1):289–314, December 1996.
- [9] I. Babuška and J. M. Melenk. The Partition of Unity Method. *International Journal for Numerical Methods in Engineering*, 40(4):727–758, 1997.
- [10] J. E. Dolbow. *An extended finite element method with discontinuous enrichment for applied mechanics*. Ph.D. Thesis, Northwestern University, 1999.
- [11] N. Moës, J. Dolbow, and T. Belytschko. A finite element method for crack growth without remeshing. *International Journal for Numerical Methods in Engineering*, 46(1):131–150, 1999.
- [12] F. P. Renken and G. Subbarayan. NURBS-based solutions to inverse boundary problems in droplet shape prediction. *Computer Methods in Applied Mechanics and Engineering*, 190(11):1391–1406, December 2000.

- [13] D. Natekar, X. Zhang, and G. Subbarayan. Constructive solid analysis: a hierarchical, geometry-based meshless analysis procedure for integrated design and analysis. *Computer-Aided Design*, 36(5):473–486, April 2004.
- [14] T. J. R. Hughes, J. A. Cottrell, and Y. Bazilevs. Isogeometric analysis: CAD, finite elements, NURBS, exact geometry and mesh refinement. *Computer Methods in Applied Mechanics and Engineering*, 194(39):4135–4195, October 2005.
- [15] J. A. Cottrell, T. J. R. Hughes, and Y. Bazilevs. *Isogeometric Analysis: Toward Integration of CAD and FEA*. John Wiley & Sons, 2009.
- [16] V. P. Nguyen, C. Anitescu, S. P. A. Bordas, and T. Rabczuk. Isogeometric analysis: An overview and computer implementation aspects. *Mathematics and Computers in Simulation*, 117:89–116, November 2015.
- [17] T. W. Sederberg, D. C. Anderson, and R. N. Goldman. Implicit representation of parametric curves and surfaces. *Computer Vision, Graphics, and Image Processing*, 28(1):72–84, October 1984.
- [18] E. Catmull and J. Clark. Recursively generated B-spline surfaces on arbitrary topological meshes. *Computer-Aided Design*, 10(6):350–355, November 1978.
- [19] D. Doo and M. Sabin. Behaviour of recursive division surfaces near extraordinary points. *Computer-Aided Design*, 10(6):356–360, November 1978.
- [20] F. Cirak, M. J. Scott, E. K. Antonsson, M. Ortiz, and P. Schröder. Integrated modeling, finite-element analysis, and engineering design for thin-shell structures using subdivision. *Computer-Aided Design*, 34(2):137–148, February 2002.
- [21] M. E. Mortenson. *Geometric Modeling*. John Wiley & Sons, Inc., New York, NY, USA, 2nd edition edition, 1997.
- [22] D. R. Forsey and R. H. Bartels. Hierarchical B-spline Refinement. *ACM SIGGRAPH Comput. Graph.*, 22(4):205–212, June 1988.
- [23] T. W. Sederberg, J. Zheng, A. Bakenov, and A. Nasri. T-splines and T-NURCCs. *ACM Trans. Graph.*, 22(3):477–484, July 2003.
- [24] T. W. Sederberg, D. L. Cardon, G. T. Finnigan, N. S. North, J. Zheng, and T. Lyche. T-spline Simplification and Local Refinement. *ACM Trans. Graph.*, 23(3):276–283, August 2004.
- [25] J. Deng, F. Chen, X. Li, C. Hu, W. Tong, Z. Yang, and Y. Feng. Polynomial splines over hierarchical T-meshes. *Graphical Models*, 70(4):76–86, July 2008.
- [26] C. Giannelli, B. Jüttler, and H. Speleers. THB-splines: The truncated basis for hierarchical splines. *Computer Aided Geometric Design*, 29(7):485–498, October 2012.
- [27] T. Dokken, T. Lyche, and K. F. Pettersen. Polynomial splines over locally refined box-partitions. *Computer Aided Geometric Design*, 30(3):331–356, March 2013.

- [28] D. C. Thomas, L. Engvall, S. K. Schmidt, K. Tew, and M. A. Scott. U-splines: splines over unstructured meshes. Preprint submitted to Elsevier, November 2018.
- [29] H.-J. Kim, Y.-D. Seo, and S.-K. Youn. Isogeometric analysis for trimmed CAD surfaces. *Computer Methods in Applied Mechanics and Engineering*, 198(37):2982–2995, August 2009.
- [30] Y. Bazilevs, V. M. Calo, J. A. Cottrell, J. A. Evans, T. J. R. Hughes, S. Lipton, M. A. Scott, and T. W. Sederberg. Isogeometric analysis using T-splines. *Computer Methods in Applied Mechanics and Engineering*, 199(5):229–263, January 2010.
- [31] M. R. Dörfel, B. Jttler, and B. Simeon. Adaptive isogeometric analysis by local h-refinement with T-splines. *Computer Methods in Applied Mechanics and Engineering*, 199(5):264–275, January 2010.
- [32] E. Cohen, T. Martin, R. M. Kirby, T. Lyche, and R. F. Riesenfeld. Analysis-aware modeling: Understanding quality considerations in modeling for isogeometric analysis. *Computer Methods in Applied Mechanics and Engineering*, 199(5):334–356, January 2010.
- [33] R. Schmidt, J. Kiendl, K.-U. Bletzinger, and R. Wüchner. Realization of an integrated structural design process: analysis-suitable geometric modelling and isogeometric analysis. *Computing and Visualization in Science*, 13(7):315–330, October 2010.
- [34] X. Li, J. Zheng, T. W. Sederberg, T. J. R. Hughes, and M. A. Scott. On linear independence of T-spline blending functions. *Computer Aided Geometric Design*, 29(1):63–76, January 2012.
- [35] L. Beirão da Veiga, A. Buffa, D. Cho, and G. Sangalli. Analysis-Suitable T-splines are Dual-Compatible. *Computer Methods in Applied Mechanics and Engineering*, 249-252:42–51, December 2012.
- [36] M. A. Scott, X. Li, T. W. Sederberg, and T. J. R. Hughes. Local refinement of analysis-suitable T-splines. *Computer Methods in Applied Mechanics and Engineering*, 213-216:206–222, March 2012.
- [37] F. Massarwi and G. Elber. A B-spline based framework for volumetric object modeling. *Computer-Aided Design*, 78:36–47, September 2016.
- [38] J. L. Lagrange. *Mechanique analytique*. Veuve Desaint, 1788.
- [39] J. C. Simo, P. Wriggers, and R. L. Taylor. A perturbed Lagrangian formulation for the finite element solution of contact problems. *Computer Methods in Applied Mechanics and Engineering*, 50(2):163–180, August 1985.
- [40] K. C. Park, C. A. Felippa, and U. A. Gumaste. A localized version of the method of Lagrange multipliers and its applications. *Computational Mechanics*, 24(6):476–490, January 2000.
- [41] J. Nitsche. Über ein Variationsprinzip zur Lösung von Dirichlet-Problemen bei Verwendung von Teilräumen, die keinen Randbedingungen unterworfen sind. *Abhandlungen aus dem Mathematischen Seminar der Universität Hamburg*, 36(1):9–15, July 1971.

- [42] J. Kiendl, K.-U. Bletzinger, J. Linhard, and R. Wüchner. Isogeometric shell analysis with Kirchhoff-Love elements. *Computer Methods in Applied Mechanics and Engineering*, 198(49):3902–3914, November 2009.
- [43] J. Kiendl, Y. Bazilevs, M. C. Hsu, R. Wchner, and K.-U. Bletzinger. The bending strip method for isogeometric analysis of KirchhoffLove shell structures comprised of multiple patches. *Computer Methods in Applied Mechanics and Engineering*, 199(37):2403–2416, August 2010.
- [44] R. Schmidt, R. Wüchner, and K.-U. Bletzinger. Isogeometric analysis of trimmed NURBS geometries. *Computer Methods in Applied Mechanics and Engineering*, 241-244:93–111, October 2012.
- [45] J. Lu. Isogeometric contact analysis: Geometric basis and formulation for frictionless contact. *Computer Methods in Applied Mechanics and Engineering*, 200(5):726–741, January 2011.
- [46] Í. Temizer, P. Wriggers, and T. J. R. Hughes. Contact treatment in isogeometric analysis with NURBS. *Computer Methods in Applied Mechanics and Engineering*, 200(9):1100–1112, February 2011.
- [47] L. De Lorenzis, Í. Temizer, P. Wriggers, and G. Zavarise. A large deformation frictional contact formulation using NURBS-based isogeometric analysis. *International Journal for Numerical Methods in Engineering*, 87(13):1278–1300, 2011.
- [48] Í. Temizer, P. Wriggers, and T. J. R. Hughes. Three-dimensional mortar-based frictional contact treatment in isogeometric analysis with NURBS. *Computer Methods in Applied Mechanics and Engineering*, 209-212:115–128, February 2012.
- [49] L. De Lorenzis, P. Wriggers, and G. Zavarise. A mortar formulation for 3D large deformation contact using NURBS-based isogeometric analysis and the augmented Lagrangian method. *Computational Mechanics*, 49(1):1–20, January 2012.
- [50] Y. Bazilevs, M.-C. Hsu, and M. A. Scott. Isogeometric fluidstructure interaction analysis with emphasis on non-matching discretizations, and with application to wind turbines. *Computer Methods in Applied Mechanics and Engineering*, 249-252:28–41, December 2012.
- [51] M.-C. Hsu and Y. Bazilevs. Fluidstructure interaction modeling of wind turbines: simulating the full machine. *Computational Mechanics*, 50(6):821–833, December 2012.
- [52] C. Hesch and P. Betsch. Isogeometric analysis and domain decomposition methods. *Computer Methods in Applied Mechanics and Engineering*, 213-216:104–112, March 2012.
- [53] A. Apostolatos, R. Schmidt, R. Wüchner, and K.-U. Bletzinger. A Nitsche-type formulation and comparison of the most common domain decomposition methods in isogeometric analysis. *InternApostolatosational Journal for Numerical Methods in Engineering*, 97(7):473–504, 2014.

- [54] V. P. Nguyen, P. Kerfriden, M. Brino, S. P. A. Bordas, and E. Bonisoli. Nitsches method for two and three dimensional NURBS patch coupling. *Computational Mechanics*, 53(6):1163–1182, June 2014.
- [55] M. Ruess, D. Schillinger, A. I. Özcan, and E. Rank. Weak coupling for isogeometric analysis of non-matching and trimmed multi-patch geometries. *Computer Methods in Applied Mechanics and Engineering*, 269:46–71, February 2014.
- [56] T. Nguyen, K. Karčiauskas, and J. Peters. A Comparative Study of Several Classical, Discrete Differential and Isogeometric Methods for Solving Poissons Equation on the Disk. *Axioms*, 3(2):280–299, June 2014.
- [57] M. Kapl, F. Buchegger, M. Bercovier, and B. Jttler. Isogeometric analysis with geometrically continuous functions on planar multi-patch geometries. *Computer Methods in Applied Mechanics and Engineering*, 316:209–234, April 2017.
- [58] A. Collin, G. Sangalli, and T. Takacs. Analysis-suitable G1 multi-patch parametrizations for C1 isogeometric spaces. *Computer Aided Geometric Design*, 47:93–113, October 2016.
- [59] D. Toshniwal, H. Speleers, and T. J. R. Hughes. Smooth cubic spline spaces on unstructured quadrilateral meshes with particular emphasis on extraordinary points: Geometric design and isogeometric analysis considerations. *Computer Methods in Applied Mechanics and Engineering*, 327:411–458, December 2017.
- [60] A. Blidia, B. Mourrain, and G. Xu. Geometrically smooth spline bases for data fitting and simulation. *Computer Aided Geometric Design*, 78:101814, March 2020.
- [61] S. E. Benzley. Representation of singularities with isoparametric finite elements. *International Journal for Numerical Methods in Engineering*, 8(3):537–545, 1974.
- [62] J. E. Akin. The generation of elements with singularities. *International Journal for Numerical Methods in Engineering*, 10(6):1249–1259, 1976.
- [63] T. N. Bittencourt, P. A. Wawrzynek, A. R. Ingraffea, and J. L. Sousa. Quasi-automatic simulation of crack propagation for 2D LEFM problems. *Engineering Fracture Mechanics*, 55(2):321–334, September 1996.
- [64] B. J. Carter, P. A. Wawrzynek, and A. R. Ingraffea. Automated 3-D crack growth simulation. *International Journal for Numerical Methods in Engineering*, 47(1-3):229–253, 2000.
- [65] T. Strouboulis, I. Babuška, and K. Copps. The design and analysis of the Generalized Finite Element Method. *Computer Methods in Applied Mechanics and Engineering*, 181(1):43–69, January 2000.
- [66] T. Strouboulis, K. Copps, and I. Babuška. The generalized finite element method: an example of its implementation and illustration of its performance. *International Journal for Numerical Methods in Engineering*, 47(8):1401–1417, 2000.

- [67] T. Strouboulis, K. Copps, and I. Babuška. The generalized finite element method. *Computer Methods in Applied Mechanics and Engineering*, 190(32):4081–4193, May 2001.
- [68] D. J. Benson, Y. Bazilevs, E. De Luycker, M.-C. Hsu, M. Scott, T. J. R. Hughes, and T. Belytschko. A generalized finite element formulation for arbitrary basis functions: From isogeometric analysis to XFEM. *International Journal for Numerical Methods in Engineering*, 83(6):765–785, 2010.
- [69] E. De Luycker, D. J. Benson, T. Belytschko, Y. Bazilevs, and M. C. Hsu. X-FEM in isogeometric analysis for linear fracture mechanics. *International Journal for Numerical Methods in Engineering*, 87(6):541–565, 2011.
- [70] S. S. Ghorashi, N. Valizadeh, and S. Mohammadi. Extended isogeometric analysis for simulation of stationary and propagating cracks. *International Journal for Numerical Methods in Engineering*, 89(9):1069–1101, 2012.
- [71] T. J. R. Hughes, L. P. Franca, and G. M. Hulbert. A new finite element formulation for computational fluid dynamics: VIII. The galerkin/least-squares method for advective-diffusive equations. *Computer Methods in Applied Mechanics and Engineering*, 73(2):173–189, May 1989.
- [72] M. J. Borden, C. V. Verhoosel, M. A. Scott, T. J. R. Hughes, and C. M. Landis. A phase-field description of dynamic brittle fracture. *Computer Methods in Applied Mechanics and Engineering*, 217-220:77–95, April 2012.
- [73] M. Ambati, T. Gerasimov, and L. De Lorenzis. Phase-field modeling of ductile fracture. *Computational Mechanics*, 55(5):1017–1040, May 2015.
- [74] M. Ambati, T. Gerasimov, and L. De Lorenzis. A review on phase-field models of brittle fracture and a new fast hybrid formulation. *Computational Mechanics*, 55(2):383–405, February 2015.
- [75] M. J. Borden, T. J. R. Hughes, C. M. Landis, and C. V. Verhoosel. A higher-order phase-field model for brittle fracture: Formulation and analysis within the isogeometric analysis framework. *Computer Methods in Applied Mechanics and Engineering*, 273:100–118, May 2014.
- [76] A. Tambat and G. Subbarayan. Isogeometric enriched field approximations. *Computer Methods in Applied Mechanics and Engineering*, 245-246:1–21, October 2012.
- [77] A. Tambat and G. Subbarayan. Simulations of arbitrary crack path deflection at a material interface in layered structures. *Engineering Fracture Mechanics*, 141:124–139, June 2015.
- [78] T. Song. *A sharp interface isogeometric strategy for moving boundary problems*. Ph.D. Thesis, Purdue University, 2016.
- [79] X. Y. Liu, Q. Z. Xiao, and B. L. Karihaloo. XFEM for direct evaluation of mixed mode SIFs in homogeneous and bi-materials. *International Journal for Numerical Methods in Engineering*, 59(8):1103–1118, 2004.
- [80] L. A. Piegl and W. Tiller. *The NURBS book*. Monographs in visual communication. Springer, 1997.

- [81] M. G. Cox. The Numerical Evaluation of B-Splines. *IMA Journal of Applied Mathematics*, 10(2):134–149, October 1972.
- [82] C. de Boor. On calculating with B-splines. *Journal of Approximation Theory*, 6(1):50–62, July 1972.
- [83] C. de Boor. *A practical guide to splines*. Applied mathematical sciences (Springer-Verlag New York Inc.) ; v. 27. Springer-Verlag, New York, 1978.
- [84] X. Zhang. *Constructive modeling strategies and implementation frameworks for optimal hierarchical synthesis*. Ph.D. Thesis, Purdue University, 2004.
- [85] M. Rayasam, V. Srinivasan, and G. Subbarayan. CAD inspired hierarchical partition of unity constructions for NURBS-based, meshless design, analysis and optimization. *International Journal for Numerical Methods in Engineering*, 72(12):1452–1489, 2007.
- [86] T. Song, K. Upreti, and G. Subbarayan. A sharp interface isogeometric solution to the Stefan problem. *Computer Methods in Applied Mechanics and Engineering*, 284:556–582, February 2015.
- [87] Y. Chen, C. Jois, and G. Subbarayan. Meshfree cad-cae integration through immersed b-rep model and enriched iso-geometric analysis. *Computer-Aided Design and Applications*, 17:1193–1214, 2020.
- [88] T. Belytschko, Y. Y. Lu, and L. Gu. Element-free Galerkin methods. *International Journal for Numerical Methods in Engineering*, 37(2):229–256, 1994.
- [89] A. Biswas and V. Shapiro. Approximate distance fields with non-vanishing gradients. *Graphical Models*, 66(3):133–159, May 2004.
- [90] A. W. Toga and B. A. Payne. Distance Field Manipulation of Surface Models. *IEEE Computer Graphics and Applications*, 12(01):65–71, January 1992.
- [91] K. Upreti, T. Song, A. Tambat, and G. Subbarayan. Algebraic distance estimations for enriched isogeometric analysis. *Computer Methods in Applied Mechanics and Engineering*, 280:28–56, October 2014.
- [92] K. Upreti and G. Subbarayan. Signed algebraic level sets on NURBS surfaces and implicit Boolean compositions for isogeometric CADCAE integration. *Computer-Aided Design*, 82:112–126, January 2017.
- [93] H. Liao, P. Vaitheeswaran, T. Song, and G. Subbarayan. Algebraic Point Projection for Immersed Boundary Analysis on Low Degree NURBS Curves and Surfaces. *Algorithms*, 13(4):82, April 2020.
- [94] M. P. Bendsøe. Optimal shape design as a material distribution problem. *Structural optimization*, 1(4):193–202, December 1989.
- [95] J. A. Sethian and A. Wiegmann. Structural Boundary Design via Level Set and Immersed Interface Methods. *Journal of Computational Physics*, 163(2):489–528, September 2000.
- [96] B. Bourdin and A. Chambolle. Design-dependent loads in topology optimization. *ESAIM: Control, Optimisation and Calculus of Variations*, 9:19–48, January 2003.

- [97] H. A. Eschenauer, V. V. Kobelev, and A. Schumacher. Bubble method for topology and shape optimization of structures. *Structural optimization*, 8(1):42–51, August 1994.
- [98] H.-Y. Lin. *Configurational optimization for optimal topological and fracture-resistant designs of solids*. Ph.D. Thesis, Purdue University, 2014.
- [99] H.-Y. Lin and G. Subbarayan. Optimal topological design through insertion and configuration of finite-sized heterogeneities. *International Journal of Solids and Structures*, 50(2):429–446, January 2013.
- [100] K. Dems and Z. Mróz. Variational approach by means of adjoint systems to structural optimization and sensitivity analysisII: Structure shape variation. *International Journal of Solids and Structures*, 20(6):527–552, January 1984.
- [101] J. S. Arora. An exposition of the material derivative approach for structural shape sensitivity analysis. *Computer Methods in Applied Mechanics and Engineering*, 105(1):41–62, May 1993.
- [102] The MathWorks Inc. Matlab 9.6.0 (r2019a). <https://www.mathworks.com>, 2019.
- [103] M. Spink, D. Claxton, C. de Falco, and R. Vázquez. The NURBS toolbox. <http://octave.sourceforge.net/nurbs/index.html>.
- [104] C. de Falco, A. Reali, and R. Vázquez. Geopdes: A research tool for isogeometric analysis of pdes. *Advances in Engineering Software*, 42(12):1020–1034, 2011.
- [105] S. Timoshenko and J. N. Goodier. *Theory of elasticity*. Engineering societies monographs. McGraw-Hill, New York, 2nd ed.. edition, 1951.
- [106] A. Seweryn and K. Molski. Elastic stress singularities and corresponding generalized stress intensity factors for angular corners under various boundary conditions. *Engineering Fracture Mechanics*, 55(4):529–556, November 1996.
- [107] Y. Luo and G. Subbarayan. A study of multiple singularities in multi-material wedges and their use in analysis of microelectronic interconnect structures. *Engineering Fracture Mechanics*, 74(3):416–430, February 2007.
- [108] T. L. Anderson. *Fracture mechanics : fundamentals and applications*. Taylor & Francis, Boca Raton, Fla., 3rd ed. edition, 2005.
- [109] M. E. Gurtin. *Configurational forces as basic concepts of continuum physics*. New York : Springer, New York, 2000.
- [110] M. E. Gurtin, E. Fried, and L. Anand. *The Mechanics and Thermodynamics of Continua*. Cambridge University Press, 2010.
- [111] P. Vaitheeswaran, A. Udupa, S. Sadasiva, and G. Subbarayan. Interface balance laws, phase growth and nucleation conditions for multiphase solids with inhomogeneous surface stress. *Continuum Mechanics and Thermodynamics*, 32(4):987–1010, July 2020.

- [112] P. Steinmann, D. Ackermann, and F. J. Barth. Application of material forces to hyperelastostatic fracture mechanics. II. Computational setting. *International Journal of Solids and Structures*, 38(32):5509–5526, August 2001.
- [113] R. Mueller and G. A. Maugin. On material forces and finite element discretizations. *Computational Mechanics*, 29(1):52–60, July 2002.
- [114] R. Mueller, S. Kolling, and D. Gross. On configurational forces in the context of the finite element method. *International Journal for Numerical Methods in Engineering*, 53(7):1557–1574, 2002.
- [115] R. Mueller, D. Gross, and G. A. Maugin. Use of material forces in adaptive finite element methods. *Computational Mechanics*, 33(6):421–434, May 2004.
- [116] N. K. Simha, F. D. Fischer, G. X. Shan, C. R. Chen, and O. Kolednik. J-integral and crack driving force in elasticplastic materials. *Journal of the Mechanics and Physics of Solids*, 56(9):2876–2895, September 2008.
- [117] O. Kolednik, J. Predan, N. Gubelj, and D. F. Fischer. Modeling fatigue crack growth in a bimaterial specimen with the configurational forces concept. *Materials Science and Engineering: A*, 519(1):172–183, August 2009.
- [118] O. Kolednik, J. Predan, and F. D. Fischer. Cracks in inhomogeneous materials: Comprehensive assessment using the configurational forces concept. *Engineering Fracture Mechanics*, 77(14):2698–2711, September 2010.
- [119] Y. G. Motlagh, W. M. Coombs, and R. de Borst. Isogeometric Configurational Force for Brittle Fracture. In *ECCM Proceedings*, Glasgow, UK, June 2018.
- [120] J. D. Eshelby and N. F. Mott. The force on an elastic singularity. *Philosophical Transactions of the Royal Society of London. Series A, Mathematical and Physical Sciences*, 244(877):87–112, November 1951.
- [121] J. D. Eshelby and R. E. Peierls. The determination of the elastic field of an ellipsoidal inclusion, and related problems. *Proceedings of the Royal Society of London. Series A. Mathematical and Physical Sciences*, 241(1226):376–396, August 1957.
- [122] G. A. Maugin. *Material inhomogeneities in elasticity*, volume 3. CRC Press, 1993.
- [123] C. Miehe, E. Gürses, and M. Birkle. A computational framework of configurational-force-driven brittle fracture based on incremental energy minimization. *International Journal of Fracture*, 145(4):245–259, June 2007.
- [124] C. Miehe and E. Gürses. A robust algorithm for configurational-force-driven brittle crack propagation with R-adaptive mesh alignment. *International Journal for Numerical Methods in Engineering*, 72(2):127–155, 2007.
- [125] M. Braun. Configurational forces induced by finite-element discretization. *Proceedings of the Estonian Academy of Sciences. Physics - Mathematics*, 46(1/2):24–31, 1997.
- [126] D. Gross, S. Kolling, R. Mueller, and I. Schmidt. Configurational forces and their application in solid mechanics. *European Journal of Mechanics - A/Solids*, 22(5):669–692, September 2003.

- [127] A.I. Sauter and W.D. Nix. Thermal stresses in aluminum lines bounded to substrates. *IEEE Transactions on Components, Hybrids, and Manufacturing Technology*, 15(4):594–600, August 1992.
- [128] T. Song, C.-P. Chen, G. Subbarayan, H. Lin, and S. Gurrum. Estimating the Modulus and Yield Strength of the Top-Layer Film on Multilayer BEOL Stacks. *IEEE Transactions on Device and Materials Reliability*, 18(3):438–449, September 2018.
- [129] Dassault Systèmes. SIMULIA ABAQUS R2017. <http://www.3ds.com/products-services/simulia/products/abaqus>, 2017.
- [130] M. Huang, Z. Suo, and Q. Ma. Plastic ratcheting induced cracks in thin film structures. *Journal of the Mechanics and Physics of Solids*, 50(5):1079–1098, May 2002.
- [131] C.-P. Chen, Y. Chen, and G. Subbarayan. Parametric stitching for smooth coupling of subdomains with non-matching discretizations. *Computer Methods in Applied Mechanics and Engineering*, 373:113519, 2021.
- [132] A. C. Fischer-Cripps. *Introduction to Contact Mechanics*. Springer Berlin / Heidelberg, Springer Berlin Heidelberg, Boston, MA, USA:Springer-Verlag, 2007.
- [133] W. C. Oliver and G. M. Pharr. An improved technique for determining hardness and elastic modulus using load and displacement sensing indentation experiments. *Journal of materials research*, 7(06):1564–1583, 1992.
- [134] J. S. Field and M. V. Swain. A simple predictive model for spherical indentation. *Journal of Materials Research*, 8(02):297–306, 1993.
- [135] M. F. Doerner and W. D. Nix. A method for interpreting the data from depth-sensing indentation instruments. *Journal of Materials Research*, 1(04):601–609, 1986.
- [136] R. B. King. Elastic analysis of some punch problems for a layered medium. *International Journal of Solids and Structures*, 23(12):1657–1664, 1987.
- [137] H. Gao, C.-H. Chiu, and J. Lee. Elastic contact versus indentation modeling of multi-layered materials. *International journal of Solids and Structures*, 29(20):2471–2492, 1992.
- [138] J. M. Antunes, J. V. Fernandes, L. F. Menezes, and B. M. Chaparro. A new approach for reverse analyses in depth-sensing indentation using numerical simulation. *Acta Materialia*, 55(1):69–81, 2007.
- [139] T. Song, G. Subbarayan, H.-Y. Lin, and S. Gurrum. Estimation of passivated metal stack modulus through simulations of micro-indentation. In *The Intersociety Conference on Thermal and Thermomechanical Phenomena in Electronic Systems (ITHERM)*, page 488. IEEE, 2016.
- [140] J. Menčík, D. Munz, E. Quandt, E. R. Weppelmann, and M. V. Swain. Determination of elastic modulus of thin layers using nanoindentation. *Journal of Materials Research*, 12(09):2475–2484, 1997.

- [141] D. Tabor. *The Hardness of Metals*. Monographs on the physics and chemistry of materials. Oxford, Clarendon Press, 1951.
- [142] M. Dao, N. v. Chollacoop, K. J. Van Vliet, T. A. Venkatesh, and S. Suresh. Computational modeling of the forward and reverse problems in instrumented sharp indentation. *Acta materialia*, 49(19):3899–3918, 2001.
- [143] J.-L. Bucaille, S. Stauss, E. Felder, and J. Michler. Determination of plastic properties of metals by instrumented indentation using different sharp indenters. *Acta materialia*, 51(6):1663–1678, 2003.
- [144] J. A. Knapp and D. M. Follstaedt. Mechanical properties of high strength aluminum alloys formed by pulsed laser deposition. In *MRS Proceedings*, volume 397, page 387. Cambridge Univ Press, 1995.
- [145] J. A. Knapp, D. M. Follstaedt, and S. M. Myers. Precipitate-hardened aluminum alloys formed using pulsed laser deposition. *Journal of applied physics*, 79(2):1116–1122, 1996.
- [146] J. A. Knapp, D. M. Follstaedt, J. C. Barbour, and S. M. Myers. Finite-element modeling of nanoindentation for determining the mechanical properties of implanted layers and thin films. *Nuclear Instruments and Methods in Physics Research Section B: Beam Interactions with Materials and Atoms*, 127:935–939, 1997.
- [147] J. A. Knapp, D. M. Follstaedt, J. C. Barbour, S. M. Myers, J. W. Ager, O. R. Monteiro, and I. G. Brown. Evaluating mechanical properties of thin layers using nanoindentation and finite-element modeling: Implanted metals and deposited layers. In *Proc. MRS*, volume 438, page 617, 1996.
- [148] J. A. Knapp, D. M. Follstaedt, S. M. Myers, J. C. Barbour, T. A. Friedmann, J. W. Ager, O. R. Monteiro, and I. G. Brown. Finite-element modeling of nanoindentation for evaluating mechanical properties of MEMS materials. *Surface and Coatings Technol.*, 103-104:268–275, May 1998.
- [149] J. A. Knapp, D. M. Follstaedt, S. M. Myers, J. C. Barbour, and T. A. Friedmann. Finite-element modeling of nanoindentation. *J. Appl. Phys.*, 85(3):1460–1474, 1999.
- [150] S. M. Myers, D. M. Follstaedt, J. A. Knapp, and T. R. Christenson. Hardening of nickel alloys by ion implantation of titanium and carbon. In *Proc. MRS*, volume 444, page 99. Cambridge Univ Press, 1996.
- [151] S. M. Myers, J. A. Knapp, D. M. Follstaedt, and M. T. Dugger. Mechanical properties of nickel ion-implanted with titanium and carbon and their relation to microstructure. *J. Appl. Phys.*, 83(3):1256–1264, 1998.
- [152] T. A. Friedmann, J. P. Sullivan, J. A. Knapp, D. R. Tallant, D. M. Follstaedt, D. L. Medlin, and P. B. Mirkarimi. Thick stress-free amorphous-tetrahedral carbon films with hardness near that of diamond. *Appl. Phys. Lett.*, 71(26):3820–3822, 1997.
- [153] Y. Du, T. Xu, T. M. Shaw, X. Hu Liu, G. Bonilla, H. Li, and H. Lu. A novel tri-layer nanoindentation method to measure the mechanical properties of a porous brittle ultra-low-k dielectric thin film. *Extreme Mech. Lett.*, 13:100–107, 2017.

- [154] Y.-T. Cheng and C.-M. Cheng. Can stress–strain relationships be obtained from indentation curves using conical and pyramidal indenters? *J. Mater. Res.*, 14(9):3493–3496, 1999.
- [155] J. Alkorta, J. M. Martinez-Esnaola, and J. G. Sevillano. Absence of one-to-one correspondence between elastoplastic properties and sharp-indentation load–penetration data. *J. Mater. Res.*, 20(02):432–437, 2005.
- [156] X. Chen, N. Ogasawara, M. Zhao, and N. Chiba. On the uniqueness of measuring elastoplastic properties from indentation: The indistinguishable mystical materials. *J. Mech. Phys. Solids*, 55(8):1618–1660, 2007.
- [157] H. Hertz. On the contact of elastic solids. *J. Reine Angew. Math*, 92(110):156–171, 1881.
- [158] J.-H. Zhao, T. Ryan, P. S Ho, A. J. McKerrow, and W.-Y. Shih. Measurement of elastic modulus, Poisson ratio, and coefficient of thermal expansion of on-wafer submicron films. *J. Appl. Phys.*, 85(9):6421–6424, 1999.
- [159] M. A. Hopcroft, W. D. Nix, and T. W. Kenny. What is the Young’s modulus of silicon? *J. Microelectromech. Syst.*, 19(2):229–238, 2010.
- [160] G. Simmons and H. Wang. *Single crystal elastic constants and calculated aggregate properties: a handbook*. Cambridge, Mass., 2d ed. edition, 1971.
- [161] A. Reddy, H. Kahn, and A. H. Heuer. A MEMS-based evaluation of the mechanical properties of metallic thin films. *J. Microelectromech. Syst.*, 16(3):650–658, 2007.
- [162] J. J. Vlassak and W. D. Nix. A new bulge test technique for the determination of Young’s modulus and Poisson’s ratio of thin films. *J. Mater. Res.*, 7(12):3242–3249, 1992.
- [163] M. Mata and J. Alcalá. The role of friction on sharp indentation. *J. Mech. Phys. Solids*, 52(1):145–165, 2004.
- [164] N. A. Sakharova, J. V. Fernandes, J. M. Antunes, and M. C. Oliveira. Comparison between Berkovich, Vickers and conical indentation tests: A three-dimensional numerical simulation study. *Int. J. Solids Struct.*, 46(5):1095–1104, 2009.
- [165] A. Van der Velden and D. Kokan. The synaps pointer optimization engine. In *Proc. Int. Design Eng. Tech. Conf. Comput. Inf. Eng. Conf. (ASME)*, pages 159–165, 2002.
- [166] S. J. Souri, K. Banerjee, A. Mehrotra, and K. C. Saraswat. Multiple Si layer ICs: motivation, performance analysis, and design implications. In *Proceedings of the 37th Annual Design Automation Conference, DAC ’00*, pages 213–220, New York, NY, USA, June 2000. Association for Computing Machinery.
- [167] S. S. Sapatnekar. Addressing thermal and power delivery bottlenecks in 3D circuits. In *2009 Asia and South Pacific Design Automation Conference*, pages 423–428, January 2009.

- [168] J. Cong and Y. Zhang. Thermal via planning for 3-D ICs. In *ICCAD-2005. IEEE/ACM International Conference on Computer-Aided Design, 2005.*, pages 745–752, November 2005.
- [169] B. Goplen and S. Sapatnekar. Thermal via placement in 3D ICs. In *Proceedings of the 2005 international symposium on Physical design, ISPD '05*, pages 167–174, New York, NY, USA, April 2005. Association for Computing Machinery.
- [170] H. Yu, Y. Shi, L. He, and T. Karnik. Thermal Via Allocation for 3-D ICs Considering Temporally and Spatially Variant Thermal Power. *IEEE Transactions on Very Large Scale Integration (VLSI) Systems*, 16(12):1609–1619, December 2008.
- [171] J. Knechtel, I. L. Markov, J. Lienig, and M. Thiele. Multiobjective optimization of deadspace, a critical resource for 3D-IC integration. In *Proceedings of the International Conference on Computer-Aided Design, ICCAD '12*, pages 705–712, New York, NY, USA, November 2012. Association for Computing Machinery.
- [172] R. Bazaz, J. Xie, and M. Swaminathan. Optimization of 3D stack for electrical and thermal integrity. In *2013 IEEE 63rd Electronic Components and Technology Conference*, pages 22–28, May 2013.
- [173] S. Mohanram, D. Brenner, and D. Kudithipudi. Hierarchical optimization of TSV placement with inter-tier liquid cooling in 3D-IC MPSoCs. In *29th IEEE Semiconductor Thermal Measurement and Management Symposium*, pages 7–12, March 2013.
- [174] P. Budhathoki, A. Henschel, and I. A. M. Elfadel. Thermal-driven 3D floorplanning using localized TSV placement. In *2014 IEEE International Conference on IC Design Technology*, pages 1–4, May 2014.
- [175] T. Borrvall and J. Petersson. Large-scale topology optimization in 3D using parallel computing. *Computer Methods in Applied Mechanics and Engineering*, 190(46):6201–6229, September 2001.
- [176] T. A. Davis. Algorithm 849: A concise sparse Cholesky factorization package. *ACM Transactions on Mathematical Software*, 31(4):587–591, December 2005.
- [177] M. P. Bendsøe and O. Sigmund. *Topology Optimization: Theory, Methods, and Applications*. Springer Berlin / Heidelberg, Springer Berlin Heidelberg, Berlin, Heidelberg, second edition, corrected printing. edition, 2003.

APPENDICES

A. TENSOR TRANSFORMATION

Assume two coordinate systems spanned by the unit vectors \hat{e}'_i and \hat{e}_j . Cartesian tensors transform from one coordinate system to another based on the following relation:

$$\text{arbitrary order tensor: } g'_{ijk\dots m} = t_{ia}t_{jb}t_{kc}\cdots t_{me}g_{abc\dots e}$$

where, $t_{ij} = \hat{e}'_i \cdot \hat{e}_j$ is the direction cosine between the primed and the unprimed systems. In mechanical systems, tensors are used to represent various of physical quantities. Displacements, stresses, and stiffness are examples of first, second and fourth order tensors, respectively. Their transformation follows the above general form given by

$$\text{1st order tensor: } v'_i = t_{im}v_m$$

$$\text{2nd order tensor: } s'_{ij} = t_{im}t_{jn}s_{mn}$$

$$\text{4th order tensor: } c'_{ijkl} = t_{im}t_{jn}t_{kp}t_{lq}c_{mnpq}$$

The transformation of tensors may also be expressed as matrix-vector or matrix-matrix multiplications. In general, vector notation can be used to represent first order tensors while matrix notation is convenient for representing second order tensors. The transformed components of a first order tensor \mathbf{v} and a second order tensor \mathbf{S} may be expressed in matrix-vector notation as:

$$\{v'\} = [T]\{v\}$$

$$[S'] = [T][S][T]^T$$

where, $[T]$ is the transformation matrix formed by direction cosines t_{ij} . In the present study, a needed transformation is between rectangular cartesian coordinates and polar

coordinates. The transformation matrix is orthogonal in nature with $[T]^T = [T]^{-1}$ as shown below.

$$\begin{Bmatrix} \hat{\mathbf{e}}_r \\ \hat{\mathbf{e}}_\theta \\ \hat{\mathbf{e}}_z \end{Bmatrix} = \begin{bmatrix} \cos\theta & \sin\theta & 0 \\ -\sin\theta & \cos\theta & 0 \\ 0 & 0 & 1 \end{bmatrix} \begin{Bmatrix} \hat{\mathbf{e}}_x \\ \hat{\mathbf{e}}_y \\ \hat{\mathbf{e}}_z \end{Bmatrix}$$

$$\begin{Bmatrix} \hat{\mathbf{e}}_x \\ \hat{\mathbf{e}}_y \\ \hat{\mathbf{e}}_z \end{Bmatrix} = \begin{bmatrix} \cos\theta & -\sin\theta & 0 \\ \sin\theta & \cos\theta & 0 \\ 0 & 0 & 1 \end{bmatrix} \begin{Bmatrix} \hat{\mathbf{e}}_r \\ \hat{\mathbf{e}}_\theta \\ \hat{\mathbf{e}}_z \end{Bmatrix}$$

A.1 Transformation of Symmetric Tensor in Voigt Form

Transformation of symmetric tensors can be re-written in a more compact manner as described below. Symmetric tensors such as Cauchy stress and strain are typically represented in Voigt notation for the purpose of computational efficiency. Given a Cauchy stress tensor with elements σ_{ij} , its Voigt form $\boldsymbol{\sigma}_V$ is obtained by condensing the unique stress components into a vector.

$$\boldsymbol{\sigma}_V = [\sigma_{11}, \sigma_{22}, \sigma_{33}, \sigma_{12}, \sigma_{23}, \sigma_{13}]^T$$

Typically, Cauchy stress in matrix form is transformed as $[\sigma'] = [T][\sigma][T]^T$ by serial matrix-matrix multiplications. With the same stress re-written in Voigt form as defined above, the transformation can be reduced into a matrix-vector multiplication of the form:

$$\boldsymbol{\sigma}'_V = \mathbf{T}_\sigma \boldsymbol{\sigma}_V$$

where \mathbf{T}_σ is the reduced transformation matrix whose elements are obtained by comparing the coefficients. The reduced transformation matrix expressed using the direction cosines between two coordinate systems t_{ij} is

$$\mathbf{T}_\sigma = \begin{bmatrix} t_{11}t_{11} & t_{12}t_{12} & t_{13}t_{13} & 2t_{11}t_{12} & 2t_{12}t_{13} & 2t_{13}t_{11} \\ t_{21}t_{21} & t_{22}t_{22} & t_{23}t_{23} & 2t_{21}t_{22} & 2t_{22}t_{23} & 2t_{23}t_{21} \\ t_{31}t_{31} & t_{32}t_{32} & t_{33}t_{33} & 2t_{31}t_{32} & 2t_{32}t_{33} & 2t_{33}t_{31} \\ t_{11}t_{21} & t_{12}t_{22} & t_{13}t_{23} & (t_{11}t_{22} + t_{12}t_{21}) & (t_{12}t_{23} + t_{13}t_{22}) & (t_{13}t_{21} + t_{11}t_{23}) \\ t_{21}t_{31} & t_{22}t_{32} & t_{23}t_{33} & (t_{21}t_{32} + t_{22}t_{31}) & (t_{22}t_{33} + t_{23}t_{32}) & (t_{23}t_{31} + t_{21}t_{33}) \\ t_{31}t_{11} & t_{32}t_{12} & t_{33}t_{13} & (t_{31}t_{12} + t_{32}t_{11}) & (t_{32}t_{13} + t_{33}t_{12}) & (t_{33}t_{11} + t_{31}t_{13}) \end{bmatrix}$$

The above stress transformation leading to the reduced transformation matrix can be applied analogously for the strain tensor. Given a strain tensor with elements ε_{ij} , the strain can be represented in Voigt form as

$$\boldsymbol{\varepsilon}_V = [\varepsilon_{11}, \varepsilon_{22}, \varepsilon_{33}, \gamma_{12}, \gamma_{23}, \gamma_{13}]^T$$

where $\gamma_{ij} = 2\varepsilon_{ij}$ is the engineering shear strain component. The transformed strain is $\boldsymbol{\varepsilon}'_V = \mathbf{T}_\varepsilon \boldsymbol{\varepsilon}_V$ with the associated reduced transformation matrix given by

$$\mathbf{T}_\varepsilon = \begin{bmatrix} t_{11}t_{11} & t_{12}t_{12} & t_{13}t_{13} & t_{11}t_{12} & t_{12}t_{13} & t_{13}t_{11} \\ t_{21}t_{21} & t_{22}t_{22} & t_{23}t_{23} & t_{21}t_{22} & t_{22}t_{23} & t_{23}t_{21} \\ t_{31}t_{31} & t_{32}t_{32} & t_{33}t_{33} & t_{31}t_{32} & t_{32}t_{33} & t_{33}t_{31} \\ 2t_{11}t_{21} & 2t_{12}t_{22} & 2t_{13}t_{23} & (t_{11}t_{22} + t_{12}t_{21}) & (t_{12}t_{23} + t_{13}t_{22}) & (t_{13}t_{21} + t_{11}t_{23}) \\ 2t_{21}t_{31} & 2t_{22}t_{32} & 2t_{23}t_{33} & (t_{21}t_{32} + t_{22}t_{31}) & (t_{22}t_{33} + t_{23}t_{32}) & (t_{23}t_{31} + t_{21}t_{33}) \\ 2t_{31}t_{11} & 2t_{32}t_{12} & 2t_{33}t_{13} & (t_{31}t_{12} + t_{32}t_{11}) & (t_{32}t_{13} + t_{33}t_{12}) & (t_{33}t_{11} + t_{31}t_{13}) \end{bmatrix}$$

The use of reduced transformation matrix results in computational efficiency by converting the matrix-matrix multiplications into a matrix-vector multiplication. The benefit is significant when transformation is needed at each quadrature point during stiffness matrix assembly. Note the difference between \mathbf{T}_σ and \mathbf{T}_ε due to the

use of engineering shear strain in the Voigt notation for shear strain. For the inverse transformation from the primed system to the unprimed system, one simply needs to invert the reduced transformation matrix using the Gaussian elimination.

B. MATERIAL PROPERTIES

The temperature-dependent material properties of the die attach and mold compound are shown in Tables B.1 and B.2, respectively. Note these properties are described in a piece-wise linear form and do not consider viscoelasticity.

Table B.1.

Temperature-dependent elastic properties of die attach.

Temperature(°C)	E (GPa)	ν	α (ppm/°C)
-65	10	0.35	50
75	10	0.35	50
125	0.5	0.35	100
260	0.5	0.35	100

Table B.2.

Temperature-dependent elastic properties of mold compound.

Temperature(°C)	E (GPa)	ν	α (ppm/°C)
-65	30	0.35	10
85	30	0.35	10
115	1	0.35	40
260	1	0.35	40

C. ESTIMATING THE MODULUS AND YIELD STRENGTH OF THE TOP-LAYER FILM ON MULTILAYER BEOL STACKS

The manufacturing process-caused variation in the modulus and the yield strength of individual layers in passivated metal stacks critically impacts the reliability of Back-End-of-Line (BEOL) structures. However, experimentally characterizing the elastic modulus and yield strength of thin films as fabricated, with sufficient sensitivity to distinguish process-induced property variations, remains a significant challenge. Towards this end, we utilize nanoindentation experiments to estimate the elastic modulus and yield strength of top-layer films in multilayer stacks. To address the challenge of extracting individual layer modulus from the composite modulus, in the present paper, we propose a depth-dependent mathematical model (dominant regime theory) by which the modulus of the top-layer can be estimated accurately. Additionally, we employ optimization-based inverse finite element analysis (IFEA) to numerically estimate the modulus and the yield strength of the top-layer film. The uniqueness of the properties estimated by IFEA is investigated through a full-factorial statistically designed numerical experiment. The developed techniques are demonstrated by estimating the modulus as well as the yield strength of tetraethylorthosilicate (TEOS) film on a two-layer stack (TEOS, Silicon) and the same film deposited on a multilayer stack (TEOS, Aluminum, Silicon Nitride, Silicon).

C.1 Introduction

As the microelectronics industry transitions to the fabless business model where device-level fabrication is carried out by outside vendors, and as integrators opt to fabricate the same device through multiple vendors, there is a critical need to assess the mechanical property of structures on the fabricated device, and to assess the

variation in the property from vendor to vendor. The Back-End-of-Line (BEOL) metal stack and its associated dielectric layer, often subject to large thermal stresses due to mismatch in the coefficient of thermal expansion (CTE) of the various layers, is an important structure that needs such an assessment. Among the key properties that influence the integrity of the BEOL stack in general, and thermal stresses in particular, are the moduli and yield strengths of the metal and the dielectric materials. The determination of the multilayer stack modulus as well as the extraction of modulus and yield strength of individual film, accurate enough to detect variation caused by manufacturing process, remains a significant challenge.

The micro- or nano-indentation technique has been widely used to characterize thin films. The technique has the advantage of not needing free-standing test specimen as well as advanced microscopy equipment. The quick and inexpensive test procedure is an additional advantage of this technique [132].

Traditional analysis of indentation load-displacement response is mostly focused on estimating the mechanical properties of a single homogeneous material. The elastic modulus of homogeneous materials has been well characterized using single low-depth indentation tests [133, 134]. However, a multi-depth indentation becomes necessary when there is a need to extract the modulus of thin films on composite stacks. In a multi-depth indentation procedure, the film modulus is determined by evaluating the effective modulus at various penetration depths and then by extrapolating the modulus to zero penetration. There exist many analytical models to describe the relationship between effective modulus and penetration depth or contact radius [135–138] for a two-layer stack ($n_{layer} = 2$, i.e., a film coating on a substrate), but models for multilayer stacks ($n_{layer} \geq 3$) are largely missing in the literature due to the complex interaction between different layers. Gao [137] is among the few to model the response of a multilayer stack. His model was of indentation of a stack by a cylindrical punch. However, the developed model depends nonlinearly on the contact radius and therefore can not be transformed into a univariate linear form for straight-forward regression analysis. Recently, the authors [139] proposed two regression strategies

(direct regression on the elastic modulus and regression on the reciprocal of the modulus) to estimate the elastic modulus of the top-most film in a stack. The study showed that regression on depth-dependent response yields more accurate property values than a single low-depth indentation; the fit was also less sensitive to errors in estimated values due to material pile-up.

The estimate of the film modulus is also influenced by the thickness of each layer, in addition to the number of layers. Due to the fact that under low penetration depths, the stack modulus is strongly dependent on the top-most film behavior, many studies [135, 138, 140] have estimated the top-most film modulus using shallow indentation. Antunes et al. [138] suggested an empirical, film thickness dependent penetration range for this purpose. But, analytical, easy-to-use models to estimate the optimal penetration depth as well as to quantitatively model the contributions of different layers to the effective modulus is largely missing in the literature.

In this paper, we propose a mathematical model (dominant regime theory) to describe the influence of the number and thickness of the films on the effective modulus, as a function of the indentation depth. Employing the dominant regime theory, we estimate the optimal range of indentation depth so that the elastic modulus of the top-most film is characterized accurately. The technique is first demonstrated by estimating the film modulus in a two-layer stack. Next, we utilize the technique to estimate the modulus of the same film deposited on a multilayer stack. It is demonstrated that indentation in the dominant regime is critical to the accuracy of the estimated parameter value.

Methods for estimating the yield strength of bulk metal through indentation is well established at the present time, for instance, the empirical relationship between yield strength and hardness of ductile materials proposed by Tabor [141]. Unlike the elastic behavior, closed-form elastic-plastic analytical model for multilayer structures does not currently exist due to the complex elastic-plastic load sharing between multiple layers during indentation. Hence, semi-analytical or numerical methods are necessary to characterize yield strengths of films. To avoid detailed elastic-plastic fi-

nite element simulations, dimensional analysis of sharp indentation was used in prior studies [142, 143] to extract dimensionless functions that enable estimation of mechanical properties given the indentation data. However, such functions are generally not valid for multilayer stacks.

Numerical studies using the finite element method (FEM), on the other hand, possess the flexibility to be applied to arbitrary multilayer stacks. A series of studies by Knapp et al. [144–149], Myres et al. [150, 151] and Friedmann et al. [152] used FEM to extract modulus, yield strength and intrinsic hardness for various types of thin films deposited on substrates. In their studies, the properties were estimated by finding the best-fit simulation to the experiment through incremental interpolation of properties. Recently Du et al. [153] also estimated the elastic properties of ultra low-k (ULK) dielectric films through indentation of a tri-layer specimen as well as inverse property estimation using FEM. In [153] the numerical fit using the finite element model was to the load-displacement response during the loading stage of indentation.

In the present study, we develop two novel procedures that enable one to estimate the mechanical properties of top-layer films in multilayer stacks. The first is the development of the “dominant regime” theory that enables one to identify the indentation depths over which a particular layer’s influence dominates. The second contribution is a numerical fitting procedure based on a rigorous application of non-linear optimization algorithms using inverse finite element analyses (IFEAs) to both the loading *and* unloading response during indentation. Arguably, the elastic-plastic response of films cannot be accurately estimated without fits to both the loading and the unloading responses. Using the developed procedure, we estimate the elastic modulus and yield strength of the top layer TEOS film in a stack. The technique is first applied to a two-layer stack with the same top layer film as in a multilayer stack to estimate the elastic modulus of the top layer without considering the buried metal film. Then, the yield strength of the top film in a multilayer stack is estimated.

In general, the existence of a unique relationship between the material’s elastic-plastic properties and macroscopic load-displacement response is often the biggest

concern when fitting data to indentation tests [154–156]. Therefore, to verify the uniqueness of fitted parameters, first, the optimization is carried out from multiple initial points in the parameter space. In addition, full-factorial statistically designed experiments are performed over the parameter space spanned by elastic modulus and yield strength to further validate the uniqueness of the estimated properties.

The rest of this paper is organized as follows. Section C.2 describes the classical indentation models and the newly proposed dominant regime theory. Section C.3 deals with the application of the developed analytical model to the experimental data on two-layer samples. The optimization-based inverse finite element analysis technique and the details of the corresponding finite element models are described in Section C.4. In Section C.5, the IFEA is applied to a multilayer stack to estimate the yield strength of the top layer of the stack. Finally, conclusions are drawn in Section C.6.

C.2 Theory

A typical indentation of a flat specimen surface is illustrated in Figure C.1 [132]. The loading process leads to an initial elastic response at low loads followed by elastic-plastic deformation at higher loads. After full elastic unloading through a distance, there remains an impression of depth due to plastic deformation.

C.2.1 Classical Indentation Models for Homogeneous Materials

Hertz [157] derived the load-displacement relationship of non-adhesive elastic contact given by the equation

$$P = \frac{4}{3}E^*R^{0.5}h_e^{1.5} \quad (\text{C.1})$$

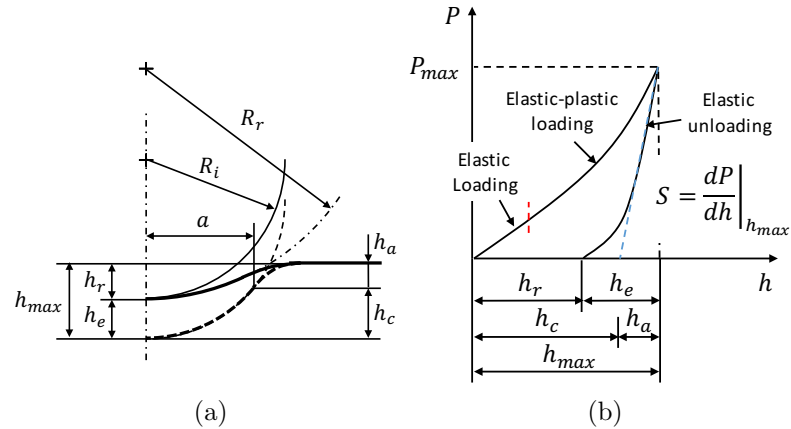


Figure C.1. (a) Schematic of indentation using spherical indenter. The thick dashed line indicates the specimen surface under maximum load whereas the thick solid line is the residual impression after unloading. (b) Typical load-displacement response with three regimes.

where, P is the applied load, h_e is the elastic displacement and R is the relative radius between spherical indenter R_i and residual impression R_r . E^* is often referred as reduced Young's modulus defined by

$$\frac{1}{E^*} = \frac{1 - \nu^2}{E} + \frac{1 - \nu_i^2}{E_i} \quad (\text{C.2})$$

where, E , E_i , ν and ν_i are the Young's modulus and Poisson's ratio of the specimen and indenter tip, respectively.

Oliver and Pharr [133] proposed a multiple-point unload method to determine the reduced elastic modulus using the initial slope of the unloading curve as follows:

$$E^* = \frac{dP}{dh} \frac{1}{2a} = \frac{1}{2} \frac{dP}{dh} \frac{\sqrt{\pi}}{\sqrt{A}} \quad (\text{C.3})$$

where, a is the contact radius as shown in Figure C.1a and $A = \pi a^2$. Note that the Eq. (C.3) can be generalized to non-spherical indenters, in which case the A is the

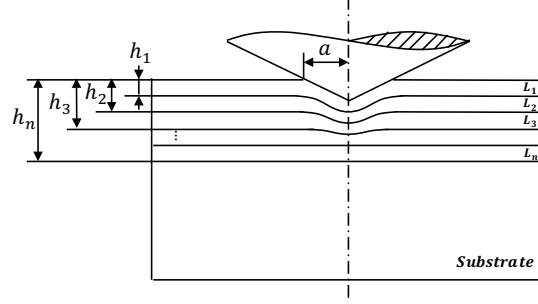


Figure C.2. Schematic of a rigid Berkovich indenter penetrating a multilayer stack consisting of a n -layer film and a substrate. L_k , $k = 1, 2, \dots, n$ represents the k^{th} layer of the stack.

projected contact area depending on the indenter tip geometry, and a is the effective contact radius given by

$$a = \sqrt{\frac{A}{\pi}} \quad (\text{C.4})$$

C.2.2 Effective Modulus of Multilayer Stacks

In the case of multilayer stacks, the elastic modulus computed by Eqs. (C.2) and (C.3) is an effective modulus of the composite (i.e., of the indenter, films, and the substrate), and is therefore a function of the total indentation depth h_{max} or effective contact radius a . For the elastic contact of a rigid indenter with a semi-infinite multilayer stack (Figure C.2), Gao et al. [137] developed a closed-form solution to the effective modulus as follows:

$$E = \Phi_0 \left(\frac{a}{h_1} \right) E_1 + \sum_{k=2}^n \left[\Phi_0 \left(\frac{a}{h_k} \right) - \Phi_0 \left(\frac{a}{h_{k-1}} \right) \right] E_k + \left[1 - \Phi_0 \left(\frac{a}{h_n} \right) \right] E_s \quad (\text{C.5})$$

where, E_s and E_k are the Young's modulus of substrate and the k^{th} -layer film, respectively. The weight function Φ_0 is of the form:

$$\begin{aligned} \Phi_0(x) &= \frac{2}{\pi} \arctan \frac{1}{x} + \frac{1}{2\pi(1-\nu)} \\ &\times \left[\frac{1-2\nu}{x} \ln(1+x^2) - \frac{x}{1+x^2} \right] \end{aligned} \quad (\text{C.6})$$

As illustrated in Figure C.3 and rigorously shown in Appendix C.7, the weight function is a monotonically decreasing function starting from a value of unity. Since $\lim_{a \rightarrow 0^+} E = E_1$, the top-layer modulus can be extracted by extrapolating the effective modulus to zero penetration. However, the original form of Eq. (C.5) is inconvenient to use for this purpose due to two reasons:

1. When only the substrate and a single film layer are present, Eq. (C.5) reduces to the simpler form $E = \Phi_0\left(\frac{a}{h_1}\right) E_1 + \left(1 - \Phi_0\left(\frac{a}{h_1}\right)\right) E_2 = E_2 + (E_1 - E_2)\Phi_0\left(\frac{a}{h_1}\right)$. However, this form is nonlinearly dependent on contact radius. The form is significantly more complex if the stack has more than two layers (i.e., substrate and more than one film). The effective modulus is then a complex nonlinear function of unknown film moduli and contact radius.
2. The weight function $\Phi_0(x)$ also depends on the Poisson's ratio (Figure C.3), which is often time unknown.

To circumvent these problems, we linearize Eq. (C.6) as follows:

$$\Phi_0(x) = 1 - \frac{2-\nu}{\pi(1-\nu)}x + O(x^3) \approx 1 - kx \quad \text{for } x < 1 \quad (\text{C.7})$$

The linearization procedure is shown in Appendix C.8. Interestingly, the quadratic term vanishes in the Maclaurin series. This suggests that $\Phi_0(x)$ possesses a good

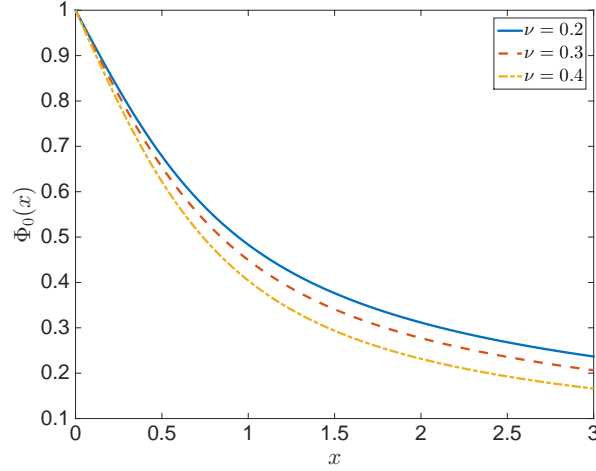


Figure C.3. The weight function Φ_0 with different Poisson's ratios.

linearity when $x < 1$, which can be also observed in Figure C.3. Substituting Eq. (C.7) into Eq. (C.5), we obtain

$$\begin{aligned}
 E &\approx E_1 + \left[-\frac{E_1}{h_1} + \sum_{k=2}^n \left(\frac{E_k}{h_{k-1}} - \frac{E_k}{h_k} \right) + \frac{E_s}{h_n} \right] ka \\
 &= c_1 + c_2 a
 \end{aligned} \tag{C.8}$$

The linearized form suggests that the top-layer modulus E_1 of a multilayer stack can be thus determined by fitting Eq. (C.8) to the effective modulus measured from multiple penetration depths. The regression using Eq. (C.8) possesses another advantage in that the Poisson's ratio is not needed *a priori*. To obtain better fits, we had also earlier considered [139] the following heuristic reciprocal form for the elastic modulus of the top layer in multilayer stacks:

$$\frac{1}{E} = c_1 + c_2 a \tag{C.9}$$

The higher order term $O(x^3)$ in Eq. (C.7) is not negligible when $x > 1$, i.e., when $\frac{a}{h_k} > 1$. Therefore, if the indentation depth is large leading to $a > h_1$, the

effective modulus will manifest a non-linear behavior, which necessitates a non-linear regression. Several heuristic regression functions of such kind are reported in the literature [135, 136, 138, 140] to estimate the film modulus of two-layer stacks.

C.2.3 Dominant Regime Theory

The mathematical model derived by Gao (Eq. (C.5)) reveals that all films contribute to the effective modulus. In order to estimate the elastic modulus of a specific film accurately, there is a critical need to quantitatively identify the contribution of each layer and to increasing the contribution of the layer of interest by identifying the appropriate indentation depth. To this end, we rewrite Eq. (C.5) as

$$E = \sum_{k=1}^{n+1} N_k(a) E_k \quad (\text{C.10})$$

where, $E_k, k = 1, 2, \dots, n$ is the elastic modulus of the k^{th} -layer film and $E_{n+1} = E_s$ is the substrate modulus. The new function $N_k(a)$ is given by

$$N_k(a) = \begin{cases} \Phi_0\left(\frac{a}{h_1}\right) & k = 1 \\ \Phi_0\left(\frac{a}{h_k}\right) - \Phi_0\left(\frac{a}{h_{k-1}}\right) & k = 2, 3, \dots, n \\ 1 - \Phi_0\left(\frac{a}{h_n}\right) & k = n + 1 \end{cases} \quad (\text{C.11})$$

The function space $\{N_k\}$ satisfies the following properties:

1. Non-negativity, i.e., $N_k \geq 0, k = 1, 2, \dots, n + 1$
2. Partition of unity, i.e., $\sum_{k=1}^{n+1} N_k = 1$
3. Linear independence

The first property indicates that each film has a non-negative contribution to the composite modulus whereas the second property implies that the effective modulus would always fall in the range $[\min_k\{E_k\}, \max_k\{E_k\}]$. The first two properties of N_k are relatively straightforward to prove (see Appendix C.9). The function N_k is thus

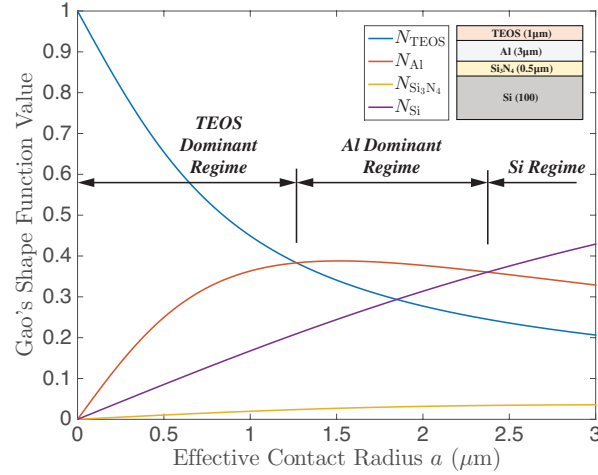


Figure C.4. Modulus participation functions of a TEOS-Al-Si₃N₄-Si multilayer stack.

termed here as the *Modulus Participation Function*. An example of modulus participation functions for a TEOS-Al-Si₃N₄-Si multilayer stack is illustrated in Figure C.4.

The *dominant regime* of a film/substrate is defined as a region where the associated modulus participation function is the largest among all functions. It can be observed in Figure C.4 that the dominant regime transitions from TEOS to Al to Si as the contact radius increases. There is no dominant regime for Si₃N₄ due to its small thickness (0.5 μm). We can extract the modulus of a film/substrate using the data within its dominant regime to minimize the influence of the other layers.

The top-layer dominant regime length of a two-layer stack can be estimated by equating the modulus participation functions of the film and the substrate:

$$\Phi_0 \left(\frac{a}{h_1} \right) = 1 - \Phi_0 \left(\frac{a}{h_1} \right) \quad (\text{C.12})$$

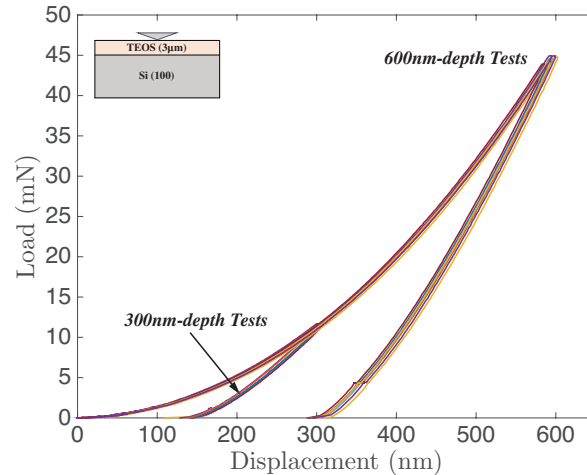


Figure C.6. Load-displacement response of the TEOS-Si two-layer stack at 300 nm and 600 nm penetration depths. Nine tests were carried-out at each depth.

C.3.1 Two-Layer Stack

A representative, experimentally obtained, load-displacement response of the TEOS-Si two-layer stack (Figure C.5a) corresponding to indentation depths of 300 nm and 600 nm is shown in Figure C.6. The large elastic recovery in the curves implies a high yield strength of TEOS. In addition, no macroscale cracking event was observed during indentation visually or in the load-displacement response.

The modulus participation functions for the two-layer stack are plotted in Figure C.7. Since the experimental indentation range is contained well within the TEOS dominant regime, we can use the data from all the test depths to estimate the TEOS modulus. The multi-depth indentation data is plotted in Figure C.8, where we can observe that the effective modulus varies linearly versus the contact radius consistent with the approximation of Eq. (C.7). Thus, the elastic modulus E_{TEOS} was estimated using the linear function (Eq. (C.8)) and the empirical reciprocal form (Eq. (C.9)). The estimated modulus values are summarized and compared against a reference value in Table C.1. The first column in the table corresponds to a single shallow

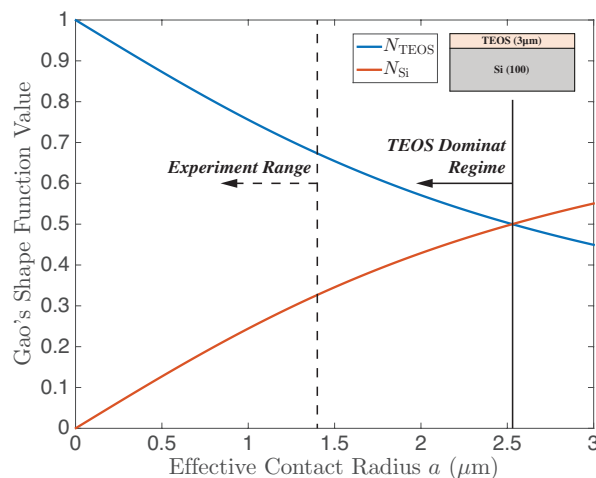


Figure C.7. Modulus participation functions of the TEOS-Si two-layer stack.

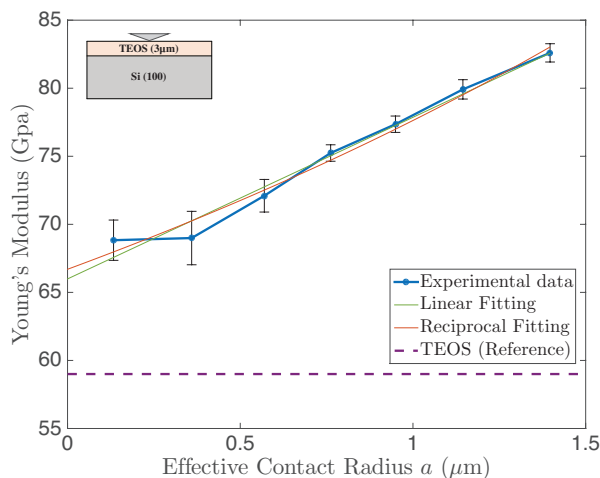


Figure C.8. Multi-depth indentation data for the TEOS-Si two-layer stack.

indent at 100 nm (as is commonly the practice) to contrast to values obtained from regression on multiple indents carried out at various depths. Both the linear as well as the reciprocal regression functions fit well to the experimental data and produce a result of approximately 66 GPa for the elastic modulus of TEOS.

Table C.1.
TEOS modulus extracted from the TEOS-Si two-layer specimen.

	100 nm	Regression Analysis		Ref. [158]
		Linear	Reciprocal	
E_{TEOS} (GPa)	68.8	66.0	66.7	59

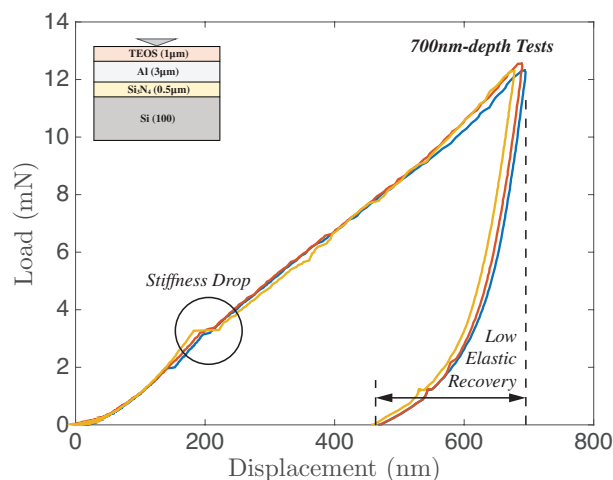


Figure C.9. Three repetitions of load-displacement response of the TEOS-Al-Si₃N₄-Si multilayer stack at 700 nm penetration depth. The stiffness drop and the low elastic recovery are likely a result of the dielectric cracking and material yielding.

C.3.2 Multilayer Stack

We next carried out indentation tests on the TEOS-Al-Si₃N₄-Si multilayer stack (Figure C.5b). The corresponding load-displacement response at 700 nm penetration depth is shown in Figure C.9. Compared with the TEOS-Si two-layer stack, the multilayer stack is more prone to cracking and yielding (see Figure C.9) due to the lower thickness of the TEOS layer and/or the low yield strength of the Al layer. This in turn results in a larger error in the calculated effective modulus at a given depth.

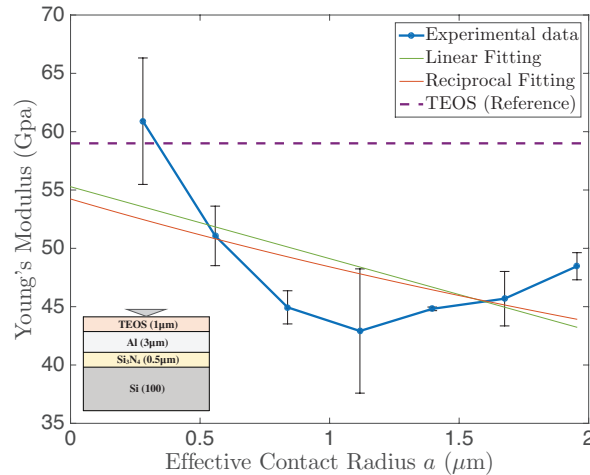


Figure C.10. Multi-depth indentation data for the TEOS-Al-Si₃N₄-Si multilayer stack. Linear regression over data from all depths leads to a poor fit.

Table C.2.

TEOS modulus extracted from the TEOS-Al-Si₃N₄-Si multilayer specimen.

	100nm	Regression Analysis		Ref. [158]
		Linear	Reciprocal	
E_{TEOS} (GPa, all data points)	60.9	55.3	54.2	59
E_{TEOS} (GPa, TEOS regime)		65.0	68.6	

The four material participation functions (N_{TEOS} , N_{Al} , $N_{\text{Si}_3\text{N}_4}$ and N_{Si}) are plotted in Figure C.4, which indicates that the TEOS layer is dominant in the modulus composition when the effective contact area does not exceed $1.25 \mu\text{m}$. This limiting contact area in turn limits the depth of indentation that should be used for estimating the E_{TEOS} . Figures C.10 and C.11 illustrate the multi-depth indentation data along with the regression analysis using all data points and the data within the TEOS dominant regime, respectively. The extrapolated E_{TEOS} are summarized in Table C.2.

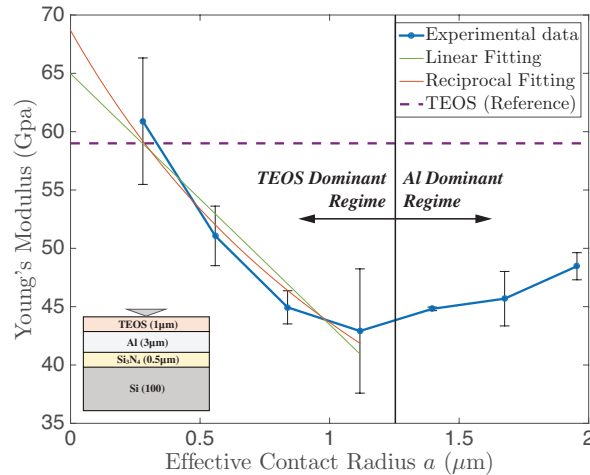


Figure C.11. Multi-depth indentation data for the TEOS-Al-Si₃N₄-Si multilayer stack. Linear regression over the TEOS dominant regime yields a good fit.

It is clear from the data that the effective modulus of the multilayer stack varies non-linearly as the indenter reaches the dominant regime of the second-layer (Al). Therefore, including the data beyond the TEOS dominant regime leads to a very poor fit. The linear regression in the TEOS dominant regime not only provides a better fit, but also yields an elastic modulus value that is consistent with that obtained from tests on the two-layer stacks ($E_{\text{TEOS}} \approx 66 \text{ GPa}$).

C.4 Inverse Finite Element Analysis Procedure

In this section, the inverse finite element analysis (IFEA) technique is described. Compared with the methods proposed in Section C.2, the numerical approach introduced in this section provides an alternative way to estimate the modulus of the top-layer film and to further estimate the yield strength through optimization-based inverse analysis. It is worth noting that the reduced modulus in Eq. (C.3) only relies on the initial elastic unloading part of the load-displacement response whereas the loading portion is completely ignored. Inverse finite element analysis, on the other

hand, attempts to fit to both the loading and the unloading part of the indentation response.

The IFEA technique includes two major components: a finite element analysis solver that numerically determines the load-displacement response based on the constructed model, and an optimization subroutine that iterates on the modulus and yield strength of the top-layer film in the finite element model to match the simulated load-displacement response to the experimental response. The approach used here differs from those in the literature [149] in using the optimization algorithm to estimate the elastic modulus and yield strength of the top layer film. The details of IFEA techniques are described in the following subsections.

C.4.1 Finite Element Model

The finite element model consists of a Berkovich indenter and the specimen to be indented. To reduce the finite element model computational cost, an axi-symmetric model is utilized in this paper. Therefore, the Berkovich indenter is modeled as an effective conical indenter with an half apex angle of $\theta = 70.3^\circ$ such that the projected contact area of the conical indenter, $A_{conical} = \pi h^2 \tan^2 \theta$, is identical to that of the Berkovich indenter, $A_{Berkovich} = 24.56h^2$, throughout the indentation process. Both the two-layer and the multilayer stacks are assumed to be $25 \mu m$ in thickness and $25 \mu m$ in width so that the far-field boundary effect around the indented region and its neighborhood is minimized. The thickness of each of the films in the model was per the nominal dimension indicated in Figure C.5a and Figure C.5b for TEOS-Si stack and TEOS-Al-Si₃N₄-Si stack, respectively.

The indenter and the test specimen were both discretized using 4-node bilinear axi-symmetric solid elements. The average element size of indenter was $0.15 \mu m$ whereas the global element size of specimen was $0.5 \mu m$. To accurately evaluate the load-displacement response during indentation, a $5 \times 5 \mu m^2$ rectangular region near the contact surface of specimen was discretized by elements of size 80 nm. Due to the

large degree of mesh distortion caused by deformation during indentation, arbitrary Lagrangian-Eulerian (ALE) adaptive mesh technique was applied to the elements of indented films to control the quality of mesh at every time step. Elements were neither generated nor eliminated during the simulation. A total of 7,366 nodes and 7,205 elements were used to represent the TEOS-Si two-layer stack model, and a total of 9,307 nodes and 9,136 elements were used to discretize the TEOS-Al-Si₃N₄-Si multilayer stack model.

The diamond indenter and Si (100) substrate were assumed to be purely elastic while the other materials in the model were considered to be elastic-plastic as summarized in Table C.3. All materials were assumed to be isotropic unless explicitly stated. Specifically, the Si (100) substrate was considered to be orthotropically elastic as suggested by Hopcroft et al. [159]. Kinematic hardening plastic behavior was assumed for the aluminum film in the multilayer stack. Elastic modulus and yield strength of TEOS were both set as parameters to be updated by the optimization subroutines whereas its Poisson's ratio was set to the constant nominal value listed in the table.

Table C.3.

Nominal mechanical properties used in the model and their literature sources.

Material	E (GPa)	ν	σ_Y (GPa)	References
Diamond	1140	0.07	-	[160]
Aluminum	70	0.33	0.116	[161]
Silicon Nitride	222	0.28	5.69	[162]
TEOS	59	0.24	unknown	[158]

The indentation process was driven in the model through the displacement boundary condition applied on the top surface of the indenter. Details of other boundary conditions such as axisymmetry along the center line and the support from the bottom surface to the Si (100) substrate are illustrated in Figure C.12. Frictionless contact between the indenter and the top layer film was assumed since the influence of the

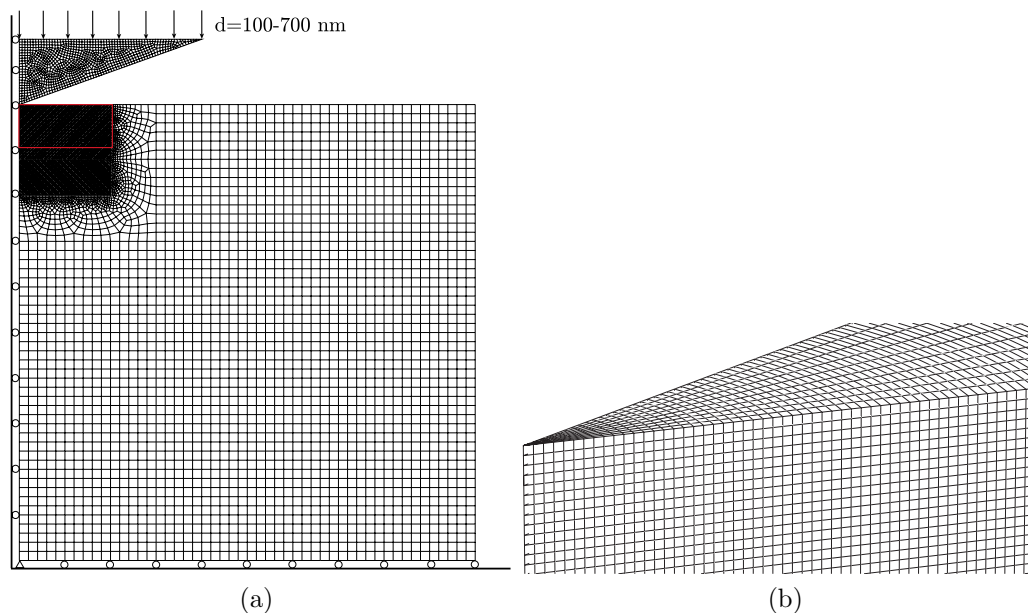


Figure C.12. (a) Mesh and boundary conditions of the TEOS-Si two-layer finite element model. (b) Enlarged 30° sweep section of the axis-symmetric model near the indented region (indicated by the red box in (a)).

friction coefficient on the indentation response was not significant for the indenter geometry, penetration depths and solids considered in this paper as suggested by previous studies [143, 163, 164]. The finite element model was constructed and analyzed using the commercial software, ABAQUS (Dassault Systèmes Simulia Corp., RI, USA).

The limitations of the finite element model used in this study include the following. First, the model does not allow any crack initiation or propagation within each layer or along the interface between adjacent films. Hence, the dissipated energy due to debonding of material during indentation experiment would be indirectly captured as a lower effective yield strength. Second, there are uncertainties in the elastic-plastic constitutive behavior and hardening behavior of the films. Third, there are uncertainties in the structure of the specimen such as the thickness or the homogeneity of each film.

C.4.2 Posing of Property Estimation as an Optimization Problem

The estimation of modulus and yield strength of top-layer film was formulated as a nonlinear optimization problem:

$$\begin{aligned} & \underset{E, \sigma^Y}{\text{minimize}} && f(E, \sigma^Y, h_{max}) \\ & \text{subject to} && E_{lb} \leq E \leq E_{ub} \\ & && \sigma_{lb}^Y \leq \sigma^Y \leq \sigma_{ub}^Y \end{aligned}$$

where, f is the objective function, E is the elastic modulus, σ^Y is the yield strength of the top-layer film and h_{max} is the penetration depth. The subscripts lb and ub denote the lower and upper bounds of the parameter to be optimized. We considered two objective functions to match the simulated response to the experimental response. The first objective function, $f_1(E, \sigma^Y, h_{max})$, was defined as:

$$\begin{aligned} f_1 = \sum_i^m \{ & [P_{load}^{EXP}(h_i) - P_{load}^{FEA}(E, \sigma^Y, h_i)]^2 \\ & + [P_{unload}^{EXP}(h_i) - P_{unload}^{FEA}(E, \sigma^Y, h_i)]^2 \} \end{aligned} \quad (\text{C.14})$$

where, m is the number of sampling points, P is the applied load, h is the indentation depth such that $h_i \in [0, h_{max}]$. The subscripts *load* and *unload* indicate the portion of the load-displacement response while the superscripts *EXP* and *FEA* indicate the response obtained from experiment or finite element analysis. The second objective function was defined as:

$$f_2 = \sum_j^n f_1(E, \sigma^Y, h_j) \quad (\text{C.15})$$

where, n is the number of indentation tests, each one corresponding to a specific penetration depth with $h_j \in [200, 700]$ nm. The 100-nm indentation was not modeled due to the need for extensively refined mesh discretization near the indented region

to reproduce the load-displacement response. The first objective function enables property estimation based on fit to the experimental response at a specific penetration depth while the second objective function yields a fit over indentations at multiple penetration depths in an average sense.

Each optimization run was started from two sets of initial parameter values, i.e., E_{TEOS} and σ_{TEOS}^Y , such that the experimental load-displacement response was bounded by the simulated responses. The starting parameters were also set as the lower and upper bounds of the optimized parameters as shown in Table C.4. Based on the nominal value reported in the literature [158], 50 and 80 GPa were chosen as the bounds for the elastic modulus of TEOS. Since very few studies have estimated the yield strength of TEOS in the literature, reasonable bounding values were estimated to be 1 and 8 GPa as shown in Figure C.13.

Table C.4.
Initial parameter values for the optimization problem.

Parameter Set	E (GPa)	σ^Y (GPa)
1 (Lower bound)	50.0	1.00
2 (Upper bound)	80.0	8.00

Finite element solver and optimization subroutines are integrated and controlled by Simulia Isight (Dassault Systèmes Simulia Corp., Johnston, RI, USA). After extensive numerical trials, Pointer control algorithm was chosen since it provided robust solutions against numerical noise resulting from finite element solution. The algorithm uses a complementary set of optimization methods including downhill simplex, linear simplex, sequential quadratic programming, and genetic algorithms. An additional advantage of this algorithm is its ability to solve optimization problem in a fully automatic manner without user's intervention [165].

In addition to the optimized solution, exhaustive sweep of the parameter space was carried out to investigate the uniqueness of the properties estimated through optimization since the search algorithms in general guarantee only a local minimum. We

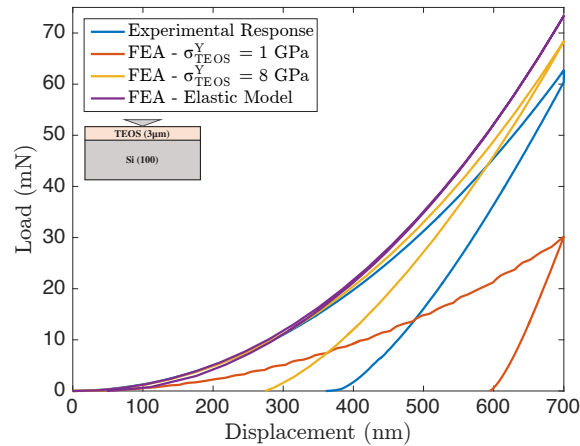


Figure C.13. Load-displacement response curves from experiment and from FEA. The impact of the value of the yield strength of TEOS film on the simulated response is illustrated.

performed full-factorial statistically designed experiments over the two-dimensional parameter space spanned by the arithmetic sequence (12×12) of TEOS modulus and yield strength values. Objective function values Eqs. (C.14) and (C.15) were then calculated over the parameter space. Response surface using triangulation-based cubic interpolation was subsequently constructed so that the uniqueness of the IFEA solution could be verified by examining the topology of the response surface.

C.5 Inverse Finite Element Analysis Results

The modulus and yield strength of TEOS film were estimated by applying IFEA using Eq. (C.14) for each penetration depth and later averaging the behavior using Eq. (C.15) over depths from 200 nm to 700 nm.

C.5.1 Two-layer Stack

The estimated elastic modulus and yield strength of TEOS film on TEOS-Si two-layer stack are tabulated in Table C.5. The predicted optimal response and the un-

Table C.5.
Estimated Young's modulus and yield strength of TEOS film on two-layer stack by IFEA

Depth (nm)	Estimated Properties		Starting Parameter Set
	E (GPa)	σ^Y (GPa)	
200	75.1	6.40	1
	75.1	6.40	2
300	72.6	5.62	1
	72.6	5.62	2
400	70.5	5.51	1
	70.5	5.50	2
500	68.3	5.53	1
	68.3	5.53	2
600	66.2	5.49	1
	66.2	5.50	2
700	65.6	5.01	1
	65.6	5.01	2
200-700	69.7	5.32	1
	69.7	5.32	2

derlying optimized property values converged to identical solutions regardless of the starting guess, that is, regardless of whether one started from the lower or the upper bound values of the parameters. In Figure C.14, the response surface contours from full-factorial statistically designed finite element simulation is shown. The topology of the response surface verifies the uniqueness of the estimated properties within the parameter space. Also, the objective function is more sensitive to the yield strength than the modulus of TEOS since the contours are elongated and nearly aligned in orientation along the modulus axis. The optimal properties obtained through IFEA are nearly identical to the solution obtained through interpolation of data from exhaustive parametric variation. As shown in Figure C.15, the finite element load-displacement responses using optimized modulus and yield strength values of TEOS fit to the experimental response very well.

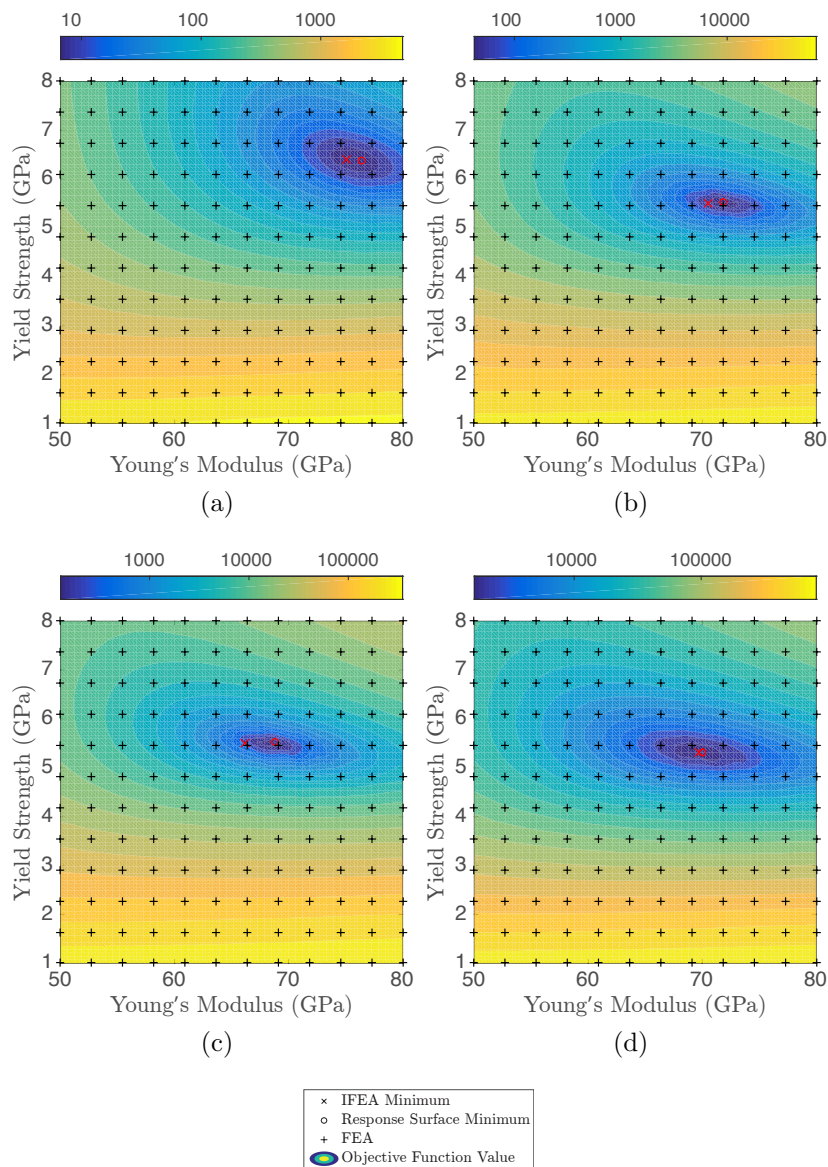


Figure C.14. Objective function response surface contours as well as optimized parameter values on the two-layer stack corresponding to indentation depths of: (a) 200 nm (a) 400 nm (c) 600 nm using Eq. (C.14) and (d) from 200 nm to 700 nm using Eq. (C.15).

From Table C.5, the high yield strength of TEOS previously suggested by the experimental response in Section C.3 appears confirmed. The estimated yield strength of TEOS decreases with increasing depth which may possibly be attributed to energy-

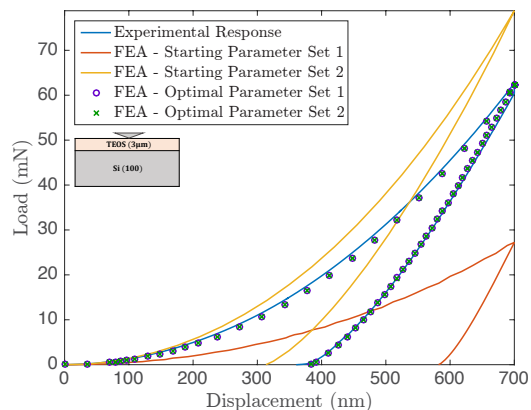


Figure C.15. Load-displacement response on the two-layer stack using the optimized properties compared against the experimental response for 700 nm indentation.

dissipating events such as micro-cracking in TEOS that do not manifest as significant discontinuity in overall load-displacement response. Hence, the estimated yield strength at the smallest depth may be considered to be the most accurate value. Elastic modulus, on the other hand, has no physical reason to vary during the indentation test. A reasonable estimation of the modulus is the value that fit to all the experimental response from 200 nm to 700 nm in an average sense. Therefore, the modulus and yield strength of TEOS based on the two-layer stack experiments were estimated as 69.7 GPa and 6.40 GPa, respectively.

C.5.2 Multilayer Stack

The estimated moduli and yield strengths of TEOS film on the multilayer TEOS-Al-Si₃N₄-Si multilayer stack are listed in Table C.6.

As with the two layer stack, the estimated properties converge to a unique value at each depth regardless of the initial guess. Figure C.16 shows the response surface contours characterized by full-factorial statistically designed finite element simulations for the multilayer stack. As before, the topology of the response surfaces indicates that the estimated properties within the parameter space is unique. But, the objective

Table C.6.
 Estimated Young's modulus and yield strength of TEOS film on multi-layer stack obtained through IFEA

Depth (nm)	Estimated Properties		Starting Parameter Set
	E (GPa)	σ^Y (GPa)	
200	66.7	4.42	1
	66.7	4.41	2
300	55.0	3.02	1
	55.0	3.02	2
400	52.7	3.22	1
	52.7	3.22	2
500	55.7	3.28	1
	55.7	3.28	2
600	60.0	3.10	1
	60.0	3.10	2
700	62.1	3.18	1
	62.3	3.19	2
200-700	59.3	3.19	1
	59.1	3.19	2

function is even less sensitive to the modulus of TEOS in comparison to the two-layer stack result of Figure C.14. The estimated modulus and yield strength of TEOS film on multilayer stack is 59.2 GPa and 4.42 GPa, respectively. Unlike the results obtained from the two-layer stack, the estimated values from the multilayer stack are much lower. A comparison between the finite element load-displacement response using the estimated modulus and yield strength of TEOS compared against the experimental response is shown in Figure C.17.

On the multilayer stack, the simulated response shown in Figure C.17, while providing a reasonable overall fit and accurate fit to the loading portion of the experimental data, is less accurate beyond the initial unloading portion of the data. One possible cause for this inaccuracy is the uncertainty in the assumed mechanical properties of the underlying films, which are less of a concern in a two-layer stack. The

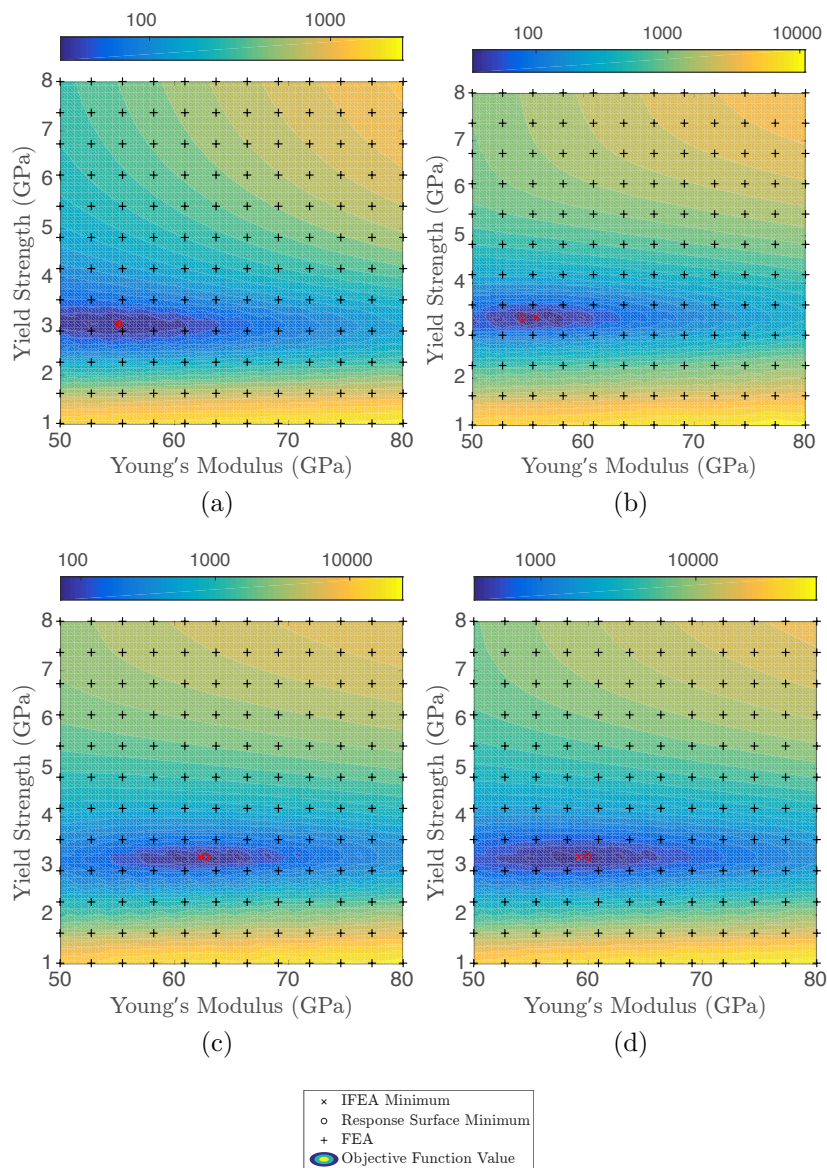


Figure C.16. Objective function response surface contours as well as optimized parameter values on the multilayer stack corresponding to indentation depths of: (a) 300 nm (b) 500 nm (c) 700 nm using Eq. (C.14) and (d) from 200 nm to 700 nm using Eq. (C.15).

yield strength of the aluminum film may be significantly different from its nominal value depending on the fabrication process but the elastic behavior of Si (100) is expected to show less uncertainty. In addition, the thickness of the TEOS film on the

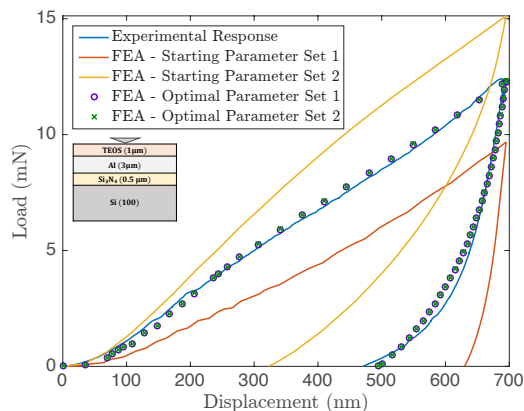


Figure C.17. Load-displacement response on the multilayer stack using the optimized properties compared against the experimental response for 700 nm indentation.

multilayer stack is one third of the thickness of the TEOS film on the two-layer stack. Hence, the overall response is influenced by the contribution from the underlying aluminum film in the multilayer stack. In order to estimate the modulus and yield strength of the top-layer film on a multilayer stack through IFEA more accurately, it is preferable to have the underlying film with greater certainty in constitutive behavior and a relatively thick top-layer film. Therefore, the estimates of properties obtained on the two-layer stack are more accurate.

C.6 Conclusion

The elastic modulus of top-layer film on multilayer stacks can be estimated by carrying-out multi-depth indentation tests and extrapolating the effective modulus to zero penetration. In the present study, two well-established functions (Gao's and reciprocal of Gao's) and two recently proposed functions (linear and reciprocal of linear) have been used in the regression analysis of two-layer and multilayer stacks, respectively.

A new dominant regime theory has been proposed to determine the layer which has the maximum contribution to the effective modulus as the indentation depth increases. Based on the theory, we can improve the accuracy of the modulus estimation by indenting the specimen only in the dominant regime of the layer of interest. The technique is demonstrated through extraction of the modulus of TEOS film on both two-layer and multilayer BEOL specimens. A consistent TEOS modulus ($E_{\text{TEOS}} \approx 66 \text{ GPa}$) is obtained with the technique.

An optimization-based inverse finite element analysis technique is proposed to estimate both the modulus and the yield strength of the top-layer film in a stack. IFEA is applied to both two-layer and multilayer stack and uniquely converged results are obtained. While both two-layer and multilayer stacks were used to estimate TEOS modulus and yield strength, the values from the two-layer stack ($E_{\text{TEOS}} \approx 69.7 \text{ GPa}$, $\sigma_{\text{TEOS}}^Y \approx 6.40 \text{ GPa}$) is likely to be more accurate than the estimated values for the multilayer stack ($E_{\text{TEOS}} \approx 59.2 \text{ GPa}$, $\sigma_{\text{TEOS}}^Y \approx 4.42 \text{ GPa}$).

C.7 Proof of the Monotonicity of the Weight Function

Theorem C.7.1 *The weight function $\Phi_0(x)$ is monotonically decreasing from one to zero in the domain $x \in (0, \infty)$.*

Proof

$$\begin{aligned}
\Phi_0'(x) &= -\frac{2}{\pi} \frac{1}{1+x^2} + \frac{1-2\nu}{2\pi(1-\nu)} \left[\frac{2}{1+x^2} - \frac{\ln(1+x^2)}{x^2} \right] \\
&\quad + \frac{1}{2\pi(1-\nu)} \frac{-1+x^2}{(1+x^2)^2} \\
&= \frac{1}{\pi(1-\nu)(1+x^2)} \left[-2(1-\nu) + 1 - 2\nu + \frac{1}{2} \right] \\
&\quad - \frac{1}{2\pi(1-\nu)} \left[\frac{1-2\nu}{x^2} \ln(1+x^2) + \frac{2}{(1+x^2)^2} \right] \\
&= -\frac{1}{2\pi(1-\nu)} \left[\frac{1-2\nu}{x^2} \ln(1+x^2) + \frac{3+x^2}{(1+x^2)^2} \right] \\
&< 0
\end{aligned} \tag{C.16}$$

i.e., $\Phi_0(x)$ is monotonically decreasing. Next we consider the limits of the function as follows:

$$\lim_{x \rightarrow 0^+} \Phi_0(x) = 1 + \frac{1 - 2\nu}{2\pi(1 - \nu)} \lim_{x \rightarrow 0^+} \frac{\ln(1 + x^2)}{x} = 1 \quad (\text{C.17a})$$

$$\lim_{x \rightarrow +\infty} \Phi_0(x) = \frac{1 - 2\nu}{2\pi(1 - \nu)} \lim_{x \rightarrow +\infty} \frac{\ln(1 + x^2)}{x} = 0 \quad (\text{C.17b})$$

Thus, $\Phi_0(x) \in (0, 1]$ ■

C.8 Linearization of the Weight Function

The Maclaurin series for the weight function $\Phi_0(x)$ is given by

$$\Phi_0(x) = \Phi_0(0) + \Phi_0'(0)x + \frac{\Phi_0''(0)}{2}x^2 + O(x^3) \quad (\text{C.18})$$

where, for the simplicity of notation, the right-hand limits as $x \rightarrow 0^+$ are represented by the function value and the derivatives at $x = 0$. Based on the derivation in Theorem C.7.1, we can obtain $\Phi_0(0) = 1$ and $\Phi_0'(0) = -\frac{2-\nu}{\pi(1-\nu)}$. The second derivative of $\Phi_0(x)$ is derived as follows:

$$\Phi_0''(x) = -\frac{1}{\pi(1-\nu)} \left[(1-2\nu) \frac{x^2 - (1+x^2)\ln(1+x^2)}{x^3(1+x^2)} - \frac{x(5+x^2)}{(1+x^2)^3} \right] \quad (\text{C.19})$$

Thus,

$$\begin{aligned} \lim_{x \rightarrow 0^+} \Phi_0''(x) &= \lim_{x \rightarrow 0^+} -\frac{1-2\nu}{\pi(1-\nu)} \frac{x^2 - \ln(1+x^2)}{x^3} \\ &= \lim_{x \rightarrow 0^+} -\frac{1-2\nu}{\pi(1-\nu)} \frac{O(x^4)}{x^3} \\ &= 0 \end{aligned} \quad (\text{C.20})$$

The Eq. (C.18) can be rewritten as:

$$\Phi_0(x) = 1 - \frac{2 - \nu}{\pi(1 - \nu)}x + O(x^3) \quad (\text{C.21})$$

C.9 Properties of the Modulus Participation Functions

Theorem C.9.1 (Non-negativity) *The material participation function N_k satisfies $N_k \geq 0, k = 1, 2, \dots, n + 1$.*

Proof The N_k is discussed as follows:

$$\text{If } k = 1, N_k = N_1 = \Phi_0\left(\frac{a}{h_1}\right) > 0.$$

$$\text{If } k = n + 1, N_k = N_{n+1} = 1 - \Phi_0\left(\frac{a}{h_n}\right) \geq 0$$

If $2 \leq k \leq n$, $N_k = \Phi_0\left(\frac{a}{h_k}\right) - \Phi_0\left(\frac{a}{h_{k-1}}\right) \geq 0$, since $\frac{a}{h_k} \leq \frac{a}{h_{k-1}}$ and $\Phi_0(x)$ is monotonically decreasing. ■

Theorem C.9.2 (Partition of Unity) *The sum of all material participation functions for a given stack is equal to unity, i.e., $\sum_{k=1}^{n+1} N_k = 1$.*

Proof

$$\begin{aligned} \sum_{k=1}^{n+1} N_k &= N_1 + \sum_{k=2}^n N_k + N_{n+1} \\ &= \Phi_0\left(\frac{a}{h_1}\right) + \sum_{k=2}^n \left[\Phi_0\left(\frac{a}{h_k}\right) - \Phi_0\left(\frac{a}{h_{k-1}}\right) \right] \\ &\quad + \left[1 - \Phi_0\left(\frac{a}{h_n}\right) \right] \\ &= 1 \end{aligned} \quad (\text{C.22})$$

■

D. TOPOLOGY OPTIMIZATION FOR EFFICIENT HEAT REMOVAL IN THREE DIMENSIONAL PACKAGES

D.1 Introduction

Three-dimensional packages are currently considered important for economically enabling heterogeneous integration, improving the device performance and to reducing package size. A high level representation of three dimensional (3D) IC consisting of a stacked/multilayer structure is shown in Figure D.1. While 3D integration can improve device performance and allow heterogeneous integration, due to the increased thermal energy per unit area along with limited dissipation pathways, thermal issues are critical to 3D IC performance and reliability [166]. Specifically, one of the major reasons for the thermal issues in 3D integration is the rise in thermal resistance with the increasing number of layers within a package.

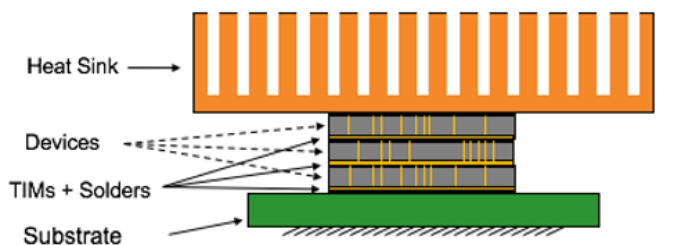


Figure D.1. Representative 3D package.

Compared to traditional 2D packages, current research on thermal management strategies for 3D packages is very limited. Common techniques to overcoming thermal challenges in 3D ICs include low power design, rearranging heat sources, improving heat sink or improving thermal conduits [167]. Passive cooling elements such as heat spreaders and thermal TSVs are commonly used to eliminate hotspots by increasing the systems effective thermal conductivity. Since the routing space in a 3D package is

limited, optimal configuration (location, size and number of heat spreading elements) needs to be determined to make the best use of space under non-uniform power distribution to achieve the desired thermal objectives. Therefore, many recent studies have focused on thermal TSV insertion algorithm or optimizing the parameters of TSVs to improve thermal pathways [168–174]. However, an efficient, systematic and automated thermal design tool that facilitates the combined thermal design including TSV, heat spreader and thermal interface material of 3D packages is currently unavailable.

In this study, a steady state heat conduction finite element analysis code is coupled with SQP algorithm to determine the optimal thermal design of heat spreader and thermal TSVs under specified metallization ratio constraint through topology optimization.

This paper will begin with a discussion on thermal modeling and numerical solution using the finite element method. Next, topology optimization using the SIMP method and sensitivity analysis to update the material distribution will be described. In the results and discussion section, a 2D example is used to validate and compare with the design solution from commercial software. The tool is then used to tradeoff the relative advantage of using heat spreaders directly on hotspot locations versus placing them homogeneously. Finally, a TSV insertion example is shown to demonstrate the ability to carryout TSV thermal design.

D.2 Thermal Conduction Analysis

For an arbitrary multilayer structure, the steady state heat conduction is described by the following governing equations:

$$-\nabla \cdot \mathbf{q} + g(\mathbf{r}) = 0 \quad (\text{D.1})$$

$$\mathbf{q} = -k\nabla T \quad (\text{D.2})$$

where \mathbf{q} is heat flux, g is heat generation per unit volume, \mathbf{r} is position vector, T is temperature, and k is the isotropic thermal conductivity. Appropriate boundary conditions for Eq. (D.1) depend on the nature of package, and may be either Dirichlet, Neumann or convection. In this study, the temperature field is solved using an efficient finite element code developed by the authors in the MATLAB environment. The code uses a mesh generated by a commercial finite element software (ABAQUS or ANSYS). The details are presented in the following subsections.

D.2.1 Finite Element Method

The well-established discretized governing equations of finite element analysis are of the form:

$$\mathbf{KT} = \mathbf{f} \quad (\text{D.3})$$

where \mathbf{K} is the global thermal conductivity matrix, \mathbf{T} is the nodal temperature vector and \mathbf{f} is the consistent nodal flux vector. Specifically, the global conductivity matrix is:

$$\mathbf{K} = \int_{\Omega} \mathbf{B}^T \mathbf{D} \mathbf{B} d\Omega \quad (\text{D.4})$$

where $\mathbf{D} = k_{el}\delta_{ij}$ is isotropic conductivity matrix, and \mathbf{B} is the thermal gradient-temperature matrix. In practice, efficiency of topology optimization largely depends on the efficiency of the solution to Eq. (D.3) [175]. Thus, the above finite element analysis (FEA) was implemented using sparse matrices, and the global conductivity matrix was integrated element-wise in parallel. Due to the sparsity and symmetric positive definite nature of global thermal conductivity matrix, a high performance library called SuiteSparse was used to manipulate and factorize sparse matrices [176].

D.2.2 Discretization

To solve the nodal temperature using finite element method, one needs to discretize the domain into elements. For general 3D packages, the simple 8-noded

serendipity element is sufficient to model the high level features of a 3D package in cross section. An example of isoparametric serendipity element that was used in the tool is shown in Figure D.2. The mesh, material properties and boundary conditions can be generated using commercial finite element software such as ABAQUS or ANSYS. Then, the mesh information along with material properties and boundary conditions are written into an ASCII input file, imported and parsed in MATLAB environment for further operation.

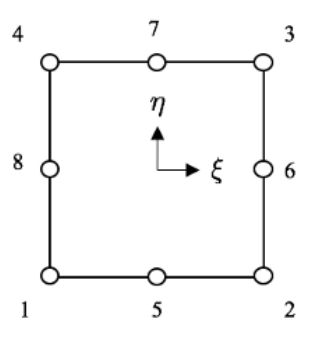


Figure D.2. Isoparametric 8-noded serendipity element.

Some of inter-device layers such as the interposer are potential regions designated for thermal TSV placement. The elements within these regions have variable thermal conductivities and are initially assigned homogeneous properties.

Note that the dependence on commercial software is only for obtaining a mesh that has minimal bandwidth in global conductivity matrix. The availability of graphical user interface to lay out the structure, material properties and boundary conditions in the commercial software is exploited in the developed tool. The sparse matrix FE solution as well as the iterative topology optimization are carried out in a standalone manner in the MATLAB environment.

D.3 Topology Optimization

Optimal thermal pathways of 3D packages were identified through topology optimization. A representative structure is shown in Figure D.3. Designated design regions such as the interposers or the top of the die are modified to enable the heat removal by thermal TSVs or heat spreader design, respectively. Thermal conductivity of TIM can also be optimized to achieve desirable thermal objectivities.

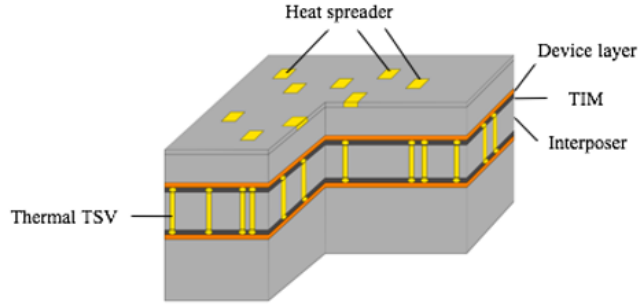


Figure D.3. Representative structure in a 3D package to perform topology optimization for efficient heat removal.

In this study, two objective functions were considered:

1. Minimizing peak temperature:

$$\min_{\rho_i} \frac{T_{max}}{T_{max,0}} \quad (D.5)$$

2. Minimizing stored energy:

$$\min_{\rho_i} \frac{\mathbf{f} \cdot \mathbf{T}}{\mathbf{f} \cdot \mathbf{T}_0} \quad (D.6)$$

with the constraints $0 \leq \rho_o \leq 1$ such that $\sum \rho_i/n_{el} \leq c_j$ in each Ω_j for each designated design region and satisfies equilibrium condition. ρ_i is the pseudo design density of the i th element used as design variable in topology optimization and c_j represents the allowable metallization ratio in the designated design regions. The second kind of

objective can be regarded as a thermal analogy to minimizing structural compliance which is commonly used in structural topology optimization problems.

The design procedure required the use of the constraint quantity shown below to ensure that no two TSVs were placed immediately adjacent to each other:

$$\sum_{i=1}^{M-1} \rho_i \rho_{i+1} + \sum_{j=1}^{N-1} \rho_j \rho_{j+1} \quad (\text{D.7})$$

This constraint was enforced by multiplying a large value and adding it to the objective as a penalty function. Here, M and N are the number of elements in the cross section of the layer containing the TSVs.

The topology optimization used in the present tool follows the typical iterative procedure shown in Figure D.4. Stopping criteria includes maximum number of iterations, maximum number of finite element analyses, minimum change in objective function value and design densities. The details of updating elemental thermal conductivity and sensitivity analysis are presented in the following sections.

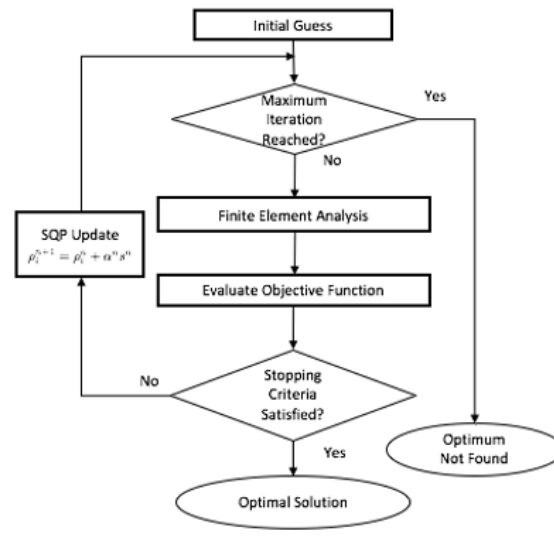


Figure D.4. Topology optimization flow of control.

D.3.1 Updating Thermal Conductivities

The solid isotropic material with penalization (SIMP) method was used to iteratively update the elemental thermal conductivities of designated regions:

$$k_i = \rho_i^p k_{i_1} + (1 - \rho_i^p) k_{i_0} \quad (\text{D.8})$$

where $p (> 1)$ is the penalty factor, and k_i is the thermal conductivity of i -th element with the subscript 1 and 0 representing the choice of new or original material respectively. The penalty factor p is chosen to be 3 so as to force the solution to either k_1 or k_0 at any point [177].

D.3.2 Sensitivity Analysis

Besides the efficient sparse matrix implementation of FEA, the use of sensitivity analysis also plays an important role in determining the efficiency of topology optimization. Assuming the derivative of consistent force vector with respect to the variation of conductivity is zero, that is

$$\frac{\partial \mathbf{f}}{\partial k_i} = 0 \quad (\text{D.9})$$

The variation of nodal temperature with respect to the perturbation of conductivity can be obtained by taking the derivative of Eq. (D.3).

$$\frac{\mathbf{T}}{k_i} = -\mathbf{K}^{-1} \frac{\mathbf{K}}{k_i} \mathbf{T} \quad (\text{D.10})$$

Specifically, the second term on the right hand side can be computed directly from the elemental conductivity matrix. By applying chain rule to Eq. (D.9), sensitivity with respect to design density can be obtained:

$$\frac{\mathbf{T}}{\rho_i} = -p \rho_i^{p-1} (k_{i_1} - k_{i_0}) \mathbf{K}^{-1} \frac{\mathbf{K}}{k_i} \mathbf{T} \quad (\text{D.11})$$

Similarly, sensitivity analysis for thermal compliance can be found using adjoint method [12],

$$\frac{\mathbf{f} \cdot \mathbf{T}}{\rho_i} = -p\rho_i^{p-1}(k_{i_1} - k_{i_0})\mathbf{T}^T \frac{\mathbf{K}}{k_i} \mathbf{T} \quad (\text{D.12})$$

The combined sensitivity of a number of elements is simply the summation of the sensitivity of the perturbation of individual design density.

D.4 Results and Discussion

The program was written in MATLAB and run on a Linux machine with AMD Opteron 2.3 GHz Processors. The optimization using the two objectives for a 2D example with a single concentrated heat source is studied and compared with homogeneous distribution of heat spreading material. Next, a multiple heat source example will be presented and compared against optimal solution obtained using a commercial software. Lastly, thermal design of a 3D package is demonstrated to determine optimal thermal TSV distribution.

D.4.1 Two Dimensional Heat Spreader Design

The optimal heat spreader design using the two objectives was carried out and compared on a problem with a concentrated heat source as shown in Figure D.5 to understand the difference between objectives, as well as against using a homogeneous layer with variable thermal conductivity. The simple plate was discretized into 21 by 21 8-noded serendipity elements. The initial thermal conductivity was set to $k_0 = 1$ $W/(m \cdot K)$ and heat spreading materials thermal conductivity was set to $k_1 = 4$ $W/(m \cdot K)$.

Peak temperature, mean temperature and max thermal gradient were investigated while the maximum metallization ratio constraint was incremented by 1%. Representative heat spreader design of 10, 20, 25 and 45% of metallization ratio using the two objectives are shown in Figure D.6. It was found that topology optimization

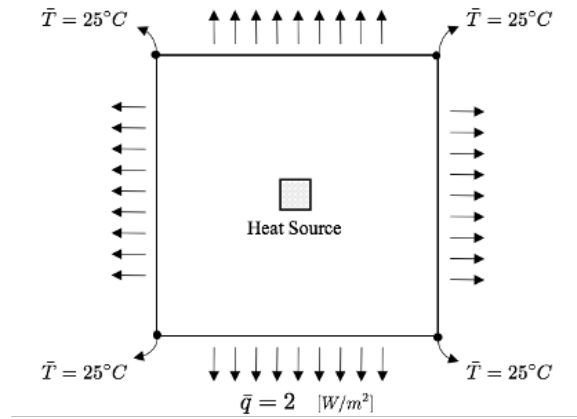


Figure D.5. Boundary conditions and power map on a plate 10 by 10 m in size.

using both objective functions reduced the peak temperature and thermal gradient in a similar (and efficient) manner as shown in Figures D.7 and D.8 but the run times of optimization with 441 design variables were 16.8 seconds and 317.8 seconds, respectively. Although the mean temperatures were different when using two objective functions as shown in Figure D.9, the importance of mean temperature is not as critical as peak temperature as well as peak thermal gradient in microelectronic devices. On the other hand, homogeneously distributed heat spreading material was not able to remove the heat as efficiently as achieved with optimal placement of heat spreading elements.

While homogeneously distributed design performed relatively poorly in reducing peak temperature and peak thermal gradient, it is a viable design alternative for the following reason. Since the cost of fabricating heterogeneous features is usually significant, homogeneous distributed heat spreading material might still be a cost effective option.

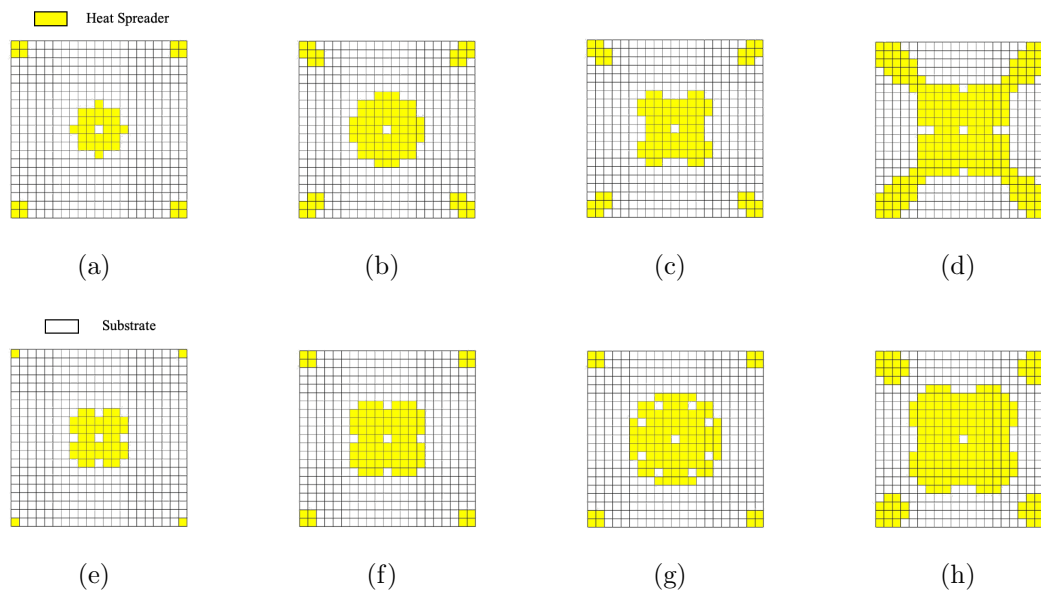


Figure D.6. Heat spreader design using (a)-(d) minimizing peak temperature and (e)-(h) minimizing stored energy objectives with metallization ratio of 10, 20, 25 and 45%, respectively.

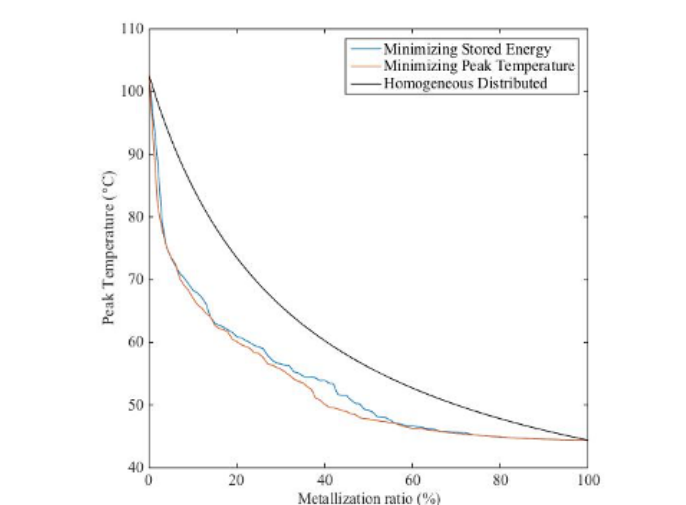


Figure D.7. Peak temperature with different metallization ratio using both objective functions and homogeneous distribution of heat spreading material.

D.4.2 Heat Spreader Design Validation

To validate the developed tool, topology optimization results was compared against the results obtained using Simulia Isight on a two dimensional multiple heat source

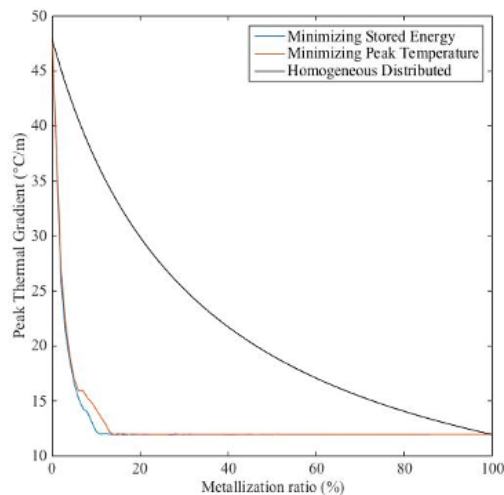


Figure D.8. Thermal gradient with different metallization ratio using both objective functions and homogeneous distribution of heat spreading material.

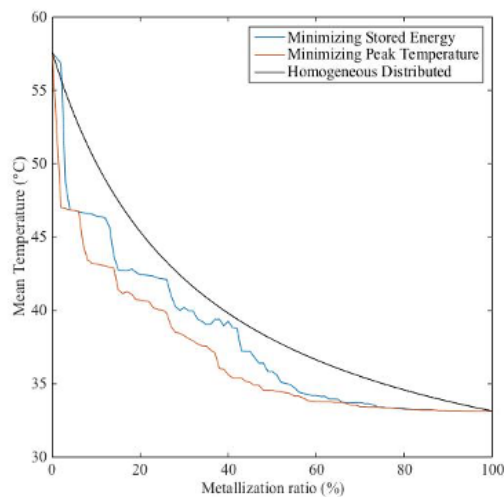


Figure D.9. Mean temperature with different metallization ratio using both objective functions and homogeneous distribution of heat spreading material.

problem shown in Figure D.10. In this problem, the plate was discretized into 11 by 11 8-noded quadrilateral serendipity elements. The initial thermal conductivity was set to $k_0 = 1 \text{ W}/(\text{m} \cdot \text{K})$ and heat spreading materials thermal conductivity was set

to $k_1 = 4 \text{ W}/(\text{m} \cdot \text{K})$. The objective was to minimize the peak temperature with a constraint on the metallization ratio of a maximum of 35%.

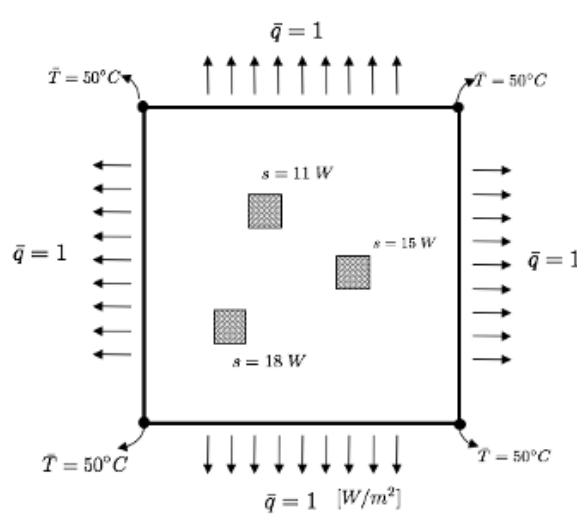


Figure D.10. Boundary conditions and power map on a plate 11 by 11 m in size.

A procedure similar to that shown in Figure D.4 was created in Simulia Isight using an SQP algorithm shown in Figure D.11. The temperature profile of initial and final iteration using Isight and the developed tool are shown in Figures D.12 and D.13, respectively.

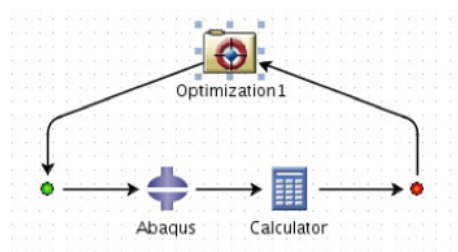


Figure D.11. Topology optimization flow of control in Isight.

The original peak temperature in the plate was 60.98°C . After topology optimization, the peak temperature was reduced to 54.90°C and 53.68°C using Isight and the developed tool, respectively. Although the heat spreader placement was different due

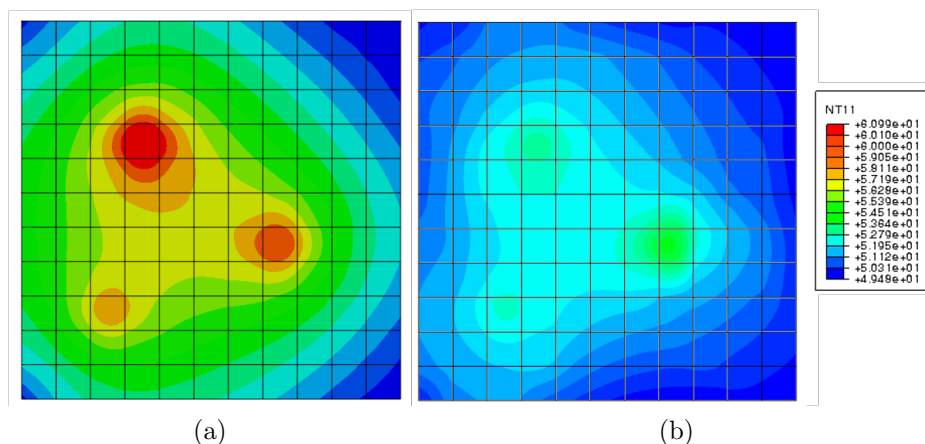


Figure D.12. Temperature profile (a) before and (b) after the topology optimization by Simulia Isight.

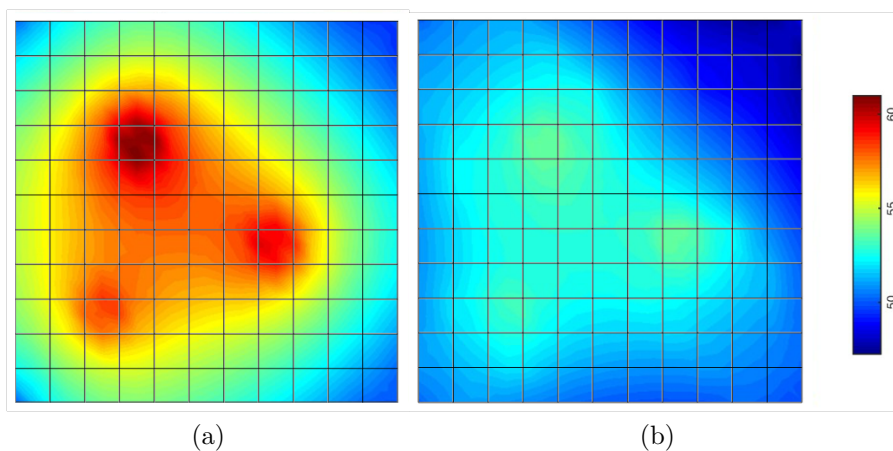


Figure D.13. Temperature profile (a) before and (b) after the topology optimization by the developed tool.

to the non-uniqueness of local optima, objective value was quantitatively very similar. One of the common concerns in topology optimization with a large number of design variables is efficiency. With the help of sensitivity analysis and the efficient sparse matrix implementation in FEA, the optimization run time of the present tool was only 22 seconds as compared to 2 hours and 39 minutes using Simulia Isight!

D.4.3 Thermal Design of TSVs

To demonstrate thermal design of stacked structures, a multilayer 3D package is considered. The structure of the model is shown in Figure D.14 which consists of 2 dies that are connected by a silicon interposer. The thickness of the stack is 5 mm in total and 5 mm in width. The dimension and bulk thermal conductivities of each layer are listed in Table 1. The boundary condition at the bottom was set to be isothermal at 50°C and the top surface had a weak Neumann boundary condition.

Table D.1.

Model thermal conductivities and thicknesses.

Component	Thickness (mm)	Thermal Conductivity ($W/(m \cdot K)$)
Die 1	2.6	116.5
Interposer	1.0	117.5
Die 2	1.4	117.5
Thermal TSV	1.0	385

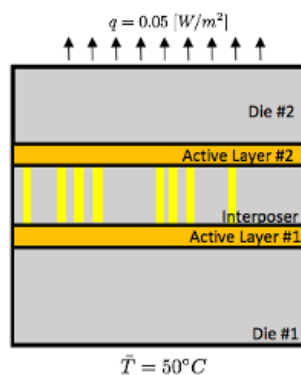


Figure D.14. Schematic of the 3D package which is integrated with a silicon interposer.

Given the power map shown in Figure D.15, the placement of thermal TSV and heat spreader were determined to reduce the peak temperature of the package. Furthermore, a non-stick constraint was exclusively applied to thermal TSV to preserve

sufficient routing space. With 20% of metallization ratio for thermal TSV, the optimal placement is shown in Figure D.16. The results shown in Figure D.17 indicate that the peak temperature dropped from 85.5°C to 79.1°C . In comparing the thermal profile and the distribution of thermal TSVs, it was observed that most of the thermal TSVs were placed around the hot zones instead of right on top of the heat source. The design solution that emerged was to spread the heat in the lateral direction first before conducting to higher levels using TSVs.

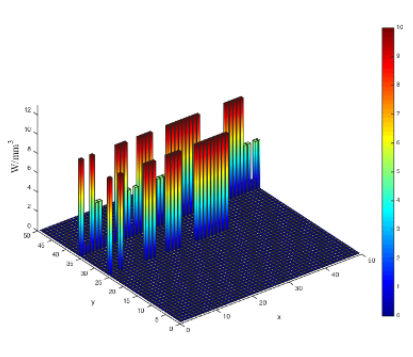


Figure D.15. Power map for active layer 1 and active layer 2.

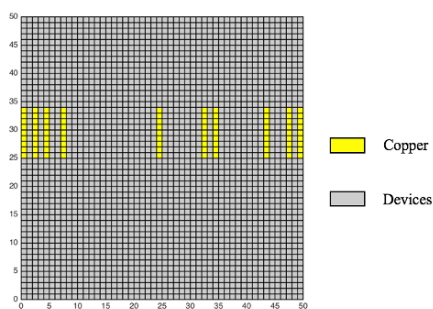


Figure D.16. Thermal TSV optimal distribution determined by topology optimization.

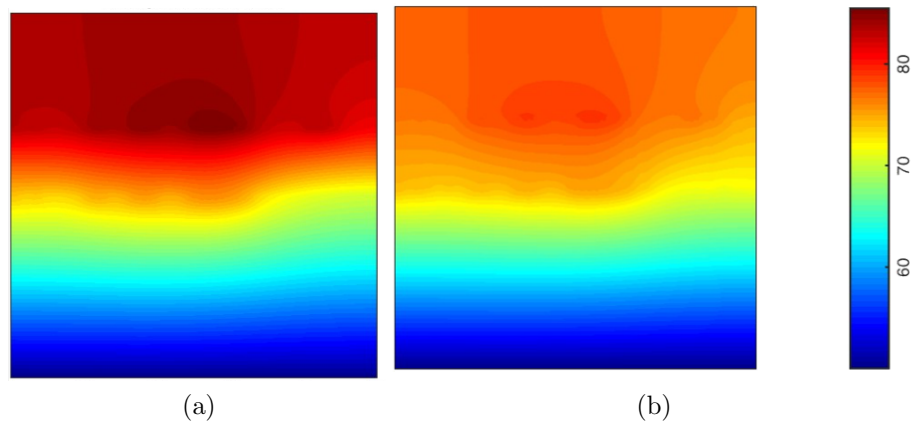


Figure D.17. Temperature profile of the 3D package (a) before and (b) after thermal TSV placement by topology optimization.

D.5 Conclusion

A topology optimization tool was developed for efficient heat removal in 3D packages by thermal TSV and heat spreader design. The developed tool required two orders of magnitude lower time for design as compared to a commercial tool. The tool will be useful for heat removal path optimization and decision during early design stages.

VITA

VITA

Chun-Pei Chen received his B.S in Mechanical Engineering from National Taiwan University in 2012. He is also the recipient of Lynn Fellowship in 2014. His research focuses on numerical methods for multi-patch coupling, stress singularities and fracture analysis. Chun-Pei's interests also involve thermal performance and thermo-mechanical reliability of microelectronics packages through characterization and numerical simulations. He was a student member of Cooling Technology Research Center at Purdue and Semiconductor Research Corporation during the course of his Ph.D.

Chun-Pei had multiple summer internships at Texas Instruments in the summer of 2011 (Taipei, Taiwan), 2017 (Dallas, TX) and 2018 (Dallas, TX). He joined the Technology and Manufacturing Group as a Packaging Engineer at Texas Instruments in December 2019.